NOVEL ENZYME-RESPONSIVE SELF-ASSEMBLED PEPTIDE NANOCARRIERS FOR THE TREATMENT OF NEURODEGENERATIVE DISEASES

YAMIR ISLAM

A thesis submitted in partial fulfilment of the requirements of Liverpool John Moores University for the degree of Doctor of Philosophy.

December 2020

Acknowledgement

I would like to express my gratitude to my supervisors, Dr Touraj Ehtezazi, Dr Andrew Leach and Dr Christopher Coxon for their kind support, valuable advice, motivation, encouragement and unmatched guidance.

I would like to special thanks to Dr Amos Fatokun for introducing me to cell culture and his guidance through the adventurous field of *in vitro* experiments. Also Dr James Downing provoked my thoughts for *in vitro* experiments. I would also like to mention Dr Kehinde Ross for training me on PCR experiments and widen my experience of cell culture. I would also like to thank Dr Darren Sexton and Dr Georgios Zouganelis for their precious support and training on flow cytometry and electrophoresis respectively. I would also like to thank Prof Jonathan Jarvis for kindly proving animals for *in vivo* experiments and supervising *in vivo* experiments. I would also like to thank Prof Harish Poptani and Dr Jack Sharkey (University of Liverpool) for their support and guidance in conducting IVIS experiments. I would also like acknowledge Dr Stefano Pluchino (University of Cambridge), Muttuswamy Sivakumaran (Peterborough City Hospital) and Meritxell Teixido (Institute for Research in Biomedicine) for their valuable advice and guidance. I would also like show my gratitude to Dr Iftikhar Khan for motivating me throughout the journey of PhD. Special thanks to my colleagues for their company on the journey of the PhD.

Last but not the least, my heartfelt thanks to my family particularly my parents and wife for their incredible love, support and encouragement through my study to achieve my goal.

Table of Contents

List of Tables

List of Figures

List of abbreviation

18A	DWLKAFYDKVAEKLKEAF peptide
7H6	Tight junction-associated antigen
α-Syn	α-synuclein
γ-T3	2R-γ-tocotrienol
Aβ	β-amyloid
AAV	Adeno-associated virus
ABCB1	ATP-binding cassette sub-family B member 1 (ABCB1)
AC	Astrocyte
AChR	Acetylcholine receptor
AD	Alzheimer's disease
AEPO	Asialo-erythropoietin
AF6	LL1-fused gene from chromosome 6 protein
AFM	Atomic force microscopy
AIDS	Acquired immune deficiency syndrome
AMT	Adsorptive-mediated transport
ANG	Angiopep
AP	Alternative complement pathway
ApoA-I	Apolipoprotein A-I
ApoB	Apolipoprotein B
ApoE	Apolipoprotein E
ApoE-rHDL	ApoE-reconstituted high density lipoprotein
AQP4	Aquaporin 4
ATRA	All-trans retinoic acid
AUC	Area under the curve
AuNP	Gold nanoparticle
AR	Adenosine receptor
ARH	Aarcuate nucleus of the hypothalamus
ASM	Acid sphingomyelinase
ASNP	Alginate-stearic acid nanoparticles
ATP	Adenosine triphosphate

B6	CGHKAKGPRK peptide
BACE1	β-site APP cleaving enzyme 1
BBB	Blood-brain barrier
BCEC	Brain capillary endothelial cell
BCRP	Breast cancer resistance protein
BCSFB	Blood-cerebrospinal fluid barrier
BL	Basal lamina
BPN	Brain penetrating particles
BSA	Bovine serum albumin
br	the ratio of drug in interstitial fluid / total drug in brain
C2-9r	H-CDIFTNSRGKRAGGGGrrrrrrrrr peptide, where r is D-arginine
C4BP	C4 binding protein
CAA	capillary cerebral angiopathy
CARPA	Complement activation related pseudoallergy
CASK	Calcium/calmodulin dependent serine protein kinase
CDDP	Cisplatin
C_{max}	Peak drug concentration
CMC	Critical micelle concentration
CMC-CBZ	Carbamazepine-loaded carboxymethyl chitosan nanoparticles
CMT	Carrier-mediated transport
CNS	Central nervous system
CNT	Carbon nanotubes
CP	Classical complement pathway
CR	Complement receptor
CR1	Complement receptor 1
CREB	cAMP response element-binding protein
CS-SA	Stearic acid-grafted chitosan
CSF	Cerebrospinal fluid
CT	Computed tomography
CVO	Circumventricular organ
CVR	Cellular vascular reactivity
DAF	Decay-accelerating factor

DBP	Vitamin D binding protein
DIV	Dynamic *in vitro*
DLS	Dynamic light scattering
DS-NP	Dextran-spermine nanoparticles
DSPE-PEG	Distearoyl-sn-glycero-3-phosphoethanolamine-poly(ethylene glycol)
DTPA	Diethylenetriaminepentaacetic acid
DTX	Docetaxel
EAE	Experimental autoimmune encephalomyelitis
EC	Endothelial cell
ECM	Extracellular matrix
EGFR	Endothelial growth factor receptor
EGFRvIII	Epidermal growth factor receptor variant III
ELIP	Echogenic liposomes
eNOS	Endothelial nitric oxide synthase
EPR	Enhanced permeability and retention
ERK	Extracellular signal-regulated kinase
ERT	Enzyme replacement therapy
ESAM	Endothelial cell adhesion molecule
FA	Folic acid
FBS	fetal bovine serum
FH	Factor H
FITC	Fluorescein isothiocyanate
fu	fraction of drug unbound to brain
FUS	Focused ultrasound
g7	7-amino acid glycoprotein, GFtGPLS (O-β-d-Glucoseglucose)CONH2
GE11	CYHWYGYTPQNVI peptide
GFP	green fluorescent protein
GLUT-1	Glucose transporter 1
GO	Graphene oxide
GSH	Glutathione
HA	Human astrocyte
hApoE	Human apolipoprotein E

HBMEC	Human brain-microvascular endothelial cells
HBVP	human brain microvascular pericytes
hCMEC/D3	Human cerebral microvascular endothelial cell line
HD	Huntington's disease
hGDNF	human glial cell-line derived neurotrophic factor
hIDS	Human iduronate-2-sulfatase
HIFU	High-intensity focused ultrasound
hiPSC	Human Induced Pluripotent Stem Cell
HIRMAb	Human insulin receptor monoclonal antibody
HIV	Human immunodeficiency virus
HM	Human microglia
HO	Human oligodendrocytes
HN	Human neurones
HSA	Human serum albumin
hsiRNA	Hydrophobically-modified siRNA
hTfR	Human transferrin receptor
HuHtt	Human huntingtin exon 1
ICAM	Intercellular adhesion molecule
IDUA	α-L-liduronidase
IDS	Iduronate-2-sulfatase
IFN-α	Interferon-α
IFN- γ	Interferon gamma
Ig	Immunoglobulin
IL-6	Interleukin-6
iNOS	Inducible nitric oxide synthase
IGF	Insulin-like growth factor
i.p.	Intraperitoneal
IP-10	Interferon gamma-induced protein-10
IR	Insulin receptor
ISF	Interstitial fluid
i.v.	Intravenous
JACOP	Junction-associated coiled coil protein (a.k.a. cingulin-like 1 or paracingulin)

JAM	Junctional adhesion molecule
L-Dopa	Leovdopa
Lamp2b	Lysosome-associated membrane protein 2b
LAT1	L-type amino acid transporter 1
LDL	Low-density lipoprotein
LDLR	Low-density lipoprotein receptor
LEX	lexiscan
Lf	Lactoferrin
LFA-1	Lymphocyte function-associated antigen 1
LMWP	Low molecular weight protein
LP	Lectin complement pathway
LPHNP	Lipid polymer hybrid nanoparticle
LRP	Low density lipoprotein receptor-related protein
LRP-1	lipoprotein receptor-related protein 1
mAb	monoclonal antibody
MAC	Membrane attack complex
MCAO	Middle cerebral artery occlusion
MAGI-1	Membrane-associated guanylate kinase
MALDI-MSI	Matrix-assisted laser desorption/ionization-mass spectrometry imaging
MAO-A	Monoamine oxidase A
MASP	Mannan-binding lectin serine protease
MB	Microbubble
MBL	Mannan-binding lectin
MCP	Membrane cofactor protein
MDR	Multiple-drug resistance
ME	Median eminence
MEF1	Murine embryonic fibroblast
Mfds2a	Major facilitator domain containing protein 2A
MHC	Major histocompatibility complex
miniAp-4	H-DapKAPETALD-NH2 peptide
MMP	Matrix metalloproteinase
MND	Motor neurone disease

MOAB	Monoaminoxidase-B
MOR	Opioid receptor mu
MPP+	1-methyl-4-phenylpyridinium
MPS	mucopolysaccharidosis (Type I, II or III)
MPTP	1-methyl-4-phenyl-1,2,3,6-tetrahydropyridine
MR	Magnetic resonance
MRgFUS	MR-guided focused ultrasound
MRI	Magnetic resonance imaging
MS	Multiple sclerosis
MSC	Mesenchymal stem/stromal cell
MTT	3-(4,5-dimethylthiazol-2-yl)-2,5-diphenyltetrazolium bromide
MTX	Methotrexate
MUPP1	Multi-PDZ Domain Protein 1
MWCNT	Multiple wall carbon nanotube
nAChR	Nicotinic acetylcholine receptor
NAD	Nicotinamide adenine dinucleotide
ND	Neurodegenerative Disease
NGF	Nerve growth factor
NP	Nanoparticle
NP-355	L-pGlu-(1-benzyl)–L-His–L-ProNH_2
NP-647	L-pGlu-(2-propyl)–L-His–L-ProNH_2
NRP1	Neuropilin 1
NIR	Near infrared
NSC	Neural Stem Cells
nSSL	nano-sterically stabilised liposomes
NVU	Neurovascular Unit
NW	Nanowire
OATP	Organic Anion Transporting Polypeptide
OD	Optical density
OL	Odorranalectin
P-gp	P-glycoprotein
PAH	Poly allylamine hydrochloride

PAMAM	Poly(amidoamine)
PAR	Partitioning Defective Protein
PBAE	Poly(beta-amino ester)
PBEC	porcine or bovine brain endothelial cell
PC	Pericyte
PCL	Paclitaxel
PD	Parkinson's Disease
PdI	polydispersity index
PEG	Polyethylene glycol
PEI	Polyethylenimine
PepH3	AGILKRW peptide
PET	Positron emission topography
PGB	Ginkgolide B pyrazine
PICHA	Polyisohexylcyanoaerylate
PLA	Poly(lactic acid)
PLCL	Poly(D,L-lactide-co-ε-caprolactone)
PLGA	Poly(lactic-co-glycolic acid)
p-MCAO	Permanent middle cerebra artery occlusion
PMNP	Polymeric nanoparticles
PMT	Poly(mannitol-co-PEI)
pSiNPs	Porous silica nanoparticles
PVP	Polyvinylpyrrolidone
RA	Retinoic acid
QD-Apt	Quantum dots conjugated with aptamer
RAGE	Receptor for advanced glycation end products
RBC	Red blood cell
RES	Reticuloendothelial system
RGS5	Regulator of G-protein signaling 5
RHA	Residual haemolytic activity
RhoA	Ras homolog gene family, member A
rhPDGF-BB	Recombinant human platelet-derived growth factor-BB
RLIP76	Ral-interacting protein of 76 kDa (a.k.a. Ral-binding protein 1, RalBP1)

RMP-7	Receptor-mediated permeabilizer 7
RMT	Receptor-mediated transcytosis
ROS	Reactive oxygen species
RVG	Rabies virus glycoprotein
RVG-29	YTIWMPENPRPGTPCDIFTNSRGKRASNG
SAH	Subarachnoid hemorrhage
SAS	Subarachnoid space
SB-3CT	(4-phenoxyphenylsulfonyl)methylthiirane
SDS	Sodium dodecyl sulfate (a.k.a. SLS)
SE	Status epilepticus
SELEX	Systematic Evolution of Ligands by EXponential enrichment
SEM	Scanning electron microscopy
SHp	Stroke homing peptide
siRNA	Small interfering RNA
SLC1A1	Solute carrier family 1 member 1
SLC2A1	Solute carrier family 2 member 1
SLNP	Solid lipid nanoparticle
SLS	Sodium lauryl sulfate (a.k.a. SDS)
SNALP	Stable nucleic acid lipid particle
SPARC	Secreted protein acidic and rich in cysteine
SPION	Superparamagnetic iron oxide nanoparticle
SPIONW	Superparamagnetic iron oxide nanowires
SQAd	Squalenoyl adenosine
SQV	Saquinavir
SVCT2	Sodium-dependent vitamin C transporter 2
SWCNT	Single wall carbon nanotube
t-MCAO	transient middle cerebral artery occlusion
TAMRA	Tetramethylrhodamine
TAT	Trans-activating transcriptional activator
TBI	Traumatic brain injury
TDS	Thiamine disulphide
TEER	Trans-endothelial electrical resistance

TEM	Transmission electron microscopy
Tf	Transferrin
TfR	Transferrin receptor
TJ	Tight junction
T_{max}	Time of peak drug concentration
TMC	Trimethyl chitosan
TNBC	Triple-negative breast cancer
TNF-α	Tumor necrosis factor-α
tPA	Tissue-type plasminogen activator
TPGS	d-α-tocopheryl polyethylene glycol 1000 succinate
TRH	Thyrotropin-releasing hormone
TUNEL	Terminal deoxynucleotidyl transferase dUTP nick end labelling
UCN	Urocortin
UPN	Un-PEGylated particles
USPIO	Ultrasmall Superparamagnetic Iron Oxide nanoparticles
VEGF	Vascular endothelial growth factor
VSOP	Very small superparamagnetic iron oxide particle
WHO	World Health Organisation
WST-1	Water-soluble tetrazolium salt 1
XTT	2,3-bis-(2-methoxy-4-nitro-5-sulfophenyl)-2H-tetrazolium-5-carboxanilide
ZO	Zonula occludens (a.k.a. tight junction protein)
ZONAB	ZO-1–associated nucleic acid binding protein

Amino acid	3-letter abbreviation	1-letter abbreviation
Alanine	Ala	A
Arginine	Arg	R
Asparagine	Asn	N
Aspartate	Asp	D
Cysteine	Cys	C
Glutamate	Glu	E
Glutamine	Gln	Q
Glycine	Gly	G
Histidine	His	H
Isoleucine	Ile	I
Leucine	Leu	L
Lysine	Lys	K
Methionine	Met	M
Phenylalanine	Phe	F
Proline	Pro	P
Serine	Ser	S
Threonine	Thr	T
Tryptophan	Trp	W
Tyrosine	Tyr	Y
Valine	Val	V

ABSTRACT

With an estimated worldwide cost over $1 trillion just for dementia, diseases of the central nervous system pose a major problem to health and healthcare systems, with significant socio-economic implications for sufferers and society at large. In the last two decades, numerous strategies and technologies have been developed and adapted to achieve drug penetration into the brain, evolving alongside our understanding of the physiological barriers between the brain and surrounding tissues. The blood brain barrier (BBB) has been described as the major barrier for drug delivery to the brain (1).

In this project, novel enzyme-responsive self-assembled peptide nanoparticles were developed for drug delivery to the brain. An enzyme, matrix metalloproteinase (MMP)-9, is crucial in the pathogenesis of neurodegenerative diseases has been targeted for our studies due to it's overexpression in neurodegenerative diseases and also due to it's function as a protease, allowing selective release of drug cargo in the brain of ND patients. Firstly, state of the art statistical and molecular modelling was used to predict the best substrate for MMP-9 by assigning a Y-score. These predictions were tested by employing novel fluorine (^{19}F) NMR spectroscopy. Novel MMP-9 sequences were identified, especially TY-26, that are better than those in previously reported studies. Secondly, novel enzyme-responsive self-assembled peptide nanoparticles were successfully synthesized with different combinations of MMP-9 sensitive and brain-targeting ligands. Most of the formulations self-assembled without sonication to form nanoparticles of 41-200 nm diameter with a zeta potential/ surface charge of 2-48 mV. The critical micelle concentration for all the self- assembled peptide nanoparticles calculated were around 7-110 mg/L. The encapsulation capacity ranged from 40-80%. TY-28, TY-39 and TY-44 were among the highest encapsulation capacity nano-formulations. Nanoparticles formulations were found to be MMP-9 sensitive and all formulations exhibited different release patterns of a model drug in the presence of external

stimuli. Novel enzyme-responsive self-assembled peptide nanoparticles were found to be least cytotoxic at lower concentration, however at higher concentration they were found to be cytotoxic, showing a range of cell viabilities.

In vitro uptake of enzyme-responsive self-assembled peptide nanoparticles was confirmed by confocal microscopy and flow cytometry. Enzyme-responsive self-assembled peptide nanoparticles showed up to 40-70% permeability when investigated by *in vitro* hCMEC/D3 blood-brain barrier model in healthy (50 ng) and diseased (100 ng) conditions. *In vivo* studies suggested that the enzyme-responsive self-assembled peptide nanoparticles managed to get into the brain of mice. Although in full body scans, no significant signal was observed, *ex vivo* experiments showed that enzyme-responsive self-assembled nanoparticles managed to permeate into the brain. These enzyme-responsive self-assembled peptide nanoparticles can be used to deliver drug molecules such as siRNA into brain.

CHAPTER – 1 LITERATURE REVIEW AND BACKGROUND

1.1. Introduction

The central nervous system (CNS) comprises the brain and the spinal cord. Any injury or damage to the CNS affects its normal functioning and may lead to permanent disability in many cases, due to a largely limited ability for neural tissue regeneration in humans (2, 3). The broad term “Neurodegenerative Diseases” (NDs) covers a range of pathologies, principally affecting neurons in the brain and causing significant neuronal dysfunction, neuronal death and neuronal loss. NDs once established are irreversible and sapping conditions resulting in progressive degeneration of neuronal cells (4). The signs and symptoms are diverse in range, depending on the affected part of the brain. The cause of an ND is often unknown but can involve a complex convergence of multiple molecular mechanisms; and disease progression is usually unpredictable. NDs include a number of conditions: Alzheimer’s disease (AD) and other forms of primary dementias, Multiple Sclerosis (MS) and other forms of chronic inflammatory neurological disease, Parkinson’s disease (PD), Motor Neurone Disease (MND), Huntington’s disease (HD) and ataxias (5-7). The World Health Organisation (WHO) reported that NDs affect around 0.1 billion individuals (24 million individuals suffer from AD and other dementias) (8) all over the world, and the incidence is on the rise as average life expectancy is increasing. Around 850,000 people in the UK are affected by dementia, costing the healthcare system over £26 billion a year (9). In the US nearly 100 million people are affected by NDs costing around $724 billion in 2014 (10). It is estimated that the cost of AD would be over 1 trillion dollars worldwide; (11) and the estimated number of people with dementia will reach 131.5 million by 2050 (12) in the absence of effective therapies. Just in Europe, the annual cost of neurological disease reaches 800 billion Euros per year, with a majority attributed to direct costs (13).

The brain is one of the most vital and sensitive organs in the body, which, to perform its functions in an appropriate way, needs nutrients and gases (14). Due to its pivotal role and functions, it is protected in a number of ways, including by the skull, the outer skin, three layers of meninges and the blood-brain barrier (BBB) (15). The BBB is a layer of endothelial cells (ECs) associated with pericytes (PCs) and astrocytes (ACs) and acts as a separator of the blood from parenchymal cells, thus preventing penetration of drugs into the CNS. It therefore, protects the brain from overexposure to substances such as potassium, glycine and glutamate, which, in high levels such as found in pathological conditions, are neurotoxic (16, 17).

Despite many advances in drug delivery systems that target the brain, it is still a challenging area. The failure of therapies administered via an intravenous (i.v.) or an oral route is often due to their inability to cross/penetrate the brain parenchyma. This review covers latest developments in drug delivery to the brain, as well as recent understanding of the physiological barriers between the brain and other tissues. The focus here is on drug delivery to the brain following i.v. injections, although other methods are briefly explained. The optimisation of nano-carriers is discussed by considering the effects of aging and diseases on brain physiological barriers.

1.2. Blood-Brain Barrier

Figure 1.1 is the schematic representation of healthy and diseased BBB. Numerous gateways have been reported to provide access to the brain; the most significant are through the blood stream or by getting access to the CSF circulation. Penetration of any molecules administered via the parenteral route is controlled by the BBB, the blood–cerebrospinal fluid barrier (BCSFB), arachnoid barrier and circumventricular organ barrier. However, drug molecules up taken by the brain are flushed back towards the blood through the return of the CSF to the blood or transporters on the BBB (18).

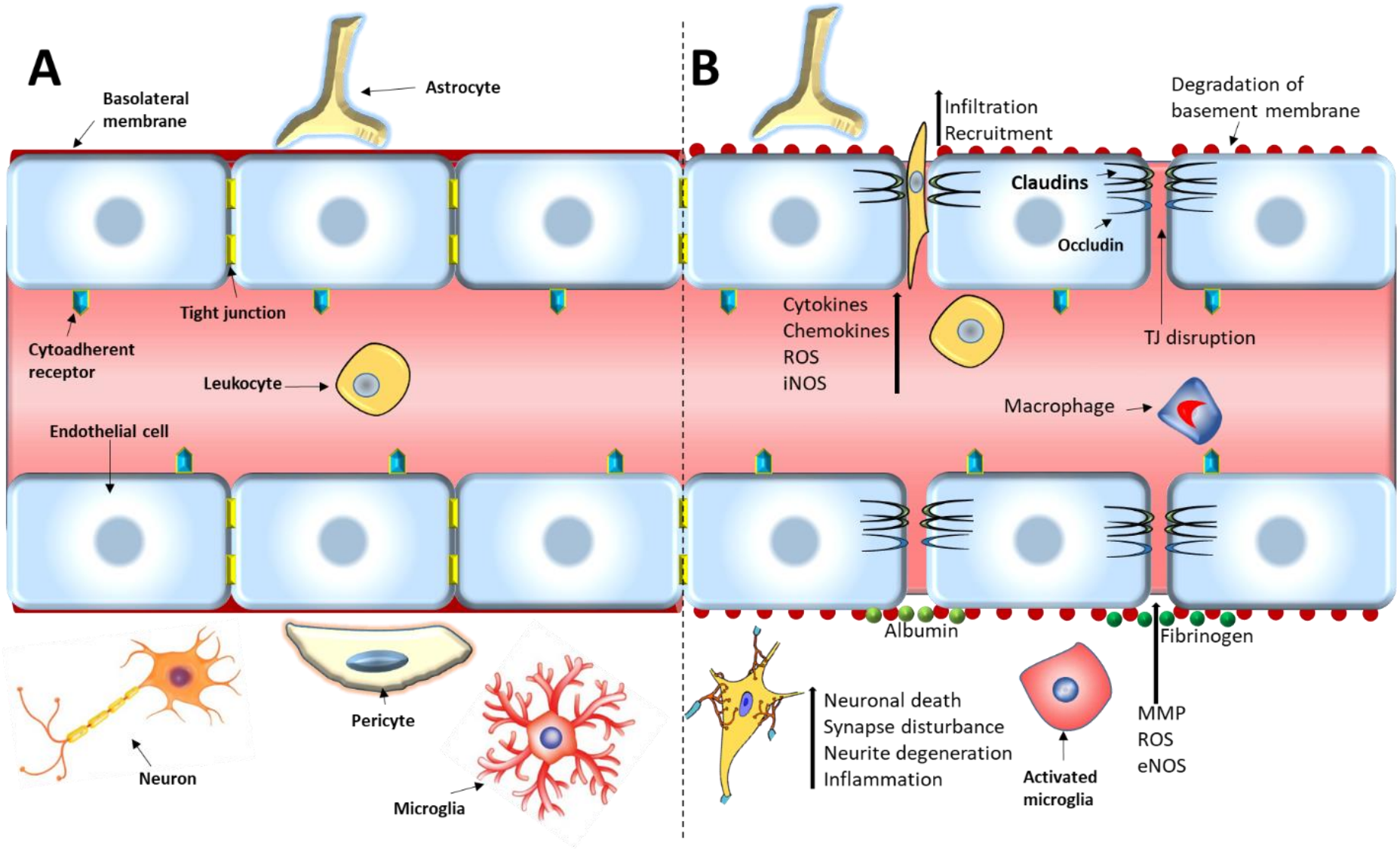
A
Basolateral membrane
Astrocyte
Tight junction
Cytoadherent receptor
Leukocyte
Endothelial cell
Neuron
Pericyte
Microglia
B
Infiltration
Recruitment
Degradation of basement membrane
Claudins
Occludin
Cytokines
Chemokines
ROS
iNOS
TJ disruption
Macrophage
Albumin
Fibrinogen
Neuronal death
Synapse disturbance
Neurite degeneration
Inflammation
Activated microglia
MMP
ROS
eNOS

Figure 1.1. BBB composition and pathological conditions. ***(A)*** *In normal states, the BBB comprises vascular endothelial cells connected with TJs and the PCs layer. A basement membrane linked with AC end-feet surrounds the endothelium.* ***(B)*** *Increased permeability of the BBB in pathological conditions results from high matrix metalloproteinase (MMP) activity and increased reactive oxygen species (ROS) and nitric oxide (NO) levels. Cytokines and chemokines are released and then activate microglia/macrophages, leading to basement membrane degradation, TJs disruption and an inflammatory response.*

The BBB acts as a guard filter that prevents the uptake of large-molecules and more than 98% of small drug molecules (15, 19, 20). Examples of CNS active agents are shown in Figure 1.2. Small molecules that are lipid soluble, electrically neutral and weak bases may be able to diffuse passively across the BBB, however weak acids due to their ionisation are unable to diffuse passively. Thus, the BBB, with its extensive blood capillary network, is considered the most important barrier that controls a molecule's access to the brain parenchyma. Neurovascular units (NVUs) comprising endothelial cells, extracellular base membrane, adjoining PCs, ACs, and microglia (although not a structural component of the BBB, are often included in the NVU as they influence barrier function in response to injury and disease (21)) are integral parts of the BBB supporting system (22) shown in Figure 1.3. NVUs collect signals from the adjacent cells and generate functional responses that are crucial for appropriate CNS function (23, 24). Both tight intracellular junctions (i.e. zona occludins, characteristic of the BBB) and the absence of fenestrations limit the permeability of drug molecules (25). Shingo et al. reported that the TJ integrity and cell proliferation in hCMEC/D3 cells (*in vitro*) is regulated by insulin signalling. The interaction of ACs and PCs with brain capillary endothelium is responsible for TJ integrity at the BBB (26).

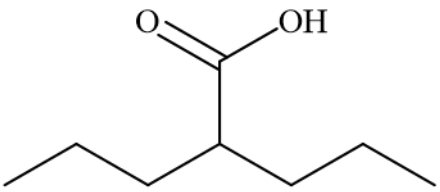

Valproic acid

MW: 144.21
Log P: 2.58
CLogP: 2.76
pKa: 4.797

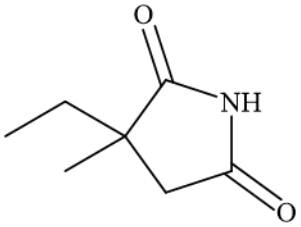

Ethosuximide

MW: 141.17
Log P: 0.66
CLogP: 0.395
pKa: N/A

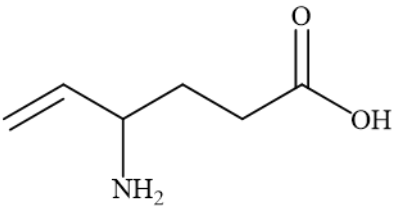

Vigabatrin

MW: 129.16
Log P: -0.14
CLogP: -2.217
pKa: 3.364, 10.067

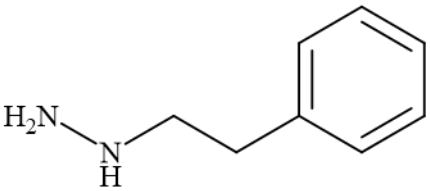

Phenelzine

MW: 136.20
Log P: 1.76
CLogP: 1.033
pKa: 7.063

Figure 1.2. Examples of CNS active agents with their physicochemical properties.

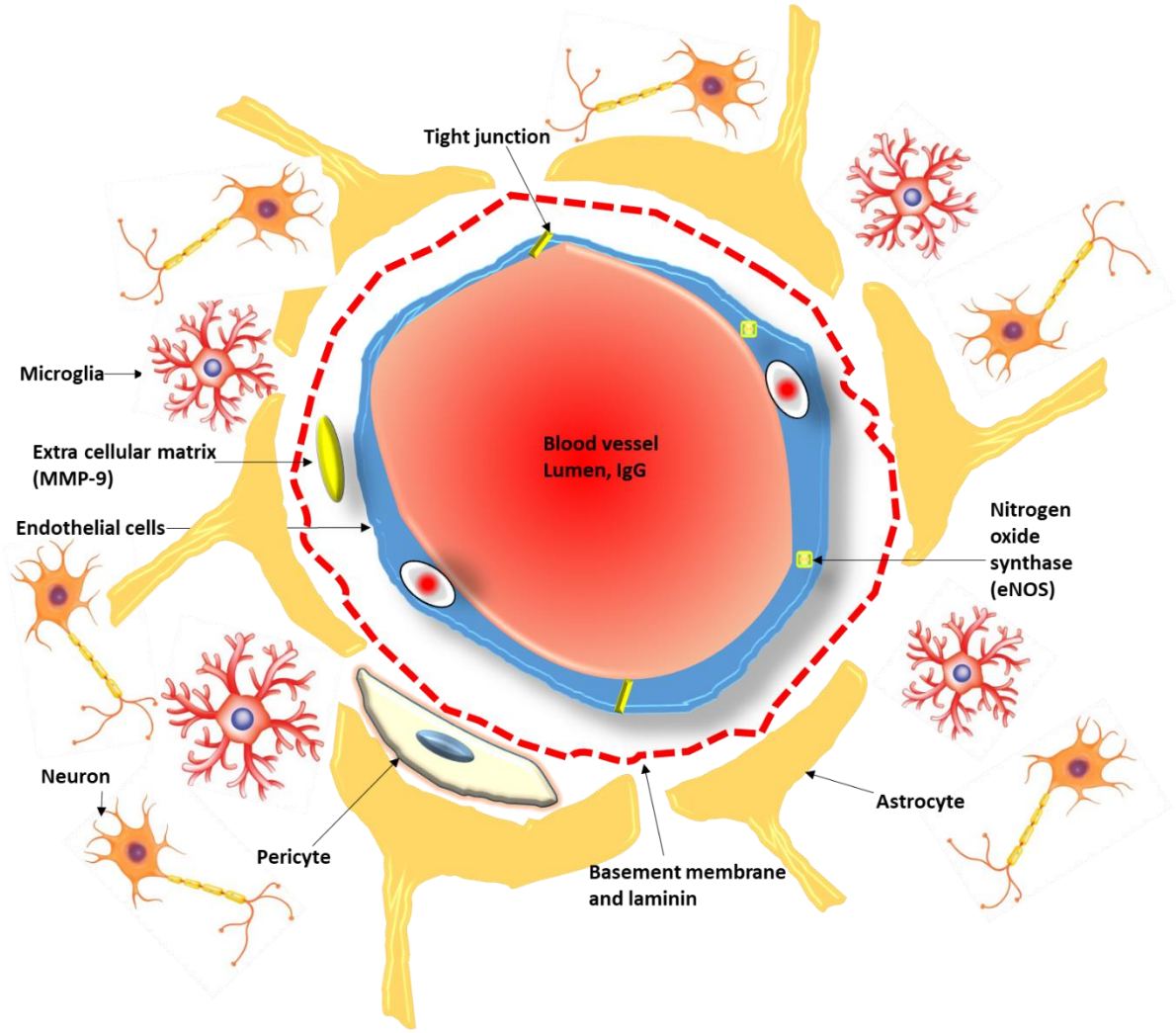

Figure 1.3. Schematic representation of the components of the Neurovascular Unit (NVU) (a combination of ACs, PCs, microglia, TJs).

In addition to being a physiological barrier, the BBB also acts as an enzymatic barrier, thus making drug transport across the BBB more difficult. Drugs are exposed to cytosolic and membrane-associated enzymes, such as c-glutamyl transpeptidase, alkaline phosphatase, aromatic acid decarboxylase, dipeptidyl(amino)-peptidase IV, and aminopeptidase A and N, which are directed at metabolizing neuroactive agents and any agents associating with the barrier (27, 28).

There are specific biological characteristics of the BBB that allow it to control the permeability of molecules, such as:

a) Very low number of pinocytotic vesicles and lack of fenestrations, but large mitochondrial volume in ECs (29, 30).

b) TJs between ECs formed by a sophisticated complex of transmembrane proteins with cytoplasmic accessory proteins, linked to the actin cytoskeleton forming close cell-to-cell connections (31). The interaction or communication of ACs and PCs with brain ECs leads to further maintenance and integrity of TJ, (32-34) shown in Figure 1.4.

c) The presence of different transporters like glucose transporter 1 (GLUT-1) for glucose, L-type amino acid transporter 1 (LAT1) for amino acids, insulin, transferrin (Tf), lipoprotein receptors, P-glycoprotein (P-gp) and multiple drug resistance (MDR) related proteins, facilitating or preventing the transport of drug molecules into the brain (31, 35). Some of the recognised transporters across the BBB are listed in Table 1.1.

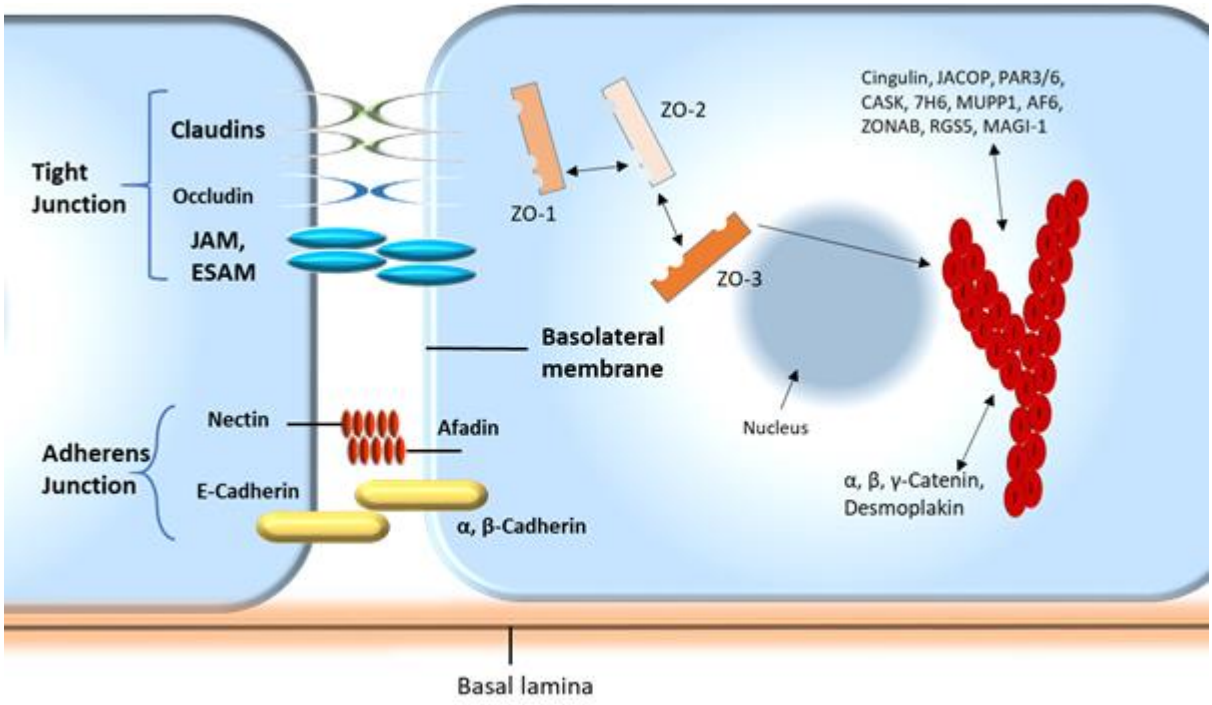

Figure 1.4. Schematic representation of molecular composition of TJs. A TJ is composed of claudins, occludin and junctional adhesion molecule (JAM) and endothelial cell-selective adhesion molecule (ESAM). Adherens junctions participate in TJ integrity.

Table 1.1. A list of recognised receptor-transporters on brain epithelium (BBB)

Transporter	Transporter (Full name)	Substrate	Ref.
GLUT-1	Glucose transporter 1	Glucose	(36, 37)
LAT1	L-type amino acid transporter 1	Amino acids	(38, 39)
IR	Insulin receptor	Insulin	(40)
hTfR	Human Transferrin receptor	Iron	(41)
ApoE	Apolipoprotein E receptor	Cholesterol	(42-44)
P-gp	P-glycoprotein	Digoxin	(45, 46)
α-1	Alpha1 adrenoceptor	Norepinephrine	(47, 48)
α-2	Alpha2 adrenoceptor	Epinephrine	(47)
AR-A_1	Adenosine receptor subtype A_1	Adenosine	(49) (50)
AR-A_{2A}	Adenosine receptor subtype A_2	Adenosine	
AR-A_{2B}/A_3	Adenosine receptor subtype $A_{2B/3}$	Adenosine	
OATPs	Organic anion transporting polypeptide	Cardiac glycosides	(51, 52)
RLIP76	RalA-binding protein 1	GSH-conjugates	(53)
SVCT2	Sodium-dependent vitamin C transporters	Ascorbic acid	(54)

1.3. Novel Systematic approaches for CNS drug delivery

Most of the therapeutics for CNS drug delivery via conventional administration get into the brain via blood circulation (18). To attain the minimum therapeutic concentration in the brain, an increased level of the drug in the systemic circulation is crucial and can be acquired (by higher dose or long-term administration), but that can lead to toxicity. Several factors that affect the concentration of the therapeutics across the BBB are listed in Figure 1.5.

Continuous efforts have been made to develop a delivery system that can deliver drugs without increasing the systemic levels of these drugs. Doxorubicin, a potent anticancer agent is under investigation to attain therapeutic concentration; for its poor penetration through the BBB (55, 56).

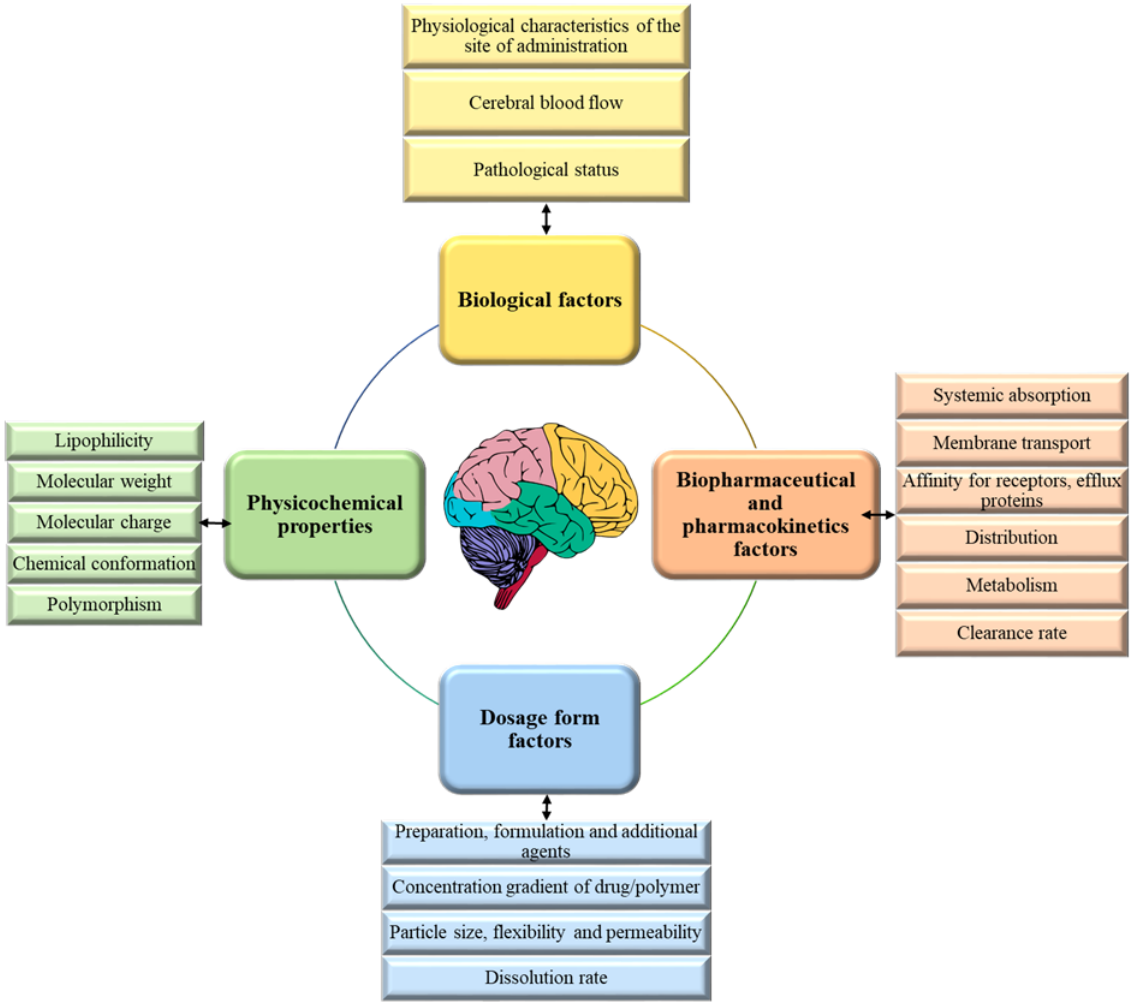

Figure 1.5. Factors affecting therapeutic concentrations of drugs in the brain following their passage through the BBB.

Various transport routes have been reported by which solutes and drug molecules can cross the BBB, (31, 57) as shown in Figure 1.6. Diffusion of substances across the BBB can be generally categorised into paracellular (namely the transfer of nutrients/drugs across an epithelium by passing through the intercellular space between the cells) and transcellular (namely the movements of solutes through a cell). In order to cross the BBB by passive

diffusion, various parameters play pivotal roles. Molecular mass is an important factor and the ideal molecular weight reported to be suitable for passive diffusion is <400 Da (58). A value of between 5.0 and 6.0 for the log of the octanol-water partition coefficient ($logP_{o/w}$), a measure of lipophilicity, is suitable for passive diffusion (59).

Compounds that are lipophilic, neutral or uncharged at pH 7.4 and have less than 8 hydrogen bonding groups are more suitable to cross the BBB (60). In another study, reported by Partridge in 2012, (61) it was found that small drug molecules can cross the BBB if their molecular mass is less than 400 and they have the ability to form 8-10 hydrogen bonds. Unfortunately, it has been reported that more than 98% of drugs for the CNS are unable to cross the BBB adequately to attain the minimum therapeutic concentration (15). Several invasive and non-invasive approaches have been anticipated to evade the BBB and enhance drug delivery to the CNS.

1.3.1. Approaches based on the route of administration/delivery

To deliver drugs into the brain, continuous efforts have been made to surmount the BBB, either by invasive techniques such as intracerebral, intraventricular and intrathecal injections or non-invasive techniques such as chemical modification, biological methods, colloidal drug carriers and using the intranasal route (62, 63).

1.3.1.1. Invasive routes of administration

As the name suggests, direct injection into brain, an intracerebral method of delivery, requires direct injection into the parenchymal space through cranium holes (63-65). The intraventricular route treatment of post-neurological intracranial infections due to multiple drug-resistance involves direct injection into the cerebral ventricle, leading to high drug distribution (66).

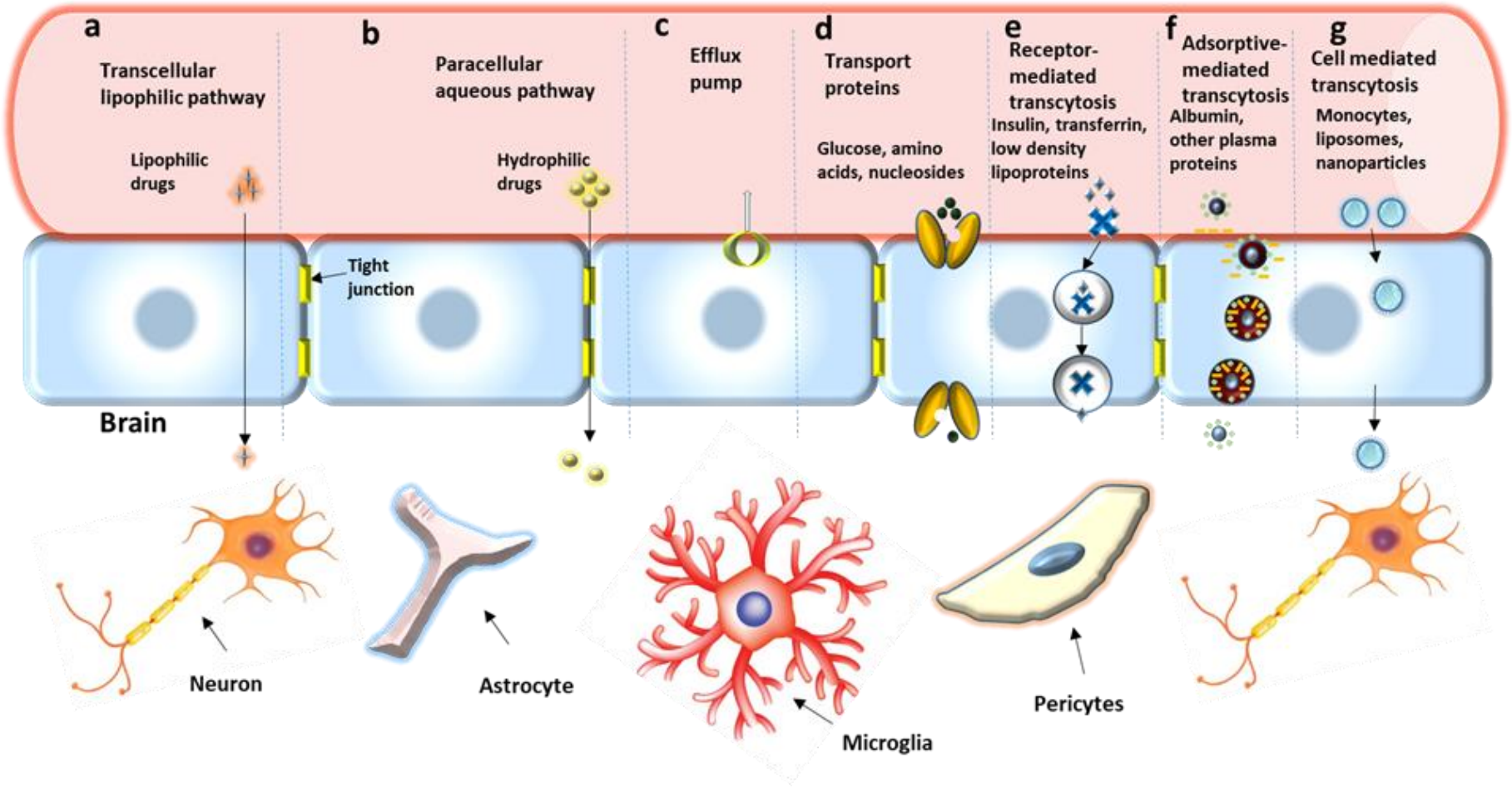

Figure 1.6. Transport routes across the BBB. Solute molecules follow from "a" to "f" pathways and the route "g" involves monocytes, macrophages and nanoparticles (NPs).

Pan et al. successfully injected polymyxin B via the intrathecal/intracerebral ventricle route, for the treatment of *Acinetobacter baumannii* (67). Kim et al. injected adeno-associated virus (AAV) into the intracerebroventricular region of the neonatal mouse brain for manipulating neuronal gene expression (68). Invasive approaches come with several limitations and hazards: post injection infection, costly procedure, the need for a neural expertise for accurate delivery of the drug in the target region.

1.3.1.2. Non-invasive routes of administration

Non-invasive routes cover several approaches for drug delivery to the brain, such as chemical modification of the therapeutic molecule, physiological transport mechanisms, chemical and physical disruption of the BBB, and nasal drug delivery. Drug delivery to the brain via the nasal route has been extensively investigated over the last decade. The external portion of the nose consisting of two nostrils (separated by the septum) occupies a third of the nasal cavity. The total volume of distribution within the nasal cavity is about 15 mL, with a surface area of approximately 150 cm^2 (69). Drug delivery to the brain via the nasal route is dependent on the olfactory and trigeminal pathways. Both olfactory and trigeminal nerves provide direct connection to the brain (70).

Carboxymethyl chitosan NPs loaded with carbamazepine have been shown to deliver the drug when administered via the nasal route. The uptake of loaded NPs was proposed via two pathways; firstly, a systemic pathway (e.g., the drug is absorbed into the systemic circulation and successively gets access to the brain after crossing the BBB); secondly, via the olfactory region linked directly with brain tissues and the CSF (71). Bio-engineered biodegradable poly(lactic-co-glycolic acid) (PLGA) NPs encapsulating NP-335 (L-pGlu-(1-benzyl)–L-His–L-ProNH_2) and NP-647 (L-pGlu-(2-propyl)–L-His–L-ProNH_2), analogues of thyrotropin releasing hormone (TRH), were successfully taken up by the brain via intranasal administration (72). Rodriguez et al. used the nasal route to deliver small interfering RNA (siRNA) encapsulated with polyethylenimine (PEI) to mice to target Beclin1 (a host

autophagic protein resulting from HIV infection) (73). The nasal route is non-invasive, non-infectious and provides an ease of self-administration. It also avoids the first pass effect, bypasses the BBB and provides rapid onset of action. On the other hand, only very small volumes (25-200 µL) can be administered, the nasal cavity has low pH and some portion of the drug can undergo metabolism in the nasal cavity (74, 75).

1.3.2. Chemical modifications of drug molecules

Chemical modification can be subcategorized into three strategies: **a)** lipidization of drug molecules, **b)** prodrug approaches, and **c)** lock-in approaches.

1.3.2.1. Lipidization of molecules

Lipidization is the introduction of lipid moieties to a drug molecule or removal of polar moieties in order to enhance the overall lipophilicity. To cross the BBB, enhanced lipophilicity, lower molecular mass and lack of any charge tend to be more favourable. As a general rule, addition of two hydrogen bonding groups to a molecule decreases the permeability by one order of magnitude (76). One of the most notorious examples of increasing lipophilicity (77) to enhance permeation across the BBB is the conversion of morphine to heroin by di-acetylation. This minor modification leads to 100 times greater permeation of heroin than morphine, (78, 79) shown in Figure 1.7. Lipidization results in enhanced permeation of the molecule across all biological membranes, not only the BBB, affecting plasma distribution and plasma clearance (80-82). Increased lipidization promotes plasma protein binding, as well as increasing the mass of the molecule (which itself would result in less permeability) (76). Lipidization can increase molecular weight and, as discussed, drugs >400-500 Da do not cross the BBB in significant amounts. It has been reported that an increase in the molecular size of the drug exponentially decreases BBB permeability, limiting the excessive use of lipidization technique (83).

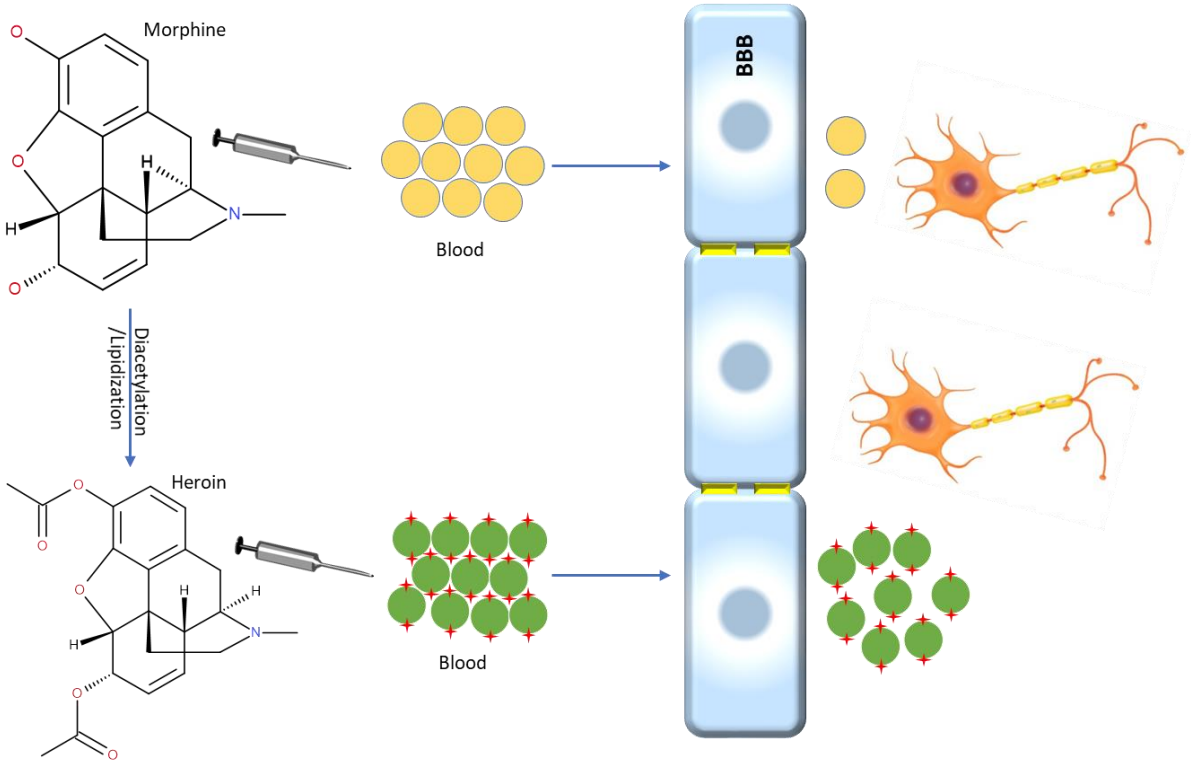

Figure 1.7. Lipidization of drug; a schematic representation. When administered intravenously, only a small number of morphine molecules get into the brain, whereas lipidization (converting to heroin) results in significant penetration into the brain.

1.3.2.2. Pro-drug approach

Prodrugs can be described as bio-reversible derivatives of drug molecules that undergo an enzymatic modification, such as that by matrix metalloproteinases (MMPs), cytochrome P450 (CYP450) enzymes, monoamine oxidases, gamma-aminobutyric acid, transaminase, aminopeptidases, endopeptidases, or chemical reactions in the body to expose the active drug molecule (84, 85). The physical obstacle of the BBB allows only a small fraction of drugs to pass through and access the brain. Amidation or esterification of active drug molecules bearing amino, carboxyl or hydroxyl groups may enhance their lipid solubility by removing hydrogen bond donors, which in turn can promote penetration as shown in Figure 1.8. The concomitant increase in molecular weight will have the opposite effect and so careful consideration should be given to which derivatives to prepare.

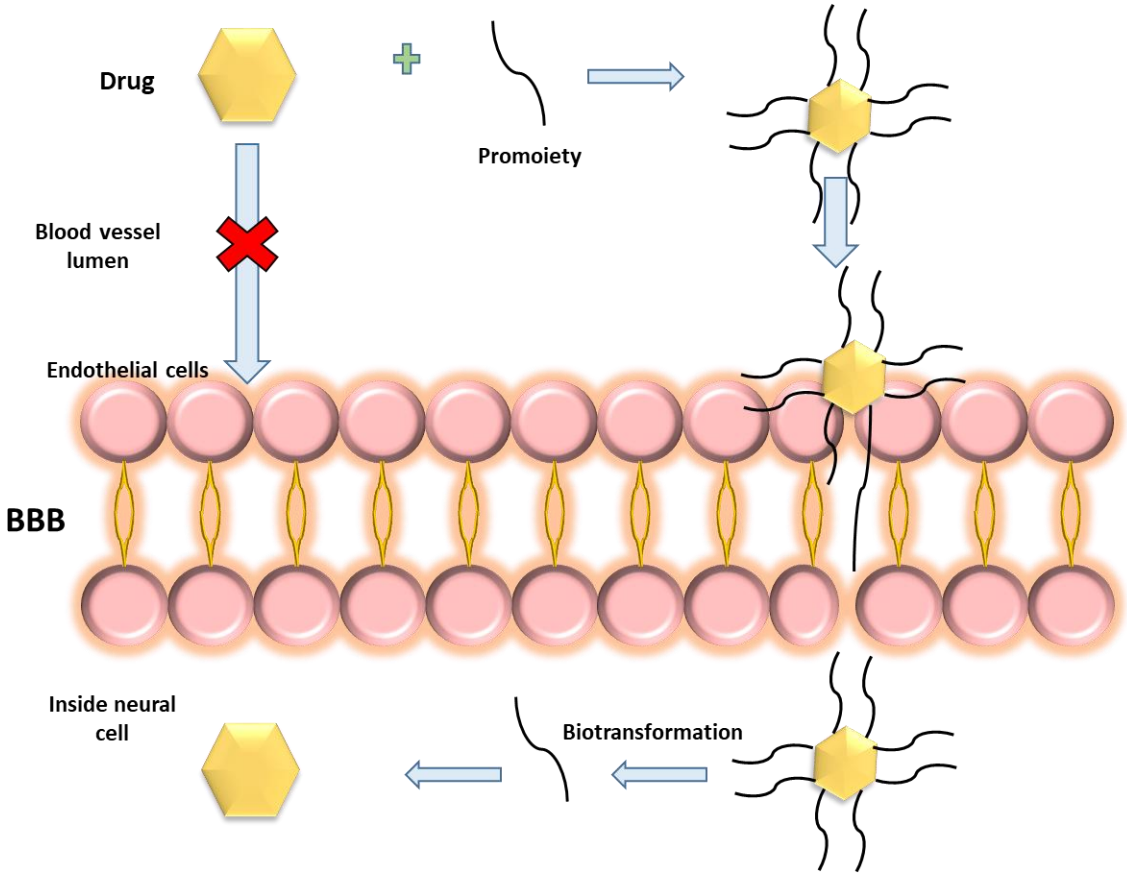

Figure 1.8. Illustration of the prodrug approach. The drug itself is unable to cross the BBB, whereas adding a pro-moiety increases the BBB penetration reasonably. Once the drug gets into the cell, the pro-moiety is cleaved off by enzymatic/chemical reaction, rendering the free drug.

Once the molecule crosses the barrier, then enzymes or chemical reactions remove the pro (lipid in some cases) part from the drug molecule, exposing the active parent drug (86, 87). Prodrugs have been used in cancer therapy and gene-directed enzyme prodrug therapy (88). While lipophilicity is generally favoured for passive diffusion of BBB-crossing drugs, poor water solubility can prove a significant impediment to drug delivery. A prodrug strategy can improve the aqueous solubility of drugs to attain site-specific delivery (87). About 7-10% of the drugs currently available are prodrugs and have been proven to control the physicochemical and biopharmaceutical properties of pharmacologically active compounds. Furthermore, the design of prodrugs can enhance permeability and bioavailability (89). Gynther et al. successfully delivered a ketoprofen-lysine prodrug (shown in Figures 1.9**a** and 1.9**b**) in rats via the LAT1 transporter and, after getting into the brain, enzymatic

bioconversion was observed (90). Wang et al. demonstrated higher uptake of naproxen when decorated with glucose and ascorbic acid (G-V-Nap, Figure 1.9**c**) compared to naked naproxen (91). TRH (pGlu-His-ProNH$_2$) and [Glu$_2$]TRH (pGlu-Glu-ProNH$_2$) are structurally related endogenous peptides that are identified both in neuronal and non-neuronal tissues. TRH has been identified to regulate the hypothalamic hormone and also acts as a neurotransmitter/neuromodulator (92, 93). [Glu$_2$]TRH is highly hydrophilic molecule that ionizes at physiological pH on the γ-carboxyl group of the central Glu residue, which hinders its diffusion into the CNS (94). Prokai-Tatrai et al. reported improved membrane affinity and analeptic effect by esterification of the Glu side chain (shown in Figure 1.9**d**) in the presence of resin-bound dicyclohexylcarbodiimide (95). *2R*-γ-tocotrienol (γ-T3), a member of the vitamin E family, exhibits antioxidant activity against brain microsomes and nitric oxide, cholesterol lowering and anticancer activities (96-98). γ-T3 is poorly water soluble (shown in Figure 1.9**e**), limiting its pharmacological use. Three aminoalkylcarboxylic acid esters of γ-T3 (shown in Figure 1.9**f**) exhibit higher water solubility and are rapidly hydrolysed in rat and human plasma. SB-3CT ((4-phenoxyphenylsulfonyl) methylthiirane) is a selective inhibitor of MMP-2 and MMP-9 used for the treatment of traumatic brain injury (TBI) (99). However, SB-3CT presents poor water solubility. Interestingly, the metabolite of SB-3CT, *p*-hydroxy SB-3CT, is a more potent inhibitor than SB-3CT. Hence, Lee et al. developed *O*-phosphate of *p*-hydroxy SB-3CT to achieve a prodrug of *p*-hydroxy SB-3CT (100). Water solubility of the SB-3CT phosphate prodrug was enhanced by 2000-fold compared to *p*-hydroxy SB-3CT. The prodrug readily hydrolysed to the active *p*-hydroxy SB-3CT in the blood, which crossed the BBB (shown in Figure 1.9**g**). The prodrug was administered in multiple doses to TBI mice. However, as administering multiple i.v. injections to mice was challenging, the authors administered the prodrug i.v. initially (30 minutes after TBI induction) followed by subcutaneous injections of *p*-hydroxy SB-3CT to achieve a sustained concentration of *p*-hydroxy SB-3CT in the

blood. It was reported that the treatment significantly reduced the brain lesion volume and improved neurological outcomes in the TBI mice. Yue et al. demonstrated the use of a prodrug approach to deliver the ibuprofen into the brain (101).

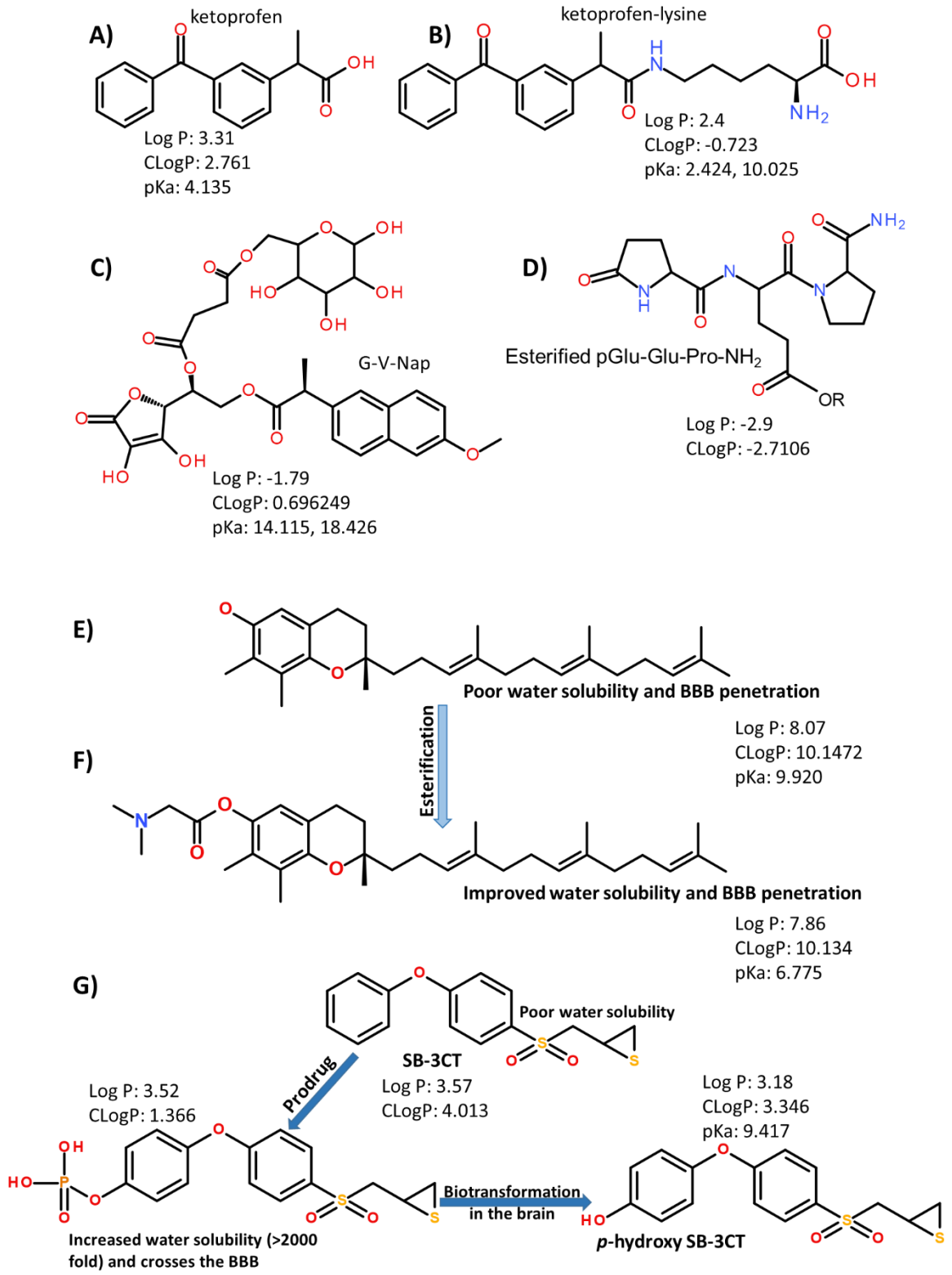

Figure 1.9. ***A)*** *Chemical structure of ketoprofen* ***B)*** *chemical structure of ketoprofen-lysine complex with improved pharmacokinetic properties* ***C)*** *chemical structure of naproxen-glucose-ascorbic acid complex which is able to cross the BBB* ***D)*** *chemical structure of esterified pGlu-Glu-Pro-NH_2 with*

*better BBB penetration **E)** Chemical structure of 2R-γ-tocotrienol with poor solubility and unable to cross the BBB, **F)** 2R-γ-tocotrienol after esterification with higher water solubility and able to penetrate the BBB. **G)** SB-3CT, a potent MMP-2 and 9 inhibitor, is poorly water soluble, whereas phosphate prodrug exhibits 2000-fold increased solubility and crosses the BBB. After crossing the BBB, it is hydrolysed into p-hydroxy SB-3CT.*

1.3.2.3. Lock-in approach

The lock-in approach is different from the lipidization and prodrug approaches (102). In this system, multi-chemical transformations are required for active drug exposure. It involves incorporation of two chemical moieties in the drug molecule. One of these is a targeting moiety and the other has switchable physical properties. Once the drug crosses the barrier, the switchable moiety is transformed (e.g. by metabolism, leading to significantly reduced lipophilicity) and the drug can no longer leave the brain. This phenomenon is known as a lock-in system. Once locked, the targeting moiety comes into action and targets a specific receptor (103).

Zhao et al. used a lock-in approach to deliver venlafaxine into brain. Glucosylation was used to enhance the brain targeting, however decreased levels of venlafaxine were observed due to bidirectional transport of the venlafaxine-glucose conjugate (V-G) through GLUT-1. To counter this problem, a thiamine disulfide (TDS) group was introduced to the V-G conjugate. *In vivo* evaluation of venlafaxine-TDS-G showed improved brain targeting and a higher level of venlafaxine as compared to administration of naked venlafaxine (104).

The lock-in approach is an advanced form of the prodrug approach, having a targeting moiety along with some switchable prodrug-like moiety. A prodrug lacks the targeting part (105). Bodor et al. reported another type of lock-in approach, where dihydropyridine acts as quaternary pyridinium ion in a redox system, mimicking the $NAD^+ \leftrightarrow NADH$ coenzyme system. The drug is modified to a 1, 4-dihydropyridine moiety-containing conjugate, exhibiting higher lipophilicity than the original drug in the brain. Upon systemic administration of the drug, conjugated drug is found all over the body, including in brain.

Oxidization of the dihydropyridine in the brain forms a hydrophilic, polar quaternary pyridinium salt that is retained in the brain. This retention of pyridinium salt in the brain is due to the 'locking in', whereas cleavage of the carrier (in the prodrug) releases the free active drug (102). Zhao et al. used a novel L-ascorbic acid thiamine disulfide delivery system (L-ascorbic acid prodrug) for the delivery of ibuprofen across the BBB by GLUT-1 and the Na^+-dependent vitamin C transporter $SVCT_2$. A schematic representation of distribution, sequential metabolism and brain lock-in pathways is shown in Figure 1.10.

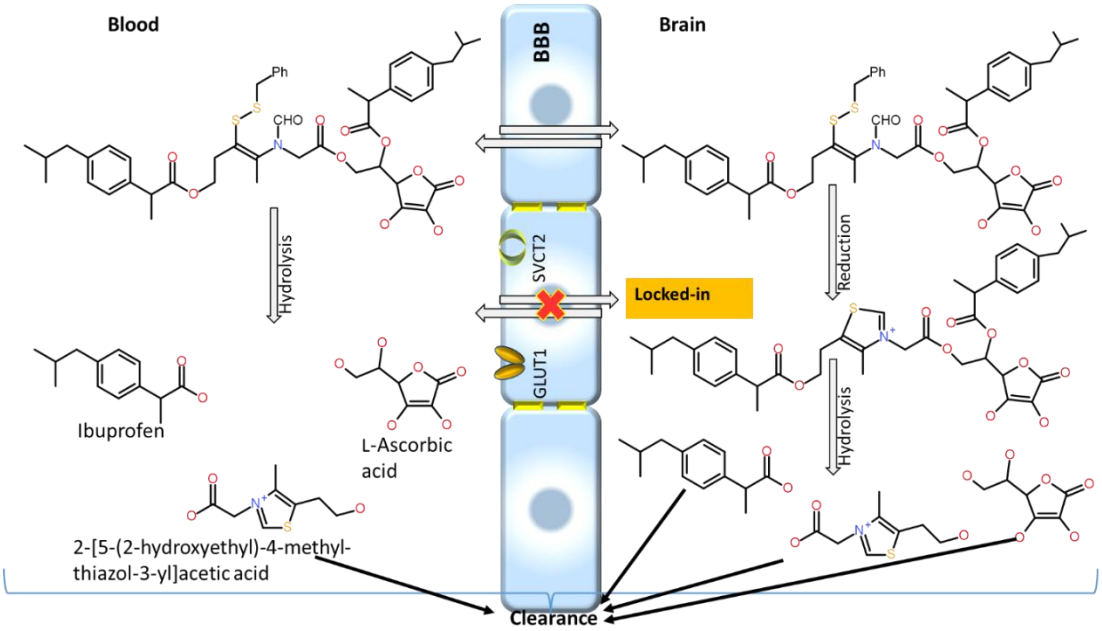

Figure 1.10. Chemical structure of ibuprofen- L-Ascorbic acid – thiamine disulphide complex which can cross the BBB via GLUT-1 and SVCT2 receptors. Once the complex reaches in the brain then it is reduced into a compound, which can't leave the brain. This complex is further hydrolysed to release the ibuprofen and ascorbic acid.

1.3.3. Physiological transport mechanisms

1.3.3.1. Adsorptive-mediated transport (AMT)

Cationic modification of albumin and antibodies (immunoglobulins; IgG) can enhance cellular uptake through adsorptive-mediated transcytosis (AMT). An electrostatic interaction between the cationic (positively charged) albumin and the anionic (negatively charged) BBB promotes the penetration, (76, 106) as shown in Figure 1.11. This electrostatic interaction between the cationic (albumin) and the anionic (BBB) has been

reported to play a part in the transport of larger molecules like β-endorphin via adsorption (107-109). Recently, PepH3, a small peptide (AGILKRW) derived from the dengue virus capsid protein, was demonstrated to cross the BBB by AMT (110). Apart from targeting the brain, AMT can lead to accumulation of the drug in other tissues such as the liver, kidneys, spleen, lungs, intestine, blood and stomach (110).

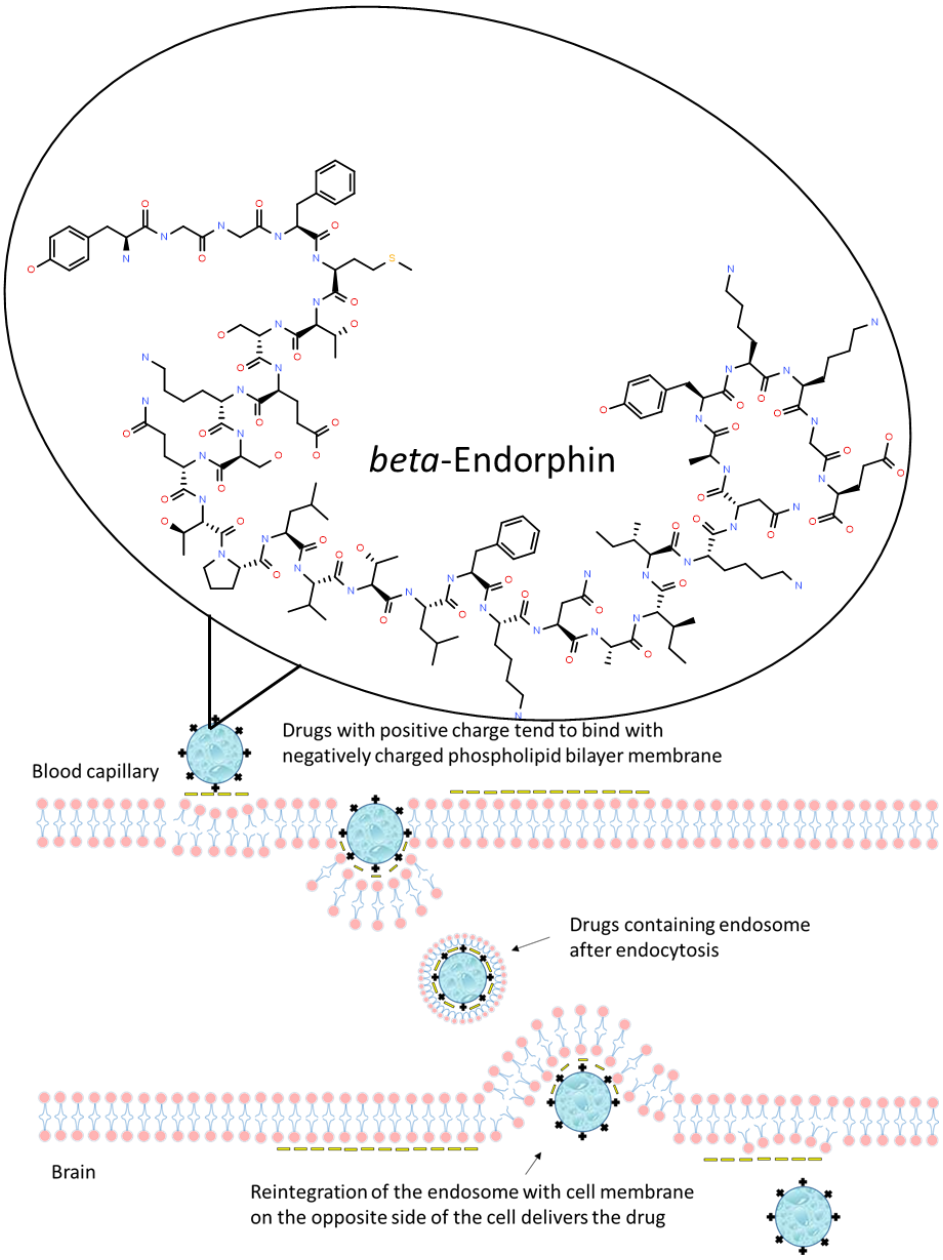

Figure 1.11. Schematic representation of AMT as a pathway for BBB penetration. Positively charged drug molecule (β-endorphin) interacts with negatively charged membrane surface. Vesicles containing drug enter intracellular space and penetrate brain endothelial cells.

1.3.3.2. Carrier-mediated transport

Carrier-mediated transport (CMT) is based on the principle of duplicating a natural key that unlocks entry via the BBB. In this approach, a drug molecule is altered in a way that mimics a natural nutrient. This modified drug molecule that may incorporate glucose or an amino acid uses one of the CMT systems in the BBB that transports amino acids and nutrients (111). Dopamine, a water-soluble drug molecule, when transformed into levodopa can easily cross the BBB using the large neutral amino acid transporter. Once the molecule crosses the BBB then it is converted to dopamine by DOPA decarboxylase. This conversion of dopamine has been used for treating PD for decades (112).

1.3.3.3. Receptor-mediated transcytosis

Macromolecules, like peptides and proteins, use receptor-mediated transcytosis (RMT). It works by conjugating the drug materials with ligands such as insulin, Tf and low-density lipoproteins, which bind to receptors that are abundant on brain epithelial cells (113) shown in Figure 1.12. Uptake of insulin is mediated by insulin receptors (IR), found on the brain endothelial cells (114, 115). Similarly, Tf and leptin uptake in the brain is carried out by the Tf and leptin receptors, respectively (116-119). Part of the drug molecules that target the receptors to cross the BBB are reported in Table 1.2.

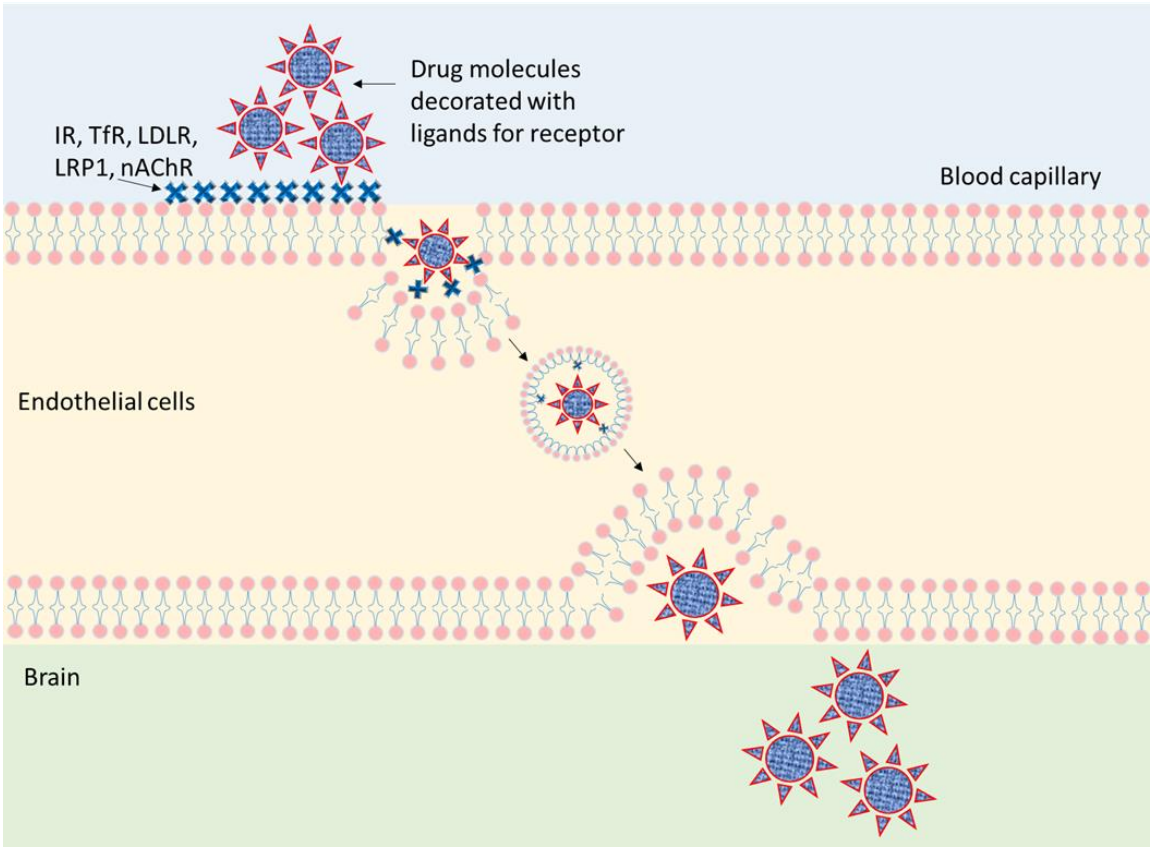

Figure 1.12. Schematic representation of receptor-mediated transcytosis (RMT) of drugs and nano-carriers. Drug molecules decorated with receptor ligands interact with the receptor, initiating the endocytosis. Once the endosome (vesicle containing the drug molecule) gets closer to the other side of the cells, it is released into the brain. IR: insulin receptor; TfR: transferrin receptor; LDLR: low-density lipoprotein receptor; LRP1: Low-density lipoprotein receptor-related protein 1; nAchR: nicotinic acetylcholine receptor.

Membrane transporters can be key determinants of the pharmacokinetic, safety and efficacy profiles of drugs. These transporters are clinically important in drug absorption and disposition. OATP1A2/O ATP-A (SLCO1A2) transporter found on brain capillaries endothelium and distal nephrons is responsible for the transport of Oestrone-3-sulphate, dehydroepiandrosterone sulphate, bile salts, methotrexate, digoxin, levofloxacin and statins (120). MDR1/P-gp present on intestinal enterocytes, kidney proximal tubule, hepatocytes (canalicular), brain endothelium regulate the transport of digoxin, loperamide, berberine, irinotecan, doxorubicin, vinblastine, paclitaxel and fexofenadine (121, 122). BCRP is expressed in the liver, gastrointestinal tract, kidney, brain endothelium, mammary tissue, testis and placenta. It has a role in limiting oral bioavailability and transport across the blood–brain barrier, blood– testis barrier and the maternal–fetal barrier of some selected substrates (123, 124).

Table 1.2. A list of the formulations that target receptors expressed on the endothelium of BBB cells.

Receptor targeted	Carrier	Drug	*In vitro/vivo* model	Ref.
IR	Insulin or an anti-insulin receptor monoclonal antibody (29B4) linked with HSA.	Loperamide	Female ICR (CD-1) mice	(125)
IR	Human insulin receptor monoclonal antibody (HIRMAb)	Iduronate 2-sulfatase (IDS)	Juvenile male rhesus monkeys	(126)
IR	83-14 MAb-grafted saquinavir (SQV)-loaded solid lipid NPs (SLNPs)	Saquinavir	Human brain-microvascular endothelial cells (HBMECs)	(127)
IR	HIRMAb–SGSH fusion protein	Sulfamidase	MPSIIIA fibroblasts rhesus monkeys	(128)
hTfR	JR-141 (anti-human transferrin receptor (hTfR) antibody and intact hIDS	Iduronate 2-sulfatase (IDS)	Human fibroblasts mice or monkeys	(129)
hTfR (OX26)	Transferrin receptor-targeted (OX26) immunoliposomes containing oxaliplatin	Oxaliplatin	Rats	(130)

TfR	Transferrin-conjugated docetaxel (DTX)-loaded d-alpha-tocopheryl polyethylene glycol 1000 succinate (vitamin E TPGS or TPGS) micelles.	Docetaxel	Rats	(131)
TfR	Anti-transferrin antibody conjugated with gold NPs (8D3-AuNPs)	-	Mice	(132)
TfR	Chimeric human IgG1 molecules with the S239D/A330L/I332E triple mutation anti–transferrin receptor-interleukin-1 receptor (IgG1 TM-IL-1RA)	-	Mice	(133, 134)
LRP1	poly(butyl cyanoacrylate) NPs coated with polysorbate 80	Dalargin/Loperamide	C57BL/6J mice	(135)
LRP1	Polyamidoamine conjugated bifunctional PEG-Angiopep/DNA NPs (PAMAM-PEG-Angiopep/DNA)	Temozolomide	C6 glioma cells ICR mice and nude mice	(136)
Lf R-Lf	PLGA NPs crosslinked with lactoferrin (Lf) and folic acid (FA)	Etoposide	Human brain-microvascular endothelial cells (HBMECs)	(137)
nAchR	C2-9r Short rabies virus glycoprotein (sRVG) linked with extra Gly and Arg (H-CDIFTNSRGKRAGGGGrrrrrrrrr)	short interfering RNA (siRNA)	M17 cells Mice	(138)

nAchR	RVG-29-9rR peptide (YTIWMPENPRPGTPCDIFTNSRGKRASNGHHHHrRrRrRrRr)	DNA	Neuro 2a cells; brain capillary endothelial cells (BCECs); KM mice	(139)

1.3.3.3.1. Insulin receptor and insulin analogue receptor

Insulin receptor exhibiting cells are present on the luminal membrane of the BBB and neural cells in the CNS,(140, 141) which import blood borne insulin into the brain via RMT (140). Potential use of insulin for drug delivery via RMT has stalled due to a short serum half-life of about 10 minutes and the possibility of hypoglycaemia (too much insulin will promote widespread uptake of glucose from the blood circulation) (142). This problem may be overcome by employing insulin-like growth factors (IGF-1 and IGF-2),(143) as higher concentrations of IGFs are required to develop hypoglycaemia (142). However, antibodies that recognize the insulin receptor have been extensively studied. Insulin receptor was targeted to treat mucopolysaccharidosis type I (MPSI) via enzyme replacement therapy (ERT). Clinical trials have been started for the utilization of IR for drug delivery and other applications. Clinical trial (NCT02045368) was designed to evaluate IGF-Methotrexate conjugate (765IGF-MTX) in patients with advanced tumors. 765IGF-MTX is administered as an IV infusion over 1 hour on days 1, 8 and 15 of a 28 d cycle. Treatment continues until disease progression, unacceptable toxicity, or patient refusal. Assessment of response will be confirmed with imaging studies performed at the end of cycle 2 +/- 7 days, and every 2 weeks thereafter. Rapid cellular uptake GF-MTX has been reported (144).

Boado and Pardridge (2017) fused a lysosomal enzyme, α-L-liduronidase (IDUA), with monoclonal antibodies to human insulin receptor (HIRMAb) to cross the BBB. Upon administration in rhesus monkeys, 1.2% of injected drug (0.1 mg/kg) accumulated in the brain, whereas the unconjugated IDUA did not penetrate the BBB (145). It is reported that HIRMAb acts like a molecular Trojan horse to deliver the IDUA across the BBB by binding to insulin receptors. Furthermore, they demonstrated the delivery of a decoy receptor (tumor necrosis factor receptor) across the BBB by fusing it with HIRMAb (146).

1.3.3.3.2. Transferrin receptor

The transferrin receptor (TfR) is one of the extensively studied receptors known to follow the RMT route and is abundantly found on the capillaries of the BBB to facilitate the delivery

of iron to the brain (147, 148). Several studies have been reported that targeted TfR for delivering payloads to the brain in animal models. TfR is a glycoprotein, having two ~80 kDa subunits linked by intramolecular disulfide bonds. Each subunit can bind with one molecule of Tf.(149) Tf and poly-L-arginine (cell penetrating peptide) linked with 1, 2-distearoyl-sn-glycero-3-phosphoethanolamine-poly(ethylene glycol) (DSPE-PEG) liposomes were developed for brain delivery of imaging agents and DNA (150). B6 (CGHKAKGPRK), a TfR-specific peptide, and GE11 (CYHWYGYTPQNVI), a peptide specific for endothelial growth factor receptor (EGFR) overexpressed on cancer cells were linked with poly(amido)amine-PEG (PAMAM-PEG) based dendriplexes for siRNA delivery (151). In another study, Sonoda et al. formulated a BBB penetrant protein conjugate (JR-141), comprising an anti-human transferrin receptor (hTfR) antibody and human iduronate-2-sulfatase (hIDS) to treat mucopolysaccharidosis II (MPS II, caused by accumulation of glycosaminoglycans) (129). Upon i.v. administration, JR-141 was detected in the brain but hIDS alone failed to penetrate into the brain. In addition, ostensibly therapeutic outcomes were observed, with a lower accumulation of glycosaminoglycans seen in brain and peripheral tissues (129). Greta et al. showed 80-times higher uptake of fused mAb158 (an antibody that binds selectively to Aβ protofibrils) than of the unmodified antibody, two hours after administration. The TfR antibody (8D3) was recombinantly fused with light chains of mAb158 (152). Furthermore, nucleic acid aptamers targeting TfR have also been investigated for their ability to pass the BBB. In one such example, an aptamer that binds to epithelial cell adhesion molecule-expressing cancer cells fused with a TfR-targeting aptamer (TEPP: 5′-GC GCG GTAC CGC GC TA ACG GA GGTTGCG TCC GT-3′) showed a reasonable penetration into brain following a single i.v. injection of aptamer (40 nmol/kg) to mice.(153) McConnell et al. describe a multi-DNA aptamer-functionalised liposome used to study cocaine-induced dopamine dysregulation: peripherally-administered (intraperitoneal, i.p.) functionalised liposomes were found to enter the brain of mice via a

surface TfR aptamer (5'-GAATTCCGCGTGTGCACACGGTCACAGTTAGTATCGCTACGTTCTTTGGTAGTCCGTTCGGGAT-3'), where upon they reduced cocaine-induced hyperlocomotion by sequestering of dopamine via a dual dopamine-aptamer payload. Additionally, animals did not suffer from neurological damages following chronic administration of the liposomes (one injection per day for six days) (154). PAMAM-PEG-NPs modified with lactoferrin (Lf) encapsulated reporter genes encoding green fluorescent protein (GFP) has been reported to successfully cross the BBB and access to neural tissues after i.v. administration (155). *In vivo* imaging showed high fluorescence in the central region of brain. On the other hand unmodified NPs were observed in the liver at much higher amounts compared to Lf-modified NPs as shown in (155).

Despite the expanding use of the TfR vector and anti-TfR antibodies for brain drug delivery, a number of factors affect the delivery efficiency. Firstly, TfR is present at the BBB as well as in other vascular beds and parenchyma of other organs, resulting in extensive distribution in the body. Secondly, there is limited transcytosis of TfR in the brain. For example, TfR-targeted immunoliposomes for brain drug delivery accumulated in the micro vessels of the rat brain. No transcytosis of the non-TfR-targeted immunoliposomes was observed (130).

1.3.3.3.3. Low density lipoprotein receptors (LDLR)

The low-density lipoprotein receptor (LDLR) and low-density lipoprotein receptor related proteins (LRP1, LRP2) are expressed on ECs in brain capillaries (156-158). LDLRs have been reported to facilitate the transport of lipoproteins and pharmaceutical substances into the brain via RMT (113, 157-159). In clinical trial phase I ANG1005 exhibited manageable toxicity and activity in patients with brain metastases from advanced solid tumors and recurrent malignant gliomas (160, 161). However, in clinical phase II trials to

date patients had a partial response and 17/30 (57%) had a stable disease, as best response (162).

Datta et al. used a receptor binding domain peptide derived from human apolipoprotein E (hApoE), LRKLRKRLLR [hApoE (141-150)] to cross the BBB. They fused hApoE (141-150) with 18A (DWLKAFYDKVAEKLKEAF) [Ac-He18a-NH_2], a high affinity lipid-associated peptide to assess the uptake and degradation of low-density lipoprotein (LDL) in murine embryonic fibroblast (MEF1). In addition, four analogues were prepared, of which, Ac-LRRLRRRLLR-18A-NH_2 [Ac-hE(R)18A-NH_2] and Ac-LRKMRKRLMR-18A-NH_2 [Ac-mE18A-NH_2] have an extended hydrophobic moiety, including the receptor binding region. Control peptides were Ac-LRLLRKLKRR-18A-NH_2 [Ac-hE(Sc)18A-NH_2], which has amino acid residues of the ApoE to disrupt the hydrophobic face, and Ac-RRRRRRRRRR-18A-NH_2 (Ac-R1018A-NH_2), which has only positively charged arginine (R) as the receptor binding domain. Increased internalisation of LDL was observed by 3-, 5- and 7-fold for Ac-mE18A-NH_2, Ac-hE18A-NH_2, and Ac-hE(R)18A-NH_2, respectively, whereas the control peptides had no significant biological activity (163). Yamada et al. demonstrated the internalization of Aβ involved in the pathogenesis of AD. They observed the penetration of Aβ in the conditionally immortalised endothelial cell line from rat brain via LRP1. Upon administration of LRP1 antagonist, low internalization of Aβ was observed (164). Wang et al. used a receptor binding peptide of ApoE (residual 159-167 [monomer: LAVYQAGAR], but the peptide had 18 amino acids, 2×monomer) fused to IDUA (a lysosomal enzyme, α-L-iduronidase) [IDUAe1] to deliver across the BBB by targeting the LRP1, for the treatment of mucopolysaccharidosis (MPS) type I (165). In this disease there is a deficiency of IDUA and accumulation of glycosaminoglycans (GAGs) with elevated β-hexosaminidase activities. The authors took an interesting approach by developing a plasmid DNA that generates the whole therapeutic vector (IDUAe1) and targeting the plasmid DNA to the liver. The gene delivery occurred by a single hydrodynamic tail-vein injection.

Therefore, the liver produced IDUAe1, which found its way to the brain in mouse model of MPS I. The animal showed normal levels of GAGs and β-hexosaminidase activity 5 months after the treatment. Furthermore, Benchenane et al. found that blood-derived tissue-type plasminogen activator (tPA) crosses the BBB without disruption of the BBB through LDL receptor related protein mediated transcytosis. This is useful to improve thrombolysis in stroke (158).

For example, Papademetriou et al. found that under inflammatory conditions such as lysosomal storage disorders the increased expression of intercellular adhesion molecule 1 (ICAM-1) on the endothelial cells compared to TfR resulted in almost 10-times more binding of anti-ICAM-1 antibodies compared to anti-TfR antibodies to the endothelial cells. The trend was maintained for 250 nm polystyrene NPs that were coated with anti-ICAM-1 or anti-TfR antibodies (2700-3000 antibodies per NP). Therefore, targeting ICAM-1 will be suitable for delivery of nano-carriers to the brain compared to TfR under diseased conditions (166).

1.4. Novel Shuttle peptides

Shuttle peptides facilitate the influx of a diverse range of small molecule cargoes across the BBB. The concept of shuttle peptides for BBB was coined by William M Pardridge in the mid-1980s (167). Small synthetic peptide shuttles (natural amino acids) have been reported to cross the BBB. Short rabies virus glycoprotein (RVG), RVG-29 (YTIWMPENPRPGTPCDIFTNSRGKRASNG), binds exclusively with the nicotinic acetylcholine (nAchR) receptor found on neuronal cells and on the endothelial cell lining of the BBB, making it possible for peptide carriers to penetrate (168). Javed et al. used C2-9r (H-CDIFTNSRGKRAGGGGrrrrrrrrr, where r is D-arginine) to deliver siRNA for suppressing the α-synuclein (α-Syn) gene, implicated in the development of PD. CDIFTNSRGKRA is a shorter version of RVG, linked with four glycines acting as a spacer and positively charged, which at the end of the C-terminus bind with negatively-charged

siRNA. It was reported that this peptide-based delivery system not only crosses the BBB, but also stabilizes the siRNA that supresses the α-Syn protein, thus mitigating PD-like symptoms (138). Although this delivery system has been derived from the rabies virus, it was reported to be non-toxic to neuronal cells. Alvarez-Erviti et al. used exosomes (obtained from self-derived dendritic cells) decorated to express Lamp2b and fused with neuron-specific RVG peptide to deliver siRNA into mouse brains (169). They also compared the immune response of siRNA-RVG exosomes and siRNA-RVG-9R *in vivo* by measuring the interleukin (IL)-6, interferon gamma-induced protein (IP)-10, tumour necrosis factor (TNF)-α and interferon (IFN)-α serum levels. They found non-substantial changes in all cytokines compared to siRNA-RVG-9R (169). Although, IFN-α and IP-10 increased in average for mice injected with siRNA-RVG exosomes compared to control mice (169). Moreover, Conceicao et al. reported that the RVG-9r peptide decorated liposomes (also referred as stable nucleic acid lipid particles [SNALPs]) were able to cross the BBB and deliver siRNA, which can target mutant ataxin-3 in the brain of Machado-Joseph disease mouse models. These SNALPs offered high encapsulation of siRNA, optimum particle size and almost no toxicity. *In vivo* experiments showed the ability of SNALPs to accumulate in the brain and silence the mutant ataxin-3 upon i.v. injection (170).

Venom-derived, peptide-based shuttles have been reported to cross the BBB and to be able to deliver drug at the desired site. Oller-Salvia et al. have demonstrated that miniAp-4 (H-DapKAPETALD-NH_2) derived from Apamin (a neurological toxin from bee venom) is able to cross the bovine-cell-based BBB model and can deliver gold NPs, showing proof of concept for drug delivery (171). PepH3 has shown greater penetration upon i.v. administration in CD1 mice. Bio-distribution was measured in mice sacrificed 5 minutes and 1 h after administration. Furthermore, its clearance and excretion is relatively fast, making it a good candidate for a shuttle carrier (110). Spontaneous internalisation of nanowires (NW) has been reported, linked with a cell penetrating peptide: the trans-activating

transcriptional activator (TAT) from human immunodeficiency virus 1 (172). PWVPSWMPPRHT and GPWVPSWMPPRHT (composed of D-amino acids) have been found to cross the BBB and are able to transport drug molecules or diagnostic substances into the CNS. These peptides have been reported to be biocompatible and non-toxic (as they were made up of amino acids) (173). In recent decades, a number of BBB shuttle peptides with improved efficiency have been reported (Table 1.3). Apolipoprotein (Apo) derivative peptides have been shown to cross the BBB (in *in vitro* and *in vivo* experiments) (174, 175). Numerous studies have demonstrated that ApoB (SSVIDALQYKLEGTTRLTRKRGLKLATALSLSNKFVEGS) and ApoE $(LRKLRKRLL)_2$ analogues are able to cross the BBB (163, 165, 176). Gao et al. reported the use PEG-(poly(ε-caprolactone) NPs (prepared by emulsion solvent evaporation) for the brain drug delivery, and contained docetaxel, a widely used drug in the treatment of several malignancies including brain tumours. They successfully conjugated a phage displayed TGN (Table 1.3) peptide and an AS1411 aptamer, which specifically targets the ligands on the BBB and cancer cells respectively. *In vitro* experiments showed excellent permeability across the C6 cells and bEnd.3 cells endothelial monolayer. *In vivo* imaging showed that unmodified NPs hardly distributed in the brain while AsNPs (AS11411 conjugated NPs) accumulated slightly in the brain. However, the accumulation of TGN conjugated NPs in the brain significantly increased and the brain distribution achieved the highest intensity at 12 hrs (177). Numerous shuttle peptides have been investigated for drug delivery to the brain but still there is a need to find a magical combination.

1.5. Adeno-associated virus delivery system

AAV gene/drug delivery is one of the most investigated mechanisms. AAV has a 4.7-kilobase, single stranded genome with two genes (178). Among AAVs, AAV9 crosses the BBB via an active transport (179). Aubourg et al. initiated phase I/II trial using an AAV serotype rh.10 (AAVrh. 10) by intracerebral administration for the effective transfer of the

ARSA cDNA coding for Arylsulfatase A (ARSA) enzyme into the brain of children suffering with metachromatic leukodystrophy (180). A Phase II trial has been initiated to evaluate the effects of CERE-110 for the treatment of AD (181). CERE-110 generates nerve growth factor (NGF), a protein that keeps nerve cells healthier (182). Raffi et al. reported the efficient delivery of NGF using AAV2. NFAAV2-NGF was found to be safe and well-tolerated through 24 months (181). The virus was delivered via stereotactic neurosurgery. Another phase I/II clinical trial has been reported the delivery of adeno-associated viral vector serotype 10 (AAV-10) by intracerebral administration, loaded/carrying SGSH and SUMF1 cDNA for the sanfilippo type A syndrome and Mucopolysaccharidosis Type III A. Safety data showed good tolerance, no toxicity and moderate improvement in behaviour, attention and sleep (183).

Zhang et al. used BBB shuttle peptides to enhance the brain transduction of AAV8 after systemic administration. THR (THRPPMWSPVWP-NH2), a shuttle peptide that binds specifically to TfR1 was used to promote the internalization and transduction of AAV8. It was reported that AAV8 transduction by THR was dose-dependent (184). Korbelin et al. reported the use of an AAV2 mutant, AAV-BR1 (where BR1 is a brain-targeted peptide NRGTEWD) for the elimination of severe cerebrovascular pathology after i.v. administration int o FVB/N mice (185). Samaranch et al. demonstrated the transduction of the non-human primate brain and spinal cord with AAV5. After bilateral infusion into the putamen and thalamus, GFP was seen instantly. It was found that AAV5 transduced the entire corticospinal axis after thalamic infusion (186). Another study reported the comparison of AAV1, 2, 5, 8 and 9 in marmoset, mouse and macaque cerebral cortices, delivered by intracerebral injection (187). All AAVs efficiently transduced (>70%) cortical cells.

AAV2 showed clear distinction in small spreading and neuronal tropism. Recombinant AAV-TT showed higher neurotropism in rodents, better distribution throughout the CNS

and improved transduction of photoreceptor cells compared to AAV2 following intracerebroventricular injections. AAV-TT exhibited better distribution compared to AAV9 and AAVrh10 standard in the nervous system of mice. At a lower dose, AAV-TT is able to overhaul the neurological phenotype in mouse model of Mucopolysaccharidosis IIIC (188). As explained above, most of AAV delivery was by intracerebral injections, which is an invasive drug delivery to the brain. However, the gene delivery was successful.

Table 1.3. A list of shuttle peptides that can target the BBB.

Peptide	Typical Sequence	Origin	Transport Mechanism	Ref
g7	GFtGPLS (*O*-β-d-glucose)$CONH_2$	Enkephalin analogues/ opioid peptides	RMT	(189-192)
Apamin	H-CNCKAPETALCARRCQQH-NH_2	Venom neurotoxin	Unknown	(171)
MiniAp-4	[Dap]KAPETALD	Venom neurotoxin	Unknown	(171)
Regulon polypeptides	PTVIHGKREVTLHL	Neurotropic endogenous Protein	LDLR	(193)
RAP	ELKHFEAKIEKHNHYQKQLE	Neurotropic endogenous Protein	LDLR	(193)
Angiopep-2	TFFYGGSRGKRNNFKTEEY	Neurotropic endogenous Protein	LRP1	(194, 195)
TAT (47-57)	GGGGYGRKKRRQRRR	HIV Protein	CD4 + T lymphocytes (CCR5, CXCR4)	(196)
PhPro	[Phenyl-Proline]$_4$	Chiral library design	Passive transport (paracellular and transcellular)	(197)
RI-OR2-TAT	Ac-rGffvlkGrrrrqrrkkrGy-NH_2	HIV Protein and Amyloid beta	Aβ peptide binding	(198)
SynB1	RGGRLSYSRRRFSTSTGR	Protegrins	AMT	(199)

Pep 22	Ac-[cMPRLRGC]c-NH_2	Phage display (receptor)	LDLR	(200)
Leptin 30	YQQVLTSLPSQNVLQIANDLENLRDLLHLLC	Leptin	RMT	(201)
TGN	TGNYKALHPHNG	Phage display	Unknown	(202, 203)
CNG-QSH	(d-CGNHPHLAKYNGT) (d-QSHYRHISPAQVC)	Phage display	Unknown/Aβ peptide binding	(204)
LNP	KKRTLRKNDRKKRC	the nucleolar translocation signal sequence of the LIM Kinase 2 protein	Caveolae-mediated endocytosis and macropinocytosis	(205)
ApoE (157-167)	$(LRKLRKRLLR)_2$	Apolipoprotein E	LRP1	(163, 165, 206)
ApoB	SSVIDALQYKLEGTTRLTRKRGLKLATALSLSNKF VEGS	Apolipoprotein B	LRP2	(176)
RVG-29	YTIWMPENPRPGTPCDIFTNSRGKRASNG	Rabies Virus Glycoprotein	nAchR	(168)
G23	HLNILSTLWKYRC	Phage display	GM1 and GT1b	(207, 208)
T7	HAIYPRH	Phage display	hTfR	(209-212)

THR	THRPPMWSPVWP	Phage display	hTfR	(173, 213-215)
THRre	pwvpswmpprht (retro-enantio version of THR)	Phage display	hTfR	
THRre_2f	$(pwvpswmpprht)_2$KKGK(CF)G	Branched - Phage display	hTfR	(216)
DKP	Phe(p-NH-Dhp)-L-N-Me[Cha]/ [2Nal]	Unknown	Passive diffusion	(217)
GSH-PEG	GSH[PEG]	Endogenous tripeptide	Glutathione	(218-220)
CDX	D-[FKESWREARGTRIERG]	Structure-guided design	nAchR	(221, 222)
CRT	CRTIGPSVC	Phage display	TfR	(223)
T7 - #2077	RLSSVDSDLSGC	Phage display	RMT	(224)

1.6. Chemical and physiological disruption of the blood brain barrier

Endothelial TJs block the passage of drugs through the BBB. Physical strategies like disruption of these junctions can result in higher drug permeability. This disruption of the BBB facilitates either paracellular or transcellular penetration of drugs and it should be reversible and rapid. The level of disruption is critical, as it may enable the invasion of harmful and toxic materials, causing seizures, amyotrophic lateral sclerosis, multiple sclerosis, and vasculopathy (225).

1.6.1. Osmotic disruption

Disruption of the BBB for the delivery of drugs to the CNS has been reported to be an alternative approach. Hyperosmotic disruption of the BBB has been suggested to enhance the penetration of hydrophilic drugs. It is believed that hyper-osmosis causes shrinkage of endothelial TJs, leading to higher penetration (226). Mannitol is reported to be used concomitantly with antineoplastic drugs such as procarbazine and methotrexate (MTX) for the treatment of brain tumours (226). Park et al. reported an improved BBB penetration for R-PEG-PMT (poly(mannitol-co-PEI) modified RVG), based on osmotic disruption of the BBB. Intra-arterial administration of the mannitol showed prominent variations in the extent and duration of BBB disruption when injected in rabbits (227). This induced disruption of the BBB should be controlled and cautious; Salahuddin et al. reported that injecting hypertonic mannitol into rats resulted in brain damage with apparent BBB disruption (228, 229).

1.6.2. Vasoactive substance-induced disruption

Vasoactive substances like inotropes, vasopressors, and inodilators have been reported to affect permeability across the BBB. Vasoactive compounds like histamine, bradykinin and analogue receptor-mediated permeabilizer (RMP)-7 exposed brain tumour barriers to external substances. Bradykinin induces opening of TJs by activating B_2 receptors on endothelial cells (230, 231). RMP-7, a bradykinin analogue, has been studied and reported

to control the opening of TJs in the BBB and promotes the permeation of drugs across the BBB. Furthermore, it has been observed that a liposomal delivery system linked with RMP-7 results in Evans blue dye crossing the BBB (232). This bradykinin-induced breakage of the BBB occurred by the calcium-dependent redistribution of occludens TJs. Ketamine supresses bradykinin-induced calcium-dependent redistribution and maintains BBB integrity,(233) as shown in. Ginkgolide B pyrazine (PGB) derivative, a potent antagonist of the platelet-activating factor receptor, has been reported to be a novel brain targeting system with good bio-distribution throughout the brain. In addition, PGB downregulated the P-gP expression in rat hippocampus and cerebral cortex (possibly in brain microvessels). Furthermore, PGB restored BBB integrity in in incomplete cerebral ischemia mice (233, 234). Lower expression of P-gP could be useful, as overexpression of P-gP in brain microvessels could return drug molecules that crossed the BBB back to the blood.

Solvents, stabilisers and surfactants used in different pharmaceutical formulations have been investigated for disruption of the BBB. Sodium lauryl sulphate (SLS, also known as sodium dodecyl sulphate, SDS), an anionic surfactant used in pharmaceutical formulations as a solubilising, wetting and foaming agent, enhanced permeation of Evan's blue across the BBB when injected into rats (235, 236). Ethanol, also used in pharmaceutical formulations, has been described to interrupt the BBB when consumed chronically (237, 238). Polysorbate 80 (Tween 80), a pharmaceutical excipient used as a stabiliser and emulsifier in aqueous formulations,(239) when injected concurrently with MTX, led to higher levels of MTX being observed in the brain due to the disruption of the BBB (240). In addition, drug-containing NPs coated with Tween 80 have been stated to be able to deliver the payload into the brain by disruption of the BBB (241-244). It should be noted that Tween 80 adsorbs ApoE from the blood, which helps Tween 80 coated NPs to deliver payload the brain by crossing the cerebral endothelium and epithelial cells in the choroid plexus (245, 246).

1.6.3. Ultrasound-induced disruption

The use of energy-based physical methods, such as ultrasound, to disrupt the BBB physiologically has been studied extensively. Acoustic technology has empowered the use of ultrasound not only as a diagnostic tool, but also as a therapeutic modality (247). Focused ultrasound (FUS) can be concentrated deep on specific tissue with less impact on the surrounding body tissues. No surgical procedures are required in this approach, as this is a non-invasive technique which induces physiological changes in the deep tissues (248). It has been revealed that the use of preformed microbubbles prior to ultrasound application opens the BBB without destruction of neurons (249, 250). High-intensity focused ultrasound (HIFU) produced reversible, non-damaging BBB disruption (251). Microbubbles (albumin coated, octafluoropropane-filled microbubbles ranging from 2 to 4.5 μm in diameter [Optison™, Mallinckrodt Inc., USA]), ultrasonographic contrast agent (enhanced images of magnetic resonance imaging [MRI]) and Evans blue have been employed to verify BBB opening (251-253). A schematic representation is shown in Figure 1.13 for ultrasound-induced disruption. One of the proposed mechanisms of action for ultrasound to work is by raising the temperature of the focal area (hyperthermia) (254). In another study, conducted on a rabbit model of the BBB, ultrasound power of 0.55 W was used and TJ openings were observed with release of payload (dye) and contrast agent (253).

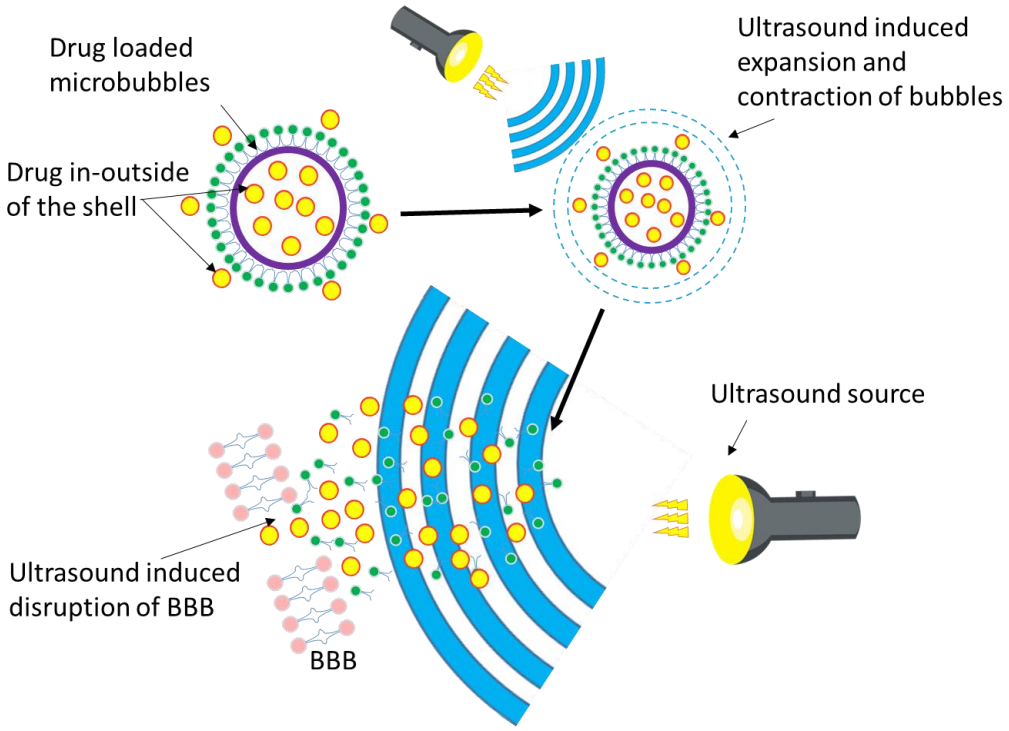

Figure 1.13. Schematic representation of ultrasound-induced disruption of the BBB.

1.7. Novel Nanotechnology for brain drug delivery

Nanoparticles (NPs) are carriers composed of natural (e.g. lipidic) or synthetic (e.g. polymeric) materials ranging from 1-500 nm in size. NPs are able to encapsulate, adsorb, or conjugate drugs or diagnostics and release the payload at a specific rate in the human body (255). The physicochemical properties of NPs such as size, surface charge (zeta potential), morphology and composition are important factors deciding the fate of NPs, such as passage across the BBB, biological activity, release profile and biocompatibility (256). A list of NPs used for brain drug delivery are summarised in Table 1.4.

1.7.1. Polymeric NPs (PMNPs)

Polymeric NPs (PMNPs) are most extensively studied for the purpose of drug delivery. These NPs can not only deliver small drug molecules but can also be used for the delivery of genes and proteins (257). PMNPs can have good penetration through cell membranes, serum stability, and can be easily manufactured. Furthermore, the surface of NPs can be modified for various medical applications. For brain drug delivery, PMNPs are made up of proteins, amino acids, polysaccharides and polyesters. Different mechanisms can be adapted

by the PMNPs to cross the BBB. They can cross the BBB either by transcytosis through endothelial cells, mucoadhesion, or by disturbing the TJ in the brain capillaries (258). On the other hand, PMNPs can be identified upon i.v. injection by the reticuloendothelial system (RES), leading to wide distribution to liver, spleen and bone marrow, resulting in elimination or very short half-lives (259).

PLGA-NPs modified with 7-amino acid glycopeptide (g7) have been shown to deliver small drug molecules across the BBB in rodents. Furthermore, g7-NPs successfully crossed the BBB with model drug (fluorescein isothiocyanate (FITC)-albumin). Injection in wild-type and knockout mice clearly showed penetration into the brain (260).

Table 1.4. A summary of formulations (NPs) targeting the BBB.

Formulation/Polymer	Drug	Disease	Method used for NP preparation	Mechanism for BBB crossing	Key Findings	Ref
g7-PLGA-NPs **(NPs of less than 300 nm)**	FITC-albumin	MPS I and MPS II	Double emulsion technique	RMT	The C57BL/6 Idua knockout and C57BL/6 Ids knockout mice were used. High MW molecule delivery across the BBB achieved	(260)
Functionalized solid lipid NPs with apolipoprotein E, (SLN-DSPE-ApoE) **(Average size was less than 200 nm with zeta potential of –10-15 mV)**	Resveratrol	Neuroprotective	High shear homogenization	LDLR	*In vitro* cytotoxicity evaluation via MTT and LDH using hCMEC/D3 cell line showed that SLNs affected neither the metabolic activity of	(261)

					the cells nor the membrane integrity at concentrations less than 1500 µg/mL. hCMEC/D3 monolayers in transwell devices showed SLN-DSPE-ApoE, permeability 1.5-fold higher than for non-functionalized SLNs	
Bovine Serum Albumin NPs with LMWP cell penetrating peptide (LMWP-albumin) [LMWP: CVSRRRRRRGGRRRR] **(Particle size less than 200 nm,)**	PTX and 4-HPR	Brain cancer	Self-assembly	Brain penetration mainly by EPR, but also through SPARC and gp60 albumin binding proteins	FACS showed *in vitro* cellular uptake of the NPs. bEnd.3 cell line showed penetration of the NPs	(262)

				overexpressed in glioma tissues	U87 cells showed cytotoxicity of NPs. The NPs were administered by i.v. injection to orthotopic glioma (Luc-U87) mouse model (bearing intracranial tumor). The mice received the NPs (LMWP-modified bovine serum albumin (BSA) NPs containing PTX and 4-HPR) showed the longest survival time	

PEG–PLA–penetratin (RQIKIWFQNRRMKWKK) (Particle size 100 nm, zeta potential -4.42 mV)	Coumarin-6	CNS disorders	Emulsion/solvent evaporation technique	AMT/RMT	MDCK-MDR cell model showed enhanced accumulation via both lipid raft-mediated endocytosis and direct translocation. *In vivo* administration showed significant brain uptake with less deposition in non-target tissues	(263)
Angiopep conjugated with poly(ethylene glycol)-co-poly(ε-caprolactone): ANG-PEG– poly(ε-caprolactone)	Paclitaxel	Glioblastoma multiforme	Sonication	LDLR	U87 MG glioma cells indicated the ANG-PEG- poly(ε-caprolactone) NPs uptake via LDLR (Angiopep-2 and	(264)

(Particle size was less than 100 nm with zeta potential of 3.28 ± 0.75 mV)					Aprotinin significantly reduced the cellular uptake of the NPs). Real time fluorescence imaging showed accumulation of ANG-NPs in the brain of intracranial U87 MG glioma tumor-bearing nude mice after i.v. injection.	
TAT-poly(ethylene glycol) (PEG)-b-cholesterol: TAT–PEG-*b*-Chol **(Particle size less than 200 nm)**	Ciprofloxacin	Encephalitis	Self-assembly	AMT	Enhanced *in vitro* cellular (ACBRI 376) uptake. NPs crossed the BBB and located around the cell nucleus of	(265)

					neurons (SD adult rats) following i.v. injection	
RVG-29-PEG-PLGA/DTX-NPs **(Particle size was around 110 nm)**	Docetaxel	Gliomas	Nanoprecipitation	nAchR	*In vitro* bEnd3 cells showed permeability across the monolayer. RVG-29-PEG-PLGA/DTX-NPs had a stronger inhibitory effect on C6 cell proliferation than free DTX. *In vivo* experiments confirmed selective accumulation of NPs in intracranial glioma tissues following i.v. injection.	(266)

PEG-Poly(ε-caprolactone)-CH2R4H2C/Stearate-CH2R4H2C (CH2R4H2C: CHHRRRRHHC peptide) **(Particle size was in the range of 50-100 nm with zeta potential of 15-20 mV)**	Dextran (as model drug)	CNS disorders	Self-assembly	Olfactory nerve channels	Hydrophobic carrier is more suitable for the delivery of drug in forebrain, while hydrophilic carrier is suitable for hindbrain (brainstem).	(267)
g7- PLGA-Np **(Particle size was in the range of 155±26 nm with zeta potential of -15±5.6 mV)**	Loperamide	CNS disorders	Nanoprecipitation	AMT	Long term *in vitro* release over 192 hours and 20% in 2 hours. *In vivo* experiments showed excellent bio-distribution in brain.	(268, 269)
mPEG−PLGA-RVG	Deferoxamine	PD	Double emulsion technique	nAchR	*In vivo* administration reduced the oxidative	(270)

(Particle size was in the range of 168.8 ± 1.9 nm with zeta potential of −27.40 ± 0.71 mV)					stress and iron contents in the substantia nigra and striatum of PD mice.	
siRNA/TMC–PEG-RVG **(Particle size was in the range of 207 ± 2 nm with zeta potential of 9 ± 2.5 mV)**	siRNA	AD	-	nAchR	*In vitro* and *in vivo* experiment showed excellent penetration into brain with low toxicity and higher serum stability.	(271)
AuNCs-RDP **(Particle size was in the range of 10 ± 2.85 nm with zeta potential of -5.92 ± 3.16 mV)**	Carboxyfluorescein	Neural cell imaging	Green synthetic route	RMT	*In vitro* and *in vivo* results suggested the effective internalization in the brain cells.	(272)

In another study, Gajbhiye et al. successfully transported galantamine into the brain by using ascorbic acid embedded PLGA-b-PEG NPs. They targeted sodium-dependent vitamin C transporters (SVCT2) expressed by neuroepithelial cells of the choroid plexus (54). Recently, Ammar et al. prepared lamotrigine-loaded poly(D,L-lactide-co-ε-caprolactone) (PLCL) NPs with a particle size of 125 nm. When administered intravenously to Wistar albino rats, these NPs showed higher pharmacokinetic measures (T_{max}, C_{max}, and AUC) in the brain compared to oral lamotrigine tablets (273). Sánchez-López et al. synthesized memantine-loaded PLGA NPs coated with PEG that showed higher endothelial monolayer crossing upon oral administration. In addition, this formulation was found to be non-cytotoxic to brain cell lines (bEnd.3 and ACs) (274).

1.7.2. Liposomes for brain drug delivery

Liposomes are self-assembled NPs made up of phospholipid bilayer membrane. Phospholipids are heterogeneous molecules containing phosphate residues, polar head groups, and non-polar alkyl chains (275) that self-assemble (according to the fluid mosaic model) into biological membranes. Liposomes for brain drug delivery have been studied extensively in the last two decades.

Miao et al. evaluated xenon (Xe), a noble gas having outstanding neuroprotective activity. Xe-containing echogenic liposomes (Xe-ELIP) were administered intravenously to deliver the xenon via ultrasound-controlled cerebral drug release for early brain injury following subarachnoid haemorrhage (SAH) (276). In another study, Mancini et al. developed L-α-phosphatidylcholine/cholesterol/DSPE-PEG-maleimide (65:32.5:2.5) liposomes encapsulated with the phenolic-rich *Annona muricate* aqueous extract (a moderate monoamine oxidase A (MAO-A) inhibitor and a strong hydrogen peroxide (H_2O_2) scavenger) for brain drug delivery (277). Pulford et al. formulated liposomes (178 ± 20 nm) containing cationic lipid octadecenolyoxy[ethyl-2-heptadecenyl-3 hydroxyethyl] imidazolinium chloride to deliver siRNA into the brain of mice following

i.v. injection. The cationic liposome-siRNA-peptide (RVG-9r) penetrate the endothelial monolayer, with the peptide moiety binding to nAChRs (278). Bender et al. used two liposomal systems for the delivery of prion protein siRNA to the brain of mice following i.v. injection. One of the liposome formulations was cationic liposomes containing 1,2-dioleoyl-3-trimethylammonium-propane (DOTAP), which formed complex with siRNA and RVG peptide. The other liposomal system contained DOTAP or 1,2-distearoyl-sn-glycero-3-phosphoethanolamine (DSPE) to encapsulate the siRNA. Both systems decreased the prion protein expression of neurons in the CNS (279). Rotman et al. used glutathione (G-technology)-decorated PEGylated liposomes (sizes in the range of 108-110 nm) to deliver llama single-domain antibody fragments (VHH-pa2H) into the brain of APP_{swe}/PS1dE9 double transgenic mice following i.v. injection. The delivery of VHH-pa2H significantly improved into brains of transgenic APP/PS1 mice by glutathione targeted PEGylated liposomal encapsulation (280). This was also supported by the work of Veszelka et al. that found higher *in vitro* BBB penetration of solid lipid NPs decorated with glutathione, compared to biotin (281). Lin et al. used gefitinib-loaded liposomes modified with glutathione and Tween 80 to cross the *in vitro* endothelial monolayer model for the treatment of brain metastases (282). These studies show that targeted-liposomal formulations can deliver therapeutic agents such siRNA to the brain following i.v. injection. An unexpected outcome is accelerated blood clearance upon repeated administration to PEGylated nano-carriers, including liposomes (283). In addition, the immunostimulatory activity of nano-carriers such as liposomes is known (284, 285). Therefore, it would be useful to conduct research about the immunostimulatory of liposomes for brain drug delivery upon repeated administration.

As well as liposomes, lipid-based formulations have been developed,(286) as carriers for drug delivery to the brain, (287) including oral administration of NPs (288, 289). Interestingly, Grinberg et al. reported novel cationic amphiphilic compounds synthesised

from vernonia oil. The quaternary methyl ester derivative of methyl vernolate self-assembled into vesicles (in the presence of cholesterol 1:1) with the size of 50-200 nm in diameter (290). Vesicles made from the quaternary vernonia oil derivative (triple-headed amphiphile) were found to be efficient in transfection of cDNA encoding for GFP into cultured COS-7 cells (290). These vesicles were employed to deliver analgesic peptides (kyotorphin or leu-enkephalin) to the brain of male ICR mice following i.v. injection. It should be noted that the vesicles were not decorated with any brain targeting ligand, and the lipid properties of vesicle surface and the cationic nature were sufficient to cross the BBB (291).

1.7.3. Exosomes

Exosomes are comprised of natural lipid bilayers with an abundance of adhesive proteins that readily interact with cellular membranes. These are small extracellular nano-vesicles secreted by numerous cell types (292, 293). Naturally-occurring extracellular vesicles such as exosomes traffic endogenous small molecules, proteins and nucleic acids between cells,(294, 295) and they have shown considerable promise for the delivery of exogenous drugs or biological therapeutics,(296-299) including to the brain (300, 301). Exosomes have several advantages over synthetic NPs in that their biocompatibility confers upon them an inherent non-immunogenicity and long circulation times, however surface-functionalisation (e.g. for targeted delivery) and synthetic analogues of ‘natural’ exosomes have also proven to be successful therapeutic strategies (302-304). Drugs delivered by means of an exosomal vector often show enhanced efficacy and fewer adverse effects. Enhancing and exploiting the innate drug-delivery capabilities of exosomes make for a highly attractive therapeutic approach.

Exosomes isolated from brain ECs regulate the exchange of molecules across the BBB (305). Yuan et al. used macrophage-derived exosomes decorated with integrin lymphocyte function-associated antigen 1 (LFA-1) and intercellular adhesion molecules

(ICAM)-1, 2 to deliver brain-derived neurotrophic factor (BDNF) to the brain (306). Yang et al. demonstrated the ability of brain endothelial bEND.3 cell-derived exosomes to traffic the anticancer drugs doxorubicin and paclitaxel across the BBB of zebrafish (307), killing xenotransplanted U87-MG human glioblastoma-astrocytoma cells (308). In a follow-up experiment, vascular endothelial growth factor (VEGF) siRNA was delivered for anti-cancer applications using a similar preparation (309).

Curcumin-loaded exosomes tagged with cyclo(Arg-Gly-Asp-D-Tyr-Lys) peptide [c(RGDyK)] were used to target the lesion region of the ischemic brain in a transient middle cerebral artery occlusion mouse model (310). Alvarez-Erviti et al. used RVG decorated exosomes to deliver siRNA to the mouse brain (169). Long et al. used A-1 exosomes (derived from human bone marrow mesenchymal stem/stromal cells (MSCs)) for the rectification of pilocarpine-induced status epilepticus (SE) (311). Exo-JSI124 exosomes derived from EL-4 cells (a mouse lymphoma cell line) were used to deliver an encapsulated anti-inflammatory drug in experimental autoimmune encephalomyelitis (EAE) mice via an intranasal route, modulating inflammation (312). Exosomes derived from dendritic cell cultures treated with interferon-γ were found to increase myelination in rats upon intranasal administration, possibly by delivery of miR-219 (313). Exosomes loaded with superparamagnetic iron oxide NPs (SPIONs) and curcumin and conjugated with neuroleptin-1-targeted peptide (RGERPRR) crossed the glioma cells and orthotopic glioma models and were used for imaging and treatment of glioma (314). Iraci et al. revealed the unexpected ability of stem cell exosomes to harbour and deliver functional enzymes (e.g. Asparaginase-like 1) extracellularly, thus behaving as fully independent small metabolic units with exciting therapeutic implications (315).

Cooper et al. describe the use of exosomes derived from murine bone marrow dendritic cells to block the aggregation of α-Syn, a pathological process implicated in PD progression. siRNA-loaded exosomes decorated with RVG (targeting ligand) effectively

reduced the α-Syn aggregation in normal mice and transgenic mice expressing the human phosphorylation-mimic S129D α-Syn (316). Dopamine-loaded exosomes derived from the blood of mice were used to deliver drugs across the BBB with lower systemic toxicity compared to i.v. administration of naked dopamine (317). As an alternative approach, Haney et al. circumvented the BBB, using intranasal delivery to successfully administer the catalase-loaded macrophage-derived exosomes to the brain of mice with a model of PD, resulting in significant neuroprotective effects (292). Conversely, a potential role of exosomes in *diagnosing* neurodegenerative conditions was highlighted by Gui et al. who developed a microRNA-profiling strategy for the early detection of PD. They used exosomes isolated from the CSF of PD and AD patients, reporting sixteen miRNAs upregulated and 11 miRNAs under regulated in PD (318).

Liu et al. successfully deployed exosomes expressing RVG on the surface loaded with opioid receptor mu (MOR) siRNA into the brain for the treatment of morphine addiction (319). Xin et al. used exosomes derived from MSCs for the treatment of stroke. They found increased levels of doublecortin (a marker of neuroblasts), von Willebrand factor (a marker of ECs) cells, improved neurite remodelling, neurogenesis and angiogenesis (320). Wu et al. also used RVG decorated exosomes for brain drug delivery. They encapsulated siRNA targeting human huntingtin exon 1 (HuHtt) transcript. HuHtt-siRNA loaded RVG-exosomes were then administered intravenously to normal mice and BACHD and N171-82Q transgenic (Huntington's Disease-model) mice at 10 mg/kg every two days for 2 weeks. siRNA-loaded RVG exosomes significantly reduced HuHtt mRNA and protein levels up to 46% and 54% respectively in transgenic animals (321). Didiot et al. successfully delivered hydrophobically modified small interfering RNAs (hsiRNAs) into the brain using exosomes. They loaded the exosomes with hsiRNAs targeting Huntingtin mRNA via incubation, without altering significant

characteristics. These exosomes were efficiently internalized by mouse primary cortical neurons and promoted dose-dependent silencing of Huntingtin mRNA and protein (322).

Preclinical studies, such as those reported by Doeppner et al. (323) and Lee et al. (324) have demonstrated that intravenously-delivered MSC-derived vesicles can affect therapeutic outcomes in models of ischemic stroke, ostensibly bypassing the BBB. Oshra et al. proposed a method for non-invasive *in vivo* neuroimaging of MSC-derived exosomes, based on computed tomography (CT) imaging with glucose-coated gold NP (AuNP) labelling. Imaging and tracking of intranasally-administered AuNP-labelled exosomes in a mouse model of focal ischemia showed accumulation and prolonged presence at the lesion area up to 24 h (325). Generally speaking, however, methods for *in vivo* tracking of exosomes require further development. Kim et al. showed that systemic (i.v.) administration of MSC-derived inflammation-modulating extracellular vesicles (mean size of vesicles ranged from 209-231 nm), shortly after induction of TBI to a rat model, rescued pattern-separation and spatial learning impairments one month after the treatment. However the mechanisms involved remain to be elucidated (326). Shen et al. demonstrated the delivery of miR-133b using MSC-derived exosomes into brain tissues. After i.v. administration of the modified exosomes, effects of miR-133b on neuronal apoptosis and degeneration were evaluated by terminal deoxynucleotidyl transferase dUTP nick end labelling (TUNEL) and fluoro-jade B staining respectively. They found that miR-133b modified exosome treatment remarkably suppressed RhoA expression and activated ERK1/2/CREB in brain tissues after intracerebral haemorrhage (327). Kojima et al. reported genetically engineered exosomes with the ability to package specific mRNAs and delivery them into the cytosol of target cells, enabling efficient cell-to-cell communication (328). As the above research shows exosomes present competitive nano-carriers for drug delivery to the brain. However, more research is needed to standardize the production and scale-up of either exosomes or tagged-exosomes (299, 329).

1.7.4. Dendrimers for brain drug delivery

Dendrimers are chemically synthesised polymeric particles with defined shapes (due to monodispersity) as shown in Figure 1.14. Dendrimers have been investigated for brain drug delivery. Moscariello et al. designed PAMAM dendrimer (third generation) bio-conjugates with a streptavidin adapter that was taken up by porcine or murine models in *in vitro* and *in vivo* models via endosomal transcytosis, avoiding lysosomes (330).

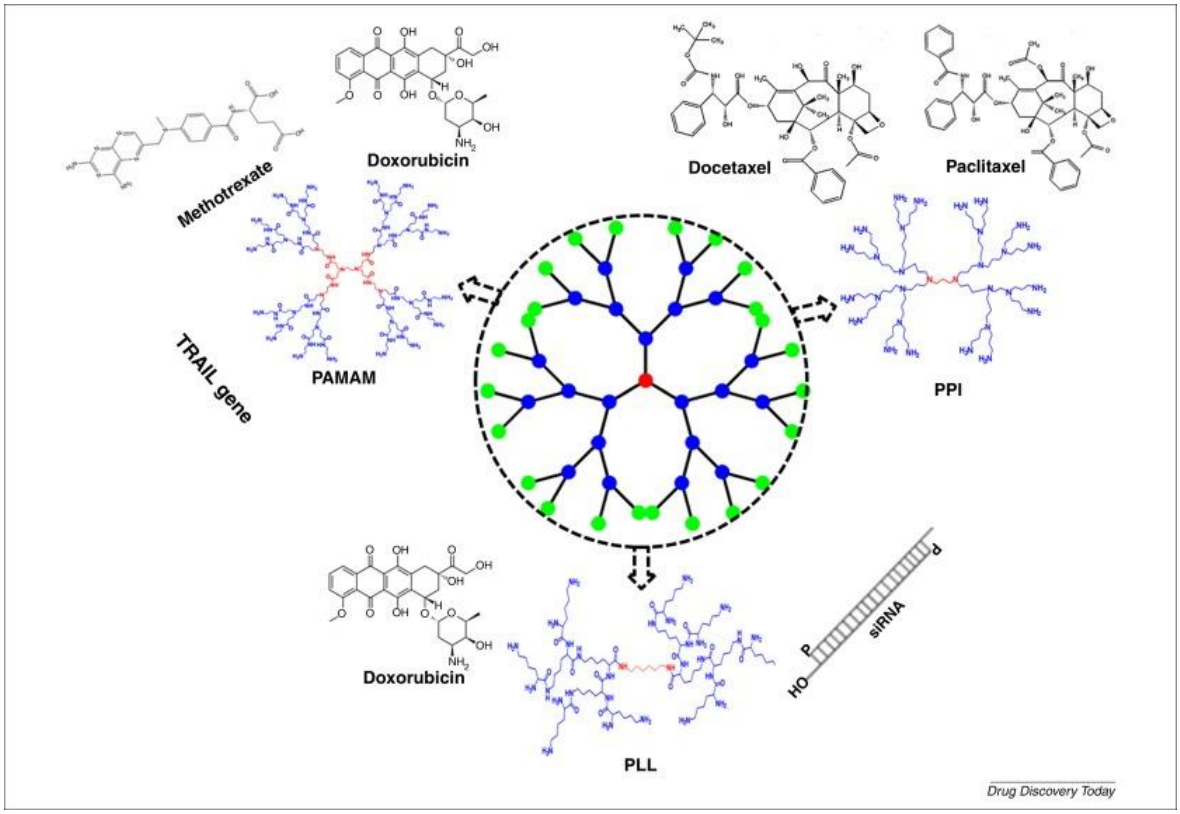

Figure 1.14. Different dendrimers involved in the delivery of drugs and gene across the BBB (331).

In another study, apolipoprotein A-I (ApoA-I) and NL4-peptide dual modified dendrimer NPs were efficient carriers for siRNA delivery to PC12 cells and efficiently penetrate through bEnd.3 monolayer via LDLR (332). Ke et al. used PAMAM–PEG–Angiopep/DNA-NPs to deliver plasmid DNA across the BBB. The PAMAM was fifth generation with 128 surface primary amino groups. *In vitro* BBB model showed clathrin and caveolae-mediated endocytosis (also partly through marcopinocytosis) of the nano-carriers containing Angiopep peptide [TFFYGGSRGKRNNFKTEEYC]. PAMAM–

PEG–Angiopep dendrimers were loaded with pEGFP plasmid; and the NPs were administered intravenously to mice. Gene expression was observed in all four regions of the mouse brain for the PAMAM–PEG–Angiopep/DNA NPs, which was much higher than those for the PAMAM/DNA NPs (333). In another study, low generation lysine dendrons (G0 and G1) conjugated with ApoE derived peptide (LRKLRKRLLR) were reported to cross the immortalized brain endothelial cell line (bEnd.3) efficiently with no cytotoxicity up to 400 µM (334). It should be noted that PAMAM/siRNA complexes appear to show significant cell toxicity even at low concentrations such as 20 µg/mL (335). As it would be expected, the cationic dendrimers show haemolytic activity. However, increasing the dendrimer generation decreases the haemolytic activity. For example, G2 dendrimers showed 100% haemolysis at 1 mg/mL concentration after 24 h incubation with RBCs, while G5 dendrimers showed no haemolysis (comparable to negative control) at the same concentration and incubation period (336). Dynamic light scattering (DLS) studies showed that PAMAM/siRNA complexes had sizes in the range of 150-200 nm, while TEM results indicated a wider size distribution with majority in the range of 30-45 nm for G7 PAMAM/siRNA with N/P ration of 10 (337). Therefore, part of the success of dendrimers could be due to small sizes of the nano-carriers in DNA or siRNA delivery to the brain.

1.7.5. Metallic NPs

Metallic NPs for brain delivery have been under investigation due to their serum stability and long half-life. Ghorbani et al. reported the use of gold-iron nanocomposites encapsulated (ligand exchange of disulfide group) with curcumin-lipoic acid, a pH-sensitive delivery system for the brain. GSH is used as a targeting ligand, leading to a 2-fold increase in cellular uptake (338). Cisplatin-conjugated gold NPs (AuNP-UP-Cis) via ionic adsorption, in conjunction with MR-guided Focused Ultrasound (MRgFUS) were investigated for the treatment of glioblastoma (339). Ivask et al. evaluated the uptake of

iron oxide NPs conjugated with biomimetic phosphorylcholine brushes in an *in vitro* BBB model system. They reported that after 24 h, 78% of the formulation crossed the *in vitro* BBB model system via AMT (340). This ability of iron oxide NPs has provided the opportunity of delivering therapeutic peptides to the brain by conjugating the peptide to the surface of iron-oxide NPs (5 nm diameter) (341). Tf-conjugated magnetic dextran-spermine NPs (DS-NPs) have also demonstrated excellent penetration across the U87MG cells (342). Sun et al. reported negatively charged iron oxide NPs (IONPs) with the size of 29 nm in conjunction with lysophosphatidic acid (LPA) effectively crossed the BBB by disrupting the TJ. With LPA treated IONPs, 4-fold increase was observed in the mouse brain compare to control (343). Najafabadi et al. (2018) used SPIONs (in the range of 30 to 50 nm) to deliver quercetin (bioactive flavonoid) to rats after oral administration. Higher concentration of quercetin were found in the brain tissues (0.52 ± 0.08 µg/mL for the dose of 100 mg of NPs/kg) for quercetin-SPIONs compared to free quercetin administration (0.052 ± 0.018 µg/mL for 100 mg of free quercetin/kg) [the loading capacity of the NPs was 42%] (344). Kirschbaum et al. used iron oxide NPs (32 nm) for the imaging of immune cells, which play a major role in pathogenesis of MS or experimental EAE. These were fluorescently labelled cross-linked iron oxide NPs, which were used for the cell tracking and high field MRI to map inflammatory infiltrates. This was a NP-based approach to image brain-resident and infiltrating innate immune cells in inflammatory lesions (345). NP uptake is specific for innate immune cells and correlated with clinical severity. Therefore, targeting innate immunity by molecular imaging may serve not only as a direct marker of disease activity, but also with the potential of clinical translation to deliver therapeutic agents to the brain via these innate immune cells. They reported 4.6-fold increased accumulation of NPs in EAE compared to control mice (345).

Kang et al. reported a single-step procedure to simultaneously load porous silicon NPs with high concentrations of siRNA and protecting them by formation of Ca_2SiO_4 at the surface of NPs (pSiNPs). These core-shell NPs had the size of 180 ± 20 nm. Then pSiNPs were surface functionalised with RVG peptide (cell targeting ligand) and a cell penetrating peptide (myr-GWTLNSAGYLLGKINLKALAALAKKIL(GGCC), a myristoylated transportan) to deliver the siRNA across the BBB. Addition of these peptides increased the size of pSiNPs to 220 nm. The pSiNPs were administered intravenously to mice with brain injury, and a significant amounts of siRNA were accumulated at the site of injury (346). Similarly, Lee et al. reported the use of rabies virus-mimetic silica-coated gold nano-rods to treat brain gliomas. The nano-rods were prepared by converting spherical gold NPs to gold nano-rods. Then coating the gold nano-rods with SiO_2. This was to adjust the size of the nano-rods to the size of rabies virus as much as possible. This was followed by coating the resulting Au-SiO_2 nano-rods by PEG and RVG-29. The nano-rods (RVG-PEG-Au@SiO_2) had the length of 117.7 ± 7.3 nm and width of 50.3 ± 3.1 nm. The RVG-PEG-Au@SiO_2 nano-rods were administered intravenously to orthotopic glioma-bearing mice, and *in vivo* fluorescence imaging indicated the accumulation of RVG-PEG-Au@SiO_2 nano-rods in the mouse brains. The mice were subjected to photothermal therapy using near infrared (NIR) laser. The temperature changes (up to 60ºC) caused by the laser therapy (localized surface plasmon resonance) of gold nano-rods resulted in irreversible damages to or death of tumour cells. Tumour volumes in mice treated with RVG-PEG-AuNRs@SiO_2 nano-rods and applying NIR laser were considerably smaller than those of mice treated with PEG-AuNRs@SiO_2 nano-rods or control saline (124.8 ± 147.5, 1067.4 ± 295.4, and 2323.2 ± 436.3 mm^3, respectively) at 7 days after the treatment. Even, the tumors of two mice treated with RVG-PEG-AuNRs@SiO_2 nano-rods nearly vanished. This therapy caused slight skin damage by 808 nm laser irradiation, which was healed after 13 days (347). This study

indicates that even the EPR of the brain tumours was not sufficient to allow accumulation of PEG-AuNRs@SiO_2 nano-rods in the tumours and use of RVG-29 cell targeting peptide was necessary to achieve desired therapeutic outcomes. In addition, the size of RVG-PEG-AuNRs@SiO_2 nano-rods could be part of the successful application of these NPs.

Numerous factors control the systemic circulation, cell penetration and BBB passage of NPs. Particle size is one of the important factors controlling the access of NPs across the BBB. Studies conducted in animal models of AD, PD and stroke have used NPs of 50-100 nm (244, 348-352). Several techniques, such as DLS, atomic force microscopy (AFM), TEM and scanning electron microscopy (SEM) are used to characterise NPs (353). A number of factors control the particle size, such as the polymers used, drug loading, drug/polymer ratio and hydrophilic/lipophilic ratio. Numerous studies have reported an increase in particle size after drug loading (354, 355). On the other hand, Lopalco et al. have reported no changes in the size of NPs made up of PLGA, PLGA-d-α-tocopheryl polyethylene glycol 1000 succinate (TGPS) and Resomer RGPd5055 pre- and post-loading of drugs (oxcarbazepine and coumarin-6) (356).

1.7.6. Carbon Nanotubes

Carbon nanotubes (CNT) are cylindrical molecules that consist of rolled-up sheets of single-layer carbon atoms. Distinctive properties of CNT such as good electronic properties, excellent penetration into cell membrane, high loading capacity, pH-dependent unloading, greater surface area and ease of modification make them one of the suitable drug delivery system for the brain (357, 358). CNT have been extensively investigated as a drug carrier to the brain in past few years. Functionalized CNT can potentially be used as a carrier for drugs that have poor permeability across the BBB and also can be used for diagnostic and for the treatment of brain disorders (359).

CNT can be synthesized by electric arc discharge and laser ablation using vaporisation of graphite target (360) or by chemical vapour deposition (361). CNT can be grouped into

single wall carbon nanotubes (SWCNT) or multi wall carbon nanotubes (MWCNT) depending on the number of layers that constitute a CNT. CNT size ranges from 0.4 nm to 100 nm depending on the layers. CNT can be functionalized covalently or non-covalently (362).

Ren et al. developed PEGylated oxidized multi-walled carbon nanotubes (O-MWNTs) modified with angiopep-2 (O-MWNTs-PEG-ANG) to treat brain glioma. They reported the high uptake and accumulation of CNT in the desired area with excellent loading capacity. Angiopep-2 specifically binds to LDLR and promotes the internalization. Doxorubicin loaded CNT were found to have better anti-glioma effects than naked doxorubicin (363). In another study, ANG functionalized radiolabelled CNT were employed to deliver drug across the BBB. *In vitro* experiments suggested higher penetration of ANG-CNT than chemically functionalized CNT. Enhanced localization of ANG-CNT was reported upon *in vivo* injection and 2% of the injected dose per g of brain (%ID/g) was accumulated in the brain within the first hour post-injection (364, 365). TAT (YGRKKRRQRRR) conjugated CNT were reported to have excellent BBB penetration and anticancer activity through increased ROS production (366).

1.7.7. Parameters affecting the BBB transport

1.7.7.1. Size, morphology and surface zeta potential

NPs in the range of 120-180 nm after crossing the BBB may be entrapped in the BL (367). However, NPs with the size in the range of 16-24 nm are able to diffuse in the brain parenchyma (367). These observations indicate that NPs should be less than 120 nm such as exosomes in order to diffuse in the brain parenchyma, otherwise they will remain trapped in the BL following crossing the BBB.

The morphology of NPs affects their bio-distribution and cellular uptake. NPs could be spherical, cubic, tubular or rod-like in shape (368, 369). A majority of the particles reported for brain delivery are roughly spherical in shape. Zeta potential or surface charge

of NPs is another factor that controls the diffusion across the BBB. It has been reported that a high (positive) zeta potential causes toxicity to the BBB (370, 371). Rassu et al. reported that a positive surface charge on NPs ensures their mucoadhesion (372). On the other hand, NP formulations have been reported for brain delivery with zeta potentials between -1 and -45 mV (130, 373, 374). Different shapes of NPs are shown in Figure 1.15.

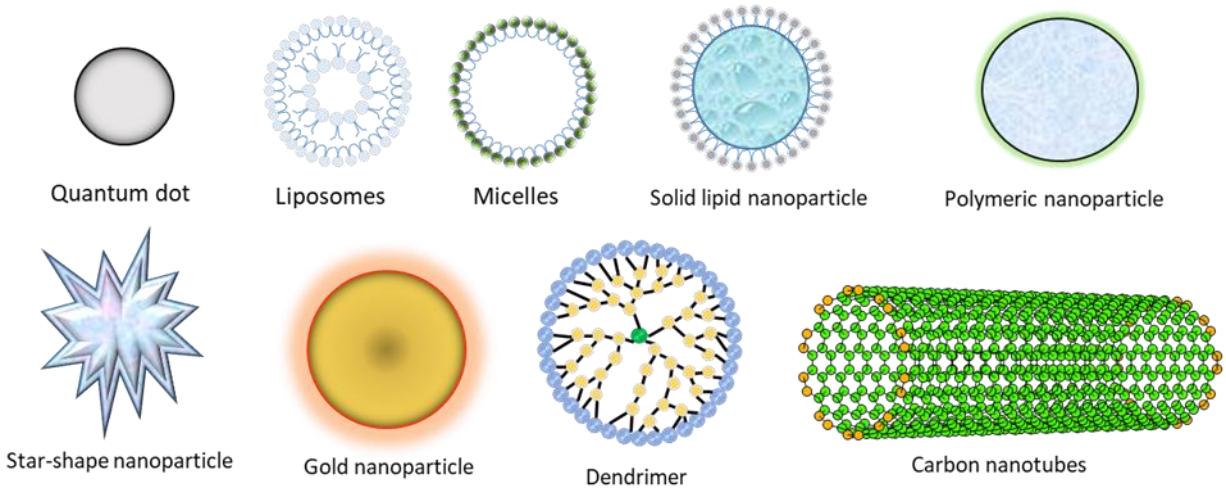

Figure 1. 15. Different morphologies and shapes of NPs used for brain drug delivery.

1.7.7.2. Critical micelle concentration (CMC)

CMC is the minimum concentration of a compound at which it forms micelles. CMC plays a major role in the stability of micelles/NPs due to excessive dilution in the blood, upon i.v. injection. If the concentration in systemic circulation drops below the CMC, then it releases the payload in the blood stream before getting to its target.

CMC can be determined by using set concentrations of a pyrene probe with serial dilution of copolymer solution (375, 376). Ruan et al. used RAP12 peptide (a part of the receptor associated protein that binds to LRP1) and decorated PEG-poly(lactic acid) (PLA) micelles to deliver drug (paclitaxel) across the BBB (101). Liu et al. reported CG_3R_6TAT (CGGGRRRRRRYGRKKRRQRRR), a self-assembled cationic antimicrobial peptide able to cross the BBB. They measured the CMC by using the pyrene

as a probe and found to be 31.6 mg/L (10.1 µM) in deionized water (375). Micelles and PMNPs both can target the brain and cross the BBB. Efficacy and efficiency of crossing the BBB are dependent on targeting via the surface of the nano-carriers.

1.7.7.3. Protein corona

NPs, upon contact with biological fluids, are surrounded by a protein layer that is called protein corona (377-380). The first layer of protein corona is bound tightly on the surface (primary contact with NPs), which is referred as ‘‘hard’’ corona. Usually, another layer is loosely bound on the first layer, which is referred as ‘‘soft’’ corona; and that consists of serum proteins, mainly comprising albumin and its derivatives (381-383). This surface adsorption of protein can alter the physiological response (382). The adsorption of proteins on NPs mostly has undesirable effects such as prompt clearance from blood stream, compromised targeting capacity (384) and toxicity (385, 386). Proteins bound to a NP surface may rearrange their structure and shape according to NP surface and environment, this is known as ‘‘conformational change’’. Conformational change accompanied with the modification of secondary or tertiary protein structure. Proteins are supposed to interact with other biomolecules to initiate biological responses, hence a small modification in protein structure has huge impact on their pharmacological activities (387).

Several factors dictate the nature of adsorbed proteins. Particle size plays an important role in protein adsorption. As NPs are bigger than proteins, NPs make proteins to adapt the NPs’ surface. Smaller NPs has less interaction with proteins (388). Surface charge of the NPs affects the secondary structure of proteins. Huhn et al. reported that gold NPs with different surface charge (positive [+9.7 ± 8.9 mV] or negative [-39.8 ± 10.0 mV]), but similar sizes adsorbed comparable amounts of HSA. Whereas, positively charged NPs showed higher cellular uptake than negatively charged NPs. This change in the activity can be due to conformation changes in protein structure due to surface charge (389).

Fleischer and Payne (2014) observed that similar NPs with identical protein corona compositions bind to different cellular receptors, suggesting that a difference in the structure of the adsorbed protein may be responsible for the differences in cellular binding of the protein–NP complexes. These authors also found that cationic polystyrene NPs showed improved cellular binding to monkey kidney epithelial cells compared to negatively charged NPs in the presence of fetal bovine serum (FBS). It should be noted that in both cases, the NPs formed protein–NP complexes immediately following exposure to FBS (386).

Media composition affects the protein corona. Silica NPs in the presence of serum proteins showed less uptake compared to serum free media (390). Gold NPs incubated with Dulbecco's Modified Eagle's Medium (DMEM) media for 48 h showed higher protein adsorption than Roswell Park Memorial Institute media (RPMI), but same amount after 1 h incubation (391). Protein concentration in media affects the protein corona. Silica NPs incubated with 3%, 20% and 80 % plasma exhibited different protein patterns. Changes in primary protein band was observed with increasing plasma concentration. Lower amounts of proteins were measured on silica NPs compared to sulfonated polystyrene ($PSOSO_3$) NPs with increased plasma concentrations (392). Exposure time affects the protein corona. Protein corona forms immediately as soon as the NPs come into contact with human plasma. Tenzer et al. reported complex protein corona (formed of 300 proteins) just after 30 s (393). In addition, temperature plays an important role in protein corona formation. Cu-NPs showed higher protein adsorption when incubated by increasing temperature from 15°C, 27°C, and 37°C to 42°C (394).

A decline (from 76% to 26%) in the cellular uptake of cRGD decorated NPs was reported by Su et al. in protein bound NPs compared to non-protein bound NPs. They found that even the targeting ability was not affected but cellular uptake was compromised (395). Tf decorated NPs were reported to lose their targeting ability in the

biological medium. Proteins in the medium are reported to shield the NPs from binding to targeted receptors on the cells and transferrin receptor and hence results in disappearance of targeting ability. However NPs can enter the cells but the targeting capacity is lost (396). Aptamer functionalized AuNPs lost the targeting ability due to protein corona blocking after serum exposure. Immune related proteins were found on the surface of aptamer that can induce immune reaction and clearance eventually (397).

1.7.7.4. Stability of NPs

The stability of NPs can be categorised into two, shelf stability, plasma and serum stability. NPs should be stable enough to retain their therapeutic effects for a specific time when stored or administered to the body. Oller-Salvia et al. tested the serum stability of peptide NPs in human serum. They found that switching from linear to monocyclic analogue didn't affect the permeability but showed 30-fold enhanced stability than linear peptide analogue (171). In addition, upon switching disulfide to a lactam bridge in Miniap-4 shuttle peptide, they found 50% higher permeability with better resistance to proteases (171). El-Marakby et al. assessed the serum stability of chitosan NPs in rat serum. They reported a sharp reduction in particle size (up to 62% of original size) prepared from the native chitosan, whereas modified chitosan showed slight increase in the size from 87.39 ± 1.56 nm to 122.33 ± 1.95 nm after 2 h incubation with the serum. After 24 h incubation no significant changes were noticed (398). Oliveira et al. tested uncoated and poly allylamine hydrochloride (PAH)-coated PLGA-NPs in biological environments: BSA solution, mouse and human plasma. Both formulations were reported to be stable in BSA and mouse plasma on incubation, but surprisingly not stable in human plasma (formed aggregates greater than 1 μm). They also studied the protein corona in all solutions. In mouse plasma uncoated NPs showed protein concentration of 4.1 ± 2.6 μg/mL, which was much greater than incubating these NPs in BSA solution. Surprisingly, in human plasma it was 2.5-fold higher (10.4 ± 3.0 μg/mL) than mouse plasma. Similarly

PAH-coated PLGA-NPs showed higher protein adsorption after incubation with human plasma than BSA solution and mouse plasma (399).

Uncoated chitosan NPs were to increase in size by storage at 25°C for 3 months in 10% glucose solution (400). This alteration in size results in modified physicochemical, pharmacodynamic and pharmacokinetic properties of the PMNPs. Lyophilisation with cryoprotectants is reported to enhance the stability and to stop contents leaking from the NPs (401-403). Cryoprotectants such as glucose, sucrose, mannitol and trehalose are most commonly used because of their low toxicity (401, 404).

Despite numerous advancements and technologies, there is always a need for delivery system with optimum characteristics. Enzyme-responsive or biodegradable delivery systems may offer less toxicity and immunogenicity. Drug delivery systems should be able to deliver/encapsulate suitable amounts of drug and should be able to protect the drug from enzymes in the blood. The scalability should be considered while designing the delivery system. As AAVs have been evaluated for gene delivery in clinical trials for AD and PD, perhaps this would indicate the future formulations of NPs for gene delivery to the brain. Since the administration of AAVs has been invasive (injection into the brain), and the outcomes were not desirable, then non-viral NPs would be preferred that can be administered i.v. and therapy can be repeated after a while, when the effects of the delivered genes wear off in the brain.

In this project we developed Novel enzyme-responsive self-assembled NPs with aim to deliver the model drug (FSS) across the BBB. In the first phase, peptide sequences which are substrates for the MMP-9 enzyme were identified by using state of the art statistical and molecular modelling techniques. Those sequences were synthesised, tested and experimentally validated using a novel 19F-labelling technique to assess their specificity towards MMP-9. In the second phase, highly sensitive peptides to MMP-9

were synthesized with a little modification (attachment of BBB targeting ligand peptides). In addition, lipophilic moieties were conjugated to maintain the hydrophilic/lipophilic balance to facilitate the self-assembly and finally NPs formation. Enzyme-responsive self-assembled NPs were characterized for the for the particle size, zeta potential, encapsulation efficiency, release profiles under different external stimuli. Critical micelle concentration was calculated for the NPs using pyrene as a probe. Morphology of the NPs was assessed by transmission electron microscopy (TEM), scanning electron microscopy (SEM). Agarose gel retardation assay was used to assess the stability of NPs against serum and ability to form complex with siRNA (MISSION® siRNA Fluorescent Universal Negative Control 1, 6-FAM) at different ratios.

NPs were further subjected to toxicity studies using two different cell lines HeLa and SH-SY5Y cells. Lactate Dehydrogenase (LDH), MTT and Alamar blue assay kits were used to assess the toxicity. *In vitro* cellular uptake was assessed by using flow cytometry and confocal microscopy. *In vitro* BBB permeability model was used to assess the ability of NPs, to cross the BBB. A monolayer of hCMEC/D3 cell line was used and TEER values were measured. *In vivo* experiments were conducted using BALB/c to visualize the targeting ability of the NPs. IVIS was used to scan the mouse for the assessment of targeting. Novel enzyme-responsive self-assembled NPs were subjected to test their transfection efficiency by using β-secretase-1 (BACE-1) siRNA and knock down of BACE-1 gene was assessed by real time PCR. BACE-1 has been associated with neurodegeneration and accumulation of amyloid precursor protein (APP) products (405, 406). The inhibition of BACE-1 reduces the levels of Aβ and is a possible therapeutic strategy for AD treatment (407).

CHAPTER – 2 STATISTICAL AND MOLECULAR MODELING

2.1. Introduction

Enzymes are biocatalysts that enhance the rate and range of chemical/biological reactions under physiological conditions, often with great specificity. They are a crucial part of life, as biosynthesis and metabolism would be impossible without them (408). Understanding and exploring enzymes and their catalytic activities can help: the discovery of new drug molecules, understanding substrates, designing enzyme inhibitors and designing new catalysts e.g. engineered enzymes (409). Enzyme structures range from the simple to the highly complex. Despite advances in experimental and theoretical studies of enzyme – substrate interactions, the exact mechanism of action at cellular level is often only poorly understood (410).

Molecular modelling and simulation have proven useful tools to provide distinctive, detailed understandings and insights for enzymatic reactions at the molecular level (409). A detailed enzyme reaction was simulated by Warshel and Levitt, who used the combination of quantum mechanics for describing the active site/region with molecular mechanics for the protein and solvent (411). This was a significant contributor to their receipt of the Nobel Prize for Chemistry in 2013.

The matrix metalloproteinases (MMPs) are the family of structurally related endopeptidases, either secreted or membrane linked, that facilitate the metabolism of the extracellular matrix, and collectively they can metabolize all different extracellular proteins. All MMPs share a common catalytic Zinc (Zn), responsible, in part, for their enzymatic action (412-415). MMPs discovered so far are categorized as collagenases, gelatinases, stromelysins and membrane type MMPs. Most MMPs are produced in zymogen form (latent, non-active) and only exhibit their catalytic activity, once the pro-domain is cleaved off, with the exception of MMP-11, 14, and 23. A known mechanism

for the activation of MMPs is through the ‘cysteine switch’ (416). The cysteine switch lies in a unique preserved sequence PR**C**G(V/N)PD that maintains the latency of MMPs (417). MMP-23 lacks this unique sequence (418). MMP-11, 14 and 23 have a RX(K/R)R sequence at the C-terminal of the pro-peptide and are activated by intracellular furin (419, 420). The domain composition of each MMP is listed in Figure 2.1.

MMP-9, also known as gelatinase B, is a 92 kDa type IV collagenase able to degrade extracellular matrix. The MMP-9 gene is encoded with a signal peptide, a pro-peptide, and a catalytic domain with three fibronectin type II domains followed by a hemopexin-like domain at the C terminal (415, 421). MMP-9 differs from the other gelatinase MMP-2 structurally and functionally: MMP-9 has a heavily O-glycosylated, elongated linker between the catalytic and hemopexin domains (422). It has been reported that MMP-9 with fewer O-glycan moieties has lower affinity towards Galectin-3 contributing to metastasis (423).

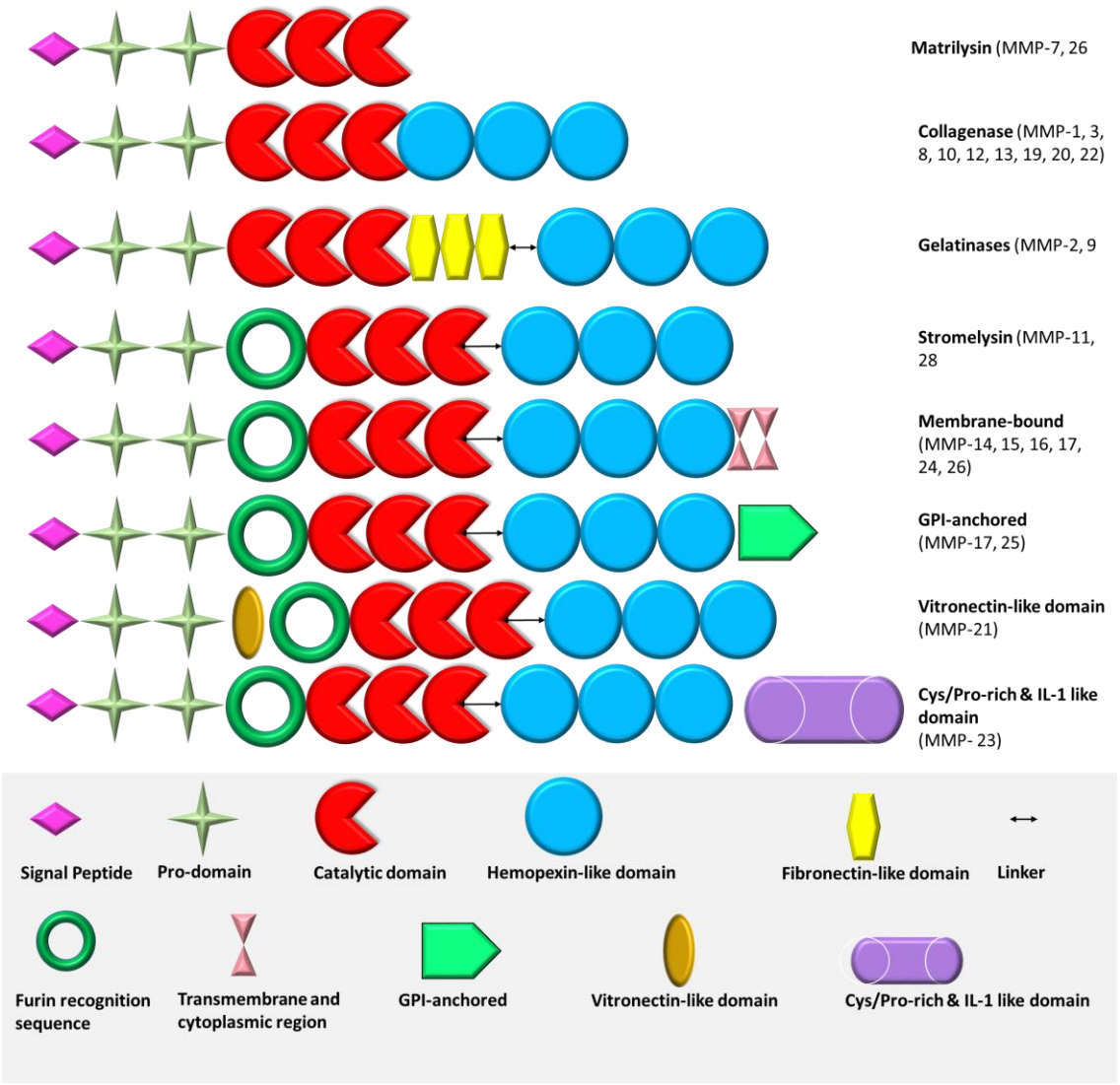

Figure 2. 1. Vertebrate members of the matrix metalloproteinase family

MMP-9 acts as a double-edged sword, providing benefits along with some pathological effects on cells and the body. It was observed that MMP-9-deficient mice exhibited resistance to endotoxin shock, such that inhibition of MMP-9 by a suitable mechanism might avoid septic shock (424). MMP-9 is believed to be influential in angiogenesis (formation of new blood vessels) (425) and it was shown that growth plate lacking gelatinase B, resulted in slow or delayed expression of angiogenic growth factor. MMP-9 is reported to have a healing effect on the respiratory epithelial lining (426). In another study (427), MMP-9 was found to activate TGF-β resulting in collagen contraction and wound closure. It has been reported, in diabetic patients, that elevated

levels of MMP-9 cause increased apoptosis of retinal capillary cells leading to diabetic retinopathy (428). MMP-9 is thought to be responsible for tumour cell invasion and metastasis as it is involved in angiogenesis by switching on the angiogenic switch by releasing vascular epithelial growth factor (429-431). It has been reported that different MMPs are found in high levels in atherosclerotic lesions, where MMP-9 is persistently in an overexpressed state, secreted by macrophages (432). MMP-9 is also involved in the pathology of tumour metastasis (433), Alzheimer diseases (434, 435), Multiple Sclerosis (436-438) and Parkinson's Disease (439), and levels are found to be elevated in patients with neurodegenerative diseases (440, 441).

Like most of the MMPs, MMP-9 is also secreted in a latent form known as pro-MMP-9 that undergoes an activation process to reveal its catalytic activity (442, 443). Pro-MMP-9 is also reported to have surface proteolytic activity that influences biological processes, such as skin carcinogenesis (444, 445). Several mechanisms have been reported to activate the pro-MMP-9 *in vitro* and *in vivo*. MMP-9 is activated in solution by MMP-2 but in cells it remains in latent from.

The catalytic domain of MMP-9, like other MMPs, is an ellipsoid-spherical shape having two hump-like projections (Figure 2.2, surface view), in between these are the catalytic zinc atoms with the catalytic domain to both sides. The first hump is due to the imidazole ring of His 411 and the second to the oxygen from the α-carboxylic acid in Pro 421. The catalytic zinc is surrounded by His 401, His 405, His 411 and Gln 402. In standard view, the cavity to the right of Zn is named the S1′ pocket and the cavity to the left is referred to as the S1 pocket. The catalytic zinc separates the larger upper domain from a smaller lower domain. The upper domain consists of five strands of highly twisted β-sheets and two α-helices; linked with each other by three surface loops. The lower domain consists of C-terminal α-helix; along with two loops, one arising from Ala 417, Leu 418, Met 419 and Tyr 420. Met 419 is responsible for a Met-turn giving support or

providing a base for the lower domain. This loop extends from the Pro 421, Met 422, Tyr 423 and Arg 424; giving a definite shape to the S1′ cavity and lower domain. The second loop, (called the specificity loop); extends from residues Arg 424 to Leu 431, overarching the S1′ pocket. A truncated [1GKC_chain A from protein data bank (PDB)] MMP-9 is shown in *Figure 2.2 (ribbon view) and (surface view)* [1GKC_chain A from protein data bank (PDB)].

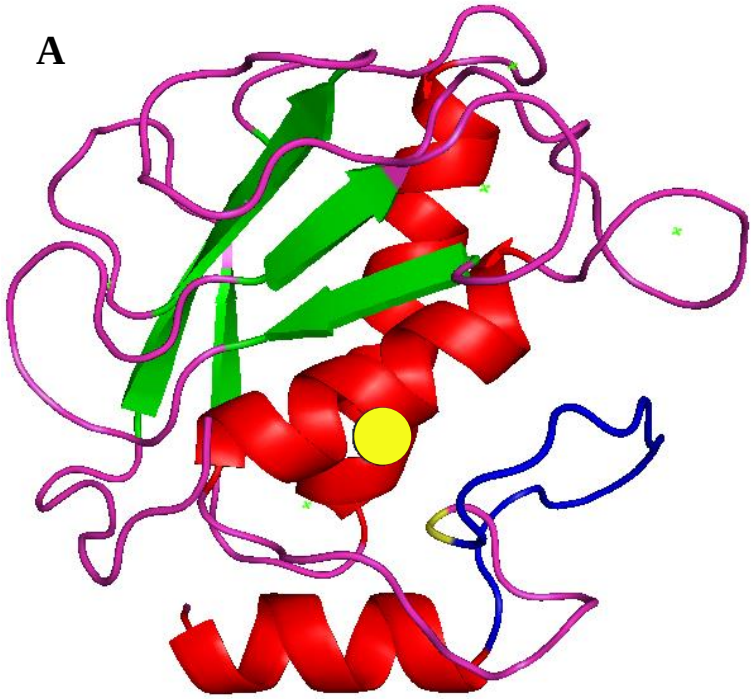

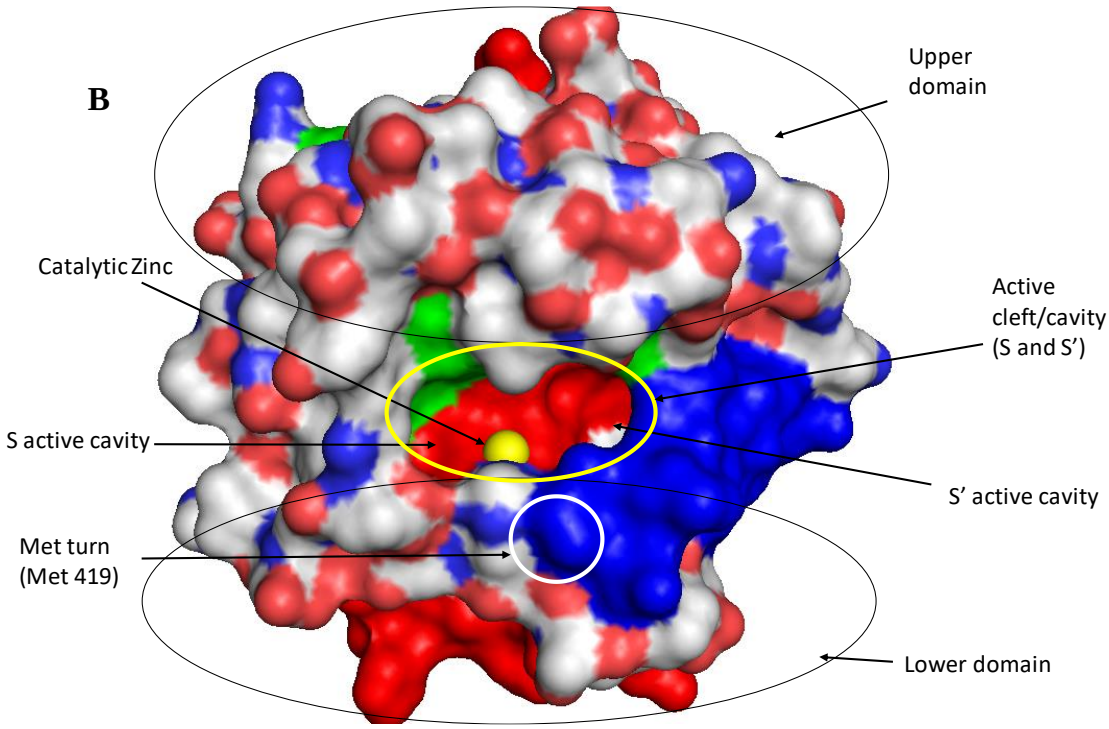

Figure 2. 2. A truncated MMP-9 A) ribbon view; zinc is shown as a yellow ball, α-helices are spiral shape coloured red, β-sheets are flat arrows in green colour. Upper and lower loop domains are coloured in purple and separated by zinc. B) surface view; zinc is shown as a yellow ball, the active cleft is encircled whereas catalytic cavities are annotated as S and S' active cavity, upper and lower domains are separated and encircled and Met turn is encircled white.

The protein structures with codes 1GKC and 1GKD from the PDB are complexes of reverse hydroxamate inhibitors with human MMP-9 and were explored previously, as shown in Figure 2.3 (446). Roswell et al. determined the crystal structure of MMP-9 at 2.3 Å resolution in order to help with designing and analysing potent inhibitors for MMP-9 to prevent cardiovascular diseases (415).

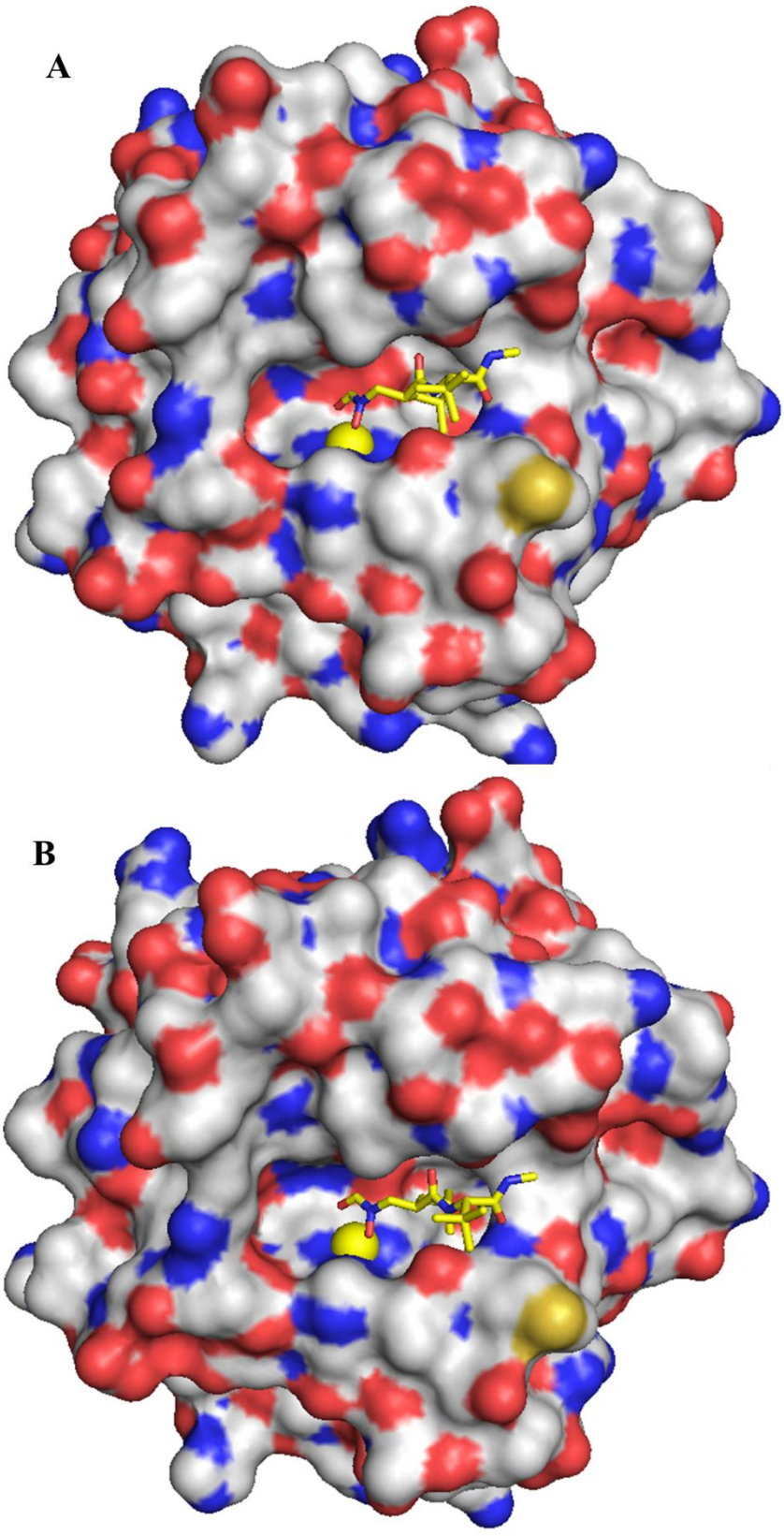

Figure 2. 3. A) Chain A of 1GKC and 1GKD showing "Zn" as a yellow ball and the inhibitor complexed with "Zn" is shown in yellow sticks. B) Chain B "Zn" as a yellow ball and inhibitor is shown in yellow sticks (valinamide).

Pro-MMP-9 is reported to be in the form of reduction sensitive dimers (447). The cysteine switch (Cys^{468}) is believed to control the dimerisation via a disulphide bond (448). In the protein structure with protein databank code 1ITV, the role of the hemopexin-(PEX)-like domain of MMP-9 was investigated. It was observed that PEX controls dimerisation of MMP-9 and it is dependent on reducing agents, a reversible dimer is formed independent of disulphide linkages.

Elkins et al. investigated the C-terminally truncated human Pro-MMP-9 in order to design inhibitors. Protein structure with code 1L6J was introduced in the PDB; it has a prodomain, and a fibronectin domain. When compared with MMP-2, a closely related MMP, the cysteine switch of MMP-9 was highly preserved (449) in prodomain. Arg 424 of MMP-9 in the S1′ pocket was reported to be in a slightly different conformation, angling it away from the pocket, suggesting that it might be useful for identifying specific inhibitors.

Protein structures 2OVX, 2OVZ, 2OW0, 2OW1 and 2OW2 were explored by Tochowicz et al. (421) to identify the flexibility of Arg 424 in MMP-9 with five different inhibitors. In the structure with code 2OVX, MMP-9 is complexed with a barbituric acid inhibitor. It was observed that the catalytic zinc is chelated with the N atom of the barbiturate ring. The lower part of the S1′ pocket is filled by the phenyl ring of the barbituric acid inhibitor.

In 2OVZ, a phosphinate inhibitor interaction with MMP-9 was described; these are thought to be the tightest binding inhibitors of many MMPs. MMP-9 inhibition by the phosphinate inhibitor is not obstructed by Arg 424 in the S1′ pocket. In protein structures 2OW0, 2OW1 and 2OW2, the interaction of MMP-9 with iodine labelled carboxylate, trifluoromethyl hydroxamate and difluoro butanoic acid inhibitors respectively is

revealed. Arg 424 is reported to be flexible, blocking partially the S1′ cavity making it difficult to accommodate long residues at P1′ of substrates (421).

Statistical modelling has been extensively used in all aspects of science and research. It ranges from designing experiments, collecting data, analysing and interpreting the data (450). Automatic linear modelling is an approach of data mining that employs a machine learning approach to find the best predictive model using the available data (451).

Numerous studies have reported the substrates for MMP-9. Peptide sequences (mostly octa-peptides) reported to be MMP-9 cleavable in different papers were obtained from the MEROPS web page https://www.ebi.ac.uk/merops/cgi-bin/substrates?id=M10.004. The MEROPS database is a one-click information source for peptidases, inhibitors and substrates. The information in MEROPS is curated manually and the database came into existence in 1996. The hierarchical classification of peptidases and their inhibitors sees them grouped by protein and species. Related sequences are clustered into families and clans. More than half a million peptidases and almost 75000 inhibitors and substrates are reported in MEROPS 9.13 (452). Each protein type is named as holotype. For each protein species, substrates and cleavage positions and their biological pathways are provided (a link to KEGG database). Multiple studies have used different techniques to predict the substrates for MMP-9. Phage display libraries (453, 454), positional-scanning peptide libraries (455) and mixture-based peptide libraries (456, 457) are the most popular (458).

Efforts were made to identify either inhibitors or substrates for MMP-9 as it plays a major role in many diseases. Turk et al. explored the cleavage site motifs for six members of the protease family using mixture-based oriented peptide libraries. They validated the results by comparing with previous literature and measuring the cleavage of individual peptides experimentally. Peptide cleavage by six different members of the MMPs was measured by treating with fluorescamine (reacts with primary amine to give fluorescence)

after incubating the peptide substrate with individual enzymes. The suitability of each peptide to be a substrate was described as k_{cat}/K_m derived from fitting the data to the Michaelis–Menten equation (459).

Kridel et al. used a phage display library of random hexamers to identify substrates for MMP-9. They reported the most common cleavage motif has the sequence of Pro-X-X-Hyd-(Ser/Thr) extending from P3 – P2′; Where X can be any amino acid and Hyd is a hydrophobic amino acid. They also used fluorescamine experimentally for measurement of kinetics of MMP-9 (453). Tauro et al. used hydrogel matrices for MMP-mediated selective peptide cleavage for chemotherapy. Experimentally, they used the same fluorescence technique (460). Ratnikov et al. also profiled substrates for MMP specificities and represented them as k_{obs} using phage display library (461). Lamort et al. explored the substrate specificity for MMPs especially MMP-12. They used the fluorescence technique for enzyme kinetics and Abz (ortho-aminobenzoic acid) was used as the fluorescent group (462).

2.2. Our Approach

The literature above suggests that there is still a need to explore and identify the most suitable and specific substrates for MMP-9. Most of them relied on the fluorescence produced from the fluorogenic material added in the experiment. This fluorescence could be from the Trp or Tyr as both are fluorescent (463, 464). We used state of the art statistical modelling and autodocking techniques to predict highly sensitive substrates for MMP-9. Our approach involved gathering data from literature and statistically applying the Natural and Non-natural Amino Acids Index to describe the amino acids (NNAAIndex) (465), assigning a novel score based on sequence, docking the interesting sequences predicted and experimental validation using a novel technique discussed in chapter 3.

NNAAIndex is based on 155 physiochemical properties of 22 natural including selenocysteine (U) (466), pyrolysine (O) (467), selenocysteine and many non-natural amino acids. NNAAIndex model can be applied to in silico peptidomimetics in a high throughput manner with desirable bioactivities for a wide range of applications. These 155 physiochemical properties were grouped in to six factors. (465). Characterisation of any peptide (like structural features, designing and predicting desired activity) can be carried out using NNAAIndex factor values. Computational docking has been extensively used to explore protein-ligand interactions for drug discovery and development. It involves the use of known protein structures, such as those obtained from x-ray diffraction by protein crystals. It works by predicting the bound conformations and binding free energy of small molecules for the target protein (468, 469).

2.3. Material and Methods

2.3.1. Materials

SPSS 23® (IBM Corporation) was used for statistical modelling, Pymol® (Schrödinger, Inc. NY) was used to generate images. Python® was used for permutation and combination to generate peptide sequence. Autodock Vina® was used for docking studies (470). Accelrys Draw 4.0 was used to generate SMILES.

2.3.2. Methods

2.3.2.1. Frequency distribution of amino acids for MMP-9 substrates

To begin investigations of MMP-9 substrates, literature searches were carried out. MMP-9 enzyme and its substrates were extensively investigated in the last decade (471). To identify and rank order MMP-9 peptide substrates, sequences were searched from the literature. A total of 369 peptide sequences were located including some that feature non-natural amino acids. The SPSS frequency distribution function was employed to assess the frequency of amino acids at different positions.

2.3.2.2. *Statistical modelling and training of prediction tool*

In order to rank all MMP-9-cleavable peptides, the Index of Natural and Non-natural Amino Acids (NNAAIndex) was used (the frequency of occurrence of residues can only be used to understand the effect of precedented residues). Factor values were given to MMP-9-cleavable sequences reported in the literature (413, 454, 460, 462, 472-475). An automatic linear model was applied and analysed using SPSS 23. To enhance the likelihood of predictability and to make it more accurate, more sequences reported in literature were included in the study. Literature data was grouped into four different categories based on the representing unit (e.g. $M^{-1}s^{-1}$, k_{obs} etc.). An automatic linear model was applied on these data sets. Models providing the most accurate predictions for each dataset (Dataset 1, Dataset 2, Dataset 3 and Dataset 4) were selected. In these models, the identity of residues at each position as well as the factor values for each residue were included as descriptors.

The SPSS scoring wizard was used to give scores to MMP-9 cleavable sequences. As a first step to developing a consensus from these four scores, a Z-score was calculated for each data set. A Z-score is computed by first finding the average score for all compounds in the set and the corresponding standard deviation. The Z-score corresponds to the number of standard deviations away from the mean each individual value is and therefore the scores are independent of the absolute score values or of the distribution of scores can be obtained. These Z-scores (unlike the original scoring by the model) can be compared between models and so an average of the Z-score predictions using the four models was then taken to give what we styled as a Y-score to each sequence. This was to train our prediction tool. These Y-scores are a general view based on all the datasets (which can provide conflicting perspectives on certain features, as might be expected for biological data). This prediction (Y-score) was plotted against the measured values of log of k_{cat}/K_m. After training our prediction tool, a new dataset (merged dataset) was developed by

combining dataset 1, 3 and another dataset 5 (476) from the literature. Automatic linear modelling was run again on the merged dataset, this time using only the factor values (in order to maintain generality). The model was analysed in detail to identify the residues that are most likely to strongly influence (in a positive or negative direction) how quickly a substrate is processed.

2.3.2.3. *Combinations and permutations*

After identifying residues at each of the positions from P5-P5′ that are likely to maximise the scores (based on the factor values for each amino acid), 100800 sequences were generated by combination and permutation. Factor values were allocated to new sequences and automatic linear modelling was run using SPSS. The scoring wizard from SPSS was used to give a score to these sequences which was normalised to give a Z-score. The predicted Z-scores from each of the models were then averaged to generate a Y-score. These Y-scores correspond to a consensus based on models that use all of the available data but without making inappropriate comparisons between data gathered in different laboratories and in different conditions.

2.3.2.4. *Molecular Docking to Understand Substrate Recognition by MMP-9*

For further understanding and prediction assessment, results from the frequency distribution of amino acids were used to identify suitable substrates with higher k_{cat}/K_m values. From the frequency analysis, the most frequently occurring amino acids at each position were identified and docked in different protein structures reported in PDB.

2.3.2.5. *Protein Structure Preparation*

There are 25 structures of MMP-9 reported in the PDB. In many of the MMP-9 structures, the protein is present more than once in the asymmetric unit. Autodocking needs special information about the receptor such as atoms, atomic charges, coordinates and the region of interest (centred around the catalytic moieties). The first occurrence of the protein, chain A, was arbitrarily selected for the docking studies. Calcium (Ca),

inhibitors and all water molecules were deleted from the structures but both active site Zinc atoms (Zn) were retained and were assigned +2 charge (Zn^{2+}). These files were then processed in the Autodock tools from MGL to create a version (PDBQT) of the structure that is ready for docking using Autodock Vina. This tool adds atomic charges to the atomic coordinates.

2.3.2.6. *Ligand Preparation*

Ligands were sketched in Accelrys Draw 4.0, which was then used to generate SMILES strings that describe the structure of each molecule. These were converted into three-dimensional structures using the open babel program. The program was also used to set a protonation state appropriate to pH 7.4. An example of the commands used is summarised in Figure 2.4.

```
GL a di-peptide
CC(C)C[C@@H](C(=O)O)NC(=O)CN
vi GL.smi
babel -p 7 GL.smi GL_PROT.smi
babel --gen3d GL_PROT.smi GL.pdbqt
```

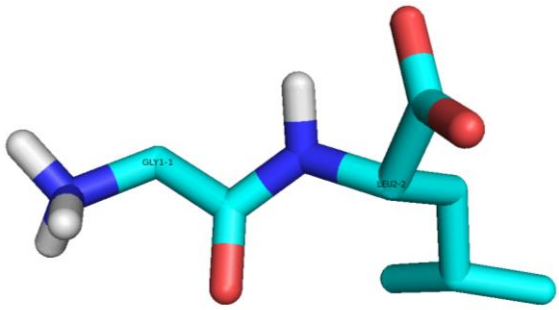

Figure 2. 4. Simple representation of ligand preparation for docking.

2.3.2.7. *Docking Setup*

Autodock Vina requires the user to specify a "box" into which the ligand will be placed. This box was centred on the catalytic zinc in these studies. In initial calculations, a box of size 5 x 5 x 5 Å was selected and docking of a series of inhibitors was carried out in order to optimise the box size. This approach was used for three protein structures. The most appropriate box size can be determined in two ways. Firstly, it can be identified directly by importing the protein structure along with inhibitor in Autodock Vina. The box should cover the inhibitor in all three dimensions. Secondly, after docking, the poses can be used to identify the optimum box size. The poses are imported into Pymol for

visualisation along with the inhibitor to serve as a reference. The box which yielded poses of inhibitor that most resemble the one in the protein-ligand crystal structure would be the best. Different box sizes were tried to get the appropriate one. For 1GKC (MMP-9 structure), a box size of 10 x 10 x 30 Å was found most appropriate.

Various dipeptides were designed based on the frequency distributions described previously. The same approach was used to generate tri, tetra, penta and hexa peptides. This array of peptides was then docked into the 1GKC structure using Autodock Vina with the box settings as obtained previously. We docked more than 600 different sequences to understand the nature and behaviour of the active site within MMP-9.

2.4. Results and Discussion

2.4.1. Statistical modelling and prediction

To identify and rank order MMP-9 peptide substrates, sequences were searched from the literature. A total of 369 peptide sequences were downloaded including some that feature non-natural amino acids from MEROPS. The frequency of each amino acid at each position is shown in Figure 2.5. Amino acid positions are labelled as P4 – P3 – P2 – P1 ↓ P1′ – P2′ – P3′ – P4′. P is used for amino acids starting in the N-terminus and P′ is used for the C-terminus (477). The cleavage site is indicated by a down arrow (↓) symbol. It was observed that in MMP-9 cleavable peptide substrates, Gly at P4 was most prominent comprising more than 32% of all the sequences followed by Ala and Leu with 8.45% for each. At P3, Pro was the most frequent, occupying about 41% followed by Ala for more than 14%. Interestingly, at P2 several amino acids were frequent: Ala, Gly, Pro, Arg, Ser; comprising 14.6%, 10.3%, 10%, 9.5% and 7.3 % respectively. Gly (almost 33%) and Ala predominantly occupy P1 (around 12.6%).

The P1′ position in octa-peptides is frequently Leu (slightly above 28%) trailed by Val (more than 10% of all sequences). Ala and Ile were also significant at P1′ (8.9 and 8.1% respectively). At P2′, a mixture of amino acids is frequent: Ala is the most frequent

with 11.1% of occurrences followed by Arg at around 9.4%. Glu, Gly, Thr were present at the same frequency of 8.4%. Gly and Ala were the most frequent at the P3′ position with 35% and 15.7% respectively. Ala and Pro were the most common residues at the P4′ position 13.3% and 13% respectively. Gly and Leu were around 10%. Gly and Ala are more prominent at the P1 position. Other residues like Val and Pro are also tolerated but probably entail lower rates of hydrolysis and this will be highlighted later in this chapter using molecular modelling. Leu and Val seem to be better residues at P1′ for cleavability.

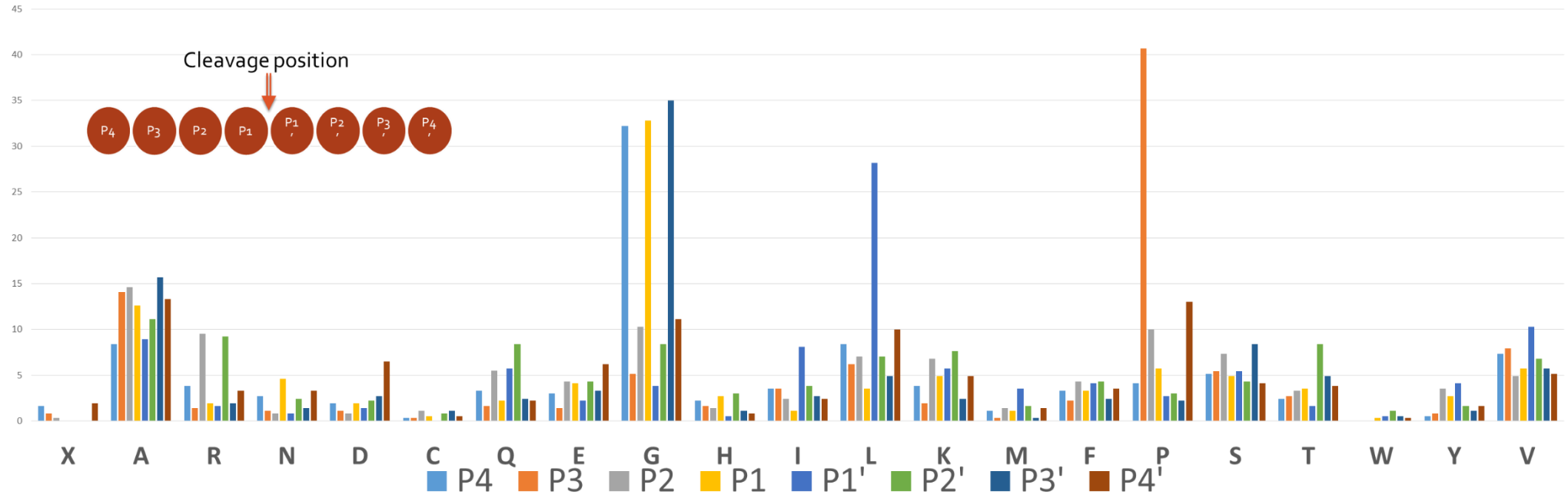

Figure 2. 5. Frequency distribution of amino acids at different positions. X is synthetic amino acid and the rest are natural amino acids.

The natural occurrence of amino acids in the human body reported in the human gene bank (NCBI Build Number 34 March, 2004) is shown in Table 2.1 (478). It is a representation of any amino acid in all human proteins encoded by the genome. In any given protein, this represents the probability of any position containing a specific amino acid if their ordering were random.

Table 2. 1. Natural occurrence (%) of each amino acid has been averaged over the total number of amino acids from complete human gene bank.

A	7.04	**G**	6.75	**M**	2.37	**S**	7.99
C	2.31	**H**	2.56	**N**	3.68	**T**	5.34
D	4.84	**I**	4.50	**P**	6.10	**V**	6.13
E	6.92	**K**	5.65	**Q**	4.65	**W**	1.21
F	3.78	**L**	9.84	**R**	5.52	**Y**	2.82

The occurrence of amino acids in MMP-9 cleavable peptide sequences (MEROPS) is shown in Table 2.2. It was observed that the percentage (rate of incidence of amino acid in any sequence) for all amino acids in any given peptide (MMP-9 cleavable reported in MEROPS) sequence at any position includes at least one amino acid that is much higher than the standard natural occurrence from the human gene bank. From this it can be deduced that MMP-9 responsive/cleavable peptides have some specific patterns/ frequency of amino acids which make them most suitable substrates for MMP-9. It can also be concluded from here; any natural peptide sequence (found in the body) is not likely to be a substrate for MMP-9.

Table 2. 2. Percentage of amino acids for reported MMP-9-responsive peptides at various positions in Merops.

Amino Acids	P4	P3	P2	P1	P1′	P2'	P3'	P4'
A	8.4	14.1	14.6	12.7	8.9	11.1	15.7	13.3
C	0.3	0.3	1.1	0.5	0.3	0. 8	1.1	0.5
D	1.9	1.1	0.8	1.9	0.8	2.2	2.7	6.5
E	3.0	1.4	4.3	4.1	2.2	4.3	3.3	6.2
F	3.3	2.2	4.3	3.3	4.1	4.3	2.4	3.5
G	32.2	5.1	10.3	32.8	3.8	8.4	35.0	11.1
H	2.2	1.6	1.4	2.7	.5	3.0	1.1	0.8
I	3.5	3.5	2.4	1.1	8.1	3.8	2.7	2.4
K	3.8	1.9	6.8	4.9	5.7	7.6	2.4	4.9
L	8.4	6.2	7.0	3.5	28.2	7.0	4.9	10.0
M	1.1	0.3	1.4	1.1	3.5	1.6	0.3	1.4
N	2.7	1.1	0.8	4.6	0.8	2.4	1.4	3.3
P	4.1	40.7	10.0	5.7	2.7	3.0	2.2	13.0
Q	3.3	1.6	5.4	2.2	5.7	8.4	2.4	2.2
R	3.8	1.4	9.5	1.9	1.6	9.2	1.9	3.3
S	5.1	5.4	7.3	4.9	5.4	4.3	8.4	4.1
T	2.4	2.7	3.3	3.5	1.6	8.4	4.9	3.8
V	7.3	7.9	4.9	5.7	10.3	6.8	5.7	5.1
W	0.0	0.0	0.0	0.3	0.5	1.1	0. 5	0.3
Y	0.5	0.3	3.5	2.7	4.1	1.6	1.1	1.6

It was observed that factor values of amino acids in MMP-9 substrate sequences is significantly different than the standard natural occurrence from human gene bank as shown in Figure 2.6. After calculating the factor values for any natural occurring given protein sequence and comparing with MMP-9 substrates. It can be deduced that MMP-9 responsive/cleavable peptides have some specific patterns of amino acids that make them suitable to be substrates for MMP-9.

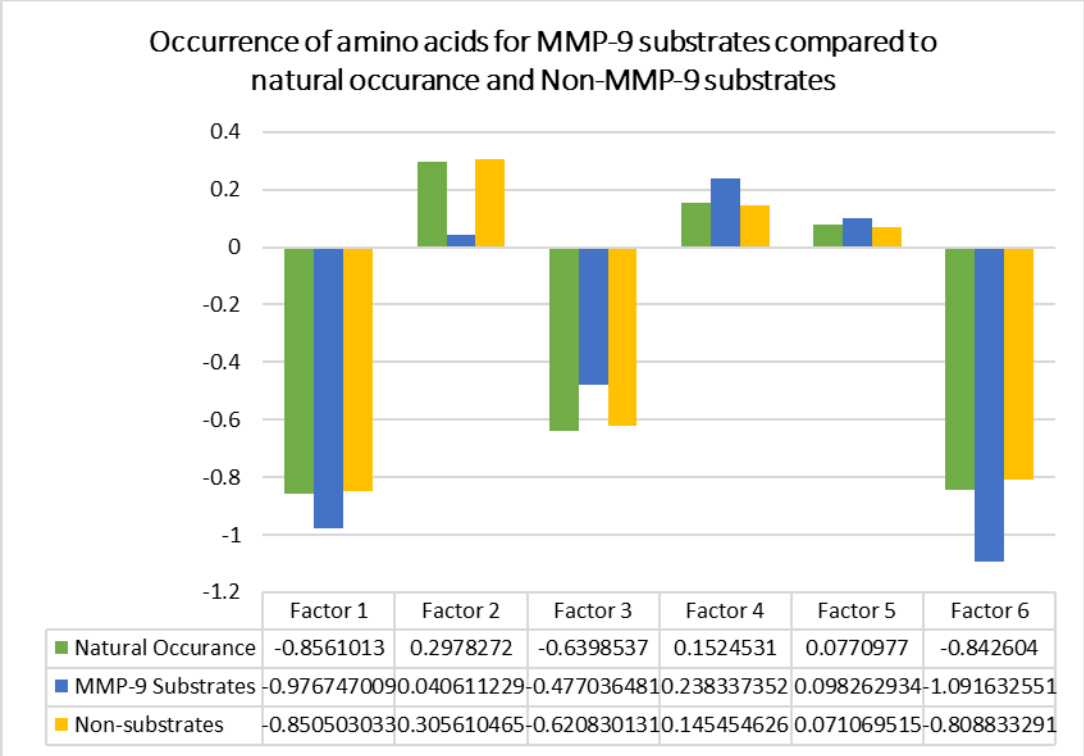

	Factor 1	Factor 2	Factor 3	Factor 4	Factor 5	Factor 6
Natural Occurance	-0.8561013	0.2978272	-0.6398537	0.1524531	0.0770977	-0.842604
MMP-9 Substrates	-0.976747009	0.040611229	-0.477036481	0.238337352	0.098262934	-1.091632551
Non-substrates	-0.850503033	0.305610465	-0.620830131	0.145454626	0.071069515	-0.808833291

Figure 2. 6. Comparison factor values of amino acids in MMP-9 substrates compared to natural occurrence and Non-MMP-9 substrates.

Factor values were computed for each amino acid in MMP-9-cleavable sequences. In dataset 1 (positions of amino acids, factor values for each position and *k*(obs) values were considered), amino acids at P3 and P2 were found to have influence on the selectivity of substrate for MMP-9. Amino acids at P1′ along with the factor 1 and P2′ positions were found to be critical for the cleavability. Factor 1 and 2, named as geometric index and H-bond index that consist of different parameters including log of aqueous solubility, spherosity, total structure connectivity index, folding degree index H-bond donor capacity, hydrophilic-lipophilic and hydrophilic volume were found to be influential for selectivity. Amino acids at P3′, P5′ and factor 5 of P5′ also have some importance towards the selectivity.

In dataset 2 (positions of amino acids, factor values for each position and k_{cat}/K_M values were considered), amino acids at P5 and P2 positions were the most important having an

importance of 0.824 and 0.091, respectively, for substrates. Factor 2 (H-bond index) at P1′, factor 1 (geometric index) at P3′ and factor 1, 4 (accessible surface area) at the P5′ position contribute towards the selectivity of substrate with an importance of 0.019, 0.026, 0.008 and 0.032 respectively.

In data set 3 (positions of amino acids, factor values for each position and cleavage efficiency values were considered), amino acids at P3 and P2 positions with an importance of 0.270 and 0.328 stood out for substrate selectivity. Factor 1, 4 and 5 for amino acids at P1′ positions with an importance of 0.090, 0.133 and 0.043 respectively and factor 6 at P4 and factor 5 at P4′ were found essential for selectivity.

In dataset 4 (positions of amino acids, factor values for each position and rate of hydrolysis values were considered), the amino acid at the P1 position and factor 4 are important with an importance of 0.104 and 0.132 respectively. Factor 1 and 2 at P5, factor 3 at P3, factor 2 at P2, factor 2 and 3 at P1′, factor 4 at P2′ and factor 6 at P4′ are important.

SPSS scoring wizard was used to give scores to MMP-9 cleavable sequences. To develop a consensus from these four scores, a Z-score was calculated for each data set. The average Z-score across the four data sets was then taken to assign a Y-score to each sequence. The individual models were investigated to identify whether they favoured high or low values of each factor at each position. These could then be used to identify the amino acid that has the highest or lowest value – even if it has never been reported at that position in an MMP-9 substrate. In this way, the sequences featuring the residues with most significant influence were identified from P5-P5'. A list of these residues from P5 - P5′ are given in Table 2.3 below.

Table 2. 3. List of all the amino acid residues having significant influence according to the prediction tool (model)

P5	P4	P3	P2	P1	P1′	P2'	P3'	P4'	P5'
W,G	G	P,W,G I,M,S, Y,A	A,W,G, Q,P,I	G,Q,P,Y,A	L,Q,P,G, W,Y,A	Y,A	W,G,Q,P,I	A,W,I	G

About 100800 sequences were generated from combinations and permutations of the residues indicated in Table 2.3. Factor values were allocated to new sequences and automatic linear regression was run using SPSS. The scoring wizard from SPSS was used to give four Z-scores to these sequences and then to generate a Y-score. A few examples are given in the Table 2.4.

Table 2. 4. List of highly sensitive novel peptides for MMP-9 suggested by prediction tool. Down arrow (↓) shows the cleavage point.

SEQUENCE	Y-Score	SEQUENCE	Y-Score
WGPIA↓LAGIG	2.20	WGPIG↓LAGAG	2.06
WGPIG↓LAGIG	2.15	WGPIA↓LAQIG	2.04
WGPIA↓WAGIG	2.12	WGPIA↓WAGAG	2.03
WGPIA↓LAGAG	2.11	WGPIP↓WAGIG	2.02
WGPIP↓LAGIG	2.10	WGPIA↓PAGIG	2.01
WGPIG↓WAGIG	2.07	WGPIP↓LAGAG	2.01

2.4.2. Docking substrates with MMP-9

A systematic approach was adopted to dock the substrates in MMP-9. From the frequency analysis, frequent amino acids at different position were identified; Gly was most common on P1 and Leu was more prominent at the P1′ position; furthermore, Pro at P3 was highest in frequency. It is reported that residues (amino acids) with long side chains are not suitable

for any sequence to be a good substrate for MMP-9 (421), whereas residues with longer side chain don't have significant effect for other MMPs like MMP-2, MMP-3 and MMP-8 (479, 480). Gly has no side chain and is the simplest amino acid having molecular mass around 57.02 g/mol, followed by Ala, with the smallest side chain and molecular mass 71.07 g/mol. Ser, Pro, Thr and Cys have molecular mass around 100 g/mol but these are not very common at P1′, whereas; Leu and Ile having molecular mass around 113 g/mol were among the highest.

2.4.3. Occupation of S1' cavity by Leucine is good for substrate binding

Docking of the substrates into the MMP-9 structure provides a means to understand how each residue in the peptide exerts it influence on the MMP-9 cleavability. Various parameters can be used to assess the poses that are obtained. The first is the docking score computed by Autodock Vina. These scores are more negative for better poses. The other parameter uses the knowledge that in order to undergo cleavage at a specific amide bond, the carbonyl of that amide must interact with the catalytic zinc atom. Therefore, poses were examined to identify those that satisfied this criterion.

The docking of di-peptide (GL) into the 1GKC protein structure results in the poses shown in Figure 2.7. In both pictures, the carbonyl interacts with the catalytic zinc atom and the di-peptide lies along the axis of the catalytic cleft. It can be clearly seen that that Leu's sidechain extends into the S1′ pocket of the catalytic cleft. The S1′ pocket consists of Val 398, Leu 397, His 401, Pro 421, Met 422 and Tyr 423, most of which are hydrophobic in nature (apart from His and Tyr which have polar groups but also are significantly hydrophobic). The Leu amino acid in the docked dipeptide is itself hydrophobic and prefers to extend into the hydrophobic zone made up of Val, Leu, Pro and Met. It suggests that this hydrophobic zone in the S1′ pocket provides a suitable environment to accommodate Leu.

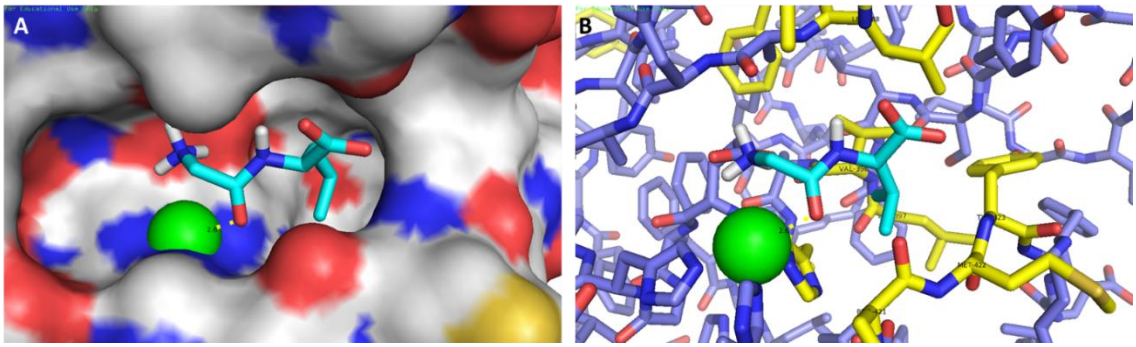

Figure 2. 7. The selected pose for "GL" a di-peptide obtained by Autodock Vina, ***A****) di-peptide (sticks) in 1GKC (surface),* ***B****) green ball is catalytic Zn, peptide in cyan.*

A tri-peptide AGL, was also docked into the 1GKC protein, as shown in Figure 2.8. The Leu (L) or Ala (A) can extend into the S1′ pocket. From nine poses obtained, six have Leu occupying the S1′ pocket, whereas some preferred Ala in this pocket. One of the possible explanations is that both amino acids are hydrophobic in nature, but Leu is slightly more hydrophobic than Ala (481, 482).

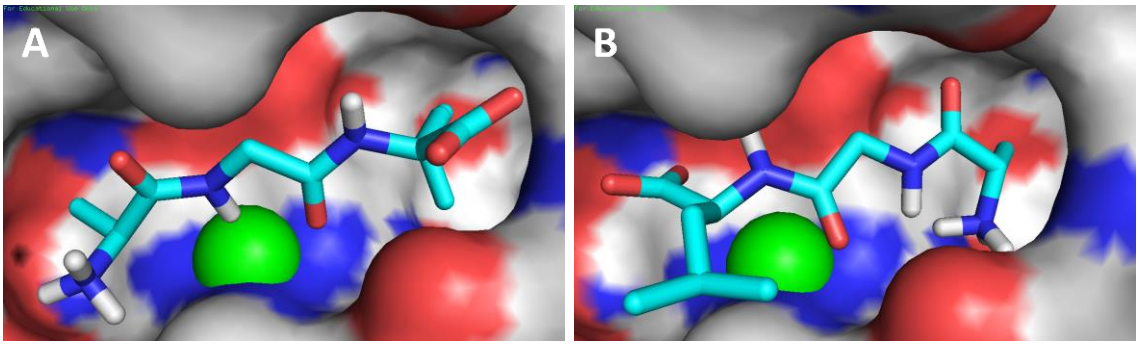

Figure 2. 8. AGL a tri-peptide docked into 1GKC (surface), the green ball is the catalytic Zn; the tri-peptide (sticks) is shown in cyan. ***A)*** *Leu can be observed extending into the S1' pocket* ***B)*** *Ala extends into the S1' pocket of the active cleft.*

To build on this, several penta-peptides were docked into 1GKC and 2OW2 using the same grid size. PLSLY a penta-peptide is shown docked in Figure 2.9. It can be noticed that Leu favoured the S1′ cavity in most of the poses after docking and the distance of the carbonyl oxygen (the site of the cleavage in these peptide sequences) from the catalytic Zn

ranges from 2.2 - 2.7 Å, which makes it a favourable cleavage position. It is believed that the carbonyl oxygen acts as a Lewis base activating the C=O bond for attack by water and subsequently amide bond cleavage (483).

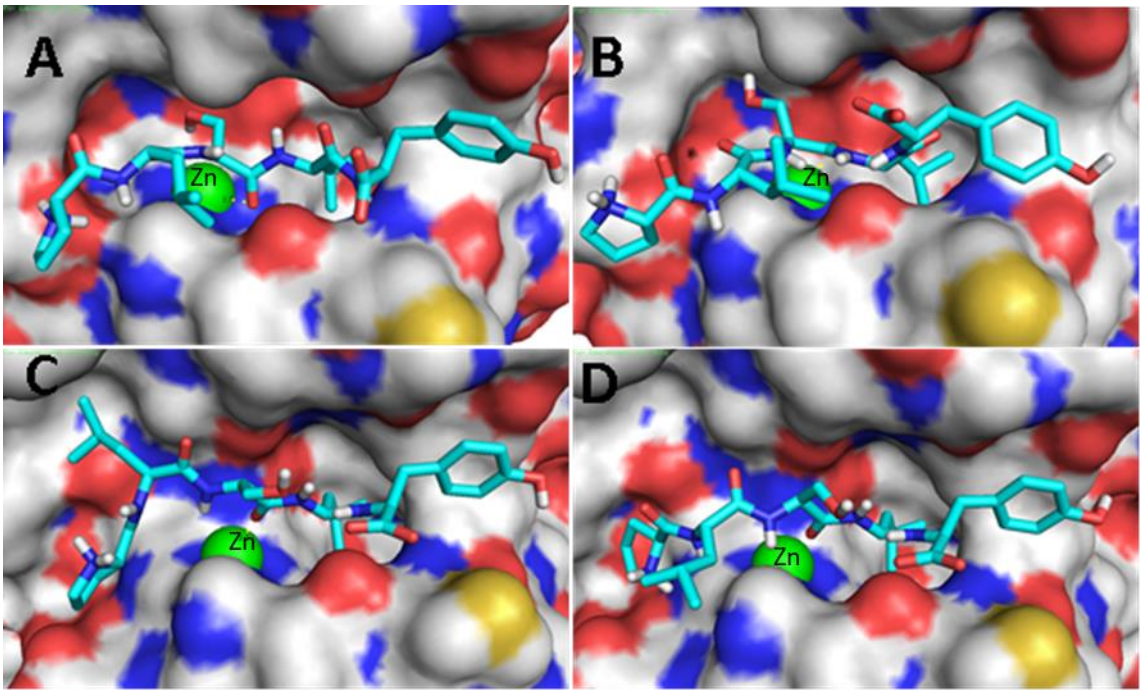

Figure 2. 9. "PLSLY" a penta-peptide after docking, 1GKC (A, B) and 2WO2 (C, D) shown in surface, green ball is catalytic Zn, peptide (sticks) in cyan. ***A)*** *Leu can be observed extending into the active cleft, Tyr twists outwards as does the other Leu ; the Pro protrudes out at the end of the trench-like shape of the active cavity* ***B)*** *Leu extends into the S1' pocket of active cleft, Tyr is folded outwards but drapes on the surface.* ***C, D)*** *Leu can be observed following the same trend (extending into the cavity), Tyr twists and wraps out of the trench but onto the surface of the protein and the second Leu prefers two different conformations in each pose. Pro sits in the cavity made up of side chain of His 405, Gly 408, Leu 409 and Asp 410.*

Several hexa-, hepta- and octa-peptides were also docked into 2OW2 with grid size of 10 x 10 x 25 Å. Some of the docked peptides are shown in Figure 2.10. GPRGLG and PRRLTA hexa-peptides docked in 2OW2 are labelled as A and B respectively. It can be clearly seen that Leu again prefers to occupy the active cleft in the S1′ cavity. The Gly on the C-terminus **(A)** twists and projects over the side of the S1′ cavity and wraps over the end of the trench-like active site. On the N-terminus, Arg twists and changes its conformation and occupies

the S1 pocket. Pro extends over the side and arranges itself in a way that covers the underlying Arg.

In PRRLTA **(B)**, from the C-terminus, the S1′ pocket is occupied by Leu, whereas Thr twists around and projects out of the pocket. Ala wraps around the end of the S1′ cavity. In the N-terminus the side chain of Arg at the P1 position projects out of the cavity in such a way that it partially obscures the catalytic Zn but presumably in this orientation the charged guanidine group is solvated by being surrounded by water. Pro sits in the cavity and Arg at P2 extends and wraps over the Pro. The carbonyl oxygen is 2.4 Å from the Zn.

In hepta- and octa-peptides (RPLGLWG and RPLGLWGA respectively), the same behaviour can be observed in most of the poses after docking. Leu at P1′ prefers to go in the S1′ cavity and the indole group of the Trp projects outside of the cavity and lies out and over the end of the S1′ pocket. Gly at P3′ and Arg at P4 twist to cover the active cleft completely.

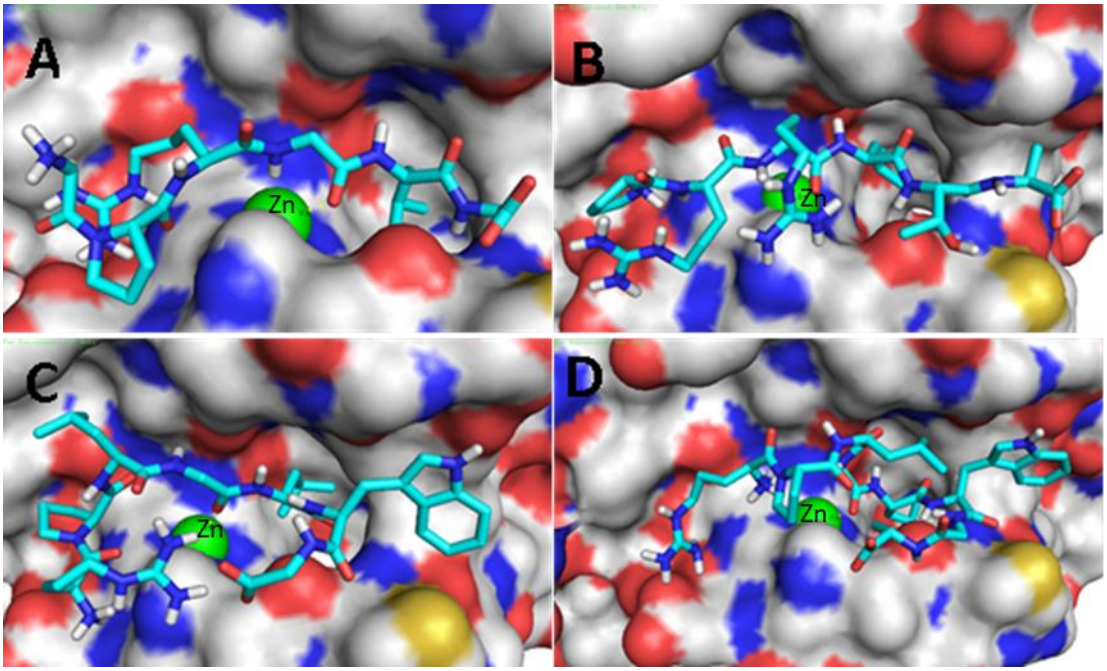

Figure 2. 10. Hexa-, hepta- and octa-peptides shown in sticks (cyan) docked into 2WO2 shown as a surface; the green ball is the catalytic Zn. ***A)*** *In* ***GPRGLG,*** *Leu can be observed extending into the S1′ pocket, Gly twists and comes out of the active cleft. The distance between O and Zn is 3.1 Å.* ***B)*** *In* ***PRRLTA,*** *Leu extends into the S1′ pocket of the active cleft, Thr twists and projects out of the*

cavity; Ala wraps over and back onto the protein surface. The side chain of Arg at P1 dangles out of the cleft. Pro at P3, sits in a part of the cavity made up of the side chains of His 405, Gly 408, Leu 409 and Asp 410. ***C)*** *In* ***RPLGLWG,*** *Leu can be observed following the same trend (extending into the S1' pocket), Trp twists and wraps over the right hand end of the trench and Gly rotates to cover the S1' active cleft. Pro sits in the cavity made up of the side chain of His 405, Gly 408, Leu 409 and Asp 410. The side chain of Arg at P4 coils in a way that it covers the S1 pocket and Pro. The distance between O and Zn is 2.6 Å.* ***D)*** *In* ***RPLGLWGA****, Leu is in the S1' pocket and Trp wraps around the end of the pocket and back onto the protein surface and the distance between O and Zn is 2.2 Å.*

Systematic substitution of different amino acids for Leu at the P1′ in the sequence PLGXW result in many interesting poses shown in Figure 2.11. Most of the poses docked nicely even in the absence of Leu. In PLGDW, Trp twisted in a way that the side chain of Trp extended out of the active cleft and the indole moiety wraps back onto the protein surface. Glu occupies the active cleft in PLGEW, in quite a different pose to that for the others. In PLGFW, the aromatic ring (phenyl) of the Phe sits in the active cleft in the space that the Leu sidechain binds. The same phenomenon was observed in PLGYW, where the aromatic ring (hydroxyphenyl) occupied the active cleft. It can be suggested the small aromatic sidechains can easily fit into the active cleft in the space occupied by Leu and could be a better substrate for MMP-9.

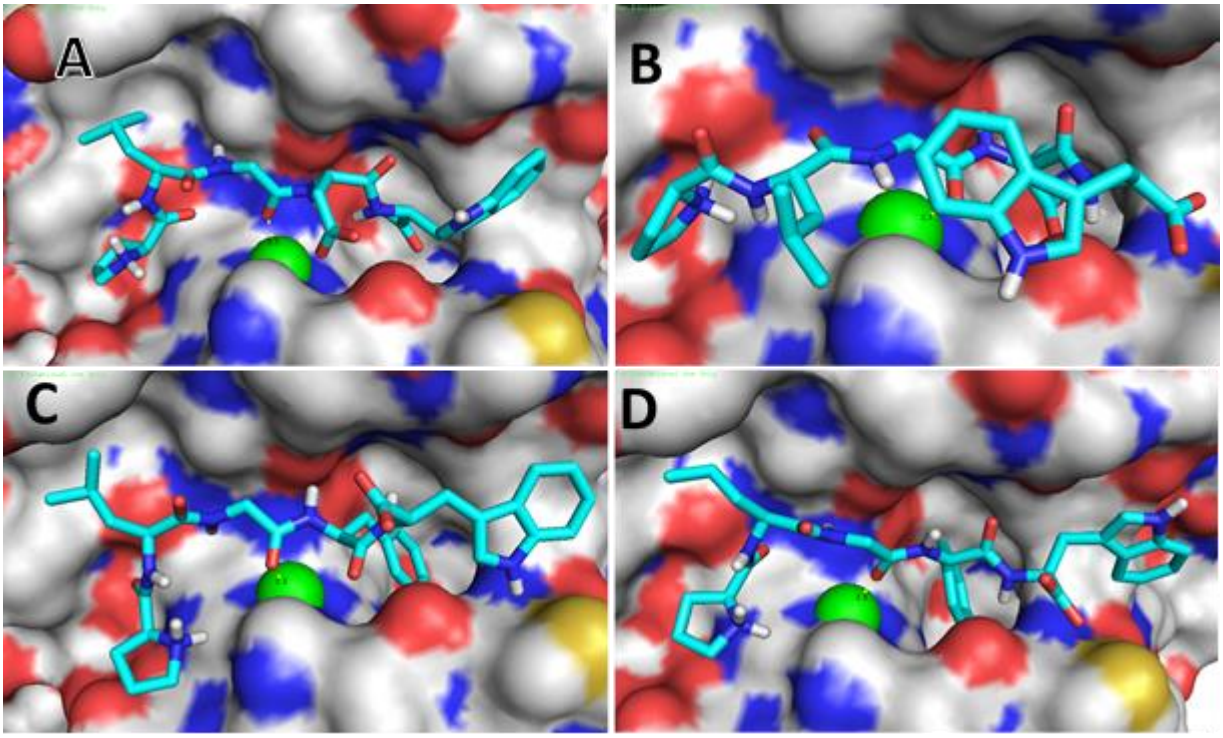

Figure 2. 11. Penta-peptides shown in sticks (cyan) docked in 2WO2 shown as a surface, green ball is catalytic Zn. ***A)*** *In* ***PLGDW,*** *the side chain of Trp can be observed extending into the active cleft, Asp twists and comes out of the active cleft. The distance between O and Zn is 2.5Å.* ***B)*** *In* ***PLGEW,*** *Glu extended into the S1' pocket of active cleft, Trp twisted and covered over the cavity, the distance between O and Zn is 2.7Å.****C)*** *In* ***PLGFW,*** *Phe (phenyl) can be observed following the same trend (extending in the cavity), Trp twists and wraps over the end of the trench-like active cavity. The distance between O and Zn is 2.6Å.* ***D)*** *In* ***PLGYW****, Tyr occupied the active cleft and Trp wraps out of the active site and the distance between O and Zn is 2.5Å. In the other two peptide sequences, replacement of amino acids at positions P3 - P2' did not affect the Leu's capability to occupy the active cleft. Even in the third peptide it was Ile instead of Leu, but it did not affect the Leu/Ile positioning. After docking these 300 peptides, it was noticed that for larger peptides, multiple docking of the same peptide did not produce consistent results due to the limited extent of sampling possible.*

2.5. Conclusion

State of the art statistical and molecular modelling tools were employed to identify the most suitable substrate for MMP-9. Y-score was calculated for more than 1 million sequences after combinations and permutations. NNAAIndex was used to assign factor values and to calculate Y-score subsequently. Novel MMP-9 substrates were identified with a range of Y-score. These predictions need to be validated experimentally.

CHAPTER – 3 EXPERIMENTAL VALIDATION OF MOLECULAR PREDICTIONS

3.1. Introduction

Several efforts have been made to identify the most suitable substrate for MMP-9. As mentioned in the previous chapter, MMP-9 regulates multiple physiological and pathological processes. Numerous studies have reported MMP-9 cleavable sequences. Chen et al. used modified ELISA to study and calculate the metabolism of phage display library peptides (454). In another study, Kridel et al. used MALDI-TOF mass spectrometry for the determination of the scissile bond for peptide sequences and fluorescamine was used to assess the peptide hydrolysis (484). Real-time monitoring of enzyme kinetic is not possible with the above-mentioned techniques.

Predictions were tested by a novel NMR technique that contrasts with previous studies that relied on the fluorescence produced from the fluorogenic material added in the experiment. This fluorescence could be from tryptophan (Trp) or tyrosine (Tyr) residues as both are fluorescent (463, 464). We designed peptide sequences that are more sensitive to MMP-9 than the sequences already reported in literature. So far, we are the first to use/introduce fluorine-19 (*F) NMR to investigate the enzyme kinetics of MMP-9 and to validate these findings. Nonetheless, NMR has previously been used for enzyme kinetics. Her et al. used NMR for real time study of the enzyme kinetics for sucrose hydrolysis to glucose (485). Papeo et al. used NMR for studying an enzymatic (trypsin) reaction on polyfluorinated peptides (486). We used the latter approach, in which peptides with fluorinated amino acids will be synthesized and the degradation profile monitored by *F NMR spectroscopy. NMR is relatively insensitive technique meaning higher concentration

of sample is required to get suitable results. Furthermore, proteins or bio-macromolecules need to be soluble. It also needs labelling with NMR active nuclei.

In this chapter, various predicted novel MMP-9 sensitive peptide sequences with a range of Y-scores have been synthesized; importantly, this includes a peptide predicted to be a poor substrate. Novel MMP-9 sensitive peptides were subjected to enzymatic degradation in the presence of active MMP-9 using *F NMR. NMR data obtained was processed using various state of art tools to calculate the k_{cat} and K_m values.

3.2. Materials and Methods

3.2.1. Materials

All L-Fmoc amino acids, Oxyma and ProTide® resin were bought from CEM. N,N′-diisopropylcarbodiimide (DIC), piperidine, cholesteryl chloroformate (CHF), trifluoroacetic acid (TFA), triisopropylsilane (TIPS), acetonitrile, formic acid and N,N-diisopropylethylamine (DIPEA) and N-(3- Aminopropyl) methacrylamide hydrochloride (APMA) were bought from Sigma-Aldrich®. Fmoc-L-4-fluorophenylalanine was purchased from Fluorochem®. Dimethylformamide (DMF), 1-(2-pyridylazo)-2-naphthol (PAN) and diethyl ether were purchased from Acros Organics®. MMP-9 recombinant human protein with a C-terminal polyhistidine tag (10327H08H5) was bought from ThermoFisher Scientific®.

3.2.2. Methods

3.2.2.1.Peptide synthesis

Peptides were synthesized using a CEM Liberty Blue® automated microwave-assisted peptide synthesizer. Briefly, Rink amide ProTide resin (147 mg; loading capacity 0.61 mmol/g) was transferred into a reaction vessel. A typical Fmoc-deprotection used 20% *v/v* piperidine in DMF for 90 s at 90^{o}C. DIC and Oxyma solutions (each 1 M) were used as

activator and coupling reagents, respectively. Solutions of amino acids in DMF (0.2 M) were singly coupled at 90ºC, except for Cys, which was coupled at 50ºC and Arg, which was double coupled at 75ºC. The peptide was cleaved from the resin by reacting with 1-2 mL of cleavage cocktail (trifluoroacetic acid: water: triisopropylsilane, 90%: 5%: 5%) for 4 h at room temperature. The solution was then filtered into cold diethyl ether, which precipitated the peptide. Precipitated peptide was washed with further diethyl ether four times to ensure the complete removal of impurities. Diethyl ether was evaporated by leaving it overnight in the fridge. Finally, the peptide was re-dissolved in water and freeze dried to afford a white solid.

3.2.2.2.Characterization of peptide by LC-MS

All of the peptides synthesized were characterised by using high-resolution (accurate) mass spectrometry. Samples were analysed using an Agilent 1260 Infinity II LC system with Agilent 6530 Accurate-Mass QToF spectrometer, using an Agilent ZORBAX Eclipse Plus C18 Rapid Resolution HD analytical column (1.8 µm particle size, 2.1 × 50 mm) with a binary eluent system comprising MeOH / H_2O (12 min gradient: 1-99% with 0.1% formic acid) as mobile phase. Operating pressures were in the range of 2000-3000 PSI. Electrospray ionisation mass spectrometry was conducted in positive ion mode (*m/z* range: 50 – 3200) using a fragmentor voltage of 150 V, gas temperature of 325 °C (flow 10 L/min) and sheath gas temperature of 400 °C (flow 11 L/min). Reference ions were purine (121.0509) and hexakis (1H, 1H, and 3H-tetrafluoropropoxy) phosphazine (922.0098) (API-TOF Reference Mass Solution Kit, Agilent). Exact mass measurements of the products were based on the protonated molecules $[M+H]^+$ and were detected as sodiated adducts $[M+Na]^+$.

3.2.2.3.MMP-9 activation protocol

MMP-9 was activated in TCNB buffer (50 mM Tris, 10 mM $CaCl_2$, 150 mM NaCl, 0.05% Brij35, pH 7.4 (TCNB)). Firstly, TCNB buffer was prepared and pH was adjusted to 7.4. 5 µg of MMP-9 was suspended in 50 µL of TCNB buffer (100 µg/mL) and incubated for 24 h with APMA to a final concentration of 1 mM at pH of 7.4. The mixture was diluted to a concentration of 2 nM and aliquoted.

3.2.2.4.NMR studies for enzyme kinetics

Enzymatic studies were conducted by using a Bruker® Ascend™ 600 MHz NMR spectrometer with broadband observe (BBO) probe. One-dimensional (1D) fluorine-19 (*F; 564.686 MHz). Preliminary NMR experiment was performed with proton decoupling at room temperature (298 K). For preliminary experiment, accurately weighed TY-6 peptide (5 mg) was dissolved in 2 mL of ultrapure distilled water. 350 µL of peptide sample and human serum were mixed in an Eppendorf tube and transferred into an NMR tube. Peptide products and metabolites containing 4-fluorophenylalanine were observed as singlets. Chemical shift values were calibrated to TFA (-76.55 ppm) as the internal standard. Data obtained was viewed and analysed by using TopSpin® and Dynamics centre 2.4.5 (Bruker®) was used for processing and calculating enzyme kinetics.

All peptides were dissolved separately in ultrapure distilled water at the concentration of 2.5 mg/mL. Peptide solutions (300 µL) were mixed with 2 nmol activated MMP-9 (450 µL) in Eppendorf tubes. The mixture was vortexed for 15 s to ensure complete mixing. These solutions were transferred into NMR tubes separately. *F NMR experiments were performed as above) with proton decoupling at room temperature (298 K) over a period of 15 h. Data was processed using Dynamics centre 2.4.5 (Bruker®) to calculate k_{cat}/K_m.

3.2.2.5.Peak shape analysis

Peak shape analysis was performed using MestReNova 6.0.2-5475. Automatic phase correction was applied. Global spectral deconvolution (GSD) was used to define all the peaks, their position, amplitude and shape in the spectrum. From GSD table, peaks were arranged in descending order based on their heights. Peaks higher than 1 cm were selected from each spectrum for analysis.

3.2.2.6.Curve fitting

Curve fitting was performed by using Dynafit (487, 488) (http://www.biokin.com/dynafit/). Dynafit was used with the task set to fit, the data to generic, code built in. The model that fit was Michaelis-Menten Progress K_m-K_s and initial guesses were provided for K_m, E_o, S_o, rP, F_o and kS. Data was provided as molar concentration against time (obtained by comparing integrals with those for TFA for which a concentration-peak area calibration curve was created). An example of the script is below.

[task]
task = fit ; simulate | design
data = generic ; progress | rates | equilibria | generic
code = built-in
[equation]
MichaelisMentenProgressKmKs
[parameters]
Km = 0.00000064
Eo = 0.000000001
So = 0.000022 ?
rP = 1
Fo = 0
kS = 29980 ?
[data]

variable t

directory M:\PhD\Results\NMR_Results\DynaFit4

sheet TY6_FOR_ANALYSIS.txt

column 7

[output]

directory M:\PhD\Results\NMR_Results\DynaFit4

[end]

In the above encoding, K_m represents the Michaelis constant. Eo represents the total or analytic enzyme concentration in appropriate units; S_o represents the substrate concentration in identical units; and rP represents the specific molar response coefficient of the reaction product. F_o denotes baseline offset and kS is the specificity number defined as k_{cat}/K_m.

3.3. Results and Discussion

To test our predictions experimentally, a range of peptide sequences with different Y-score was synthesized using a CEM Liberty Blue® automated microwave-assisted peptide synthesizer shown in Table 3.1. After cleaving the peptides from the resin, LCMS was conducted to assess the purity of peptides and results are shown in Figure 3.1 – 3.11.

Table 3. 1. Predicted peptide sequences synthesized for experimental validation with *F. Note: these Y-scores are calculated with modified sequences as *F was included for analytical purposes only.

Peptide	Sequence	Y-score
TY-6	PLG-L*FGAQ	2.393
TY-9	PLG-LWG*FQ	2.07
TY-10	WGPIA-LAG*FG	2.20
TY-19	GGPIG-LAG*FG	1.93
TY-21	*FPIAQAQI	1.50
TY-22	GGPIA-LAG*FG	1.98

TY-23	GGPIA-WAG*FG	1.89
TY-24	GGPWA-LAG*FG	1.76
TY-25	GGPIA-AAG*FG	1.63
TY-26	GGPIP-LAI*FG	2.57
TY-27	GGYGQ-GYW*FG	-2.18
TY-43	RPLA-LR*FSQ	2.04

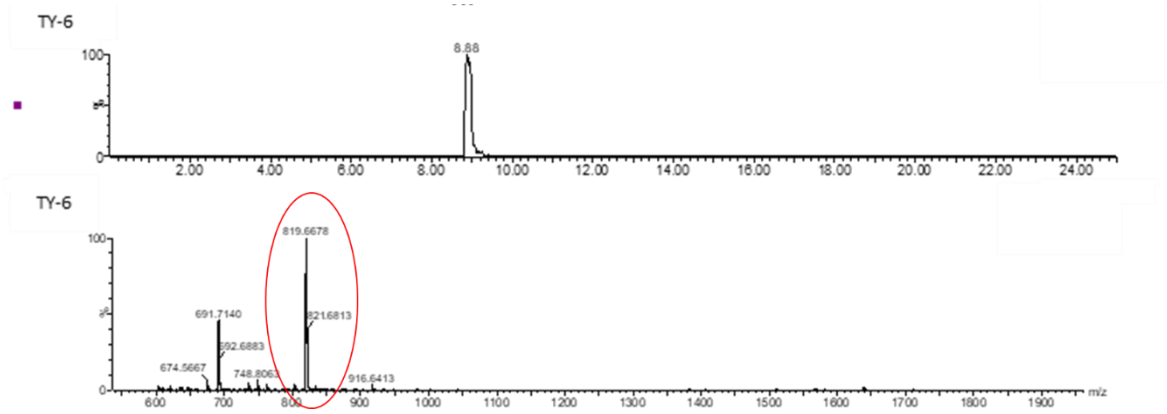

*Figure 3. 1. LCMS spectrum of TY-6 (PLGL*FGAQ), a modified version of a literature reported standard peptide. The spectrum shows the theoretical mass of 819 Da (encircled red), indicating the successful synthesis of the peptide. *F represents L-Fmoc-4-fluorophenylalanine serving as a probe for NMR.*

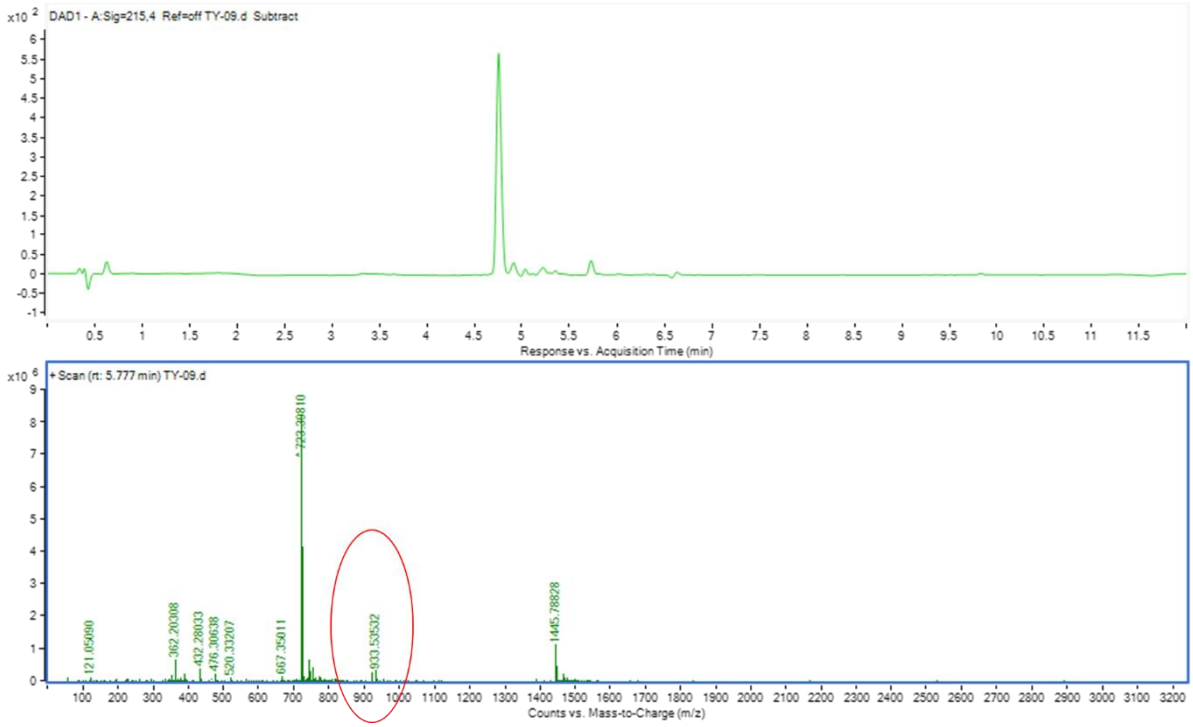

*Figure 3. 2. LCMS spectrum of TY-9 (PLGLWG*FQ), a modified version of a literature reported standard peptide. The spectrum shows the theoretical mass of 933 Da (encircled red), indicating the successful synthesis of the peptide. *F represents 4-fluorophenylalanine serving as a probe for NMR.*

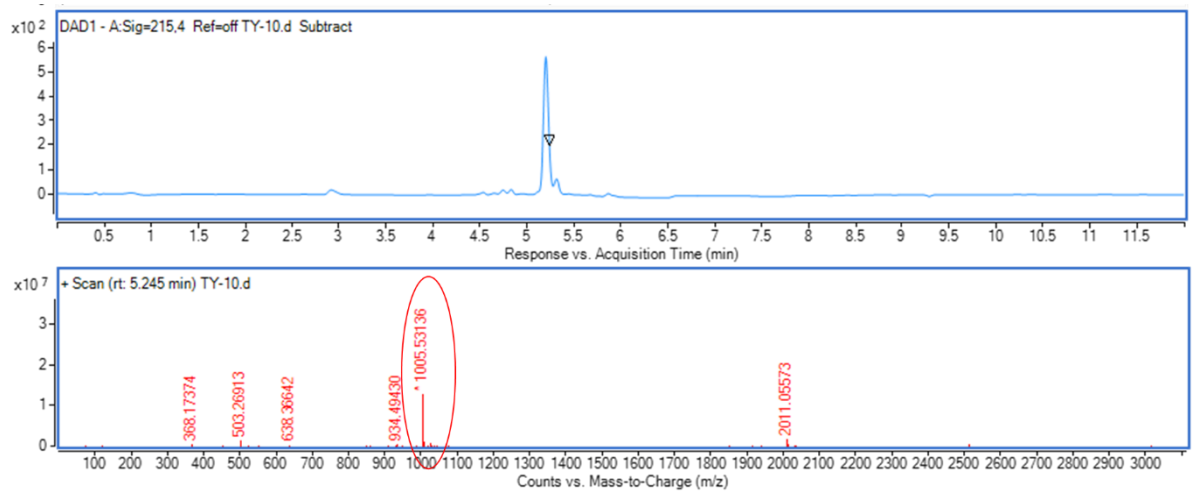

*Figure 3. 3. LCMS spectrum of TY-10 (WGPIALAG*FG), a modified version of a novel predicted peptide. The spectrum shows the theoretical mass of 1005 Da (encircled red), indicating the successful synthesis of the peptide. *F represents 4-fluorophenylalanine serving as a probe for NMR.*

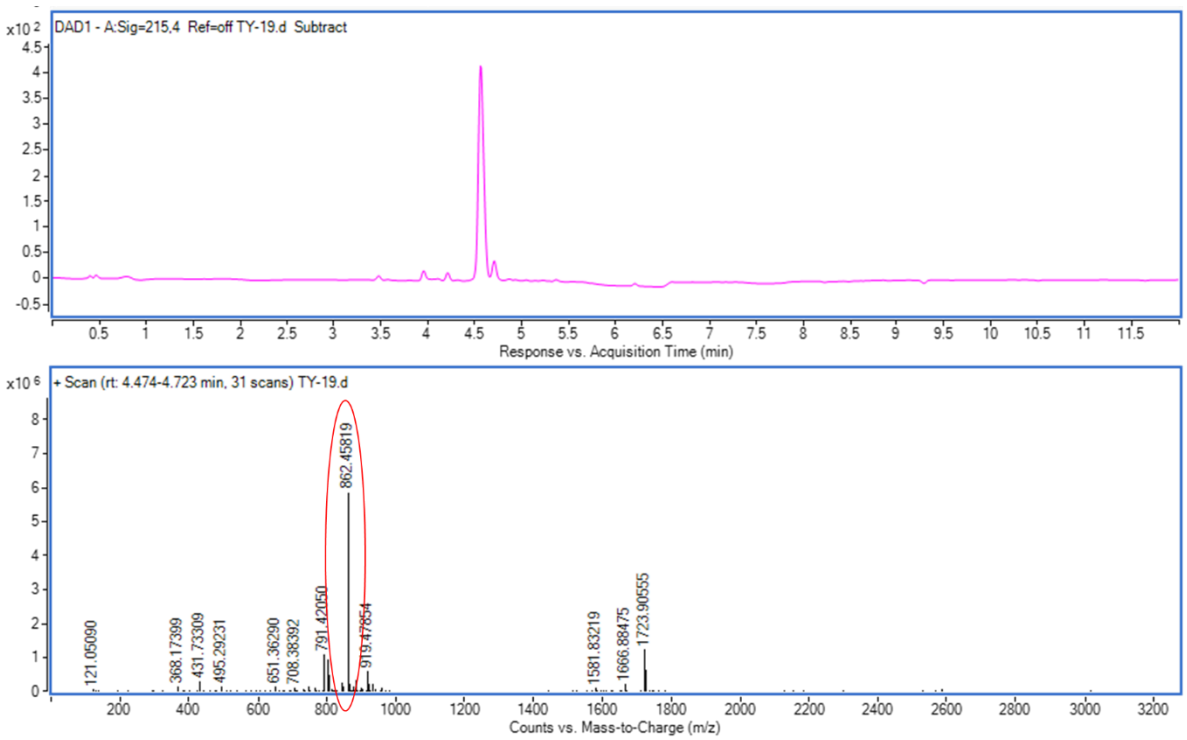

*Figure 3. 4. LCMS spectrum of TY-19 (GGPIGLAG*FG), a modified version of novel predicted peptide. The spectrum shows the theoretical mass of 862 Da (encircled red), indicating the successful synthesis of the peptide. Whereas *F is L-Fmoc-4-fluorophenylalanine serving as a probe for NMR.*

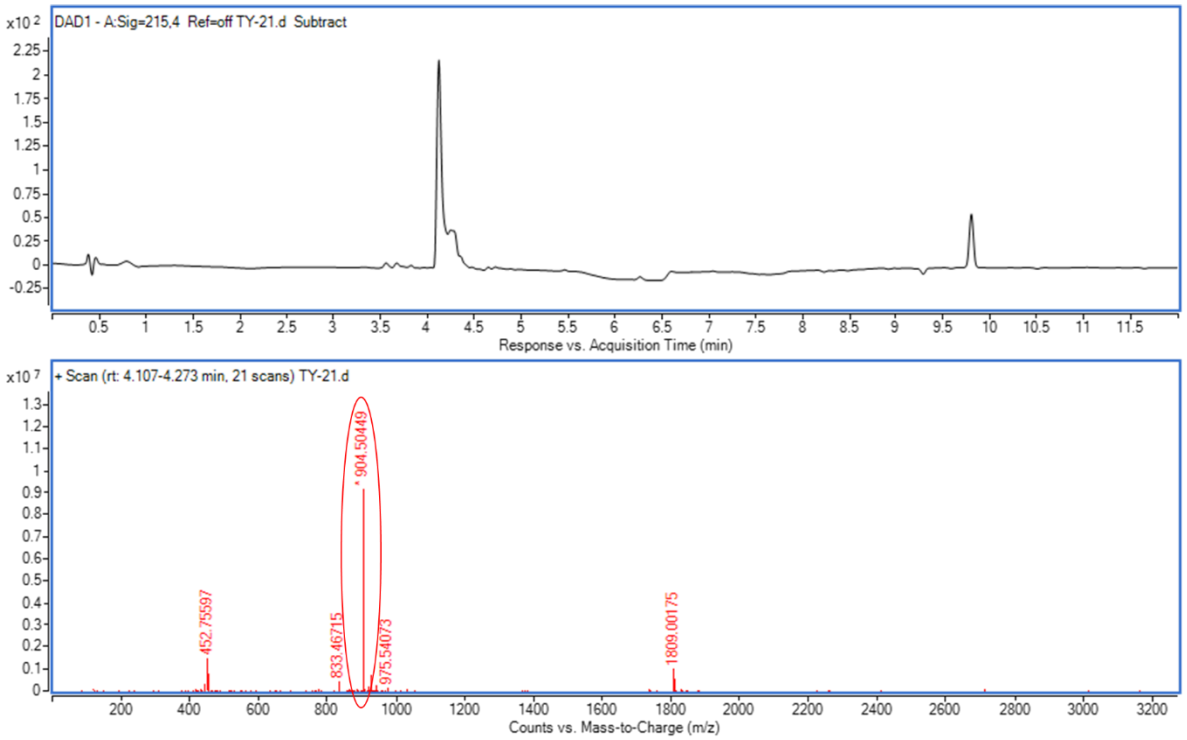

*Figure 3. 5. LCMS spectrum of TY-21 (*FPIAQAQI), a modified version of a novel predicted peptide. The spectrum shows the theoretical mass of 904 Da (encircled red), indicating the successful synthesis of the peptide. *F represents 4-fluorophenylalanine serving as a probe for NMR.*

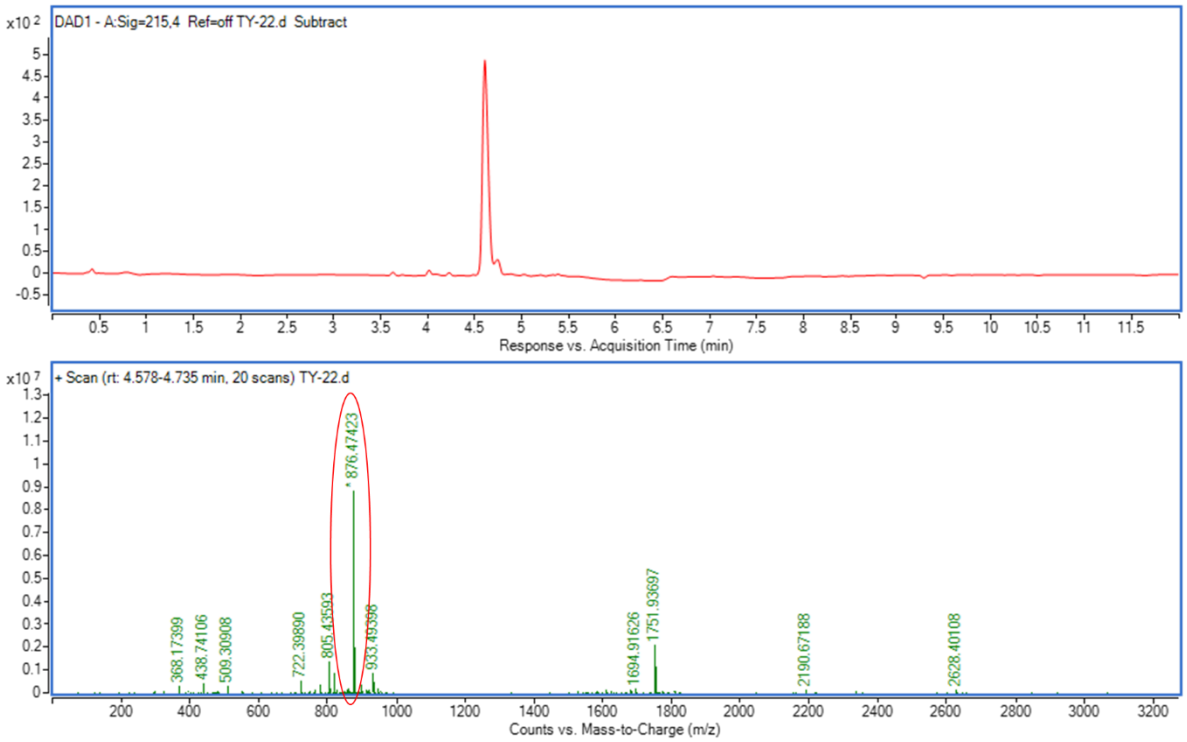

*Figure 3. 6. LCMS spectrum of TY-22 (GGPIALAG*FG), a modified version of a novel predicted peptide. The spectrum shows the theoretical mass of 876 Da (encircled red), indicating the successful synthesis of the peptide. *F represents 4-fluorophenylalanine serving as a probe for NMR.*

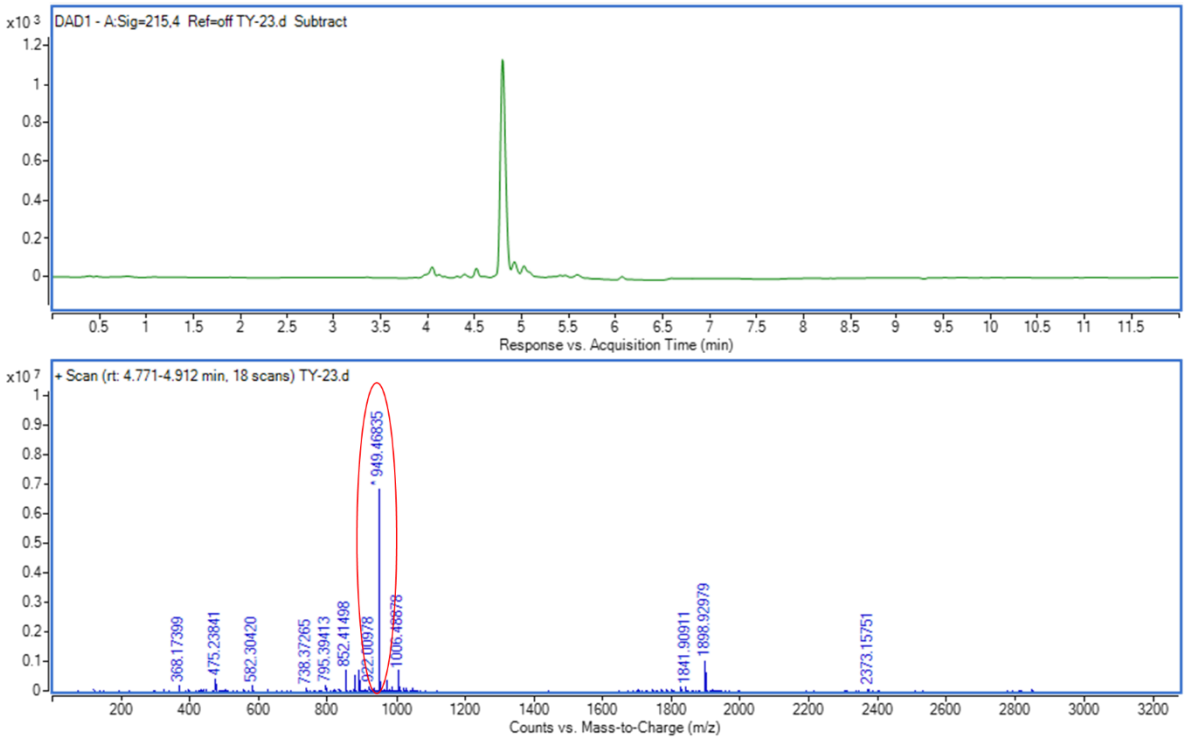

*Figure 3. 7. LCMS spectrum of TY-23 (GGPIAWAG*FG), a modified version of a novel predicted peptide. The spectrum shows the theoretical mass of 949 Da (encircled red), indicating the successful synthesis of the peptide. *F represents 4-fluorophenylalanine serving as a probe for NMR.*

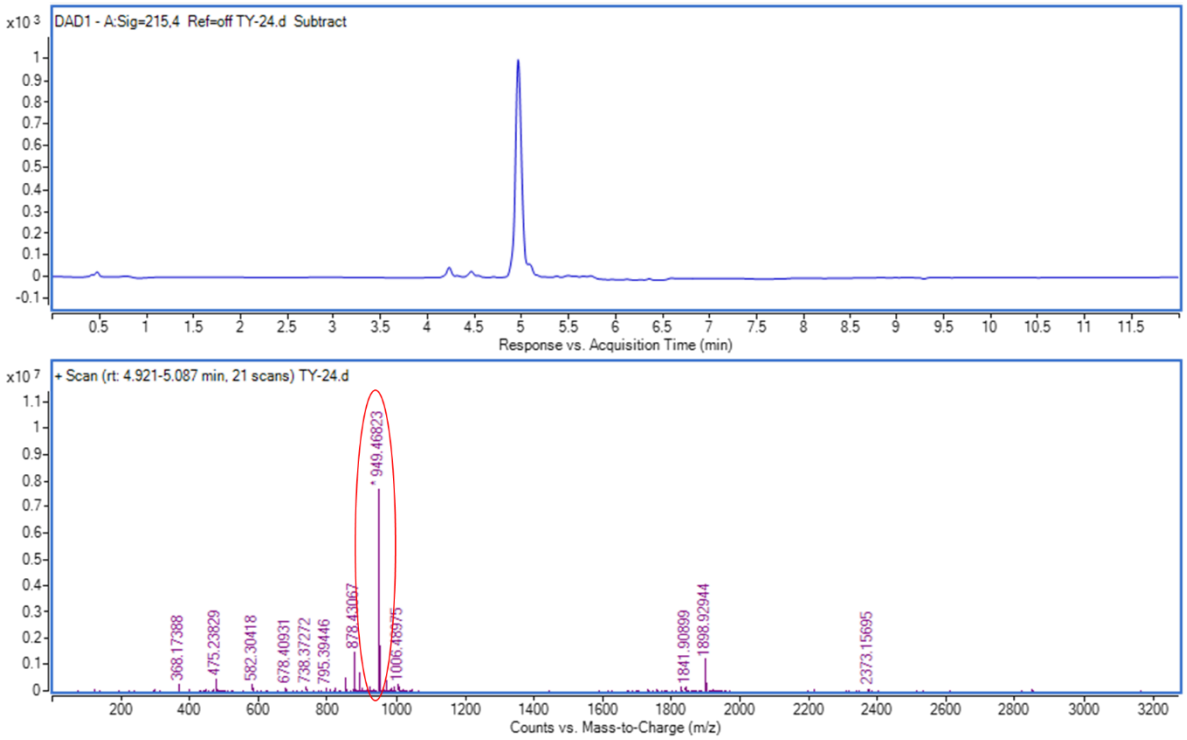

*Figure 3. 8. LCMS spectrum of TY-24 (GGPWALAG*FG), a modified version of a novel predicted peptide. The spectrum shows the theoretical mass of 949 Da (encircled red), indicating the successful synthesis of the peptide. *F represents 4-fluorophenylalanine serving as a probe for NMR.*

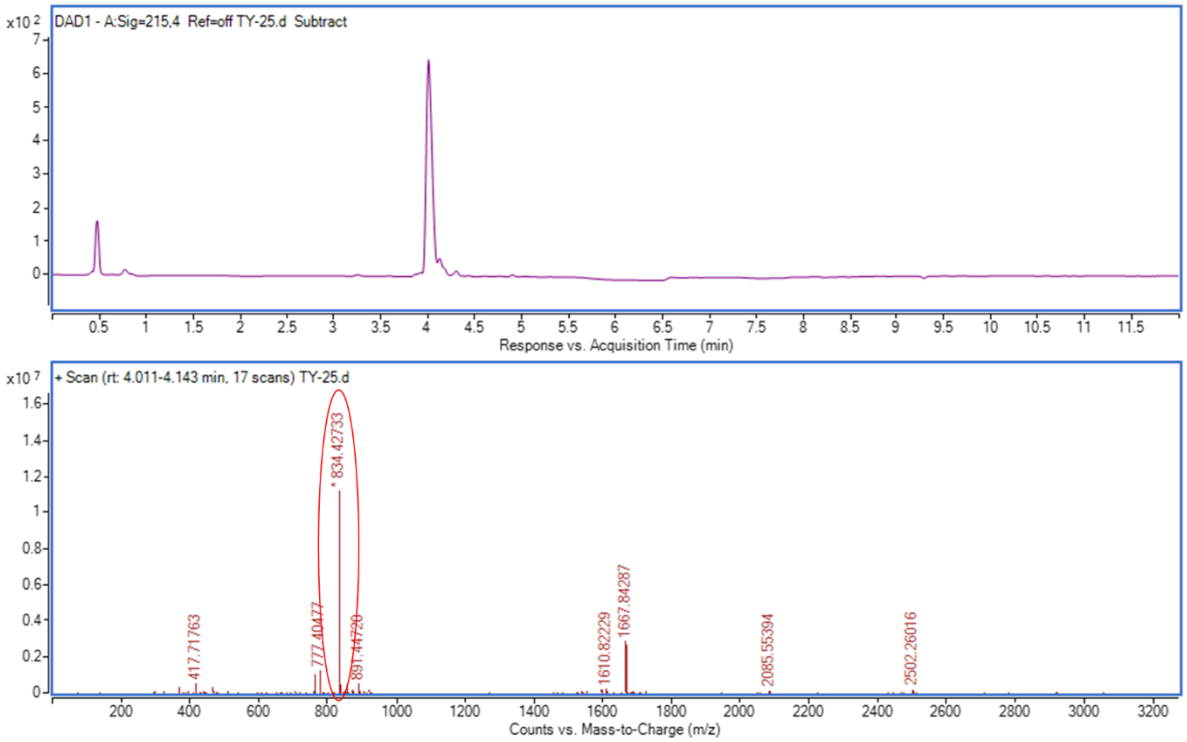

*Figure 3. 9. LCMS spectrum of TY-25 (GGPIAAAG*FG), a modified version of a novel predicted peptide. The spectrum shows the theoretical mass of 834 Da (encircled red), indicating the successful synthesis of the peptide. *F represents 4-fluorophenylalanine serving as a probe for NMR.*

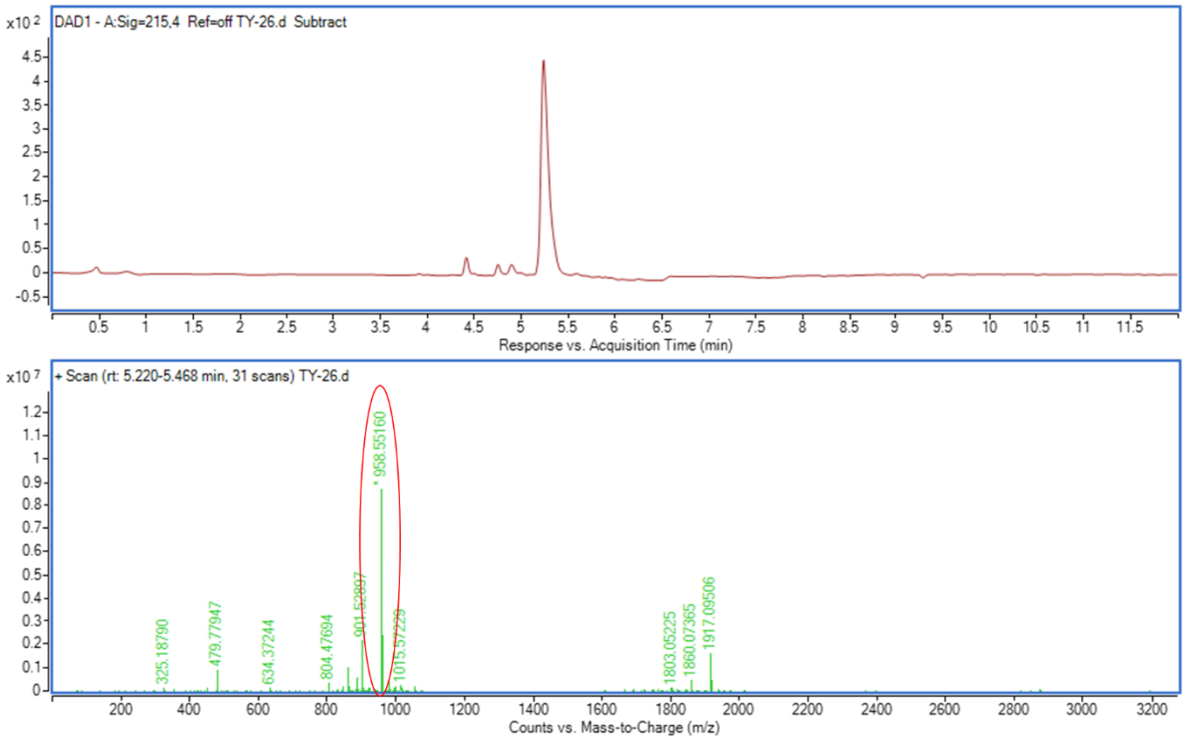

*Figure 3. 10. LCMS spectrum of TY-26 (GGPIPLAI*FG), a modified version of a novel predicted peptide. The spectrum shows the theoretical mass of 958 Da (encircled red), indicating the successful synthesis of the peptide. *F represents 4-fluorophenylalanine serving as a probe for NMR.*

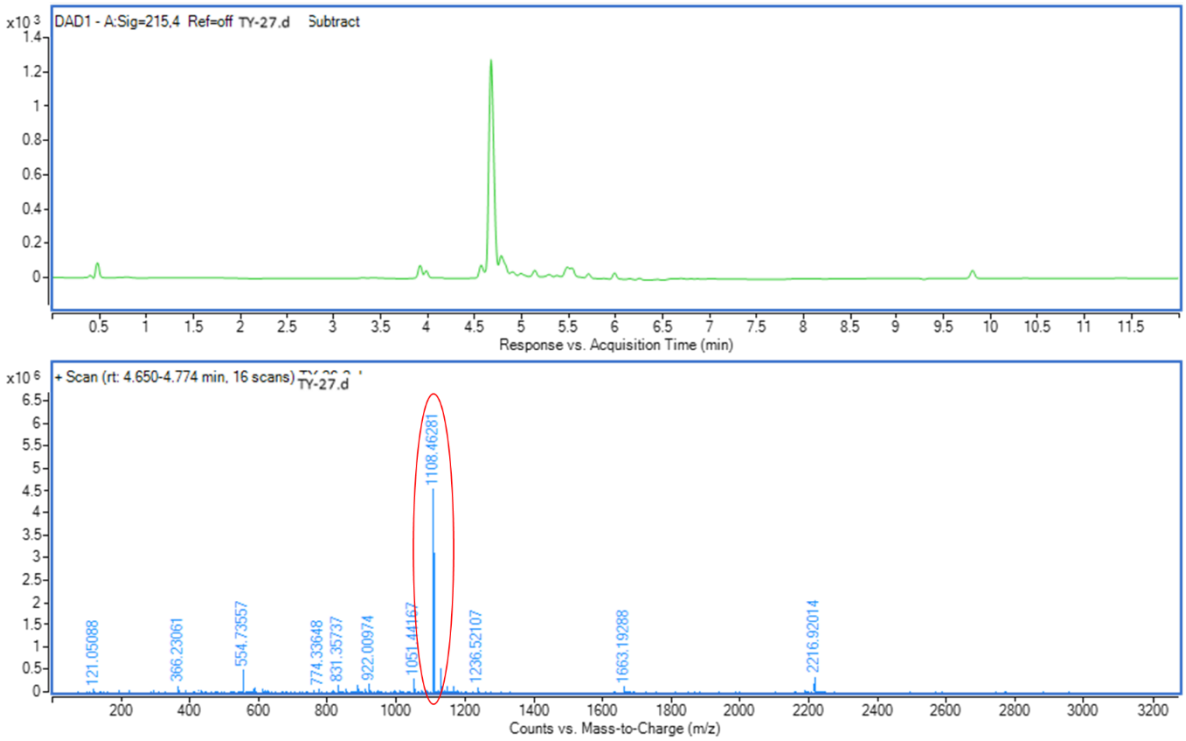

*Figure 3. 11. LCMS spectrum of TY-27 (GGYGQ-GYW*FG), a modified version of a novel predicted peptide. The spectrum of shows the theoretical mass of 1108 Da (encircled red), indicating the successful synthesis of the peptide. *F represents 4-fluorophenylalanine serving as a probe for NMR.*

The real time enzyme kinetics of the peptide substrates (novel predicted sequences with literature reported peptide sequences serving as standard) for activated MMP-9 are shown in Figures 3.12 – 3.18. It can be observed that peptide goes under metabolism in human serum more than once suggesting that multiple enzymes present in serum are metabolizing peptide from different positions as shown in Figure 3.12.

Figures 3.12 – 3.17 show the changes in substrate (and product) concentrations in the presence of activated MMP-9 over a period of time. In Figure 3.13 the substrate peak in the spectrum is at -116.688 ppm and TFA at -76.55 serves as an internal standard. After two h, another peak appears at -116.792 ppm that represents product. This product peak kept rising over time and the reactant peak finally disappeared after 15 h. Similarly, for all the novel and predicted MMP-9 substrate the peptides reactant peak is disappearing over time and product peak is increasing with different rates for each peptide indicating the specificity of the MMP-9 for the specific peptide. Some peptides are being metabolized by MMP-9 quicker than others making them substrates that are more suitable.

Non-specific degradation was observed as shown in Figure 3.12 compared to 3.13, however, the peptide started to degrade in serum after two hours, and more likely the start was by serum MMP-9. Also comparing Figures 3.12 and 3.13 suggests that there is a 2 h window in the serum for targeting the brain before the peptide cleavage by serum peptidases and proteinases.

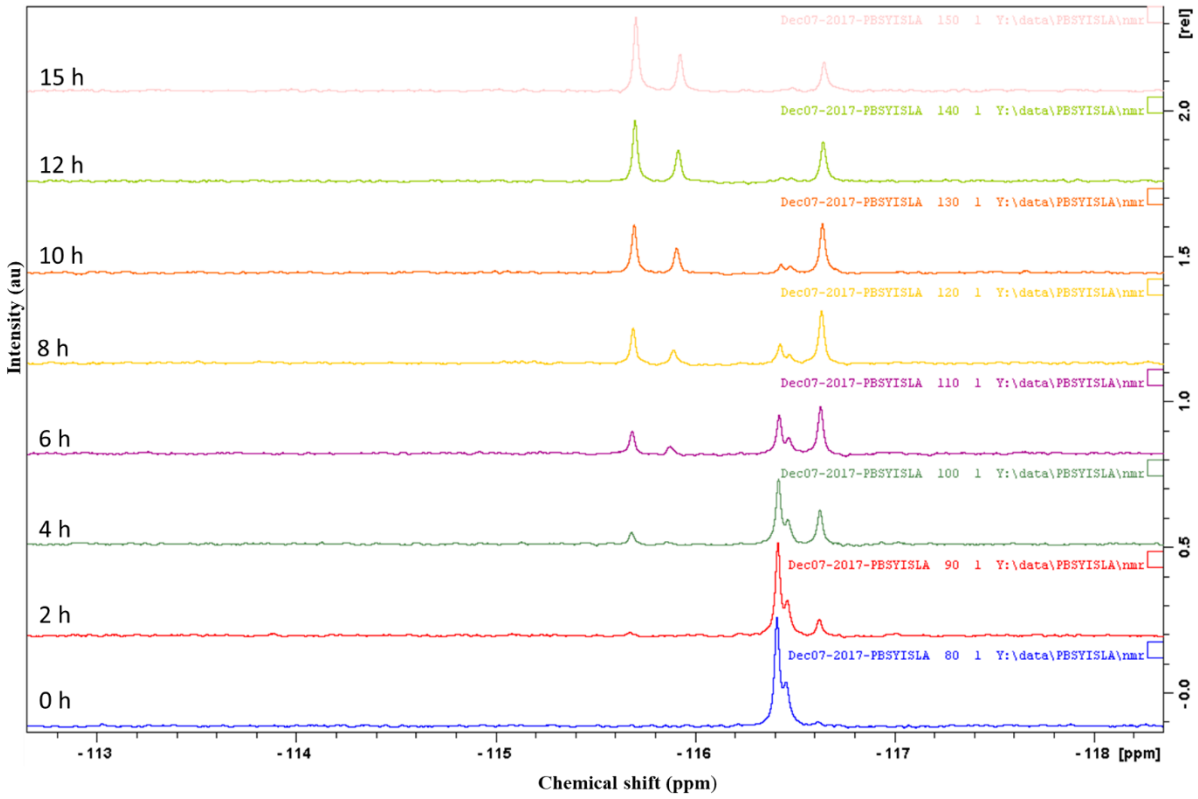

*Figure 3. 12. Evolving NMR spectrum for TY-6 (PLGL*FGAQ) in the presence of human serum over the course of 15 h. At 0 min, there is only one peak visible in the spectrum (blue) highlighting the intact peptide. After two h, another peak start appearing that shows the cleaved product of the peptide (red). After 6 h, two small peaks start appearing which are the products of the metabolites of reactants. Similarly, over the period up to 15 h, reactant peak disappeared, and the product peak becomes dominant. This disappearance of the reactant peak is due to enzymatic cleavage of the peptide which are present in serum. It can be observed the reactant peaks changed/metabolized into products which further undergoes enzymatic degradation to produce further peaks. This suggests that multiple enzymes present in human serum are metabolising the peptide from different positions.*

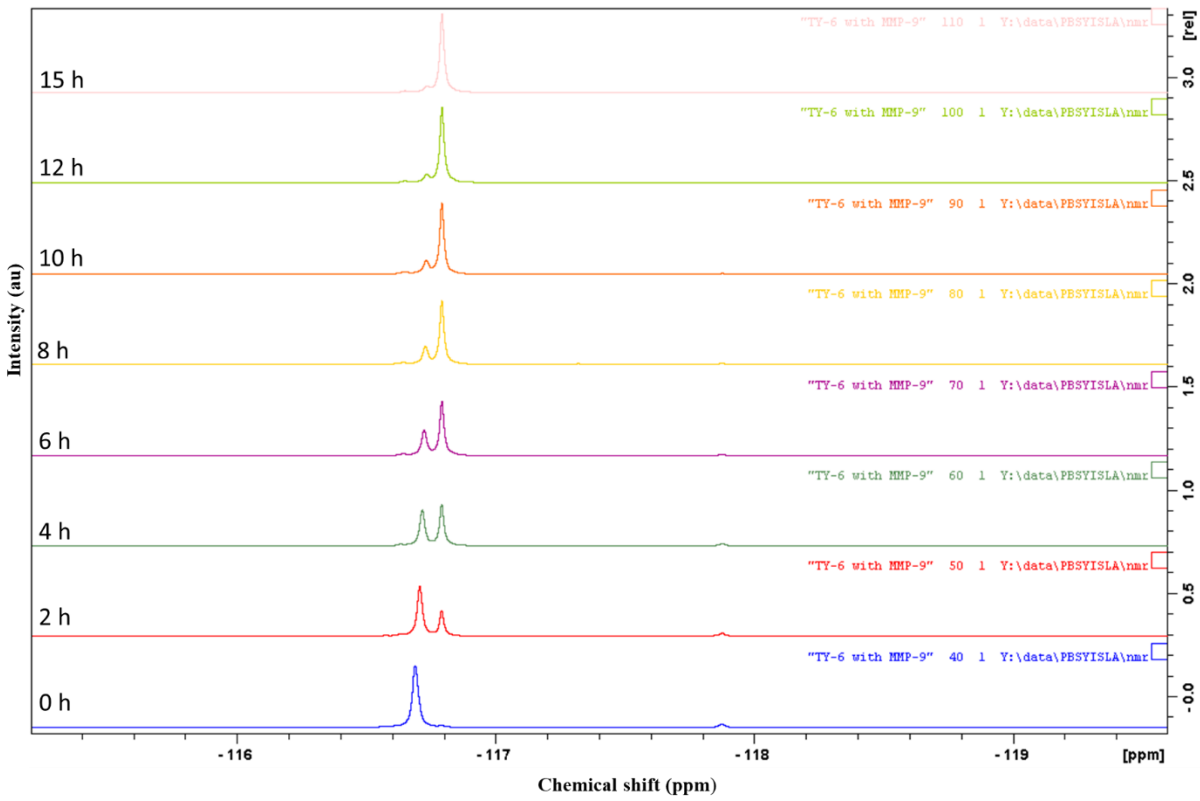

*Figure 3. 13. Evolving NMR spectrum for TY-6 (PLGL*FGAQ) in the presence of activated MMP-9 over the course of 15 h. At 0 min, there is only one peak visible in the spectrum (blue) highlighting the intact peptide. After two h, another peak starts appearing that shows the cleaved product of the peptide (red). Similarly, over the period up to 15 h, reactant peak disappeared, and the product peak becomes dominant. This disappearance of the reactant peak is due to enzymatic cleavage of the peptide.*

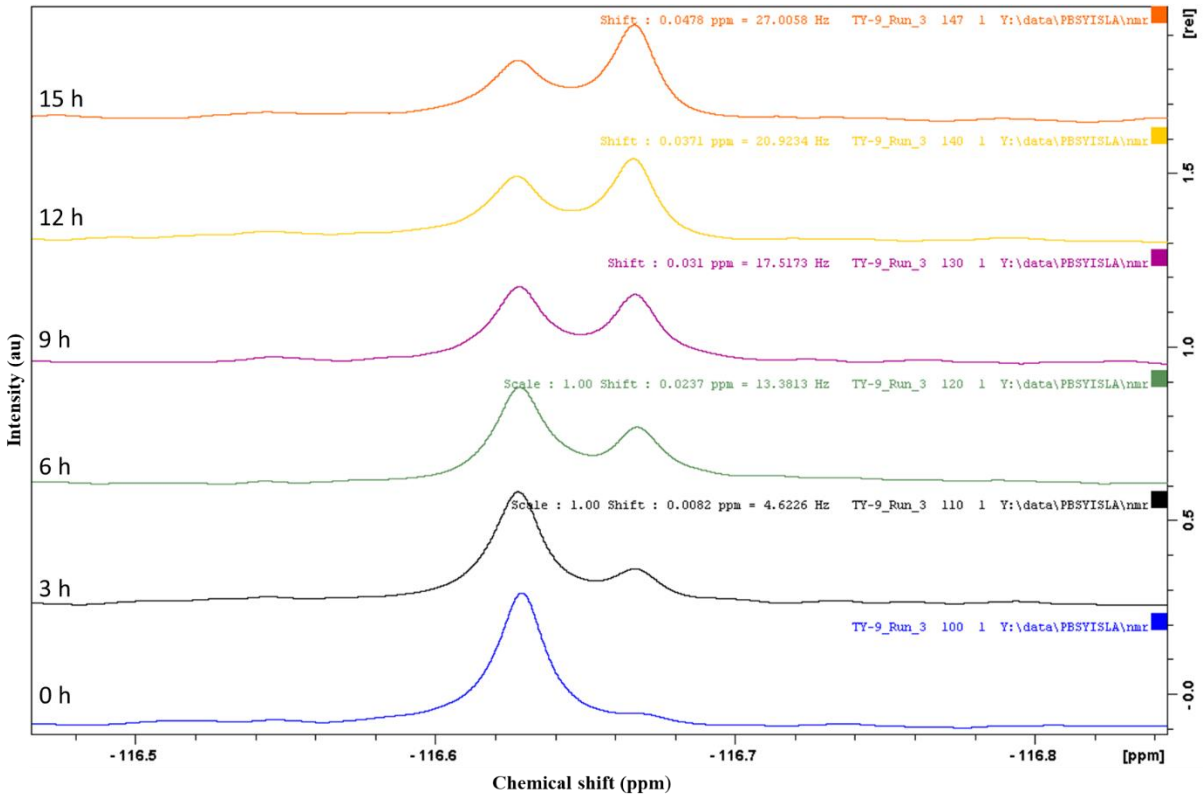

*Figure 3. 14. Evolving NMR spectrum for TY-9 (PLGLWG*FQ) in the presence of activated MMP-9 over the course of 15 h. At 0 min, there is one dominant peak visible in the spectrum (blue) corresponding to the intact peptide. After two h, another peak starts appearing that shows the cleaved product of the peptide (black). Similarly, over the period up to 15 h, the reactant peak is disappearing, and product peak is increasing. This disappearance of the reactant peak is due to enzymatic cleavage of the peptide.*

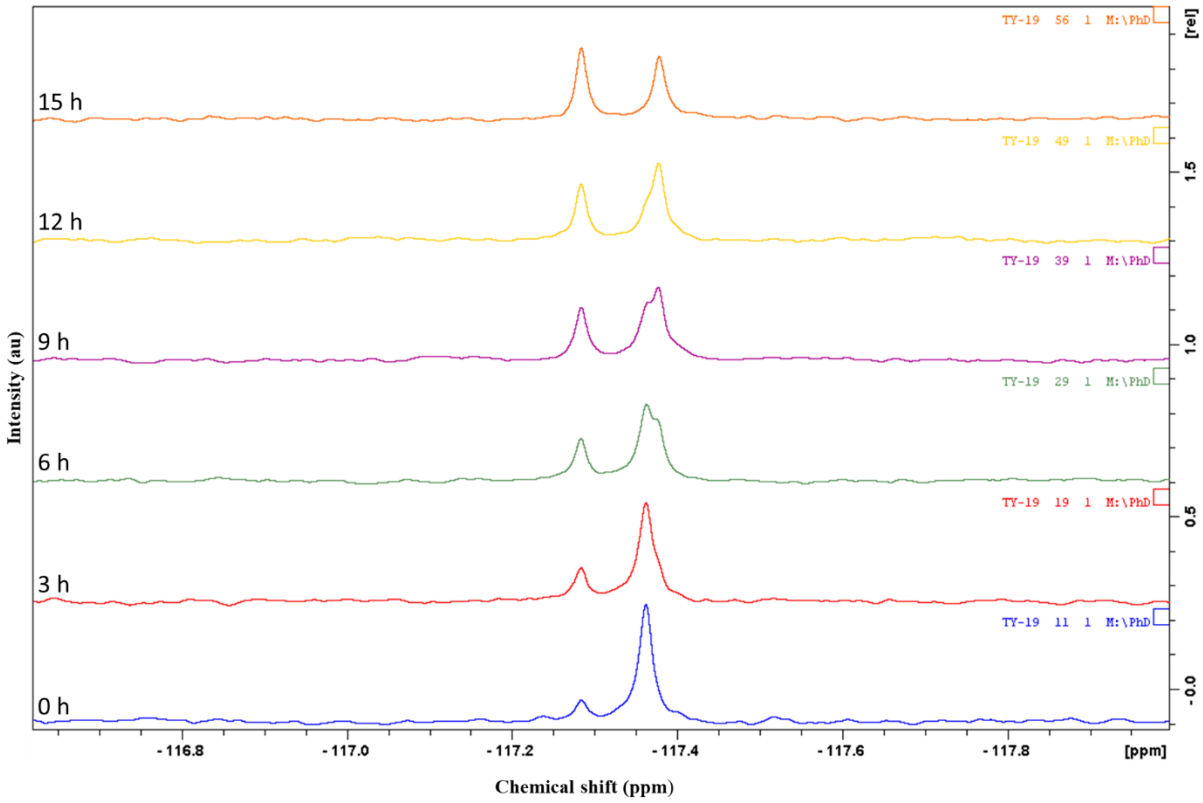

*Figure 3. 15. Evolving NMR spectrum for TY-19 (GGPIG-LAG*FG) in the presence of activated MMP-9 over the course of 15 h. At 0 min, there is one peak dominant in the spectrum (blue) highlighting the intact peptide. After two h, another peak is increasing that shows the cleaved product of the peptide (red). Similarly, over the period up to 15 h, reactant peak is disappearing, and product peak is increasing. In this case, there is support for more than one product peak. The disappearance of the reactant peak is due to enzymatic cleavage of the peptide.*

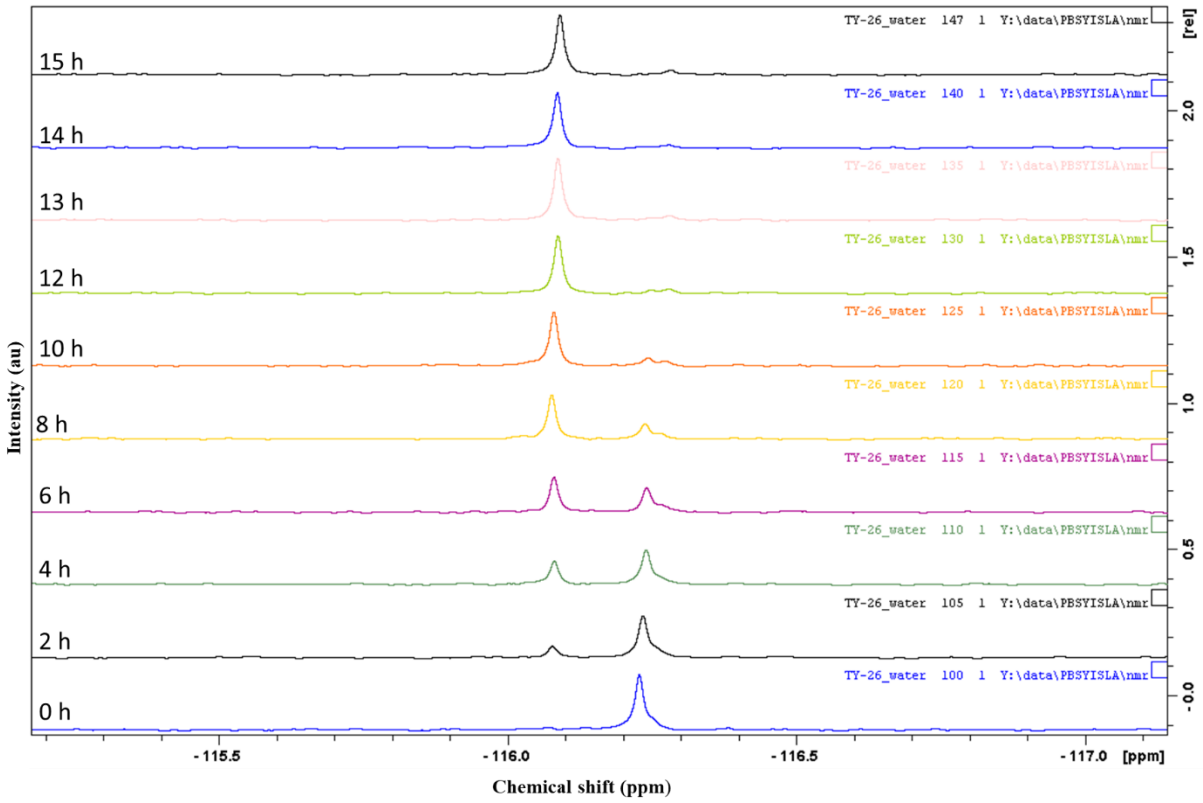

*Figure 3. 16. Evolving NMR spectrum for TY-26 (GGPIPLAI*FG) in the presence of activated MMP-9 over the course of 15 h. At 0 min, there is only one peak visible in the spectrum (blue) highlighting the intact peptide. After two h, another peak starts appearing that shows the cleaved product of the peptide (black). Similarly, over the period, the reactant peak completely disappeared, and product peak is increasing. In this case, it is the fastest cleaving peptide and best substrate for MMP-9. This disappearance of the reactant peak is due to enzymatic cleavage of the peptide.*

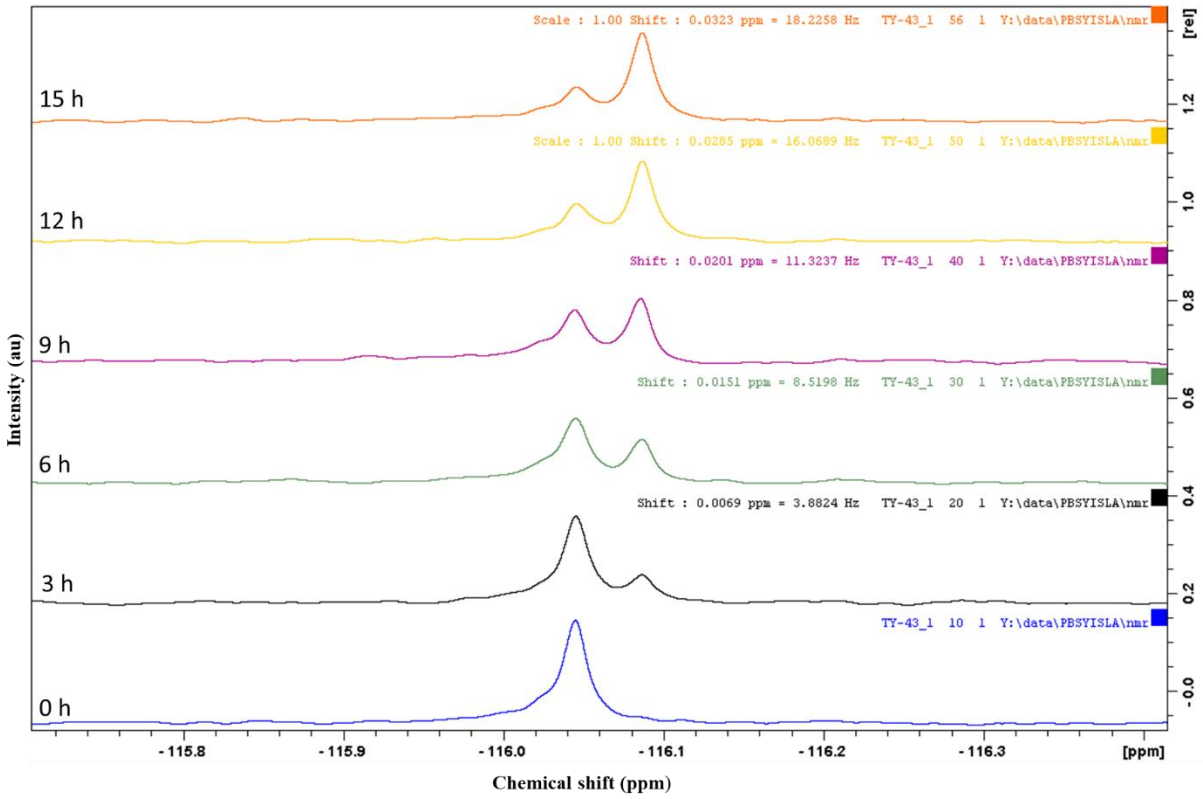

*Figure 3. 17. Evolving NMR spectrum for TY-43 (RPLALR*FSQ) in the presence of activated MMP-9 over the course of 15 h. At 0 min, there is one dominant peak visible in the spectrum (blue) corresponding to the intact peptide. After two h, another peak starts appearing that shows the cleaved product of the peptide (black). Similarly, over the period up to 15 h, the reactant peak is disappearing, and product peak is showing up. This disappearance of the reactant peak is due to enzymatic cleavage of the peptide.*

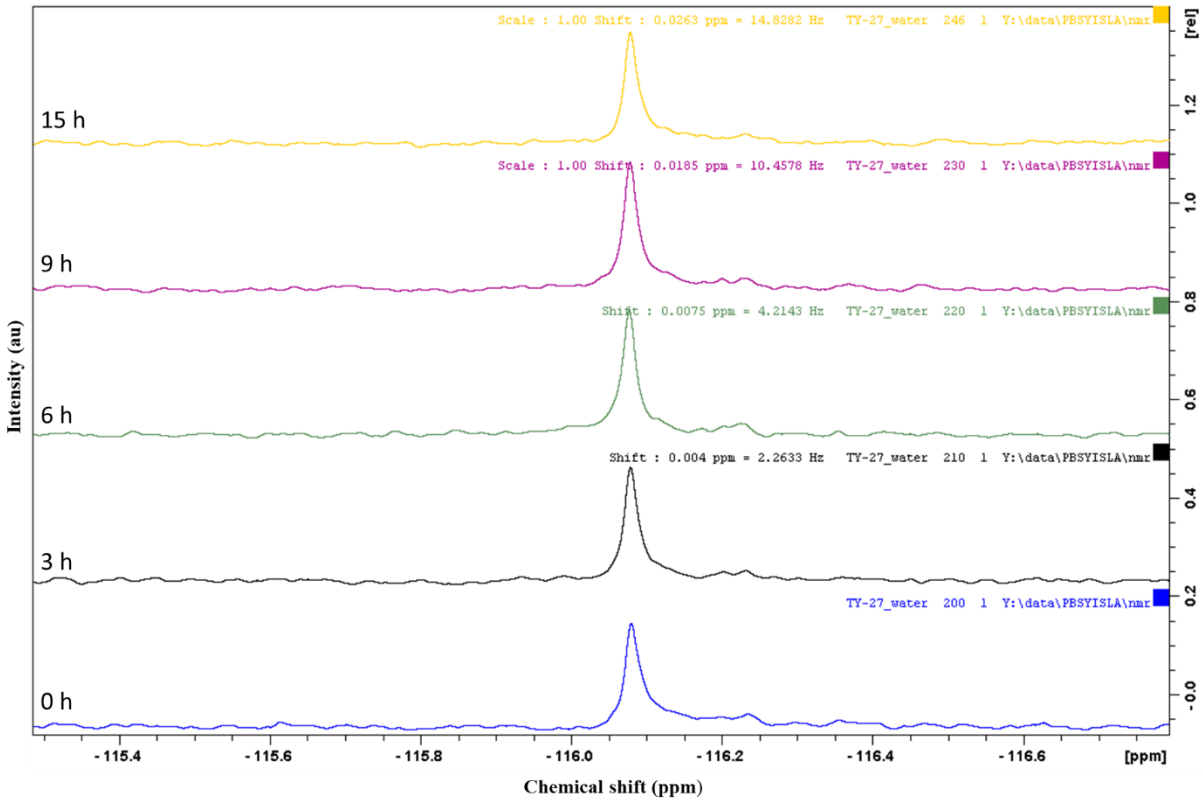

*Figure 3. 18. Evolving NMR spectrum for TY-27 (GGYGQGYW*FG) in the presence of activated MMP-9 over the course of 15 h. At 0 min, there is one dominant peak visible in the spectrum (blue) corresponding to the intact peptide. Over the period up to 15 h, there is little change to the spectrum.*

The product peaks are not clearly distinct and visible in some peptide sequences. In TY-24 and TY-25 there was no clear product peak visible as shown in Figures 3.19 and 3.20. To investigate that issue, LCMS analysis was run, where possible, especially for TY-24, TY-25, TY-26 and TY-27 straight after 15 h. It was found in LCMS data that both peptides TY-24 and TY-25 are being cleaved, as expected and shown in Figures 3.21 – 3.24, but probably the resolution of the NMR is not high enough to detect the change in chemical shift between reactant and product. The distance of the *F atom from the cleavage site is proposed to be responsible for this lack of sensitivity. In TY-24 and TY-25 the *F is positioned at P4', too far from the cleavage site, the through-bond influences are not sufficient to discriminate between the intact substrate and the cleaved product.

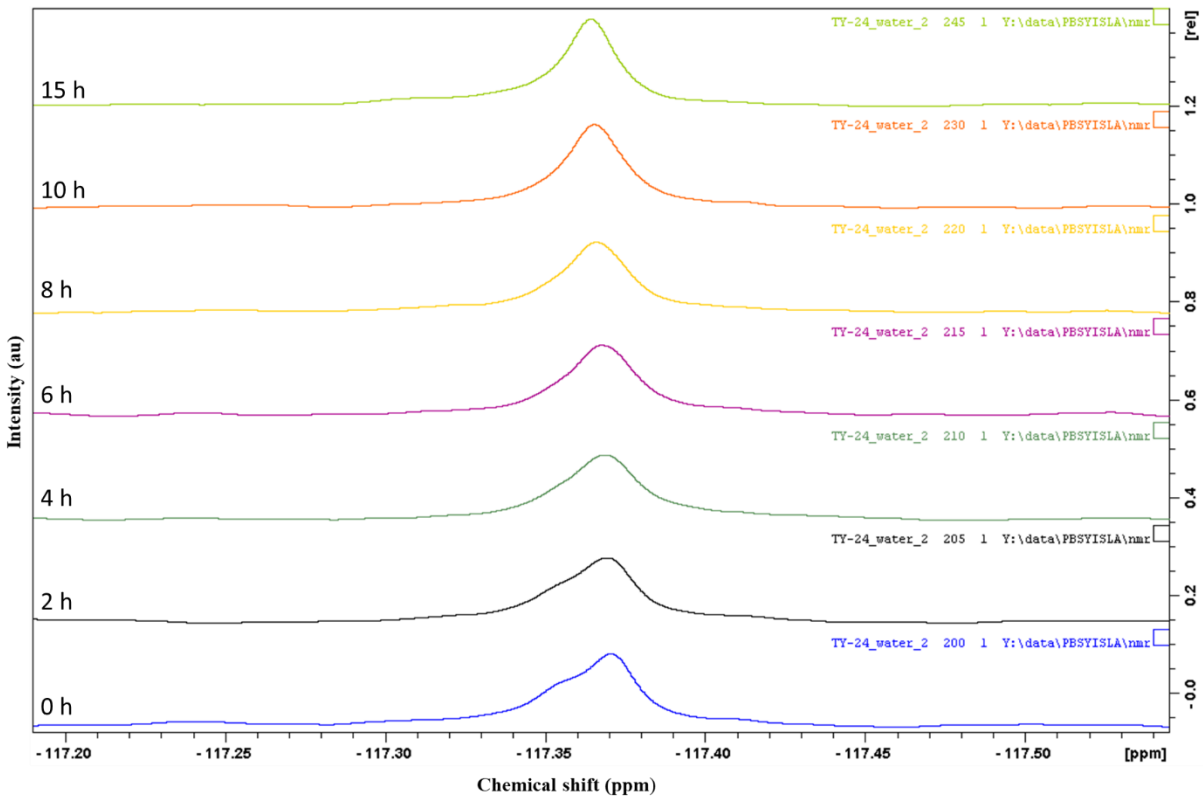

*Figure 3. 19. Evolving NMR spectrum for TY-24 (GGPWALAG*FG) in the presence of activated MMP-9 over the course of 15 h. At 0 min, there is only one extended peak visible in the spectrum (blue) possibly due to the peptide binding with the MMP-9 active site cavity. Similarly, over the period up to 15 h, the peak changed its shape but there is no product peak visible.*

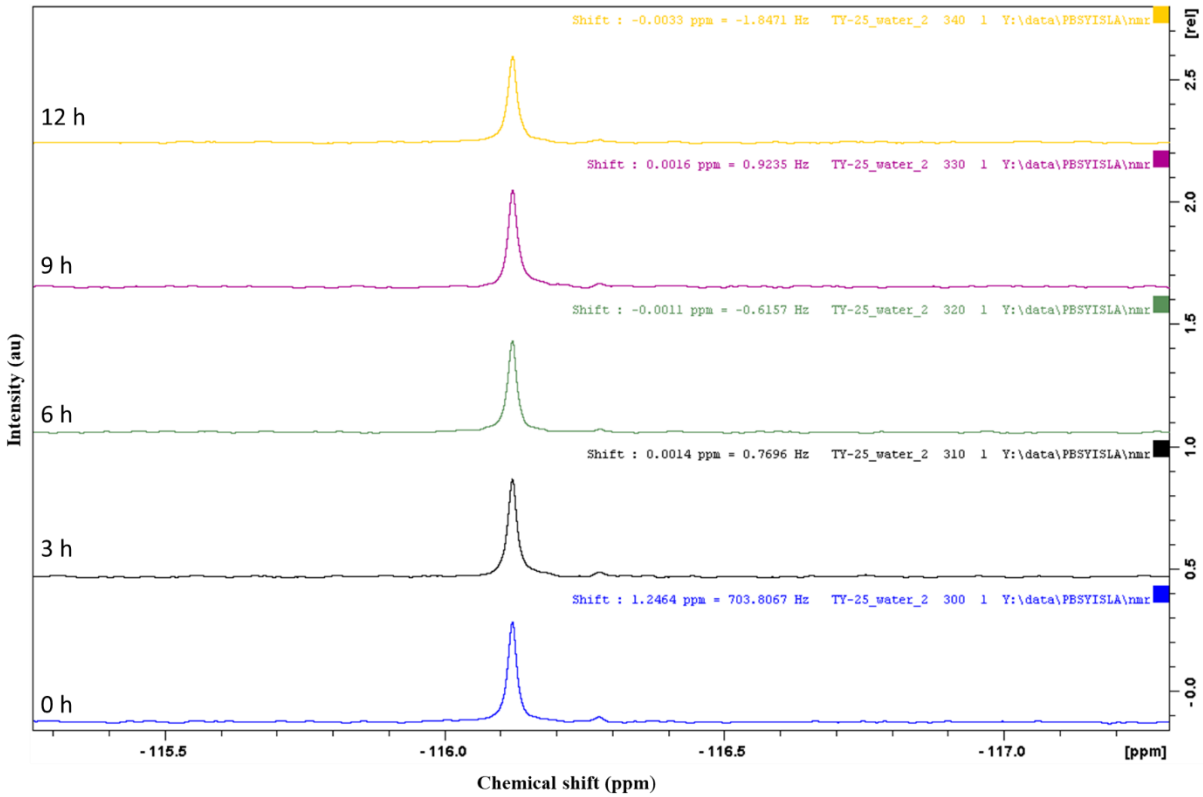

*Figure 3. 20. Evolving NMR spectrum for TY-25 (GGPIAAAG*FG) in the presence of activated MMP-9 over the course of 15 h. At 0 min, there is only one peak visible in the spectrum (blue) corresponding to the substrate. Over the period up to 15 h, the peak did not change its shape.*

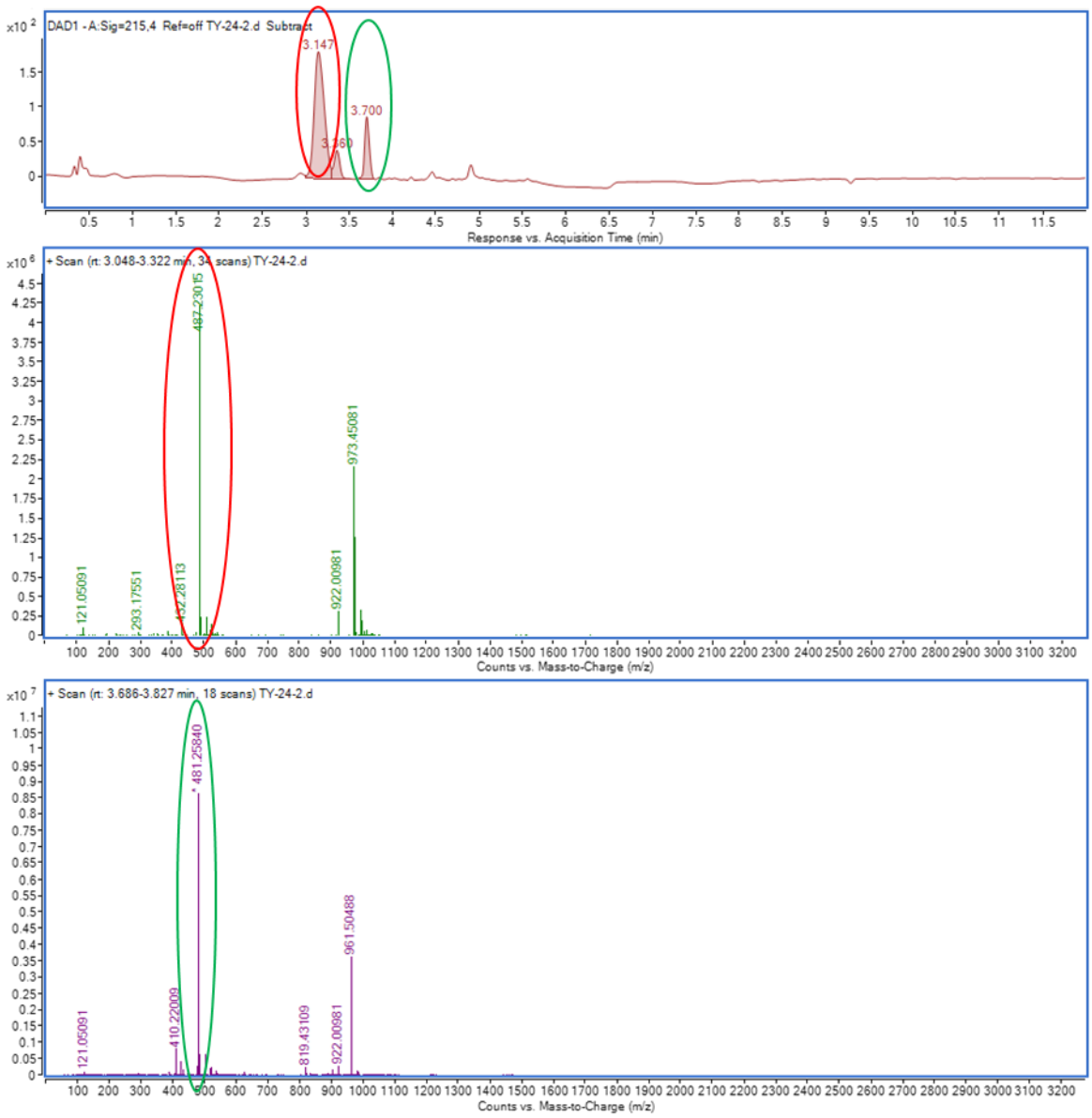

*Figure 3. 21. LCMS spectrum of TY-24 (GGPWALAG*FG), a modified version of a novel predicted peptide after 15 h in the presence of MMP-9. The spectrum shows the theoretical masses of cleaved product 487(encircled red) and 481 (encircled green) Da, indicating the degradation of peptide by active MMP-9 at the predicted position.*

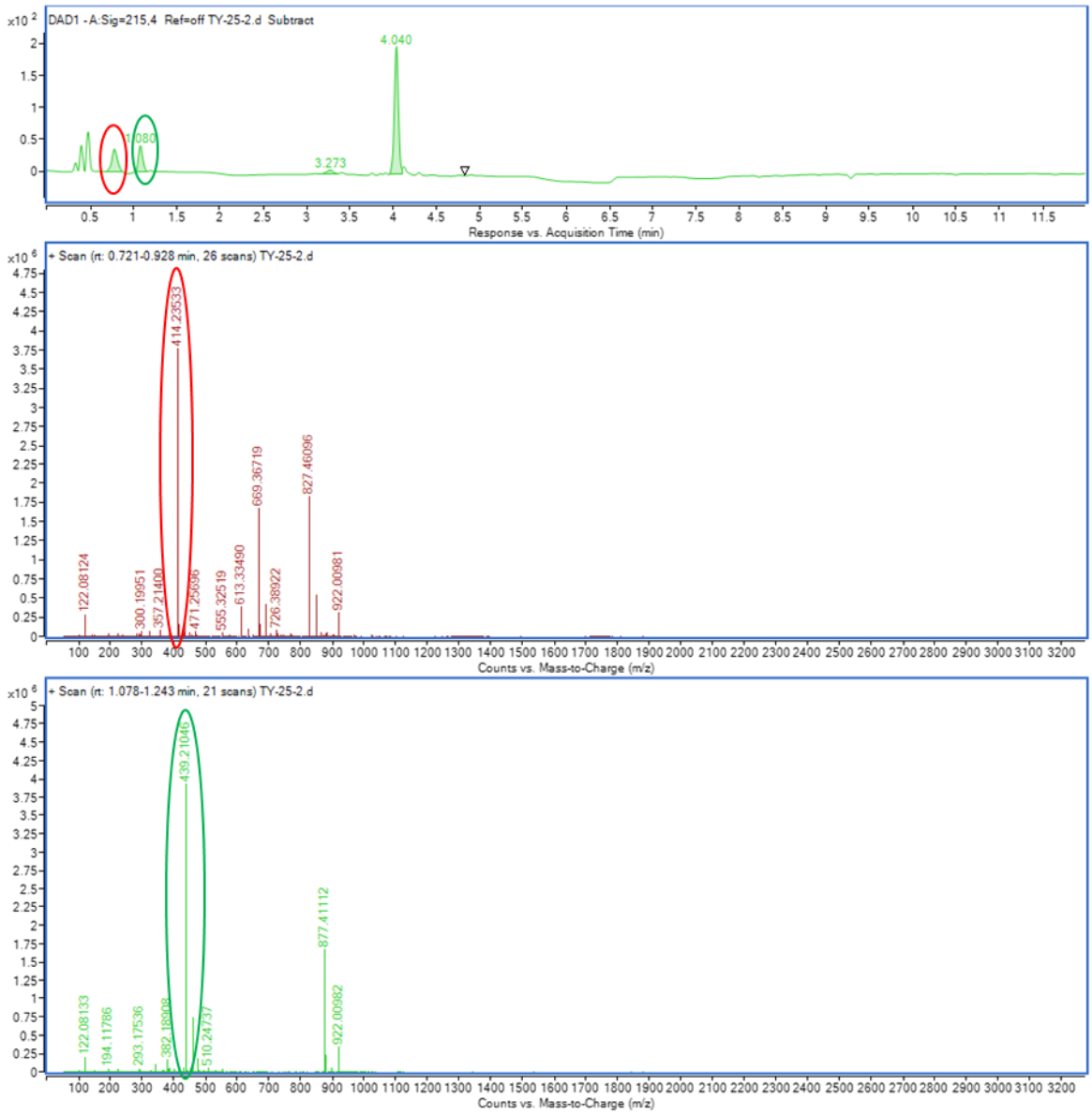

*Figure 3. 22. LCMS spectrum of TY-25 (GGPIAAAG*FG), a modified version of a novel predicted peptide after exposure to MMP-9 for 15 h. The spectrum shows the theoretical masses of cleaved product 414 (encircled red) and 439 (encircled green) Da, indicating the degradation of peptide by active MMP-9 at the predicted position.*

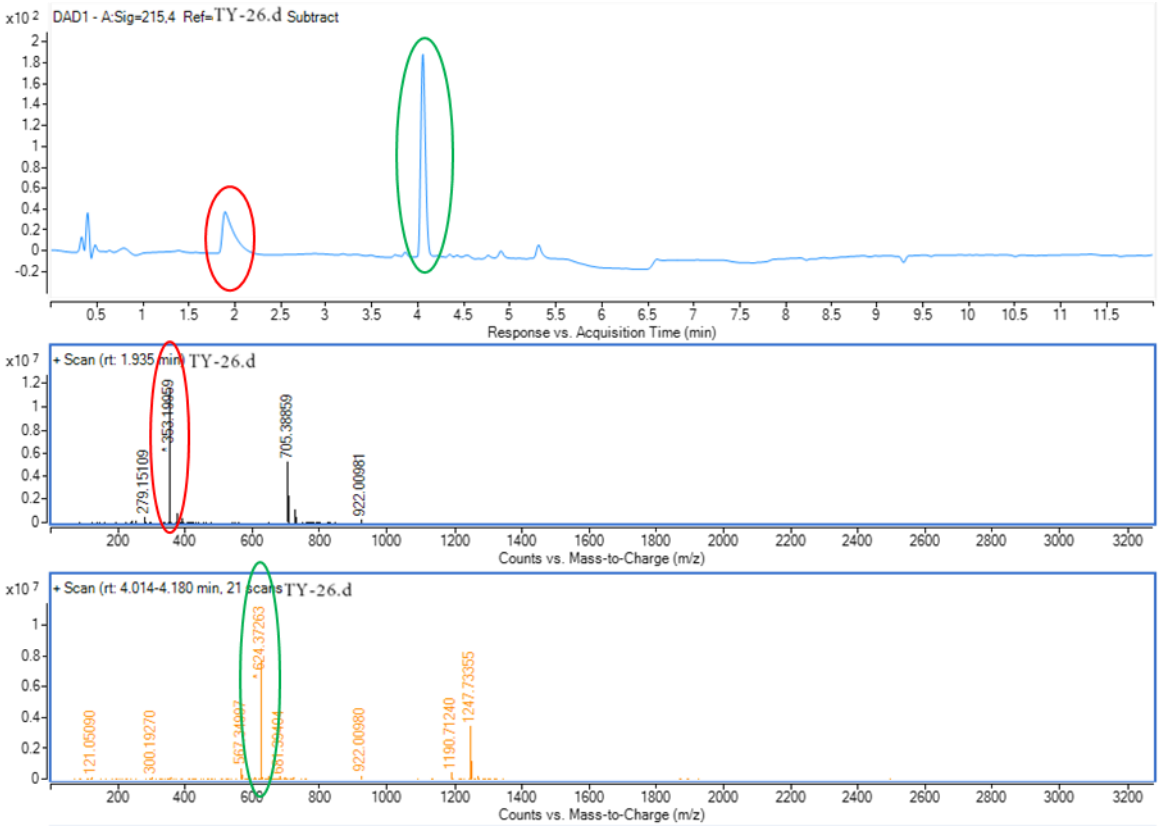

*Figure 3. 23. LCMS spectrum of TY-26 (GGPIPLAI*FG), a modified version of a novel predicted peptide after exposure to MMP-9 for 15 h. The spectrum shows the theoretical masses of cleaved product 624 Da (encircled red) and 353 Da (encircled green), indicating the degradation of peptide by active MMP-9 at the predicted position.*

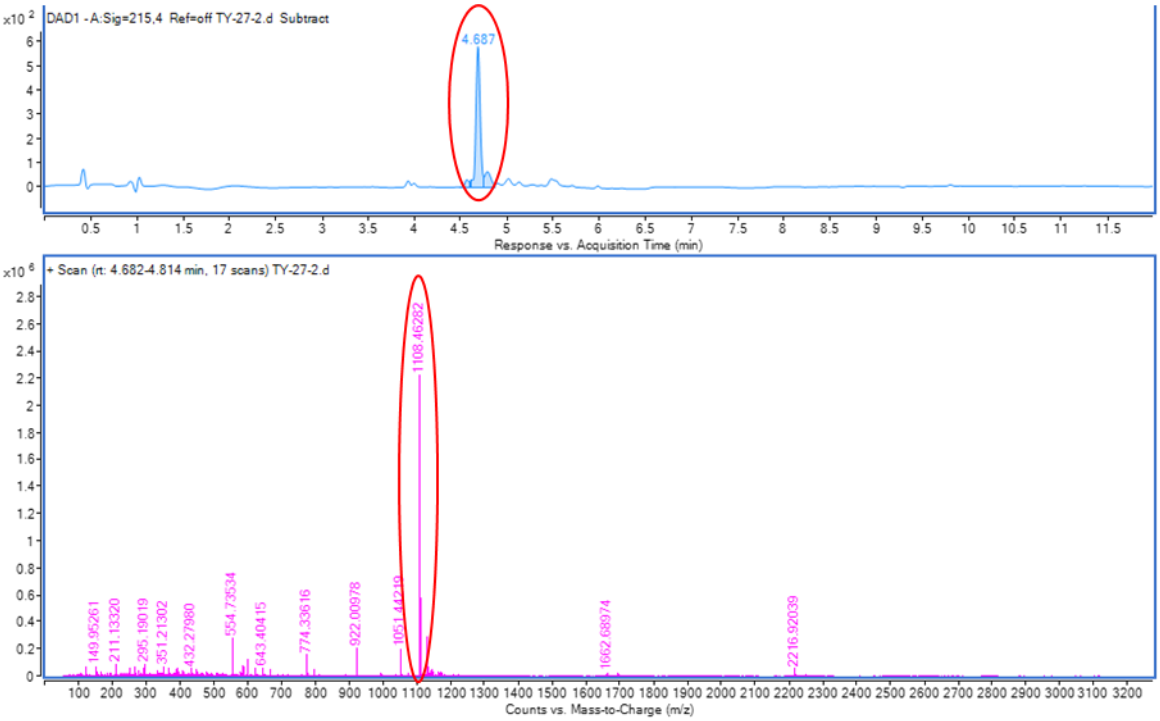

*Figure 3. 24. LCMS spectrum of TY-27 (GGYGQ-GYW*FG), a modified version of a novel predicted peptide after exposure to MMP-9 for 15 h. The spectrum shows the theoretical mass of 1108 Da, indicating no change of peptide in the presence of active MMP-9.*

From the LCMS data in Figures 3.21 and 3.22 the exact theoretical masses for the products can be observed. In TY-24, theoretical masses for the products were detected as 487 (P5-P1) and 481(P1'-P5'). Similarly, TY-25 showed the theoretical masses of 414 (P5-P1) and 439 (P1'-P5'). These LCMS chromatograms support that the peptides are being degraded by active MMP-9, but NMR is not able to detect the change, because the analytical *F is too far removed from the cleavage site to change chemical shift upon cleavage.

TY-26 (GGPIPLAI*FG), a novel predicted peptide showed clear distinct peaks for reactants and product. The reactant peptide was completely cleaved by MMP-9 into products within 5 h making it the best substrate for MMP-9. Interestingly, LCMS data showed it was cleaved at a different position than that predicted. The theoretical mass of the peptide was 958 Da as shown in Figure 3.16, and the cleaved products should have the masses of 439 and 519, but LCMS data showed the masses of 624 and 353 as shown in Figure 3.23. The presence of two proline (Pro) residues in the sequence probably causes this change in the cleaving position. It cleaved in-between what had been predicted to be P2' and P3' (alanine (Ala) and isoleucine (Ile)) instead of the predicted positions P1 and P1'. Pleasingly, TY-27, a negative control with a Y-score of -2.18 did not change at all after 15 h and was detected intact in the LCMS as shown in Figure 3.24.

Peak shape analysis was performed using MestReNova 6.0.2-5475 as shown in Figure 3.25. In Figure 3.24A, two unprocessed peaks are shown which are overlapping preventing accurate integration as standalone peaks, In Figure 3.24B the fitting of two appropriately shaped peaks that would accurately recapitulate the observed spectrum is shown and an

accurate assessment of the peak areas (and therefore concentrations of the corresponding species) can be made.

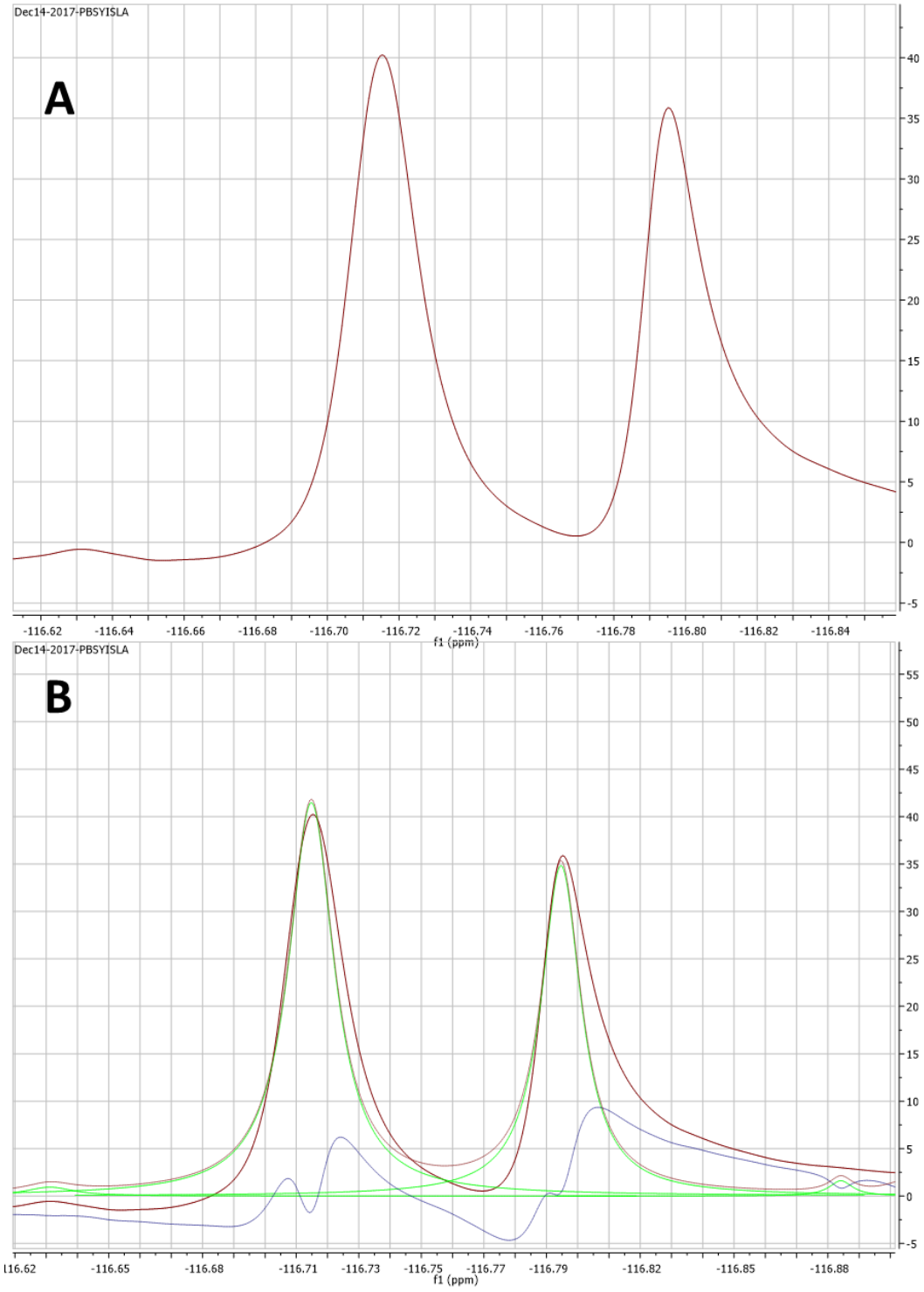

Figure 3. 25. A NMR spectrum showing the peaks before and after processing.

The peak areas from the NMR spectra were converted into absolute concentrations by using the presence of TFA in each sample as an internal standard. It is assumed that the TFA concentration remains constant throughout the NMR experiment. Using a serial dilution of an independently prepared sample of TFA, a calibration curve linking the concentration of TFA to peak areas obtained under the same NMR conditions as the enzyme kinetics was obtained (Figure 3.26). In the enzyme kinetics experiments, the time-averaged integration of the TFA peak was calculated for each system and converted to a concentration by multiplying with 0.00007019 from the calibration curve (giving a TFA concentration in mg/ml) and dividing it by 114 (MW of TFA) to get the molar concentration of TFA in each sample. At each time point, the integral of peaks for reactants and products was compared to the integral of the TFA peak at that time point. It was then multiplied by the average concentration of TFA for the specific peptide to give molar concentration of peptide species at each time point.

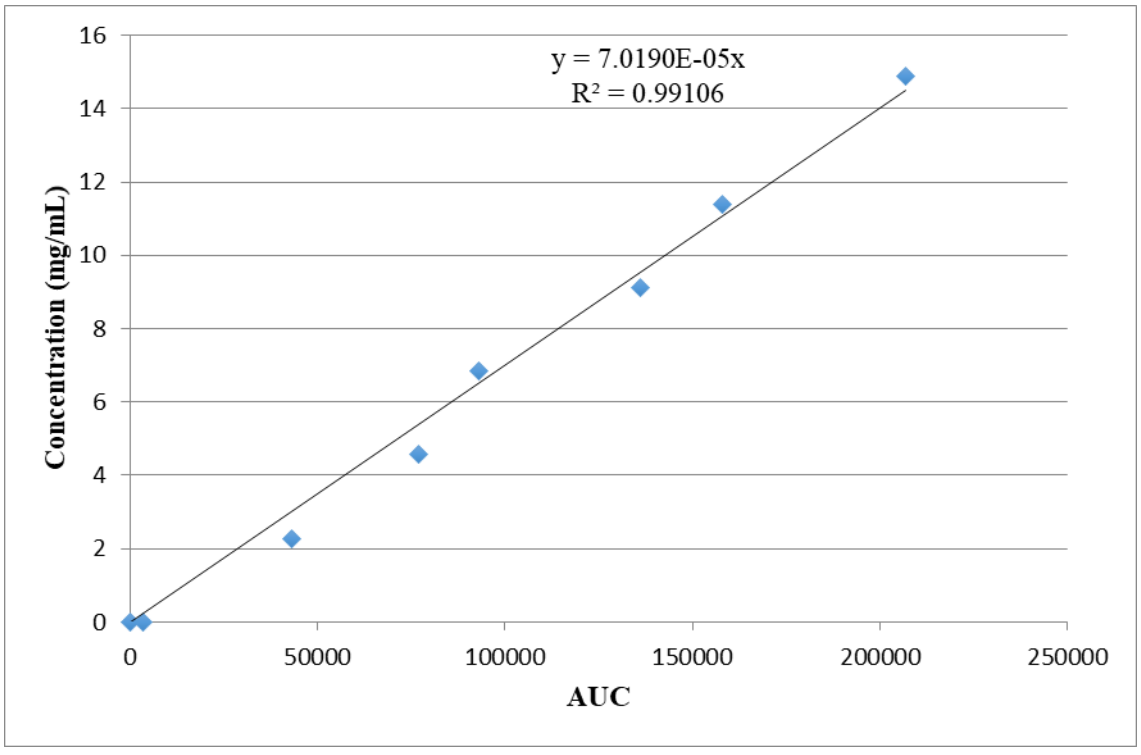

Figure 3. 26. Calibration curve for AUC of TFA in NMR spectrum.

Dynafit was used to fit to the concentration changes with time in order to calculate likely values of k_{cat}/K_m and K_m. The results are summarized in Table 3.2. The kinetic parameters obtained support that novel predicted TY-26 is the most suitable substrate for MMP-9 following real time monitoring using *F NMR. It was cleaved and metabolized by the active MMP-9 faster than a literature reported best MMP-9 substrate TY-10. Real time monitoring of enzyme reaction can be observed in the Figure 3.27 and shows TY-26 peptide undergoing enzymatic metabolism in the presence of MMP-9 using *F NMR.

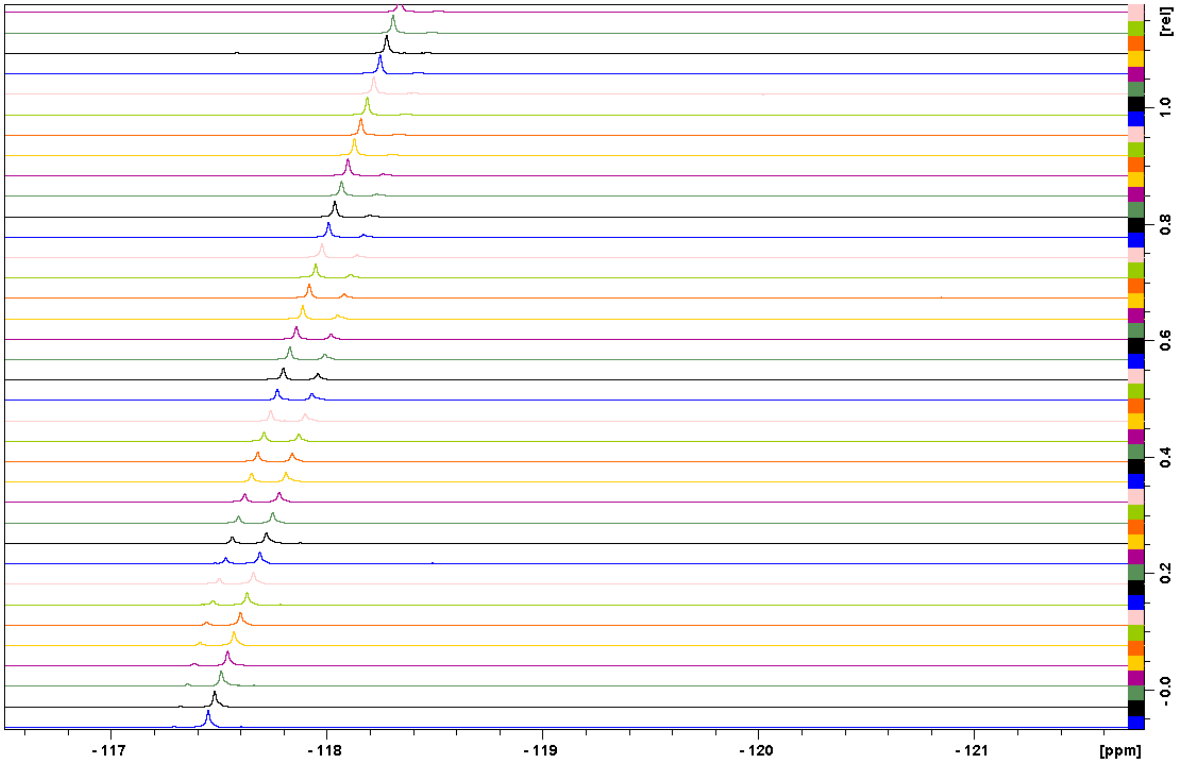

Figure 3. 27. NMR spectrum for TY-26 (GGPIPLAI*FG) in the presence of activated MMP-9 for 15 h. At 0 min, there is only one peak visible in the spectrum (blue) highlighting the intact peptide. Each spectrum corresponds to 20 min. Over time, the reactant peak is decreasing whereas the products peak is increasing.

Table 3. 2. Predicated peptide sequences with Y-score before and after $^{*}F$ and calculated k_{cat}/K_m.

Peptide	Sequence	Y-score	Y-score after $^{*}F$	k_{cat}/K_m ($M^{-1}s^{-1}$)
TY-6	PLG-L*FGAQ	2.33	2.01	3.05 x 10^{00}
TY-9	PLG-LWG*FQ	2.07	2.03	1.39 x 10^{01}
TY-10	WGPIA-LAG*FG	2.20	2.69	9.65 x 10^{00}
TY-19	GGPIG-LAG*FG	1.93	2.48	2.24 x 10^{01}
TY-22	GGPIA-LAG*FG	1.98	2.55	1.05 x 10^{01}
TY-24	GGPWA-LAG*FG	1.76	2.55	1.93 x 10^{01}
TY-26	GGPIP-LAI*FG	2.57	1.99	3.16 x 10^{01}
TY-43	RPLA-LR*FSQ	2.04	2.21	2.24 x 10^{01}

Substitution of different amino acids with fluorinated phenylalanine has changed the Y-scores for some sequences significantly. This can possibly make them more susceptible to enzymatic degradation or vice versa.

Dynafit was used to determine the rate constants such as K_m and k_{cat}. Michaelis-Menten progress method used for the curve fitting (Figure 3.28). The results are summarized in Table 3.3, and k_{cat}/K_m values calculated. A graphical representation of the results is shown in Figure 29.

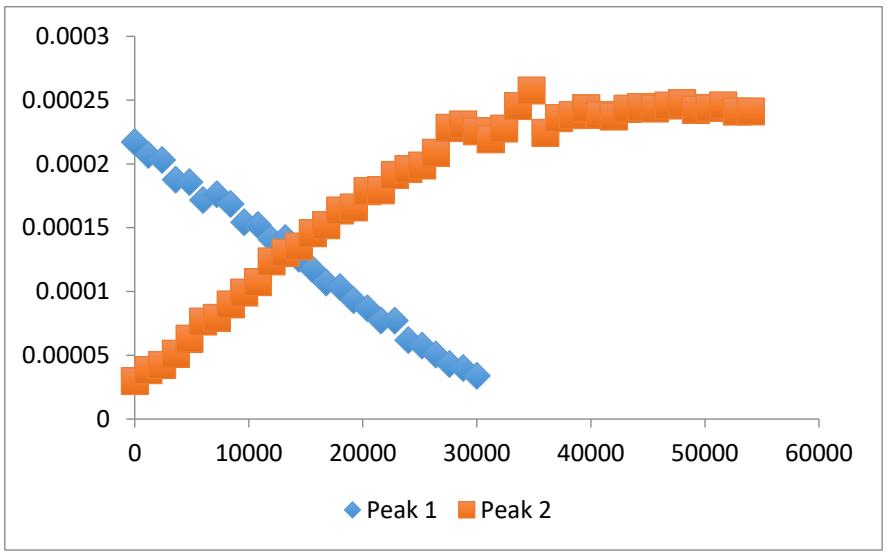

Figure 3. 28. An example after curve fitting by dynafit. Peak 1 is reactant and peak 2 corresponds to product after enzymatic digestion of peak 1.

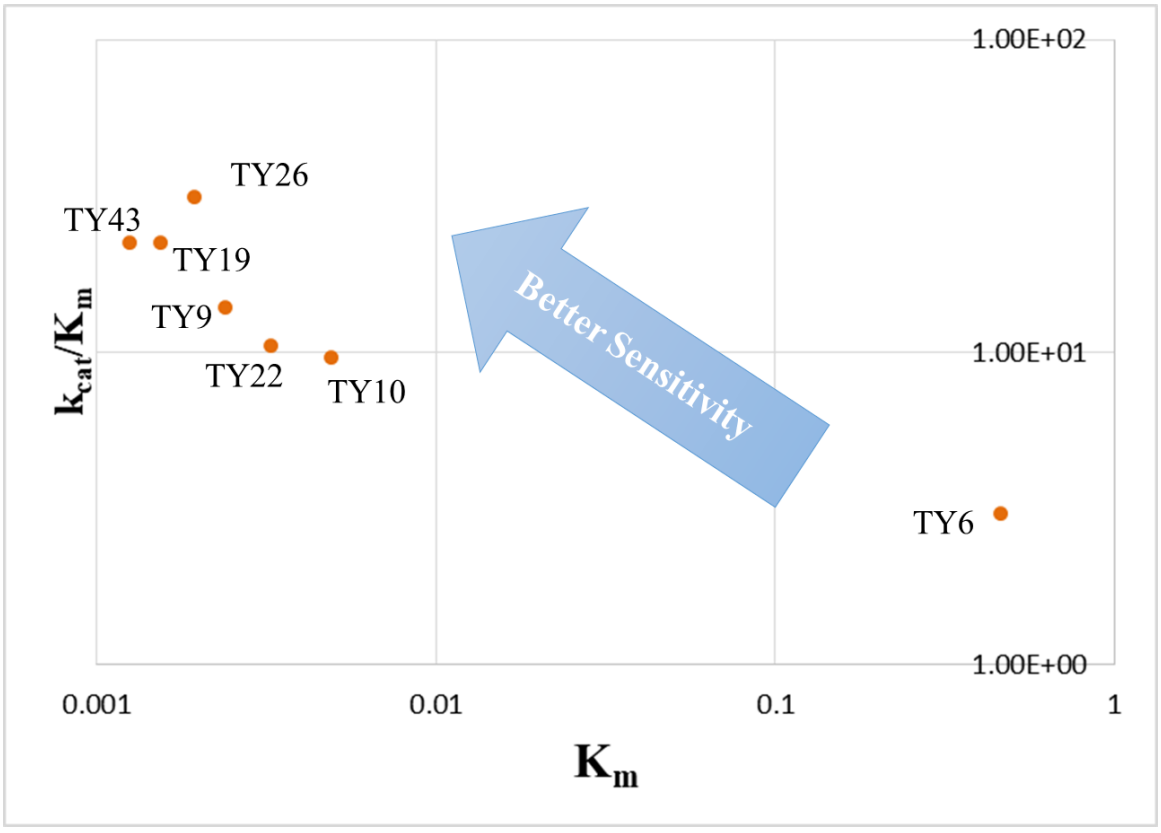

Figure 3. 29. Graphical representation of sensitivity of peptide sequences towards MMP-9.

Table 3. 3. Rate constants calculated from processed NMR data of MMP-9 cleavable peptides in the presence of active MMP-9.

PEPTIDE	Peak	Shift (ppm)	Inc/Dec	K_m (M)	S_0	k_{cat} (s^{-1})
TY6	1	-116.7236	Dec	4.8×10^{-05}	1.6×10^{-05}	1.63×10^{0}
TY6	2	-116.7942	Inc	3.3×10^{-05}	2.1×10^{-05}	1.19×10^{0}
TY6	3	-117.8711	Dec	6.8×10^{-08}	9.8×10^{-07}	2.11×10^{-02}
TY9	1	-117.2128	Inc	2.5×10^{-07}	1.2×10^{-06}	3.75×10^{-02}
TY9	2	-117.1731	Dec	1.7×10^{-07}	1.1×10^{-06}	2.89×10^{-02}
TY10	1	-117.3666	Inc	4.3×10^{-07}	3.7×10^{-07}	4.73×10^{-02}
TY19	1	-117.3781	Inc	1.3×10^{-05}	3.7×10^{-07}	3.12×10^{-02}
TY19	2	-117.3622	Dec	1.4×10^{-07}	8.6×10^{-07}	3.78×10^{-02}
TY19	3	-117.2828	Inc	7.6×10^{-06}	1.3×10^{-06}	7.60×10^{-01}
TY22	1	-117.3672	Inc	1.1×10^{-07}	2.3×10^{-06}	2.20×10^{-02}
TY22	2	-117.3495	Dec	4.6×10^{-07}	1.2×10^{-06}	4.60×10^{-02}
TY24	1	-117.3678	Inc	5.6×10^{-02}	1.6×10^{-06}	1.23×10^{4}
TY26	1	-117.4502	Dec	1.7×10^{-07}	2.4×10^{-06}	6.12×10^{-02}
TY26	2	-117.2873	Inc	5.1×10^{-07}	2.3×10^{-06}	9.69×10^{-02}
TY43	1	-117.2054	Inc	1.2×10^{-07}	1.2×10^{-06}	3.12×10^{-02}
TY43	2	-117.1633	Dec	1.0×10^{-07}	1.1×10^{-06}	2.50×10^{-02}

3.4. Conclusion

In summary, we used state of the art computational modelling tools to predict substrates for MMP-9 with higher sensitivity/cleavability. We utilized NNAAIndex descriptors to build QSAR models leading to a consensus value, the Y-score. Peptide sequences with higher Y-scores are predicted to be the better substrates for MMP-9. In this study, we introduced the use of fluorine (*F) NMR to study the enzyme kinetics of MMP-9, providing real time monitoring compared to fluorescence-based studies. We supported our findings with auto docking (chapter 2) of the peptide molecules in 25 reported MMP-9 enzyme structures. We found sequences, especially TY-26, that are better than those in previously reported studies. Furthermore, this predicting tool can be used to predict Y-score for the peptide sequences.

CHAPTER – 4 DEVELOPMENT OF NANOPARTICLES

4.1. Introduction

Numerous invasive (intrathecal/intracerebral ventricle route) (68, 489) and non-invasive (such as chemical modification of the drug molecule, physiological transport mechanism, chemical and physical disruption of the BBB and nasal drug delivery) (73) techniques have been employed to treat NDs. Nanotechnology has gained significant attention in the past decade for the delivery of drugs across the BBB (490-493). Polymer (494), liposomes (276), exosomes (328), dendrimers (330), metallic NPs (495) and shuttle peptides (496) have all been explored for brain drug delivery. The physicochemical properties of NPs such as size, surface charge (zeta potential), morphology and composition are important factors deciding the fate of NPs, such as passage across the BBB, biological activity, release profile and biocompatibility (256).

Enzyme-responsive self-assembling polypeptide nano-carriers are a highly promising, fast-growing area of research into drug delivery systems that do not suffer from the shortcomings mentioned in Chapter 1. Peptides generally do not involve the use of harmful chemicals toxic cross-linkers in their self-assembly, and the degradation products are natural amino acids that are usually non-toxic in controlled amounts. Self-assembling peptides provide a platform that makes them ideal for nano-medical applications as they are also non-immunogenic, non-thrombogenic, and biodegradable (497, 498). Self-assembled peptide nanoligand derived from phage display library was used to down regulate the BACE1 without toxicity and inflammation (499).

The specific primary sequence of amino acids is crucial in designing polypeptide nano-carrier systems that effectively cross the BBB and are metabolized by MMP-9. This is to

ensure that designed nano-carriers can reach the brain and carry siRNA; and at the same time can be degraded by suitable brain enzymes to release the siRNA. A schematic of our proposed approach is shown in Figure 4.1.

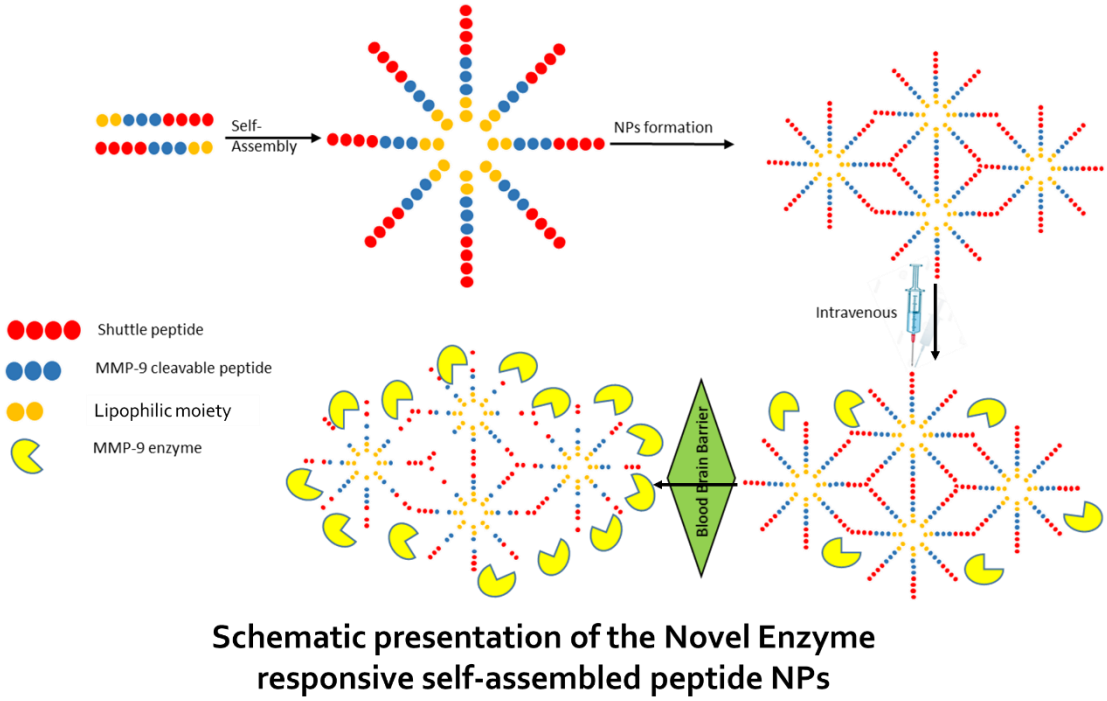

Figure 4. 1. Schematic presentation of the core of the smart biomaterial and mechanism of action of Smart-MMP-9 Responsive drug delivery system.

4.2. Material and Methods

4.2.1. Materials

All L-Fmoc amino acids, Oxyma and ProTide® resin were purchased from CEM. N,N′-diisopropylcarbodiimide (DIC), piperidine, palmitic acid (PA), cholesteryl chloroformate (CHF), trifluoroacetic acid (TFA), triisopropylsilane (TIPS), acetonitrile, formic acid and N,N-diisopropylethylamine (DIPEA) were bought from Sigma-Aldrich®. Dimethylformamide (DMF), 1-(2-pyridylazo)-2-naphthol (PAN) and diethyl ether were purchased from Acros Organics®. 12mm square polystyrene cuvettes (DTS0012) and

DTS1070 disposable cuvettes were purchased from Malvern analytical. Formvar Carbon coated Cu grids were obtained from Agar Scientific Ltd (Stansted, UK).

4.2.2. Methods

4.2.2.1. *Peptide synthesis*

Peptides were synthesized using a CEM Liberty Blue® automated microwave-assisted peptide synthesizer. This employed ProTide resin (147 mg; loading capacity 0.61 mmol/g) and typical Fmoc-deprotection required 20% piperidine in DMF for 90 s at 90°C. DIC (1 M) and Oxyma (1 M) solutions were used as activator and coupling reagents, respectively. Amino acids solutions (0.2 M in DMF) were singly coupled at 90°C, except for Cys, which was coupled at 50°C and Arg, which was double coupled at 75°C. The completed peptide sequence was cleaved from the resin by treatment with 1-2 mL of cleavage cocktail (trifluoroacetic acid: water: triisopropylsilane, 90%: 5%: 5%) for 4 h. The solution was then filtered into cold diethyl ether, which precipitated the peptide. The precipitated peptide was washed with further diethyl ether four times to ensure the complete removal of impurities. Diethyl ether was evaporated by leaving it overnight in the fridge. The peptide was dissolved in water, flash frozen (liquid N_2) and was freeze dried to afford a white powder.

A list of the peptides synthesized is given in Table 4.1. Peptide sequences synthesized can be divided in two parts; one part (N-terminus) of the self-assembled peptide was a literature reported MMP-9 substrate (462), (serving as a standard for further characterization) or a novel experimentally validated MMP-9 sensitive peptide, and the second part (C-terminus) was a shuttle peptide (which have been reported to cross the BBB in numerous studies (138, 500, 501)). Three extra Gly residues were used as a spacer motif on the N-terminus to facilitate the conjugation of the lipophilic groups as reported in the literature (375). Four shuttle peptides were used to find the best combination with better sensitivity to

MMP-9, higher BBB permeability and minimal toxicity to cells. First few peptides synthesized were conjugated with CHF to facilitate the self-assembly by maintaining the hydrophilic-hydrophobic balance (HLB). Later, conjugation of the lipophilic moieties was stopped due to complications of the reaction and time consumption (1-2 weeks). Peptides self-assembled to form nanoparticles themselves, without added lipophilicity, when the appropriate HLB is achieved after the addition of water. Synthesized peptides were freeze dried before further characterization. Briefly, peptides were dissolved in 10-12 mL of deionized water. Liquid nitrogen was used for instant freezing of peptide solutions and the samples were lyophilized affording the corresponding peptides as a white/yellow powder (Heto 2.5 FD, UK).

4.2.2.2. *Characterization of peptide by LC-MS*

All of the peptides synthesized were characterised by using high-resolution (accurate) mass spectrometry. Samples were analysed using an Agilent 1260 Infinity II LC system with Agilent 6530 Accurate-Mass QToF spectrometer, using an Agilent ZORBAX Eclipse Plus C18 Rapid Resolution HD analytical column (1.8 µm particle size, 2.1 × 50 mm) with binary eluent system comprising MeOH / H_2O (12 min gradient: 1-99% with 0.1% formic acid) as mobile phase. Operating pressures were in the range of 2000-3000 PSI. Electrospray ionisation mass spectrometry was conducted in positive ion mode (*m/z* range: 50 – 3200) using a fragmentor voltage of 150 V, gas temperature of 325 °C (flow 10 L/min) and sheath gas temperature of 400 °C (flow 11 L/min). Reference ions were purine (121.0509) and hexakis (1H, 1H, and 3H-tetrafluoropropoxy) phosphazine (922.0098) (API-TOF Reference Mass Solution Kit, Agilent). Exact mass measurements of the products were based on the protonated molecules $[M+H]^+$ and were detected as sodiated adducts $[M+Na]^+$.

4.2.2.3. *Conjugation of CHF/PA to Peptides*

Conjugation of CHF to the on-resin synthesised peptide was commenced as reported previously (16). Briefly, ProTide resin-bound peptide (1 eq. based on loading capacity 0.61 mmol/g) was added to a solution containing CHF (2 eq.) and DIPEA (4 eq.) in DMF (4 mL), which was shaken at 40 ºC for 24 h (16). The Kaiser test was performed to assess the completeness of conjugation and the process was repeated until coupling was judged to be complete by the absence of a blue/purple colour. The amphiphilic peptide was cleaved from the resin using a cleavage cocktail [5 mL; comprising TFA, TIPS and water (9 : 0.5 : 0.5 *v*/*v*)] with regular shaking at room temperature for 4 h. The solution was then filtered into ice cold diethyl ether followed by centrifugation. The precipitated amphiphilic peptide was repeatedly re-suspended in diethyl ether with subsequent centrifugation for three times. Diethyl ether was evaporated by leaving it overnight in the fridge. Amphiphilic peptides were dispersed in water, flash frozen in liquid nitrogen and freeze dried, removing excess volatiles, to obtain the conjugated peptide (TFA salt) as powder. No further steps were taken to cyclise the cysteine amino acids in the peptides or purify the conjugated peptides.

For Kaiser Test fresh reagents were prepared. Briefly, for reagent 1, 500mg of Ninhydrin (Acros Organics) was dissolved in 10 mL of Ethanol. For reagent 2, 40gm of phenol (Fischer Scientific) crystals were dissolved in 10mL of Ethanol. Small amount of the resin was placed in Eppendorf tubes separately. Five drops of reagent 1 and 2 were added and heated for 5 minutes at 100ºC. Color changes were observed to confirm the complete conjugation.

4.2.2.4. *Nanoparticle Formation*

Peptide nanoparticles were formed by self-assembly. Briefly, peptide (3mg) was weighed into an Eppendorf tube. Ultrapure de-ionised water was added to Eppendorf tube to facilitate the self-assembly. Peptide was dissolved/dispersed readily without sonication or mixing.

Self-assembly is believed to be dependent on the upon the hydrophile/lipophile balance (HLB).

4.2.2.5. *Dynamic Light Scattering (DLS)*

Particle size and zeta potential were measured by using a Malvern Zetasizer Nano ZS® (Malvern, Worcestershire, UK) containing a HeNe laser source (l ¼ 632.8 nm, 22 mW output power). Cuvettes used were DTS0012 from Malvern. Peptides were dissolved in water (2.5 mg/mL) and sizes were measured with a delay time of two minutes. Sample was stabilized for 120 s before measurement. For zeta potential measurements, specialized DTS1070 cuvettes were used. The refractive index of 1.3 and viscosity of 0.9 cP were used for water. Three readings were performed for each peptide. All measurements were carried out in triplicates, means and standard deviations (SD) were also calculated.

4.2.2.6. *Scanning / Transmission Electron Microscopy (S/TEM)*

Self-assembled peptide nano-carriers were visualized and characterized morphologically by FEI Morgagni transmission electron microscopy. Carbon filmed copper grids were used. 2.5 mg/mL peptide solution was prepared in distilled water. A small droplet of the peptide solution was placed on the grid and left for drying in a fume cupboard. Sample was analyzed in TEM after drying. Peptide (2.5 mg/mL) micelles were observed by using the FEI Inspect S (Oxford-instruments) at an accelerating voltage of 100 kV. No staining (negative or positive) was used. Sample (TYR-3_CHF) was visualized by scanning electron microscopy (FEI Quanta 200). The particle size was not measured by TEM, it was only assessed by scale bar.

4.2.2.7. *Critical Micelle Concentration (CMC) determination*

CMCs were determined by using a Genesys® 6 UV/Vis spectrophotometer. 20mL volume of peptide solution was prepared at 0.5 mg/mL. Peptide solution was serially diluted from 0.01 – 0.3 mg/mL solution with saline (0.9 %) solution in volumetric flasks. The peptide

solutions were shaken around 20 times to ensure peptide and saline solution is thoroughly mixed. PAN is used as probe and dissolved in pentane at the final concentration of 1.6 mM. PAN is a water-insoluble organic dye which exhibits low solution absorption below CMC, by not dissolving in the aqueous surfactant solution. 500µL of PAN solution was added into each volumetric flask containing peptide solution. Samples were left for 30 min for the evaporation of pentane in the fume cupboard. After complete removal of pentane, UV absorbance was measured.

The CMC was also measured by fluorescence. Firstly, a pyrene solution was prepared in acetone at a concentration of 6.16×10^{-7} M. Next, volumetric flasks were each filled with 20 mL of the pyrene solution and placed in a water bath at 80°C to allow rapid evaporation of the acetone and deposition of pyrene. A stock solution of peptide was then prepared at a known concentration. Once acetone had been evaporated, pyrene flasks were removed from the water bath and again peptide solutions were prepared at a range of concentrations directly in the pyrene flasks. The solutions were shaken thoroughly. The samples were then equilibrated for 24 h at 35°C in an oven. Following 24 h of equilibration, the samples were removed from the oven and taken to the fluorescence spectrometer to be analyzed. The intensity of each solution was recorded (I335 and I320) and the results were plotted onto a graph and the inflection point was extracted as the CMC.

4.3. Results and Discussion

In this project, we selected a range of peptides [(sRVG, CDIFTNSRGKRA) (138), (Apo E, LRKLRKRLLR) (500), (miniAp-3, CKAPETALC) (501)] and T7 (HAIYPRH) (209-212) based on the BBB targeting capacity, including specific modifications that were expected to enhance the binding with negatively charged cell membranes, exhibit sensitivity to MMP-9

and facilitate self-assembly (502). LCMS was performed to confirm the peptide molecular mass as shown in Figures 4.2 – 4.4 (Example LCMS chromatograms are shown here, and remaining chromatograms can be found in the appendix). From the LCMS chromatograms, it was observed that peptides synthesized exhibited the suitable purity and the peptides were used as crude for further characterization.

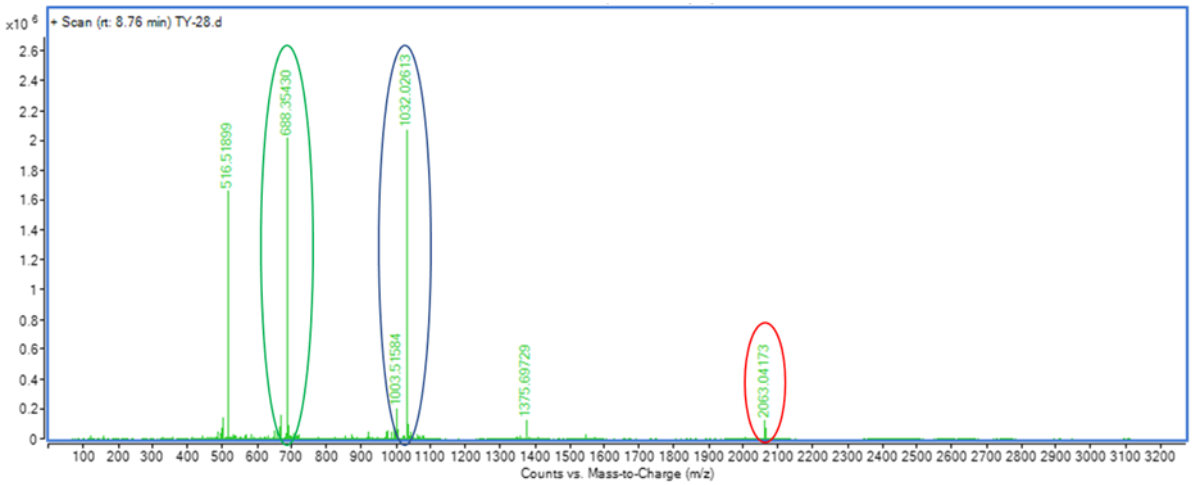

Figure 4. 2. LCMS chromatogram of TY-28 (GGGWGPIACDIFTNSRGKRA) showing the masses of 1032.02613(encircled blue, $[M+2H]^{2+}$), 688.35430 (encircled green, $[M+2H]^{3+}$) and 2063.04173 (encircled red, $[M+2H]^{+}$) with retention time of 8.75 minutes.

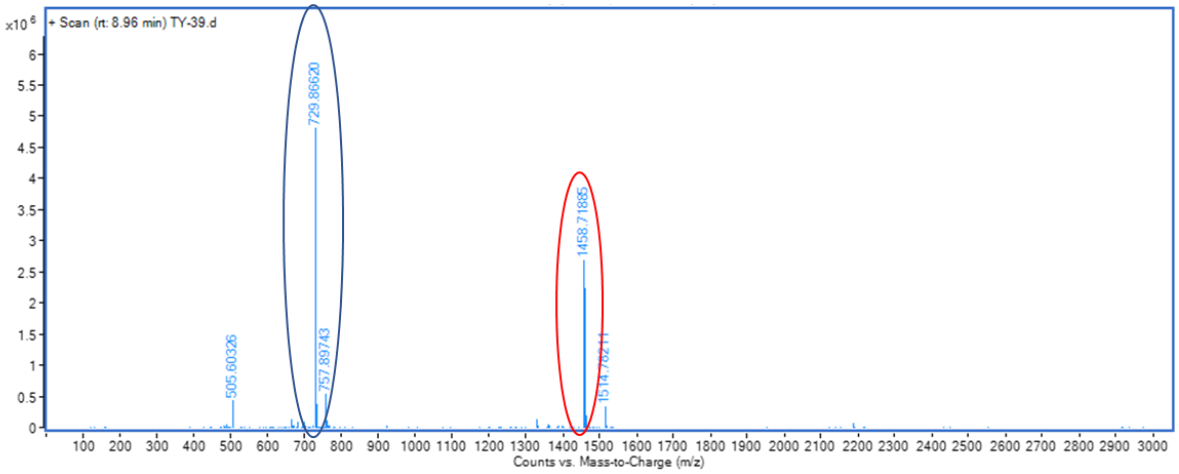

Figure 4. 3. LCMS chromatogram of TY-39 (WGPIACKAPETALC) showing the masses of 729.86620 (encircled blue, $[M+2H]^{2+}$), and 1458.71885 (encircled red, $[M+2H]^{+}$) with retention time of 8.96 minutes.

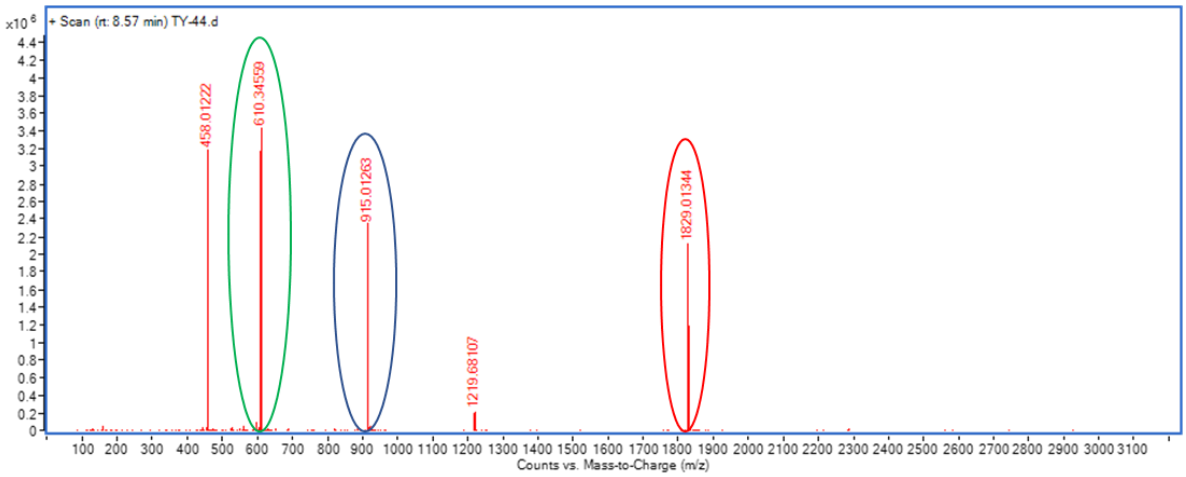

Figure 4. 4. LCMS chromatogram of TY-44 (WGPIALAGIGHAIYPRH) showing the masses of 915.012263 (encircled blue, $[M+2H]^{2+}$), 610.34559 (encircled green, $[M+2H]^{3+}$) and 1829.01344 (encircled red, $[M+2H]^{+}$)with retention time of 8.58 minutes.

Table 4. 1. List of the enzyme-responsive self-assembled peptide nanoparticles synthesized using the CEM Liberty blue synthesizer. The part of the sequence responsible for MMP-9 sensitivity is shown in black and the brain targeting ligand is highlighted in red.

Name	Peptide Sequence	Molecular Weight before Conjugation	Molecular Weight after Conjugation
TY-1	CDIFTNSRGKRA	1366.68	1366.68
TY-2	KGPRQITACDIFTNSRGKRA	2218.18	2218.18
TYR-3_CHF	C_{27}-GGGRPLGLWCDIFTNSRGKRA	2260.16	2672.77
TYR-3_PA	C_{16}-GGGRPLGLWCDIFTNSRGKRA	2260.16	2496.57
TY-7_CHF	C_{27}-WGPIALRKLR	1208.75	1621.36
TY-8_CHF	C_{27}-GGGWGPIALRKLR	1379.81	1793.20
TY-12_CHF	C_{27}-GGGWCKAPETALC	1291.57	1704.18
TY-13_CHF	C_{27}-GGGCKAPETALC	1105.49	1518.1
TY-16	LLLLLCKAPETALC	1499.85	1499.85
TY-18	LLLCKAPETALC	1273.68	1273.68
TY-20_CHF	C_{27}-GGGWGPIALRKLRKRLLR	2046.28	2458.89
TY-28	GGGWGPIACDIFTNSRGKRA	2062.02	2062.02

TY-29	GGGWGPIACKAPETALC	1629.76	1629.76
TY-32	GGPIPLAIFGCDIFTNSRGKRA	2289.21	2289.21
TY-35	WGPIAHAIYPRH	1416.74	1416.74
TY-37	PIPLAIFCKAPETALC	1685.89	1685.89
TY-38	PIPLAHAIYPRH	1383.78	1383.78
TY-39	WGPIACKAPETALC	1458.7	1458.7
TY-41_CHF	GGGCDIFTNSRGKRA	1537.74	1950.35
TY-42	GGPIAAAGFGCDIFTNSRGKRA	2165.08	2165.08
TY-44	WGPIALAGIGHAIYPRH	1829.11	1829.11

The morphology of NPs affects their bio-distribution and cellular uptake. NPs could be spherical, cubic, tubular or rod-like in shape (368, 369). A majority of the particles reported for brain delivery are roughly spherical in shape. Zeta potential or surface charge of NPs is another factor that controls the diffusion across the BBB. It has been reported that a high (positive) zeta potential causes toxicity to the BBB (370, 371). Rassu et al. reported that a positive surface charge on NPs ensures their mucoadhesion (372). To assess the morphology and particle size of NPs, solutions/suspensions (2.5 mg/mL) were prepared. Interestingly, peptide powder dissolved instantly with the addition of water giving a clear solution-like appearance except for TYR-3_CHF, which exhibited a cloudy suspension upon sonication. The samples were subjected to DLS and particle size and zeta potential were measured, and the results are shown in Figures 4.5 – 4.6 (only selected examples of DLS chromatograms are shown here, remaining data can be found in the appendix). Particle sizes and zeta potential for all enzyme-responsive self-assembled peptide nanoparticles are summarized in Table 4.2. NPs were formed without CHF/PA due to sufficient hydrophobicity provided by MMP-9 cleavable sequences that facilitate the self-assembly.

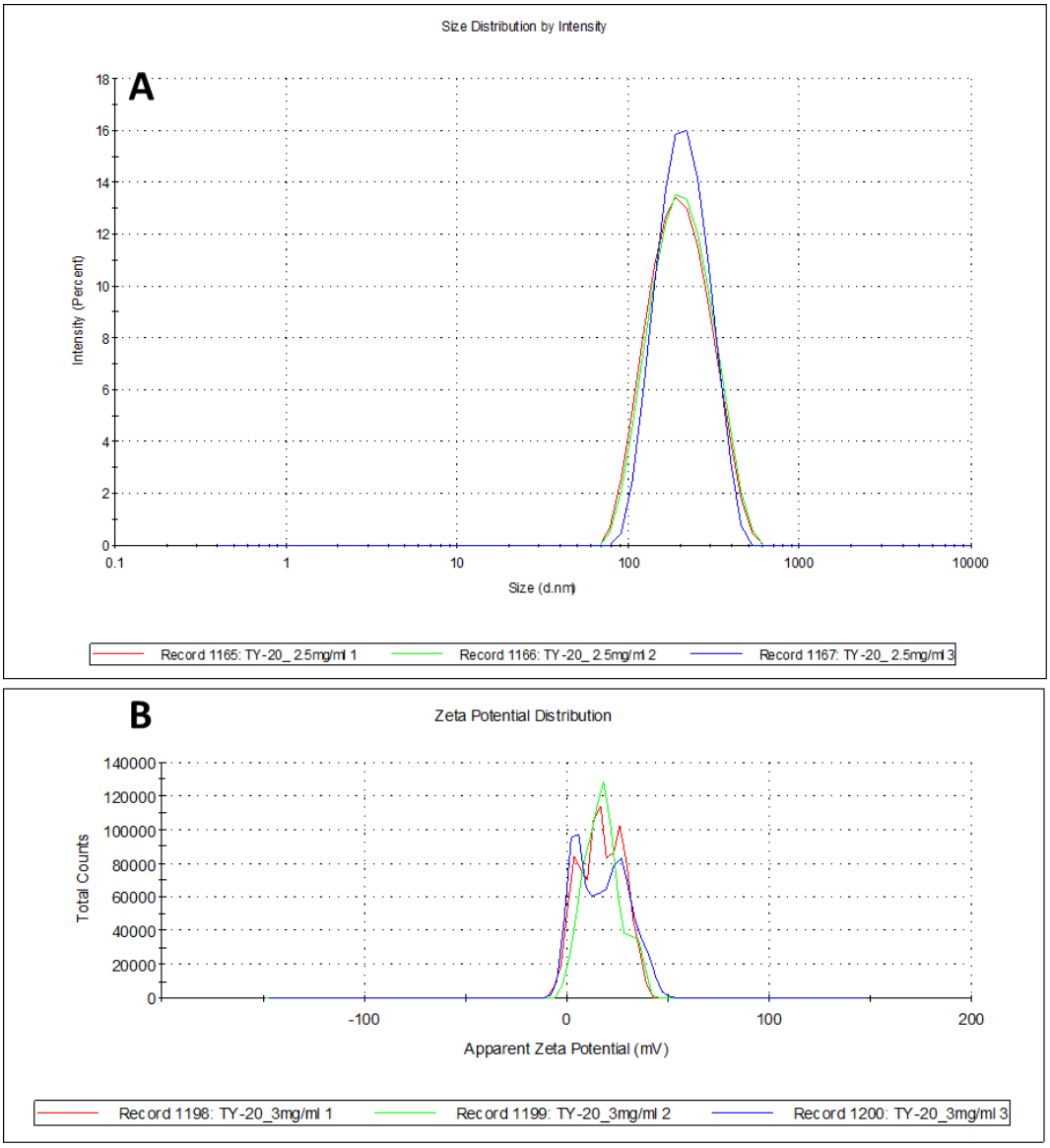

Figure 4. 5. DLS chromatograms for TY-20_CHF (GGGWGPIALRKLRKRLLR) at 2.5 mg/mL in distilled water. A) Particle size graph for TY-20_CHF showing NPs size of 166.2 ± 62.76 nm with Pdi of 0.197, ***B)*** *Zeta potential graph for TY-20_CHF showing the surface charge of 16.5 ± 2.89.*

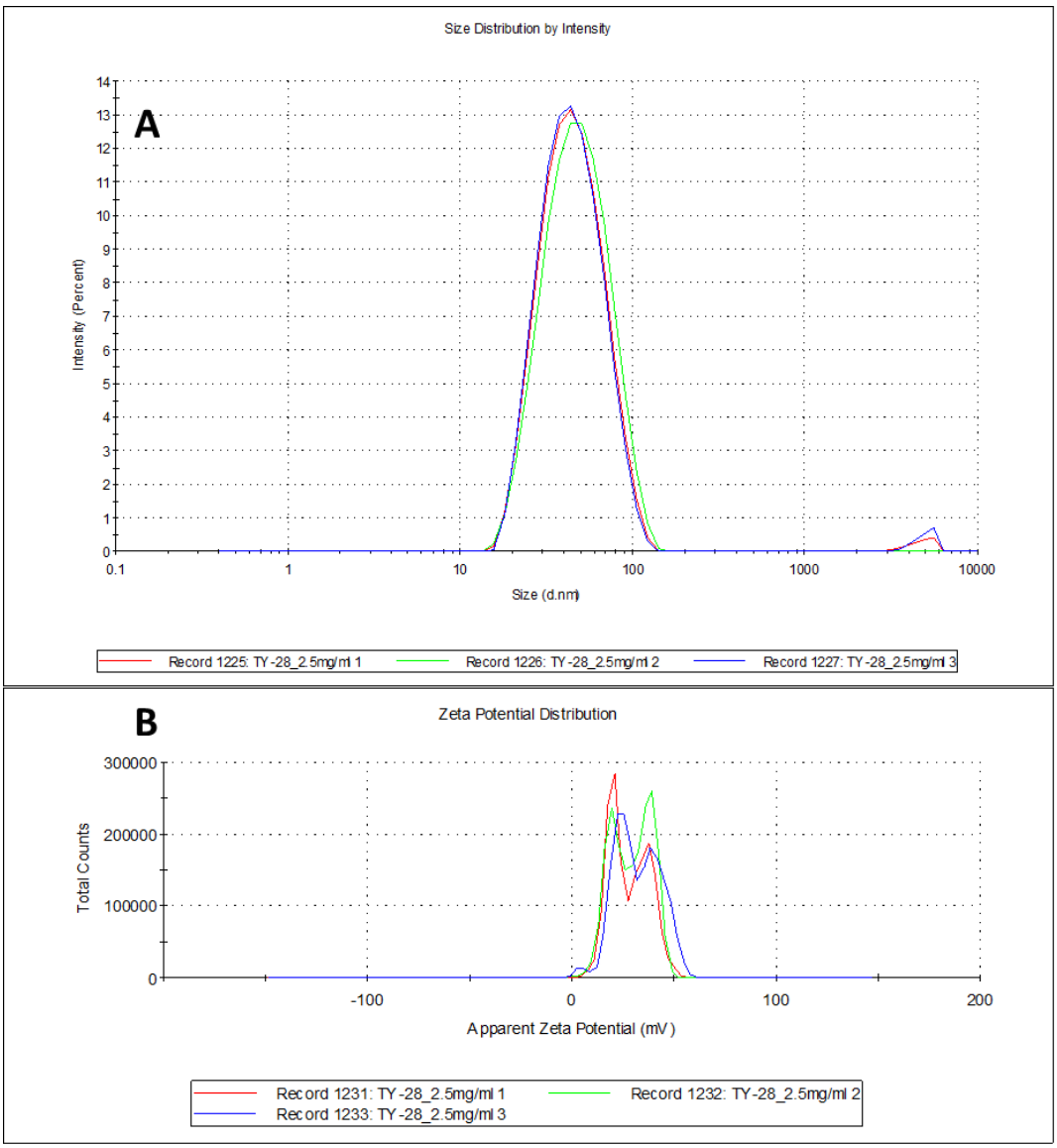

Figure 4. 6. DLS chromatograms for TY-28 (GGGWGPIACDIFTNSRGKRA) at 2.5 mg/mL in distilled water. A) Particle size graph for TY-28 showing NPs size of 41.66± 19.12 nm with Pdi of 0.189, B) Zeta potential graph for TY-28 showing the surface charge of 31.90 ± 5.08.

Table 4. 2. Summary of particle size and zeta potential of self-assembled NPs (n=3)

Formulation	Size (nm)	Charge (mV)	Pdi	CMC (mg/L)
TYR-3_CHF	**726.03 ± 18.16**	**25.43 ± 0.33**	**0.385**	**7, 50**
TYR-3_P.A	**72.60 ± 1.62**	**34.5 ± 4.36**	**0.426**	**75**
TY-7_CHF	**111.66± 12.39**	**2.96 ± 6.18**	**0.223**	**100**
TY-8_CHF	**32.89 ± 17.17**	**22.9 ± 5.39**	**0.565**	**80**
TY-12_CHF	**2796 ± 739.5**	**38.68 ± 2.14**	**0.986**	**15**
TY-13_CHF	**81.4 ± 7.65**	**36.53 ± 1.37**	**0.429**	**40**
TY-18	**1527.05 ± 43.13**	**24.5 ± 5.59**	**0.958**	**N/A**
TY-20_CHF	**166.2 ± 62.76**	**16.5 ± 2.89**	**0.197**	**95**
TY-28	**41.66 ± 19.12**	**31.90 ± 5.08**	**0.189**	**74**
TY-29	**1207.33 ± 42.82**	**48.61± 3.99**	**0.658**	**N/A**
TY-32	**48.30 ± 18.61**	**31.10 ± 4.95**	**0.467**	**78**
TY-35	**439.61 ± 29.16**	**17.53 ± 1.40**	**0.414**	**110**
TY-37	**108.51 ± 17.84**	**23.8 ± 2.63**	**0.654**	**86**
TY-38	**536.80 ± 120.82**	**15.6 ± 6.76**	**0.704**	**98**
TY-39	**473.2 ± 97.25**	**37.4 ± 5.70**	**0.461**	**88**
TY-41_CHF	**293.7 ± 21.75**	**26.45 ± 6.72**	**0.625**	**82**
TY-42	**2078.33 ± 325.99**	**24.5 ± 4.43**	**0.895**	**N/A**
TY-44	**266.9 ± 22.43**	**27.40 ± 4.97**	**0.408**	**91**

DLS analysis revealed that particles were of different sizes ranging from 41.66 nm - 2796 nm with zeta potential of 2-40 mV. The NPs formulations which exhibited larger particle sizes were not dissolved readily and cloudy appearance was observed. The particle sizes are

in the same range as those in the literature in various studies 10-207 nm (268-271, 503). Studies suggest that NCs should have sizes in the range of 10-24 nm to cross the glia limitans and penetrate the brain parenchyma following crossing the BBB or after intrathecal injection. It should be added that larger NPs may manage to cross the glia limitans, if the surface of the NPs is decorated with appropriate targeting ligands. For example, as explained above, albumin NPs decorated with ApoE entered neurons following i.v. injection into mice (504). It has been reported that a high (positive) zeta potential causes toxicity to the BBB (370, 371). Fatouros et al. reported the lipid like self-assembling peptide nano-vesicles of 126/169 nm for delivery hydrophilic and hydrophobic compounds (505). Bovine Serum Albumin NPs with LMWP cell penetrating peptide (BSA-LMWP-NPs) of less than 200 nm in size showed excellent *in vivo* experiments (262). In another study, functionalized solid lipid NPs with apolipoprotein E (SLN-DSPE-ApoE-NPs) of less than 200 nm have been reported to 1.5 fold enhanced permeability compared to non-functionalized SLNs (261). Angiopep conjugated with poly(ethylene glycol)-co-poly(ε-caprolactone): ANG-PEG– poly(ε-caprolactone) NPs with particle size of less than 100 nm have been reported to permeating in the mice brain by targeting the LDLR (264). Some of our formulations (especially TY-28 and TY32) were below 50 nm in size. Similarly, the surface charge for brain penetrating nanoparticles have been reported to span a diverse range. Kanazawa et al. reported PEG-poly(ε-caprolactone)-CH2R4H2C/stearate- CH2R4H2C nanoparticles of 15-20 mV for brain drug delivery (506). g7- PLGA-NPs with the particle size of 155±26 nm and surface charge of 15±5.6 mV has been employed for brain drug delivery (268, 269). Wu et al. reported the use of nano ligand carriers (NLCs) with a zeta potential of 1.55 – 37.8 mV for BACE-1 silencing (499). Our novel enzyme- responsive self-assembled peptide nanoparticles exhibited the same characteristics in terms of particle size (41.66 – 2796 nm) and surface charge of 2.96 – 48

mV. It was observed that changing lipophilic moiety from CHF to PA led to significantly (from 726 nm to 72) nm reduced particle size. It was also observed that by adding more positively charged amino acids lead to higher surface zeta potential.

It has been reported that NPs ranging from 10 -207 nm were able to deliver the payload across the endothelial monolayer (266, 268-272). In this project, NPs used for *in vitro* and *in vivo* work of 41 – 200nm except TY-39 and TY-44. It could be possible that larger the particles size, lower the chances of transmigration across the endothelial monolayer. Surface charge/zeta potential has been reported to influence the ability of NPs to transmigrate the endothelial monolayer. It has been reported that high positive charge is linked to cytotoxicity (370, 371). On the other hand, positive charge has been linked to enhanced muco-adhesion due to electrostatic interaction on the negatively charged cellular membrane. Our NPs were positively charged (3 – 48mV) could possibly enhance transmigration across the endothelial monolayer by adhering to negatively charged cell membrane.

Although DLS data suggest that particles size goes above 200 nm, when TEM was performed, the particle size was found to be less than 200nm. The reason for the difference in size by both techniques is due to presence of solvent molecules that interact with the particles via various non-covalent interaction types (such as hydrogen bonding and van der Waals forces and aggregation) in the DLS. It measures hydrodynamic particle size, (507) whereas in TEM, particle size is measured in a dry state so no interaction with solvent molecules is present and a smaller proportion of sample is measured or observed (508). TEM measures particle size, on the other hand DLS is based on intensity. DLS can identify larger particles easily compared to small particles (509). In DLS, due to the presence of solvent, particles can easily agglomerate giving a false impression of larger particles, which can be seen Figure 4.7a and c (510). It can be due the multiple NPs present in close proximity to

each other gave a false impression of being a single particle. For morphology, SEM/TEM was performed. Unstained self-assembled peptide NPs were visualized by SEM/TEM. Most of the self-assembled NPs were found to be spherical except TY-35 (elongated in shape) as shown in Figure 4.7 and Figure 4.7a (SEM). TEM revealed that particle size of TY-13_CHF (4.7e) is much smaller than it was reported in DLS data as shown scale bar measurement. This is due to possible agglomeration of NPs in the presence of water. Zeta potential of proteins is a significant physical property that could affect their state aggregation and behavior (511). It has been reported that higher the zeta potential lower the tendency to form aggregates. The point at which the zeta potential is closer to zero is known as the isoelectric point (IEP). At this point electrostatic repulsion is minimised and Van der Waals forces facilitate agglomeration (511). As mentioned in methodology, CHF was replaced with PA. It was observed that conjugation of CHF to the peptide was complex and time-consuming process. Larger particle size was observed after successful conjugation of CHF to the peptide. For example, TYR-3_CHF, the particle size was around 726 nm, whereas TYR-3_PA exhibited around 72 nm.

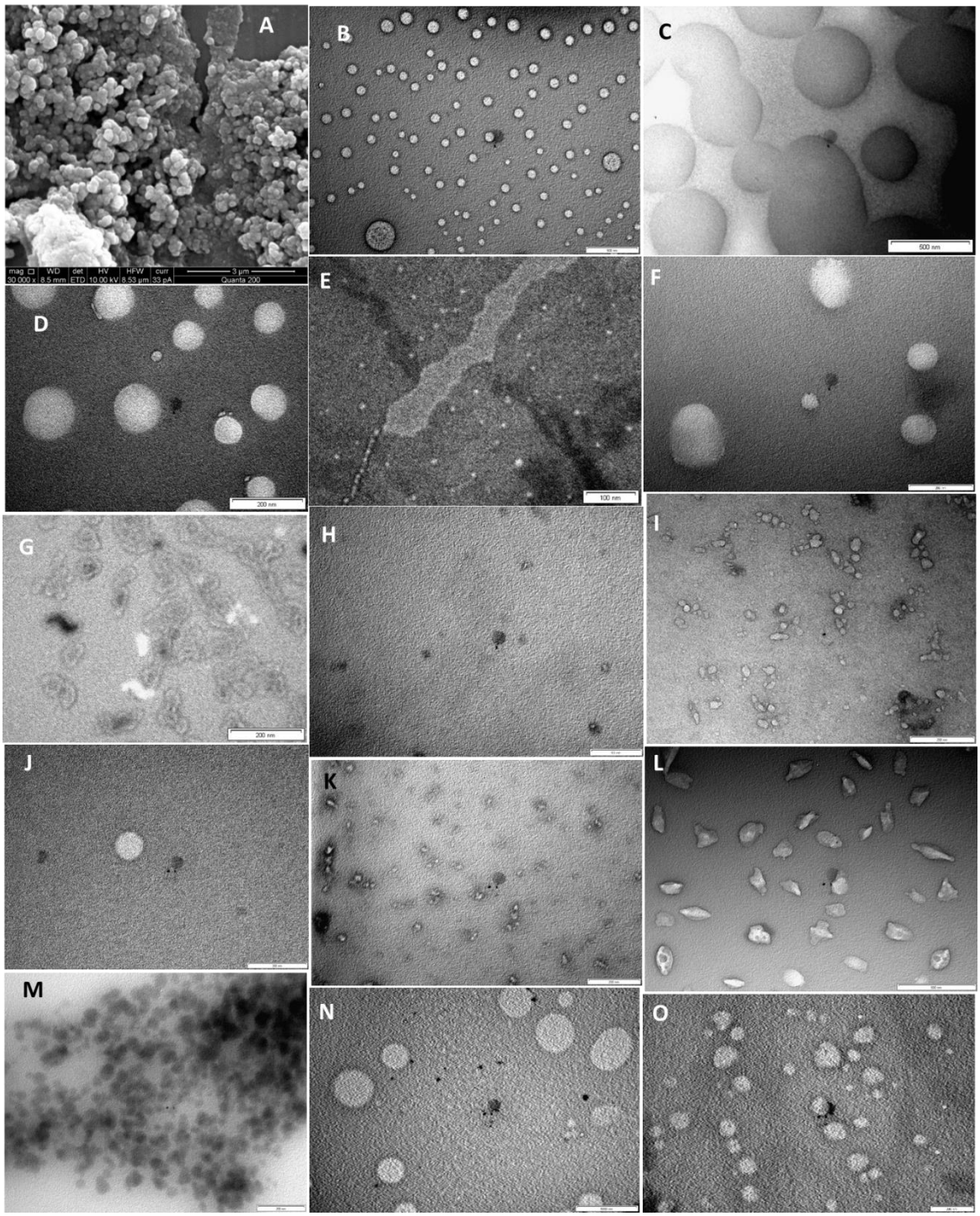

Figure 4. 7. Morphological studies of unstained self-assembled peptide NPs at a concentration of 2.5mg/mL on carbon coated grid. ***A)*** *SEM image of TYR-3_CHF,* ***B)*** *TEM image of TYR-3_PA,* ***C)*** *TY-7,* ***D)*** *TY-8,* ***E)*** *TY-13_CHF,* ***F)*** *TY-20_CHF* ***G)*** *TY-12_CHF,* ***H)*** *TY-20_PA and* ***I)*** *TY-28* ***J)****TY-29,* ***K)*** *TY-32,* ***L)*** *TY-35,* ***M)*** *TY-37,* ***N)*** *TY-39* ***O****) TY-41*

The self-assembly of these peptide NPs is based on the CMC. Self-assembled peptide NPs rearrange themselves at concentrations greater than the CMC to form NPs (375). The CMC of all the peptide formulations were determined and are summarized in Table 4.2. Two different techniques were used to determine the CMC, PAN (512) and pyrene (513). The CMC for all self-assembled NPs were found to be between 7-110 mg/L. CMC graphs are shown in Figures 4.8 – 4.10 (remaining CMC graphs are provided in the appendix). The CMCs for all the formulations were closer to the reported CMC of antimicrobial peptides of 36.1 mg/L (375) except for TYR-3_CHF. TYR-3_CHF exhibited two CMC concentrations for unknown reasons (one possible explanation could be: two tier self-assembly, firstly, few molecules arrange themselves in to smaller structures and secondly, formation of larger assemblies) as shown in Figure 4.8. Fan et al. reported a CMC of P45 peptide NPs 1.25 mM which is almost closer to that for our formulations (503).

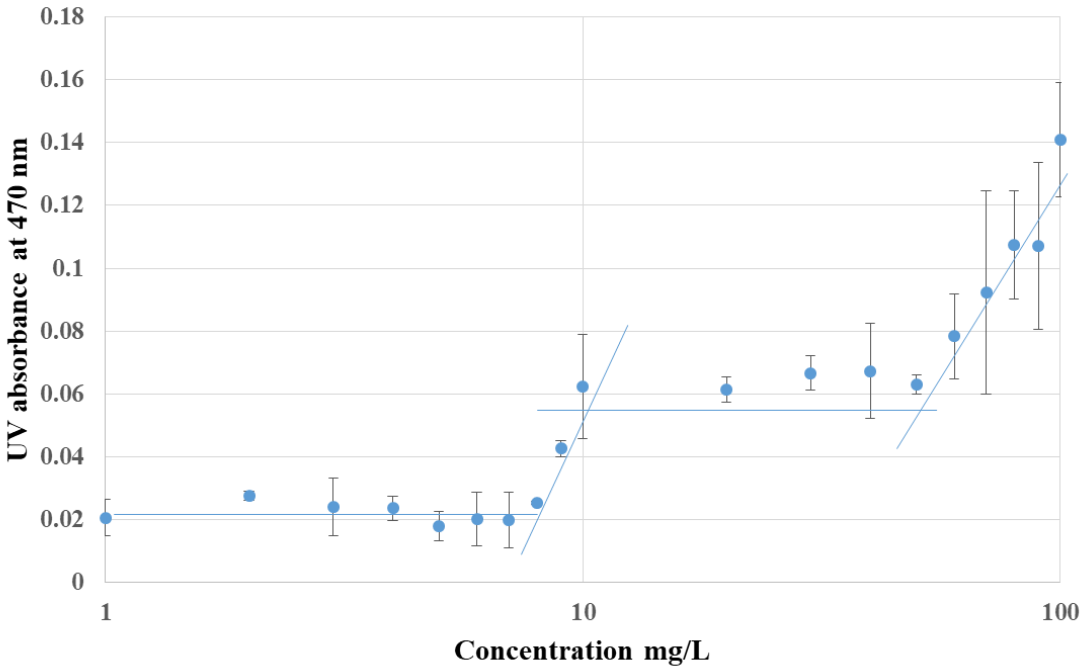

Figure 4. 8. CMC plot for TYR-3_CHF (GGGRPLGLWCDIFTNSRGKRA) in saline solution. In the plot, two different CMC can be observed for unknown reason. It could be possible that this NPs exhibits dual characteristics, first CMC value could be due to small NPs and second CMC value could be due vesicles formation.

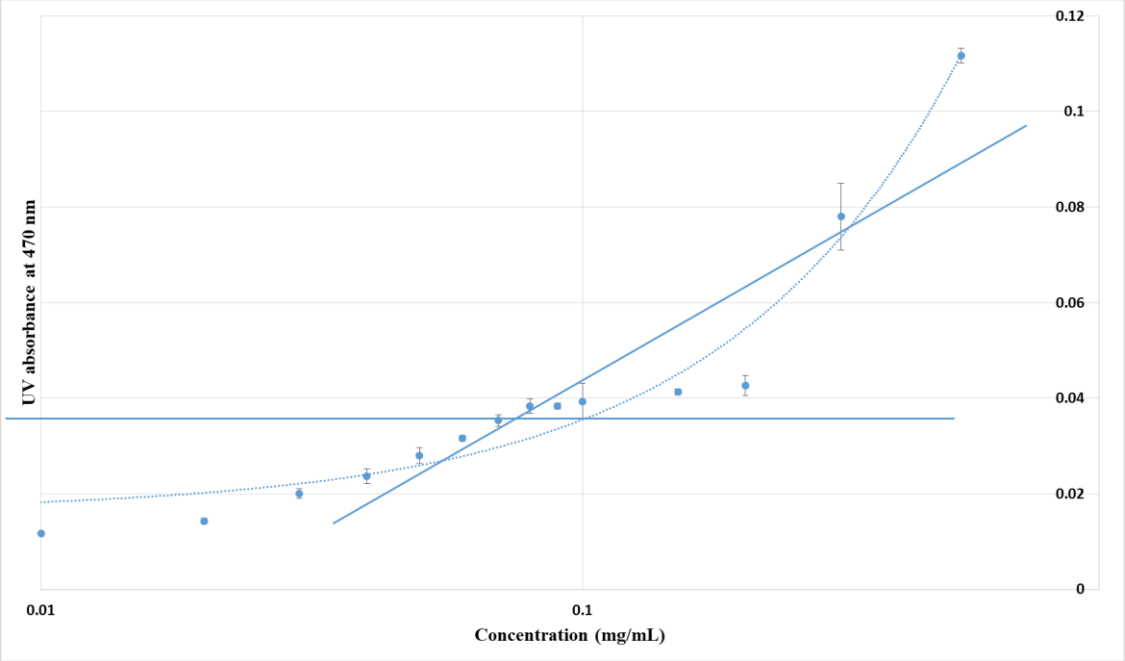

Figure 4. 9. CMC plot for TY-20_CHF (GGGWGPIALRKLRKRLLR) in saline solution. The CMC for TY-20_CHF is 95mg/L that is not far from the literature reported CMC (375).

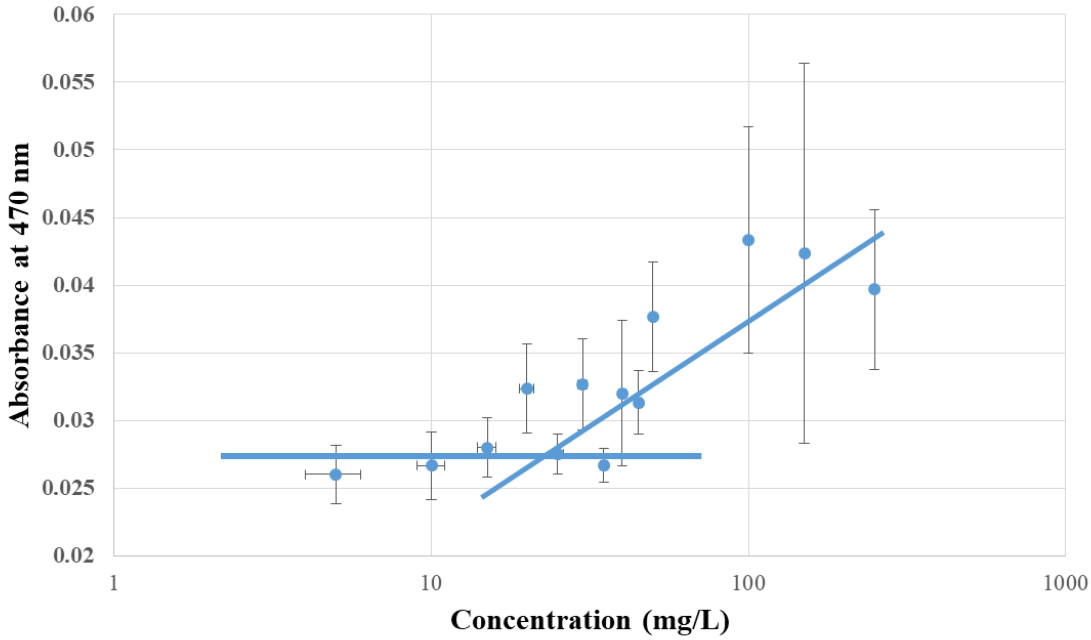

Figure 4. 10. CMC plot for TY-13_CHF (GGGCKAPETALC) in saline solution.

4.4. Conclusion

Novel enzyme-responsive self-assembled peptide nanoparticles were successfully synthesized with different combinations of MMP-9 sensitive and brain-targeting ligands. Adding hydrophobic moiety such as CHF and PA led to self-assembly. In addition, MMP-9 cleavable peptide sequence was hydrophobic enough to facilitate the self-assembly. Most of the formulations self-assembled to form nanoparticles without sonication of 41-200 nm diameter with a zeta potential/ surface charge of 2-48 mV. All self-assembled peptide nanoparticle formulations were characterized by LC-MS. All self-assembled peptide nanoparticles were spherical in shape upon microscopy except TY-35. CMCs for all the self-assembled peptide nanoparticles calculated were around 7-110 mg/L.

CHAPTER – 5 CHARACTERIZATION OF NANOPARTICLES

5.1. Introduction

NPs used for drug delivery should have specific characteristics: such as drug incorporation/encapsulation, drug release, toxicity and bio-distribution (514). Encapsulation efficiency is the percentage of drug that is entrapped into the micelle/NPs (515). NPs are able to encapsulate, adsorb, or conjugate drugs or diagnostics and release the payload at a specific rate in the human body (255). The *in vitro* release study is a critical test to assess the safety, efficacy, and quality of nanoparticle-based drug delivery systems, but there is no compendial or regulatory standard (516). The release of drug from NPs follows three possible ways: desorption of surface adsorbed drug, diffusion and erosion/degradation/metabolism of NPs (517). Dialysis release is simple and well-established technique, which involves the physical separation of a reservoir from the acceptor media through a semi-permeable membrane. Un-encapsulated drug molecules permeates out of the membrane easily, whereas encapsulated drug takes time and get released depending on the method of drug release from NPs (518).

It is quite critical that NP formulations are assessed and confirmed to be safe in terms of their non-toxicity to cells, lack of (or negligible) capacity to provoke unwanted immunological reactions, and non-lytic effects on the red blood cells. The NP formulations targeting the CNS are tested on neuronal cells *in vitro* to assess their cytotoxicity and immunogenicity (519). There is a battery of assays that can be used to assess the effects of a substance on cell viability (or its induction of cell death), usually by quantifying treatment-induced changes to the levels or activities of a specific enzyme or a group of enzymes, or residual cellular energy content as indicated by intracellular levels of adenosine triphosphate (ATP) (520-522), or residual levels of some other intermediate for metabolic activity. The

assays are commonly based on absorbance, fluorescence, or luminescence readouts. Some of them are destructive (lytic) and are, therefore, only useful for endpoint determinations, while some are non-destructive and, therefore, able to assess changes in either endpoint or kinetic mode, thus having an additional advantage of allowing the cells assayed for viability to be used for other assays, if required. Examples include the absorbance-based, tetrazolium reduction (MTT) assay (one of the most commonly used) or any of its more recent improved versions (MTS, XTT, WST-1); the alamar blue assay (fluorescence- or absorbance-based); and the bioluminescence-based ATP assays (521, 523, 524).

Following the successful synthesis of enzyme-responsive self-assembled peptide nanoparticles, the particle size, surface charge, CMC and morphology were assessed. The next step was to assess the encapsulation efficiency and release profiles of different nanoparticle formulations in the presence of external stimuli such as water, fetal bovine serum (FBS), glucose, sodium chloride (NaCl), bovine serum albumin (BSA), oral rehydrating solution (ORS) and active MMP-9. The toxicity profile for the enzyme-responsive self-assembled nanoparticles was also been determined using two different cell lines; HeLa cells and SH-SY5Y cells. Two different techniques; lactate dehydrogenase (LDH) and MTT were used to assess the toxicity profile.

5.2. Material and Methods

5.2.1. Materials

Fluorescein sodium salt (FSS) was purchased from Acros Organics®. Pierce LDH cytotoxicity assay kit was bought from ThermoFisher Scientific®. Gibco DMEM growth media with 10% FBS, 5% L-Glutamine, sodium chloride (NaCl), bovine serum albumin (BSA), glucose, FAM tagged negative siRNA, MTT, cellulose dialysis tubing of 10000 Da MWCO and 5% anti-anti were purchased from Sigma Aldrich. Amicon cellulose centrifugal

unit Ultra 0.5mL 3K, was obtained from Merck Millipore Ltd. HeLa cells and SH-SY5Y cells were kindly provided by Dr Amos Fatokun.

5.2.2. Methods

5.2.2.1. *Encapsulation efficiency and drug loading*

We investigated the encapsulation efficiency of self-assembled peptide NPs *via* an indirect method. FSS solution (1 mL of 0.09 µg/mL) was transferred into an Eppendorf tube containing of peptide powder (3 mg). Upon contact with water, peptides self-assembled into NPs encapsulating the FSS.

The solution (450 µL) was transferred into cellulose centrifugal filter units (Amicon Ultra 0.5mL 3K, Merck Millipore Ltd.) and centrifuged for 10 min at a speed of 10000RPM. The filtrate was then transferred to a clear falcon 96 well plate and the fluorescence was measured by using a SpectraMax i3X multi-mode microplate reader with an excitation wavelength of 460 nm and measuring emission at 515 nm. The encapsulation efficiency was calculated using the equation derived from the calibration curve generated by serial dilutions. Each experiment was performed four times (n=4). Drug loading capacity was calculated by dividing the entrapped drug by the amount of peptide used.

For *in vitro* experiments siRNA was used instead of FSS. siRNA is negatively charged large molecule which can adsorb on the surface of positively charge NPs. Encapsulation and loading capacity for siRNA was not calculated. It is suspected that the siRNA favours the adsorption on the surface of NPs than encapsulation due to their size and negative charge.

5.2.2.2. *Release studies*

In vitro FSS release was investigated using a dialysis bag method (525). Release studies of the self-assembled peptide NPs were conducted in the presence and absence of fetal bovine serum (FBS), distilled water, BSA (4 mg/mL), NaCl (0.9%), Glucose (7.8 mM as normal

body level), activated MMP-9 (2 nM) and Dioralyte an oral rehydrating solution containing glucose 3.56 g / 200 mL (18 mM), NaCl (0.47 g, 12 mM), potassium chloride (0.30g, 4 mM), and disodium hydrogen citrate (0.53 g, 2 mM).

Briefly, a suitable size (12 cm) of cellulose tube was soaked in distilled water for 5 min to help with knotting on both ends. Peptide (3 mg) was transferred into an Eppendorf tube to which FSS solution (1 mL, 0.09 µg/mL) was added with gently swirling. The solution was transferred to dialysis bag (Cellulose with a diameter of 1″ and 10000 Da MWCO). This was dialyzed against distilled water (40 mL). A sample was withdrawn every hour and returned after measurement. Release of FSS was calculated by using the equation derived from the calibration curve generated by serial dilutions. Each experiment was performed in triplicate. For comparison, FSS release from the dialysis bag in the presence of external stimuli without NPs formulations was conducted. The release study for TYR-3_CHF was not conducted as the NPs had tendencies to precipitate.

5.2.2.3. *Cytotoxicity studies*

The lactate dehydrogenase (LDH) assay was used to assess the potential toxicity of the enzyme-responsive self-assembled peptide NPs. HeLa and SH-SY5Y cells were grown in Dulbecco's Modified Eagle Medium (DMEM) supplemented with 10% FBS and 2 mM L-glutamine. Cells were then washed with phosphate-buffered saline (280 - 315 mOsm/kg, pH 7.4), trypsinised, re-suspended in the growth medium, counted and seeded into an opaque, micro-clear, flat bottom 96 well tissue culture plate at a density of 7.5 x 10^4 cells/mL (7500 cells/ well at 100 µL/well). The 96 well plate was then incubated overnight at 37°C with a 5% CO_2 supply. Then the NPs were added to the culture wells in triplicate. DMSO (5%) was added to the positive control wells. The treated 96 well plate was then incubated for 24 h at 37°C and 5% CO_2, at the end of which, the LDH assay was carried out according to the

manufacturer's protocol (ThermoFisher, Pierce LH Cytotoxicity Assay Kit, Cat. No. 88953). Included in the design was a spontaneous LDH activity control (10 µL of sterile water, to capture minimum LDH release, i.e., completely healthy cells representing 0% LDH release) and a maximum LDH activity control (10 µL of 10× lysis buffer, expected to fully lyse the cells, indicative of 100% LDH release). The 96 well plate was then incubated for a further 45 min at 37°C with a 5% CO_2 supply. Following this incubation, 50 µL of medium from each test or control well was transferred into a new 96 well flat-bottom plate. Then 50 µL of reaction mixture was added to each of these wells and the plate was tapped gently. This plate was then incubated at room temperature for 30 min whilst covered in foil to protect it from light, after which, 50 µL of stop solution (strong acid) was added to each of the wells and was mixed by gentle tapping. Any bubbles made were removed with a syringe needle. Using the Clariostar plate reader (BMG Labtech Ltd), the value for the blank well (non-cell-containing) was subtracted from the negative control value and each treatment value. The resultant value at 680 nm was then subtracted from the corresponding resultant value at 480 nm. These final values were then analysed by expressing the value for the positive control or for each treatment as a percentage of the maximum LDH release value.

For the MTT assay, after treatment with enzyme-responsive self-assembled peptide NPs, MTT was added to each experimental well and incubated for 3 h. The supernatant was aspirated carefully, and a blue crystal of formazan was dissolved in DMSO by shaking gently for 5 min whilst covered in foil to protect it from light. The suspension was read at 570 nm and analysis was performed.

5.2.2.4. *Statistical analysis*

GraphPad Prism Software 8.0.1 for Windows (GraphPad Software, Inc., La Jolla, CA, USA) was used to conduct one-way analysis of variance (ANOVA) followed by Tukey's

post-hoc test for multiple comparisons in order to identify any statistically-significant differences between the means of treatment groups. For statistical comparisons, $P<0.05$ was considered a statistically significant difference.

5.3. Results and Discussion

The encapsulation capacity of NPs was calculated by an indirect method (526). To calculate the encapsulation efficiency of nanoparticle formulations a calibration curve was generated by using different concentrations of FSS solution in distilled water. The calibration curve is shown in Figure 5.1.

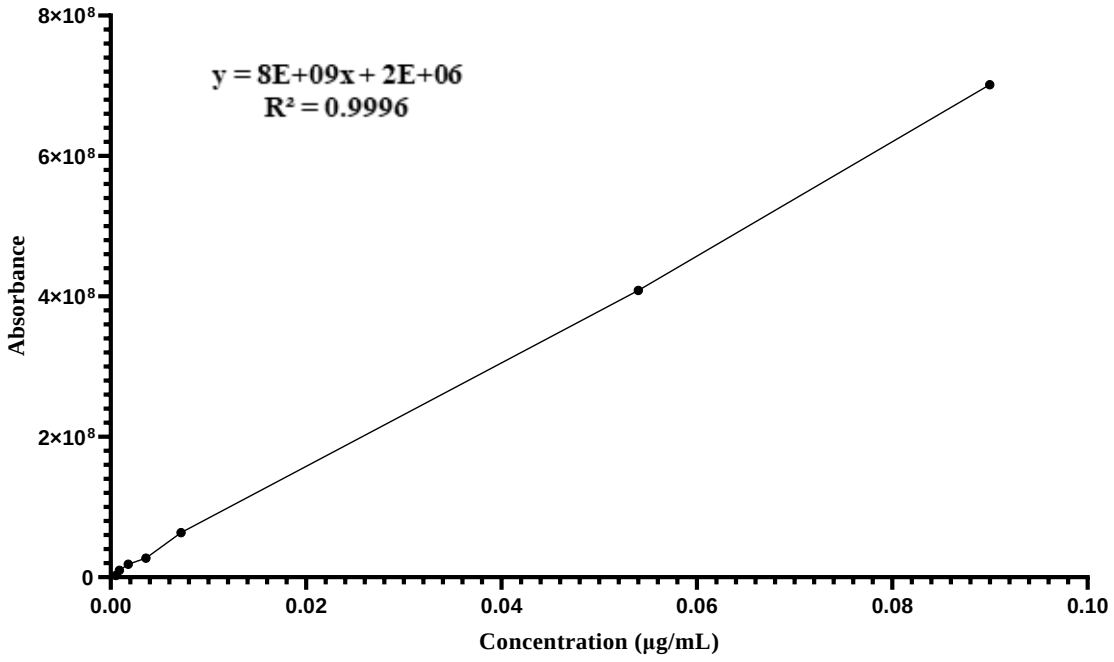

Figure 5. 1. Calibration curve of FSS for encapsulation efficiency with R^2= 0.9996.

The encapsulation efficiency for all enzyme-responsive self-assembled peptide nanoparticles ranged from 40-85% as shown in Figure 5.2. It was not possible to determine the drug loading in the NPs as they needed solvent to maintain their self-assembly.

Furthermore, these self-assembled peptide NPs constantly releasing FSS, and this could affect loading capacity. Luo et al. developed high-intensity focused ultrasound (HIFU) responsive angiopep-2-decorated poly(lactic-co-glycolic acid) (PLGA) hybrid NPs able to transport doxorubicin/perfluorooctyl bromide (ANP-D/P). Decorated-NPs showed 17-fold increased accumulation in glioblastoma and 13.4 fold higher than unmodified NPs. Significant amount (47%) of drug released within two minutes after HIFU irradiation, causing apoptosis of tumour cells (527). Fornaguera et al. reported encapsulation efficiency of PLGA nanoparticles around 99.92%, which is higher than our nanoparticles. This could be due to the rigid outer core provided by polymer. Ghorbani et al. reported the use of gold-iron nanocomposites encapsulated with curcumin-lipoic acid, a pH-sensitive delivery system for the brain. GSH is used as targeting ligand, leading to 2-fold increases in cellular uptake (338). Loading capacity of enzyme-responsive self-assembled peptide NPs was calculated and represented in Table 5.1. It should be noted here that the loading capacity is calculated from the data of FSS. It is extremely low, as the FSS was used only as a tracer dye to visualise the NPs fate.

Table 5. 1. Loading capacity of enzyme-responsive self-assembled peptide NPs

Formulation Name	Loading Capacity µg/100mg (drug/peptide)	Formulation Name	Loading Capacity µg/100mg (drug/peptide)
TY-8	**2.0316**	**TY-35**	**1.2460**
TYR-3_P.A	**2.3355**	**TY-37**	**2.3279**
TY-13_CHF	**2.3881**	**TY-39**	**2.4137**
TY-20	**2.2658**	**TY-41**	**2.0733**
TY-28	**2.5415**	**TY-44**	**2.3562**
TY-32	**1.3855**		

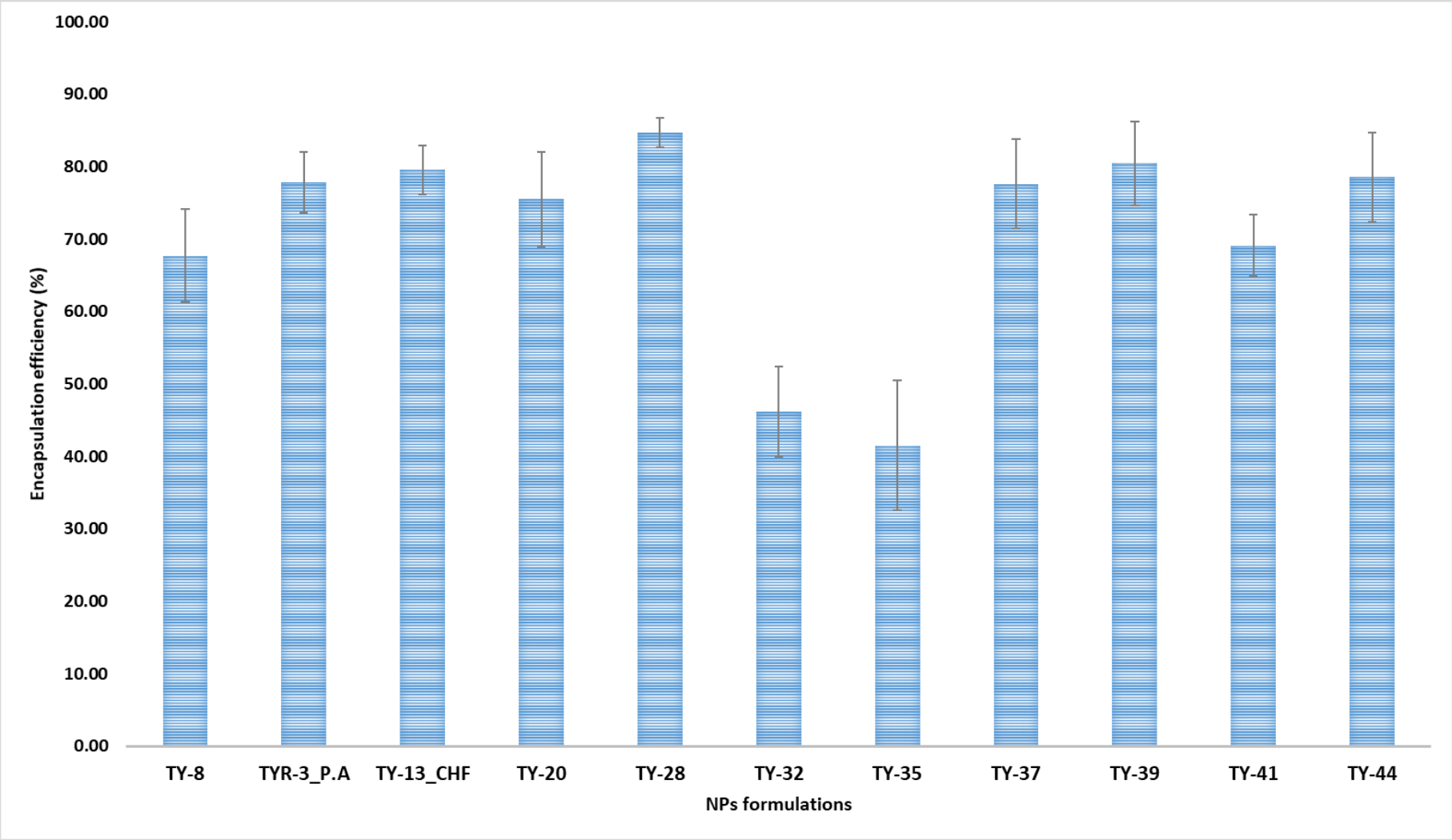

Figure 5. 2. Encapsulation efficiency for enzyme-responsive self-assembled peptide nanoparticles calculated via an indirect method.

The drug release profile is an important property of nanoparticles, that directly relates to the loaded drug stability, therapeutic results and drug-carrier nanoparticle stability (528). Release profiling provides the critical information about dosage form behavior and is a key parameter used to assess product safety and efficacy (529). To understand the mechanism of release of FSS from NPs (all formulations) dialysis was run in the presence of different solutions acting as external stimuli. A calibration curve was generated with $R^2 = 0.9986$ as shown in Figure 5.3.

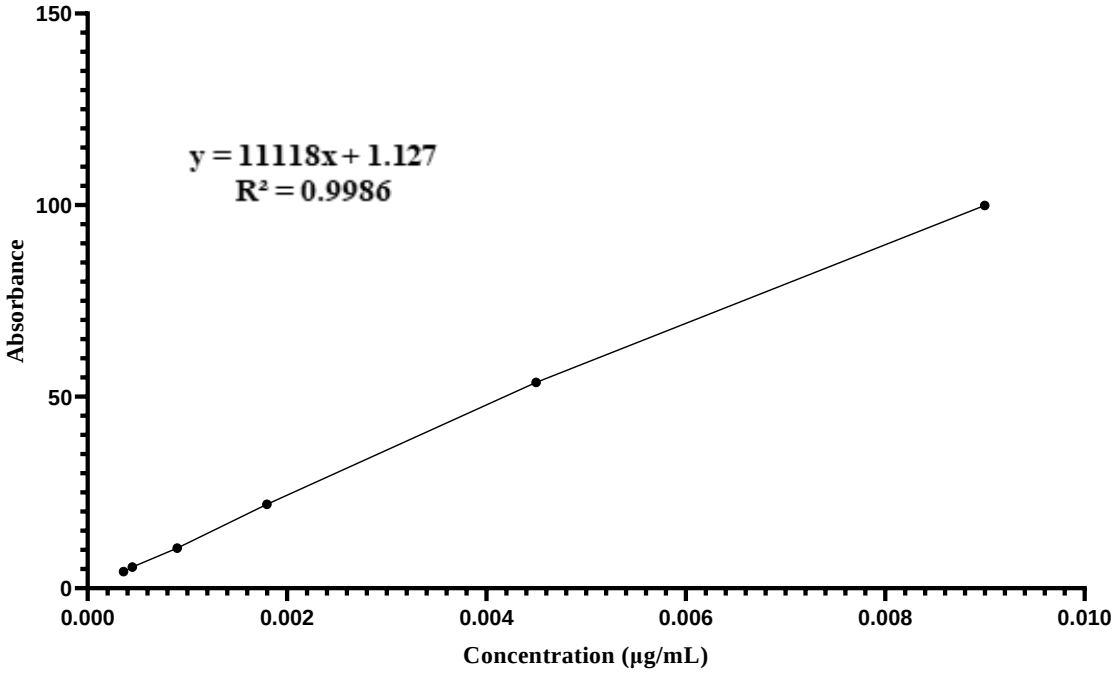

Figure 5. 3. Calibration curve of FSS for release profiling with a R^2 = 0.9986.

In vitro release of encapsulated drug was conducted by using a dialysis bag. Seven external stimuli were used to assess the pattern of release from the NPs such as: water, FBS, NaCl, BSA, glucose, ORS and MMP-9. The rationale behind using multiple external stimuli

was to ensure and explore the impact of different stimuli and to mimic the physiological characteristics. It was observed that upon addition of FSS solution into a peptide-containing Eppendorf tube, self-assembly of the peptide nanoparticles was consistent with encapsulation of the FSS, affording the apparent color change as shown in Figure 5.4.

Figure 5. 4. Encapsulation of FSS in TY-20_CHF peptide. Clear colour differentiation can be observed. FSS bag is more yellow in colour compare to the bag containing the peptide nanoparticles suggesting the encapsulation of the FSS.

The release profiles for all the enzyme-responsive self-assembled peptide nanoparticles is shown in Figures 5.5 – 5.16.

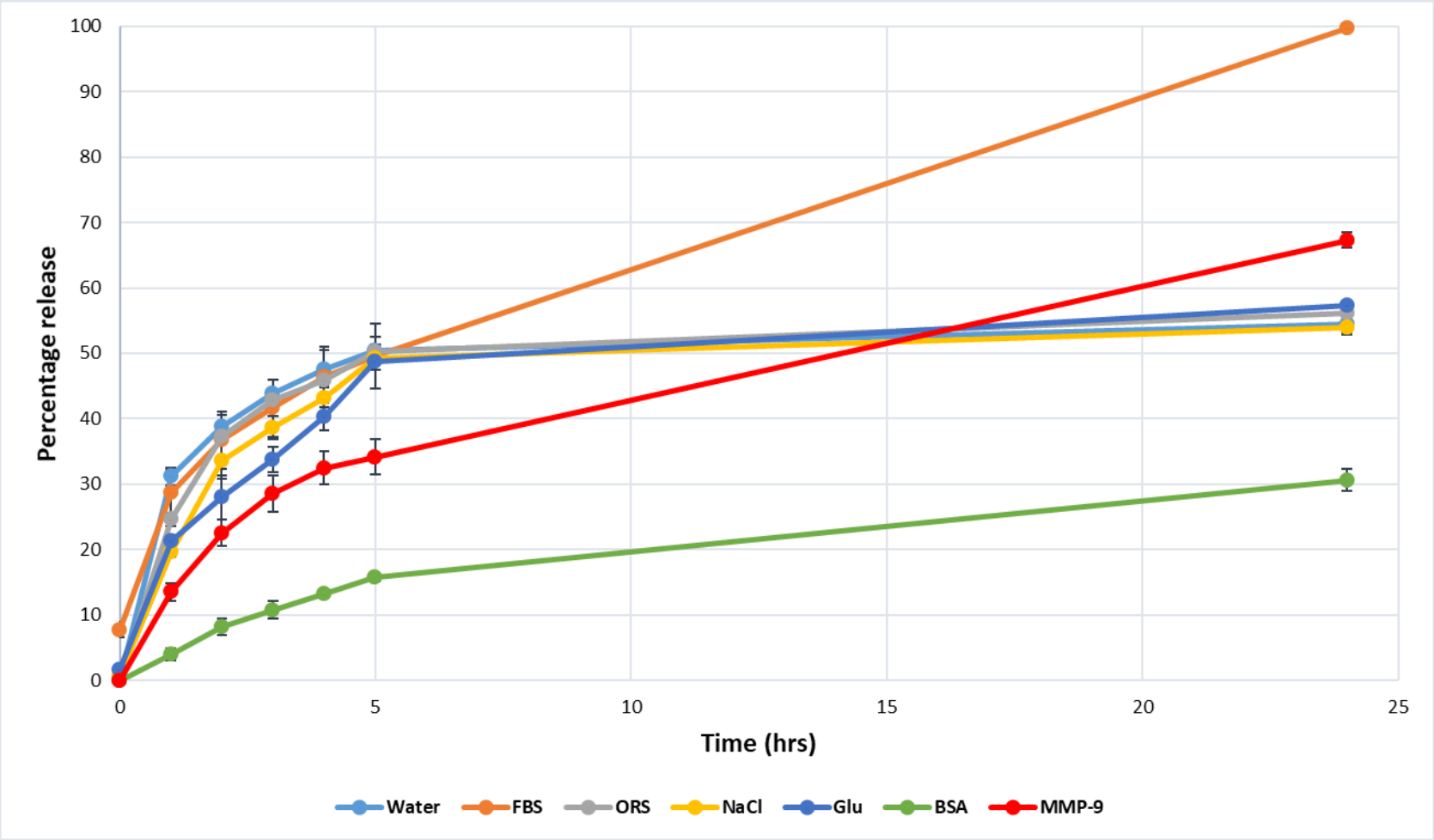

Figure 5. 5. Percentage release profile for TY-13_CHF (GGGCKAPETALC) in the presence of different solutions, such as: BSA (4 mg/mL), NaCl (0.9%), Glucose (7.8 mmol as normal body level), foetal bovine serum (FBS), distilled water, activated MMP-9 (2 nM) and Dioralyte an oral rehydrating solution containing glucose 3.56 g / 200 mL (18mmol), NaCl (0.47 g, 12 mmol), potassium chloride (0.30 g, 4 mmol), disodium hydrogen citrate (0.53 g, 2 mmol).

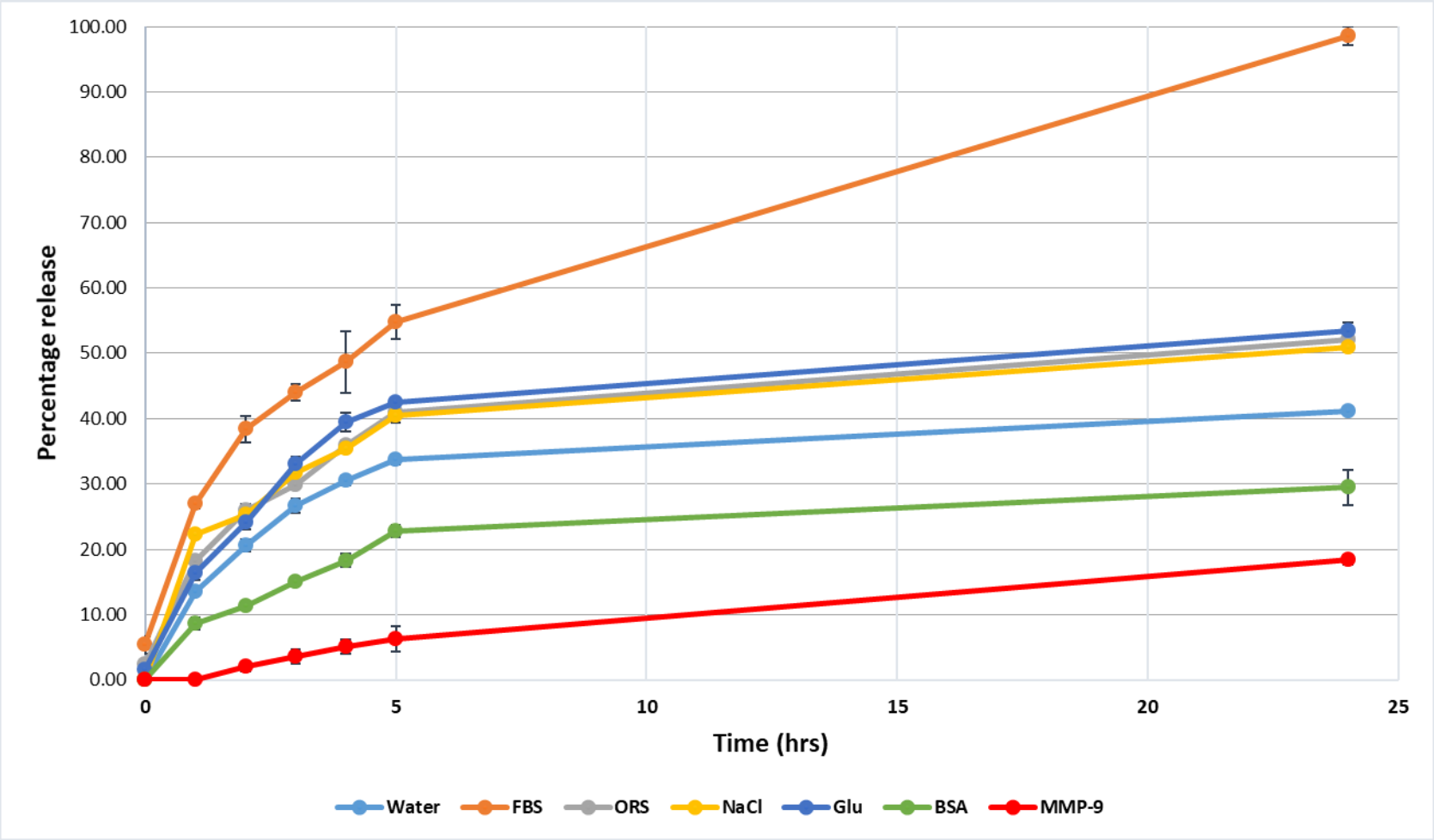

Figure 5. 6. Percentage release profile for TYR-3_PA (GGGPLGLWCDIFTNSRGKRA) in the presence of different solutions, such as: BSA (4 mg/mL), NaCl (0.9%), Glucose (7.8 mmol as normal body level), foetal bovine serum (FBS), distilled water, activated MMP-9 (2 nM) and Dioralyte an oral rehydrating solution containing glucose 3.56 g / 200 mL (18mmol), NaCl (0.47 g, 12 mmol), potassium chloride (0.30 g, 4 mmol), disodium hydrogen citrate (0.53 g, 2 mmol).

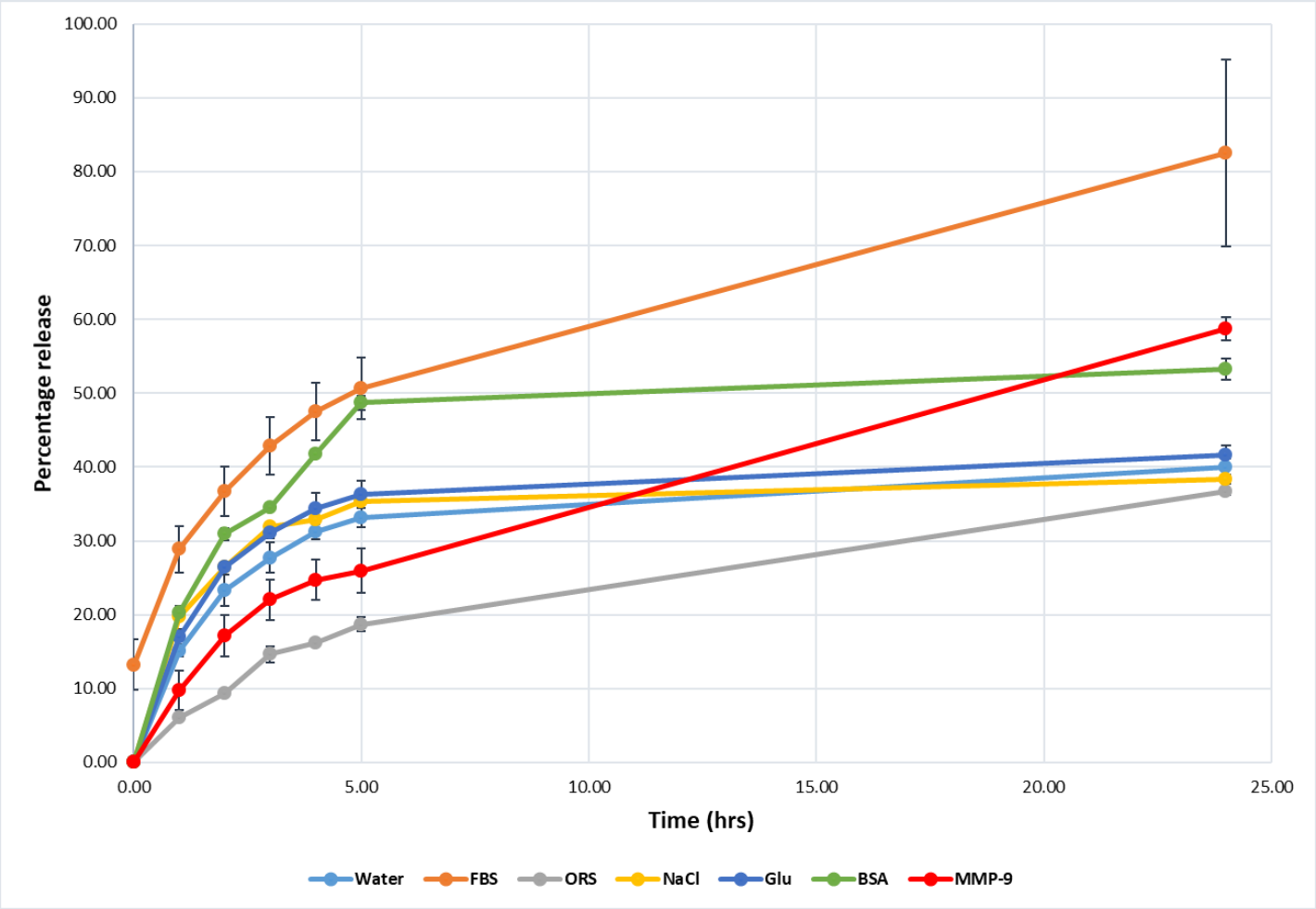

Figure 5. 7. Percentage release profile for TY-20 (GGGWGPIALRKLRKRLLR) in the presence of different solutions, such as: BSA (4 mg/mL), NaCl (0.9%), Glucose (7.8 mmol as normal body level), foetal bovine serum (FBS), distilled water, activated MMP-9 (2 nM) and Dioralyte an oral rehydrating solution containing glucose 3.56 g / 200 mL (18mmol), NaCl (0.47 g, 12 mmol), potassium chloride (0.30 g, 4 mmol), disodium hydrogen citrate (0.53 g, 2 mmol).

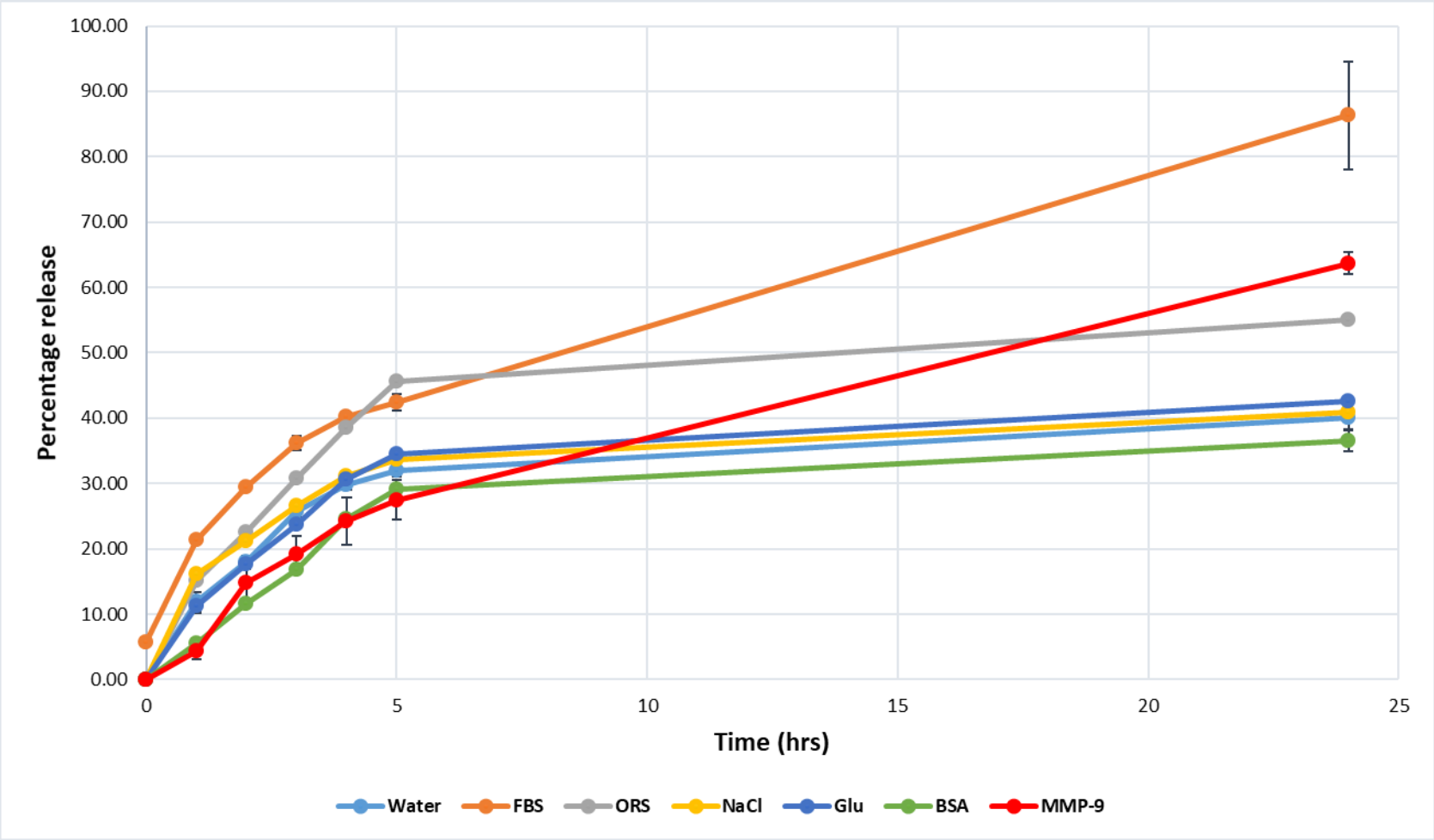

Figure 5. 8 Percentage release profile for TY-28 (GGGWGPIACDIFTNSRGKRA) in the presence of different solutions, such as: BSA (4 mg/mL), NaCl (0.9%), Glucose (7.8 mmol as normal body level), foetal bovine serum (FBS), distilled water, activated MMP-9 (2 nM) and Dioralyte an oral rehydrating solution containing glucose 3.56 g / 200 mL (18mmol), NaCl (0.47 g, 12 mmol), potassium chloride (0.30 g, 4 mmol), disodium hydrogen citrate (0.53 g, 2 mmol).

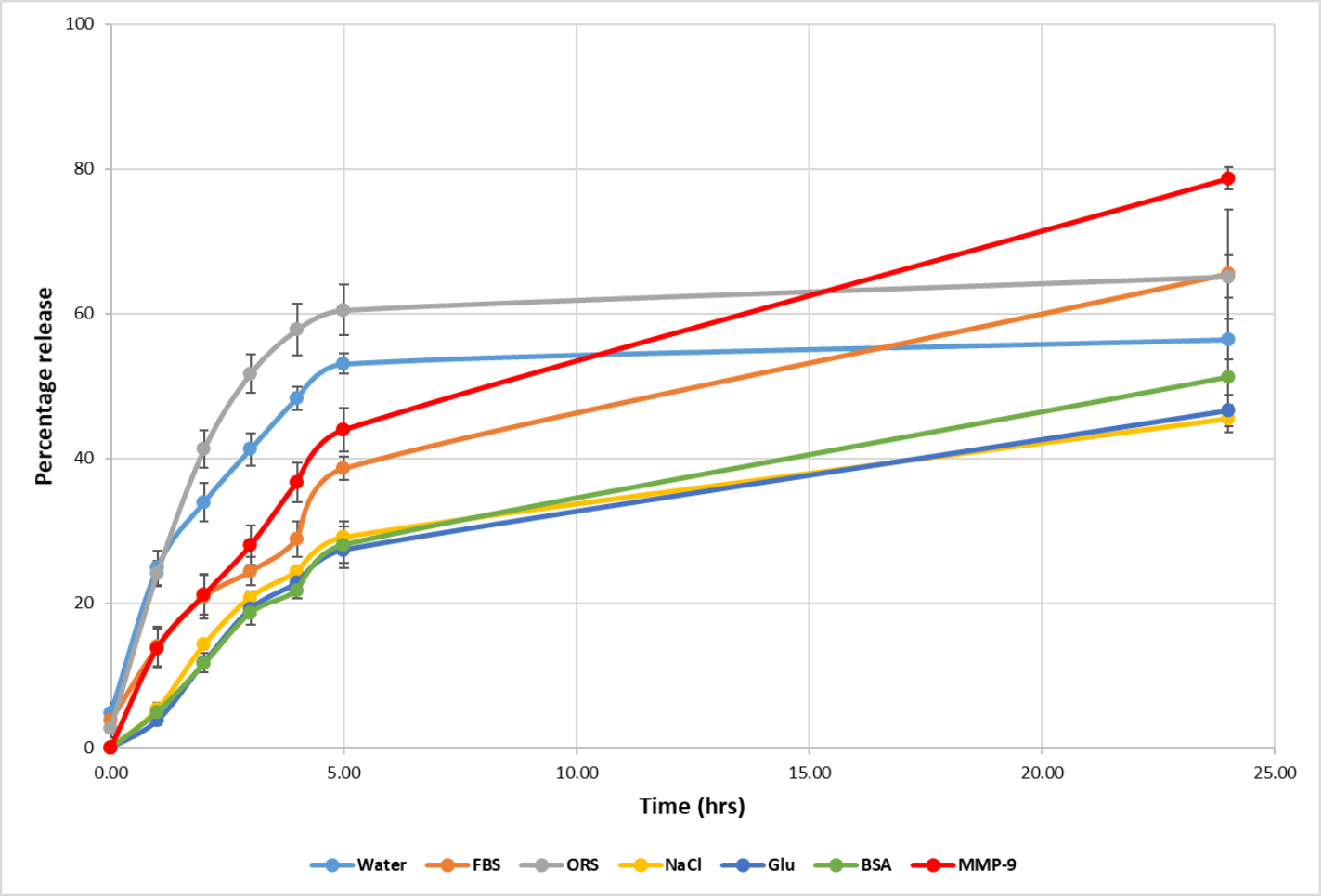

Figure 5. 9. Percentage release profile for TY-32 (GGPIPLAIFGCDIFTNSRGKRA) in the presence of different solutions, such as: BSA (4 mg/mL), NaCl (0.9%), Glucose (7.8 mmol as normal body level), foetal bovine serum (FBS), distilled water, activated MMP-9 (2 nM) and Dioralyte an oral rehydrating solution containing glucose 3.56 g / 200 mL (18mmol), NaCl (0.47 g, 12 mmol), potassium chloride (0.30 g, 4 mmol), disodium hydrogen citrate (0.53 g, 2 mmol).

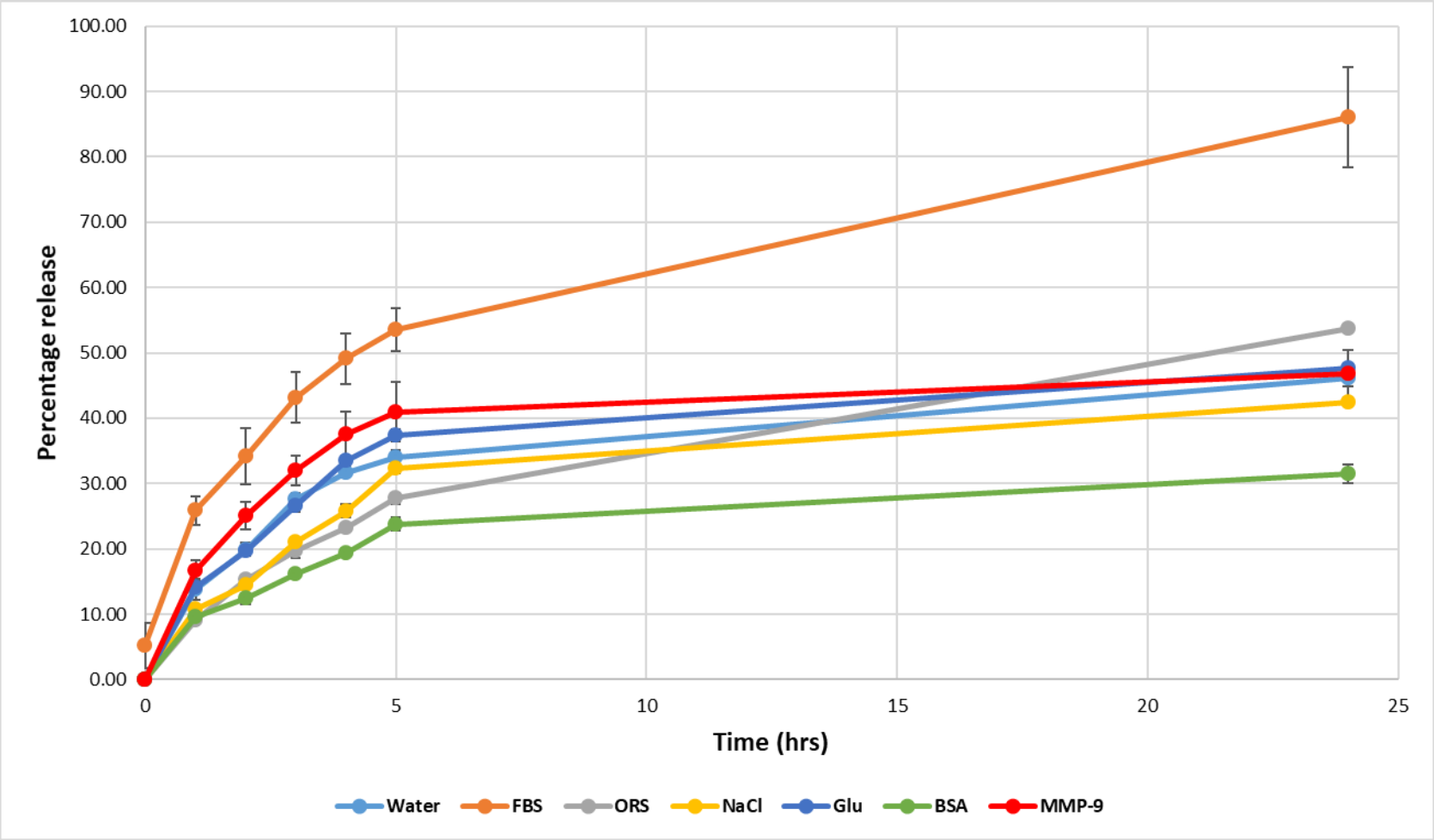

Figure 5. 10. Percentage release profile for TY-35 (WGPIAHAIYPRH) in the presence of different solutions, such as: BSA (4 mg/mL), NaCl (0.9%), Glucose (7.8 mmol as normal body level), foetal bovine serum (FBS), distilled water, activated MMP-9 (2 nM) and Dioralyte an oral rehydrating solution containing glucose 3.56 g / 200 mL (18mmol), NaCl (0.47 g, 12 mmol), potassium chloride (0.30 g, 4 mmol), disodium hydrogen citrate (0.53 g, 2 mmol).

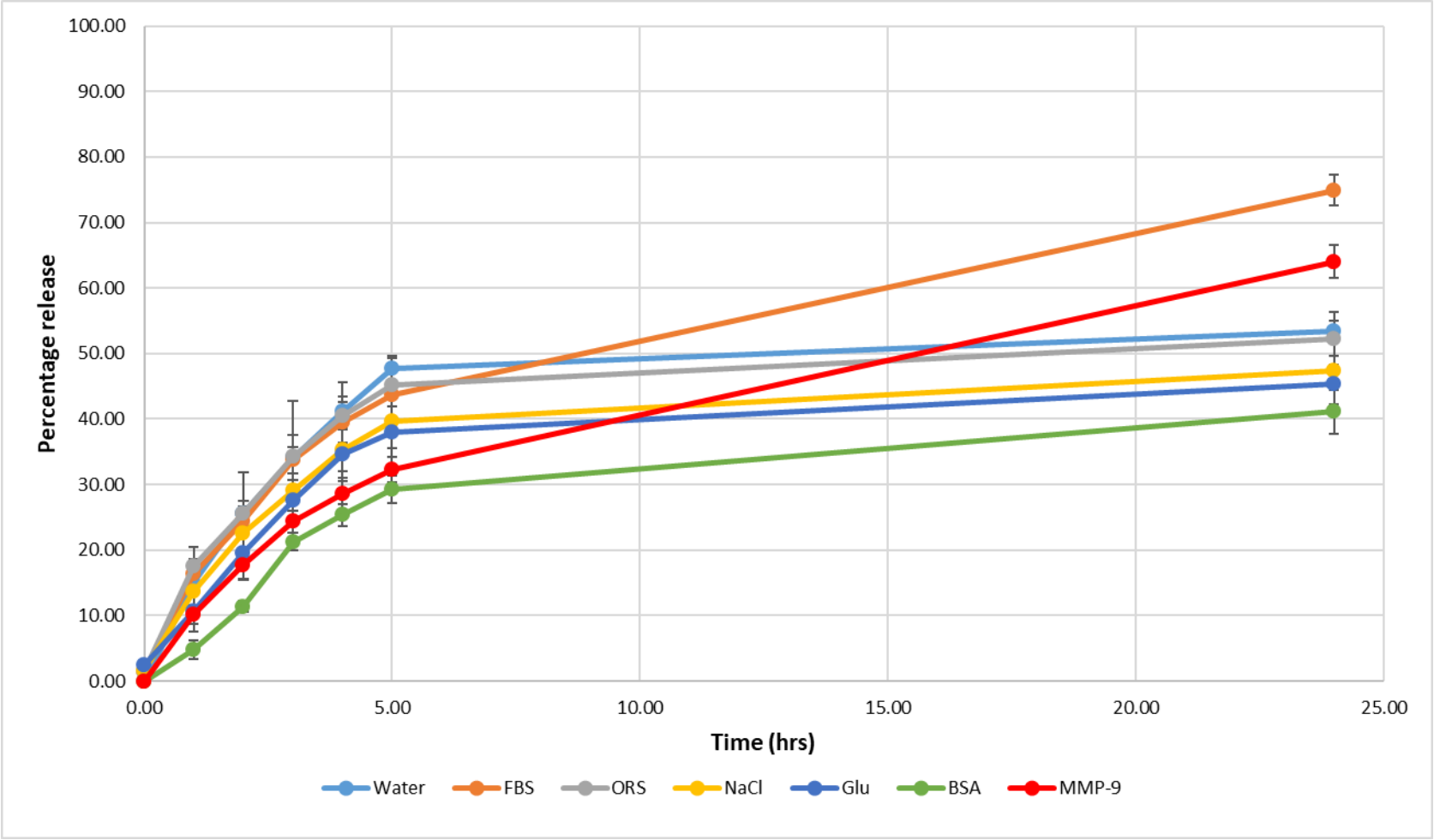

Figure 5. 11. Percentage release profile for TY-37 (PIPLAIFCKAPETALC) in the presence of different solutions, such as: BSA (4 mg/mL), NaCl (0.9%), Glucose (7.8 mmol as normal body level), foetal bovine serum (FBS), distilled water, activated MMP-9 (2 nM) and Dioralyte an oral rehydrating solution containing glucose 3.56 g / 200 mL (18mmol), NaCl (0.47 g, 12 mmol), potassium chloride (0.30 g, 4 mmol), disodium hydrogen citrate (0.53 g, 2 mmol).

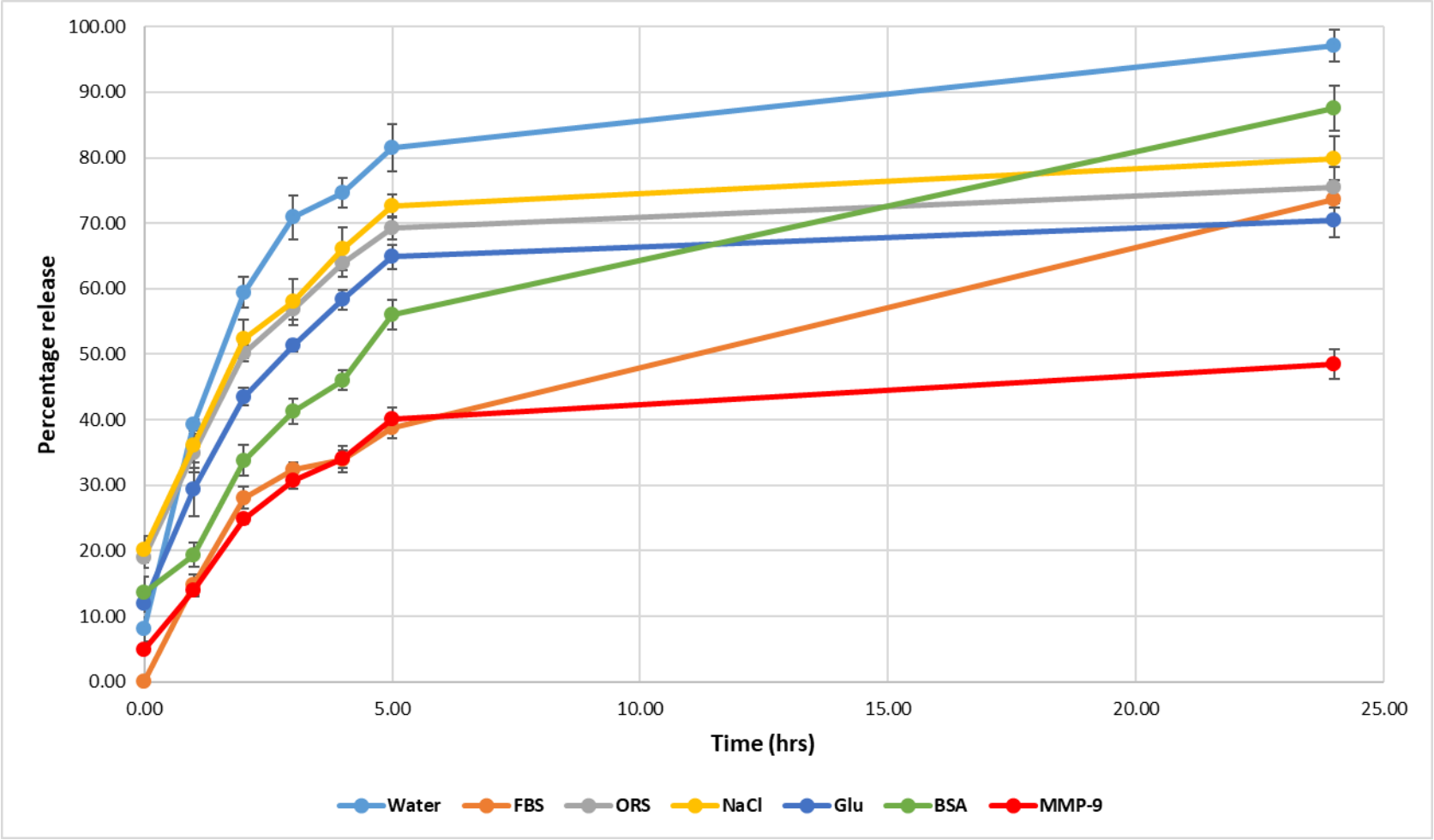

Figure 5. 12. Percentage release profile for TY-38 (PIPLAHAIYPRH) in the presence of different solutions, such as: BSA (4 mg/mL), NaCl (0.9%), Glucose (7.8 mmol as normal body level), foetal bovine serum (FBS), distilled water, activated MMP-9 (2 nM) and Dioralyte an oral rehydrating solution containing glucose 3.56 g / 200 mL (18mmol), NaCl (0.47 g, 12 mmol), potassium chloride (0.30 g, 4 mmol), disodium hydrogen citrate (0.53 g, 2 mmol).

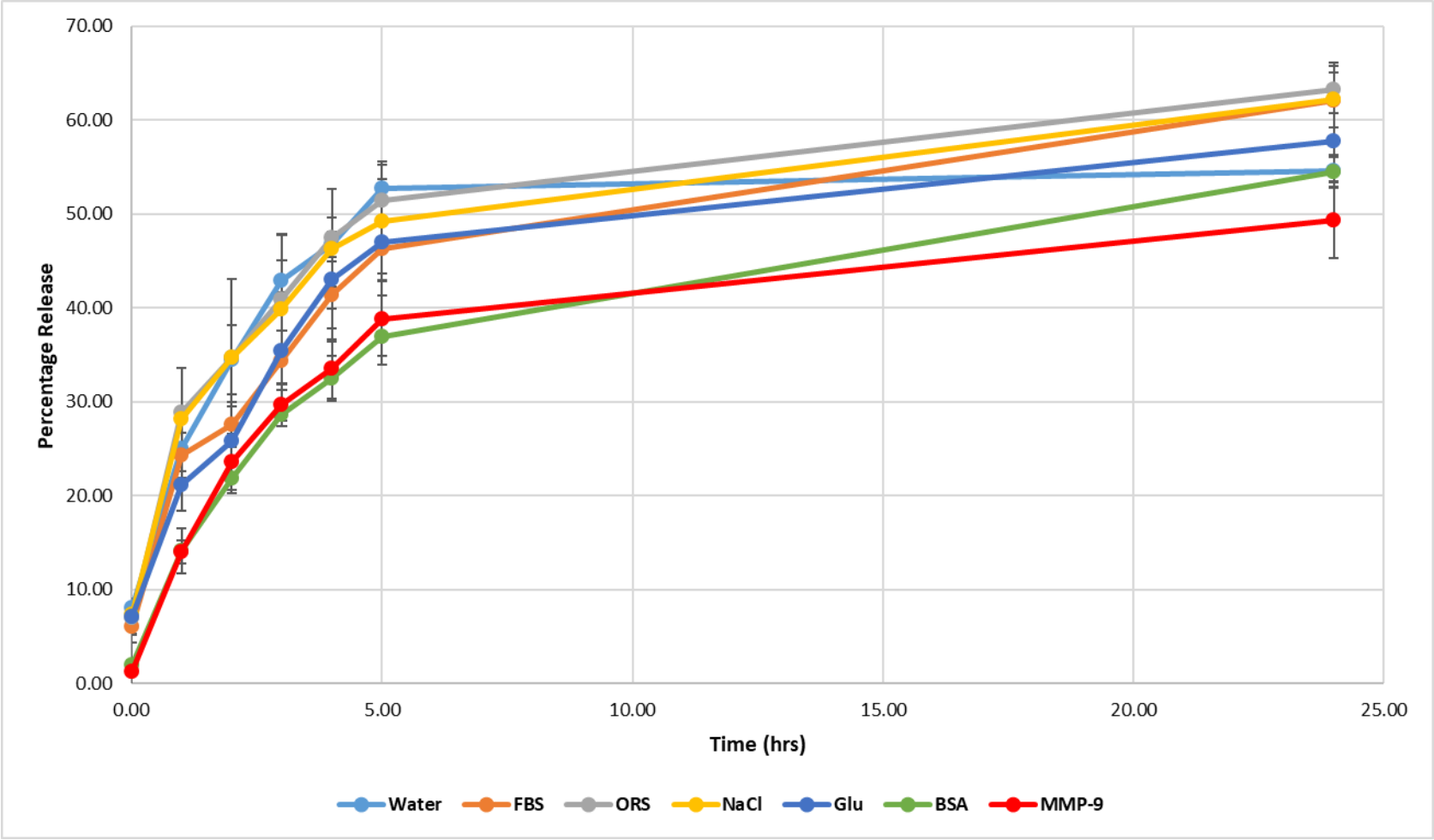

Figure 5. 13. Percentage release profile for TY-39 (WGPIACKAPETALC) in the presence of different solutions, such as: BSA (4 mg/mL), NaCl (0.9%), Glucose (7.8 mmol as normal body level), foetal bovine serum (FBS), distilled water, activated MMP-9 (2 nM) and Dioralyte an oral rehydrating solution containing glucose 3.56 g / 200 mL (18mmol), NaCl (0.47 g, 12 mmol), potassium chloride (0.30 g, 4 mmol), disodium hydrogen citrate (0.53 g, 2 mmol).

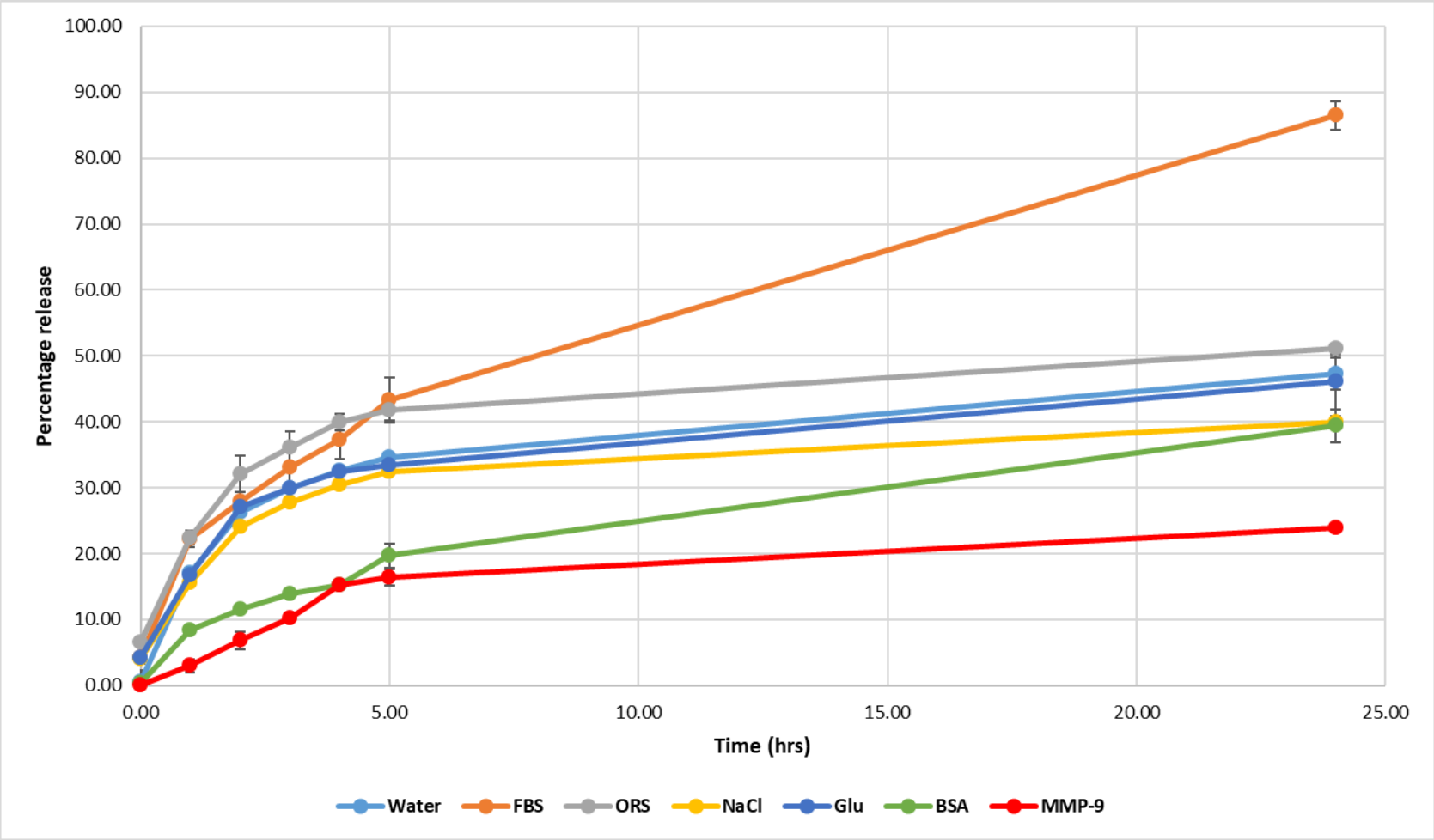

Figure 5. 14. Percentage release profile for TY-41_CHF (GGGCDIFTNSRGKRA) in the presence of different solutions, such as: BSA (4 mg/mL), NaCl (0.9%), Glucose (7.8 mmol as normal body level), foetal bovine serum (FBS), distilled water, activated MMP-9 (2 nM) and Dioralyte an oral rehydrating solution containing glucose 3.56 g / 200 mL (18mmol), NaCl (0.47 g, 12 mmol), potassium chloride (0.30 g, 4 mmol), disodium hydrogen citrate (0.53 g, 2 mmol).

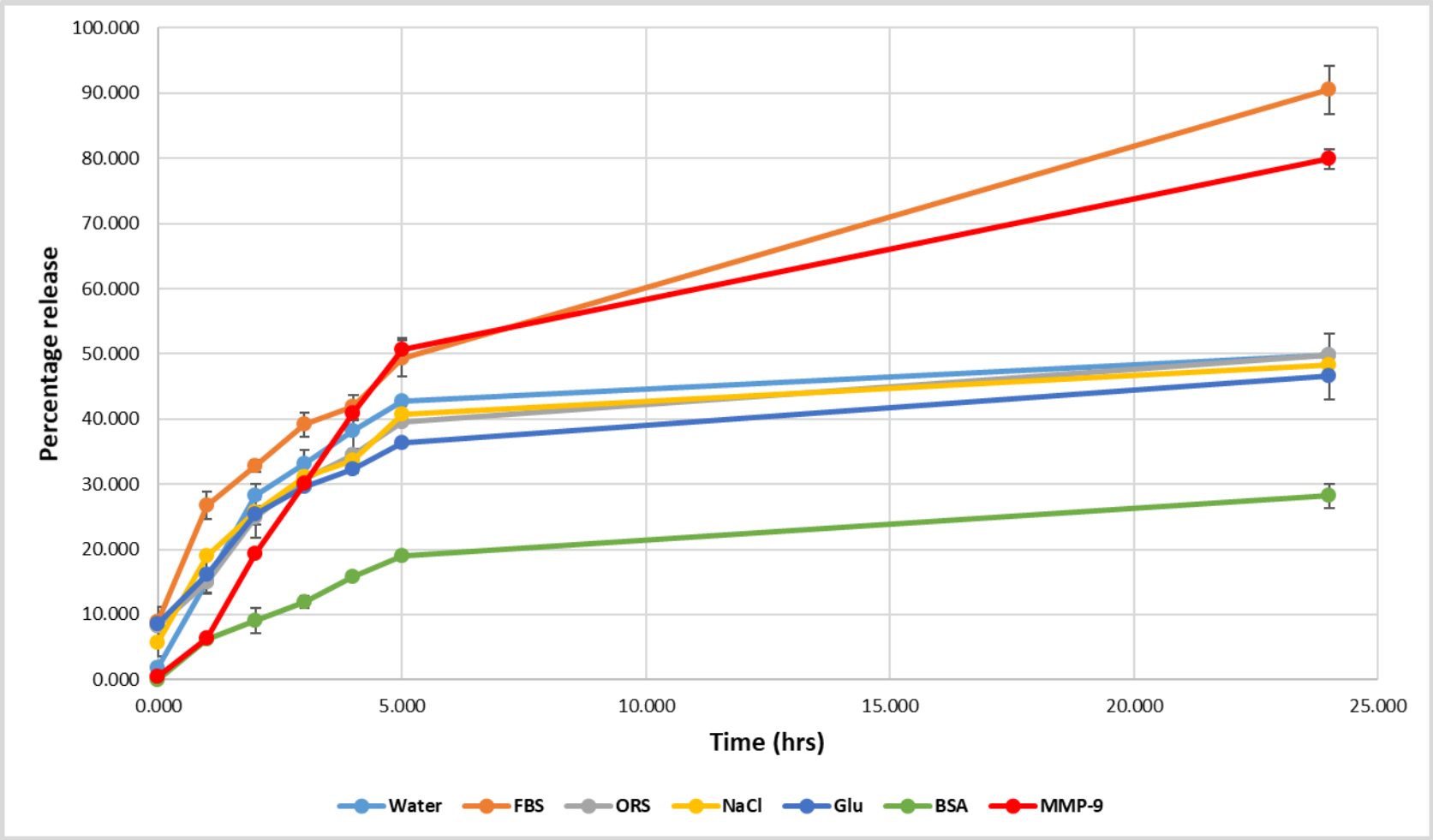

Figure 5. 15. Percentage release profile for TY-44 (WGPIALAGIGHAIYPRH) in the presence of different solutions, such as: BSA (4 mg/mL), NaCl (0.9%), Glucose (7.8 mmol as normal body level), foetal bovine serum (FBS), distilled water, activated MMP-9 (2 nM) and Dioralyte an oral rehydrating solution containing glucose 3.56 g / 200 mL (18mmol), NaCl (0.47 g, 12 mmol), potassium chloride (0.30 g, 4 mmol), disodium hydrogen citrate (0.53 g, 2 mmol).

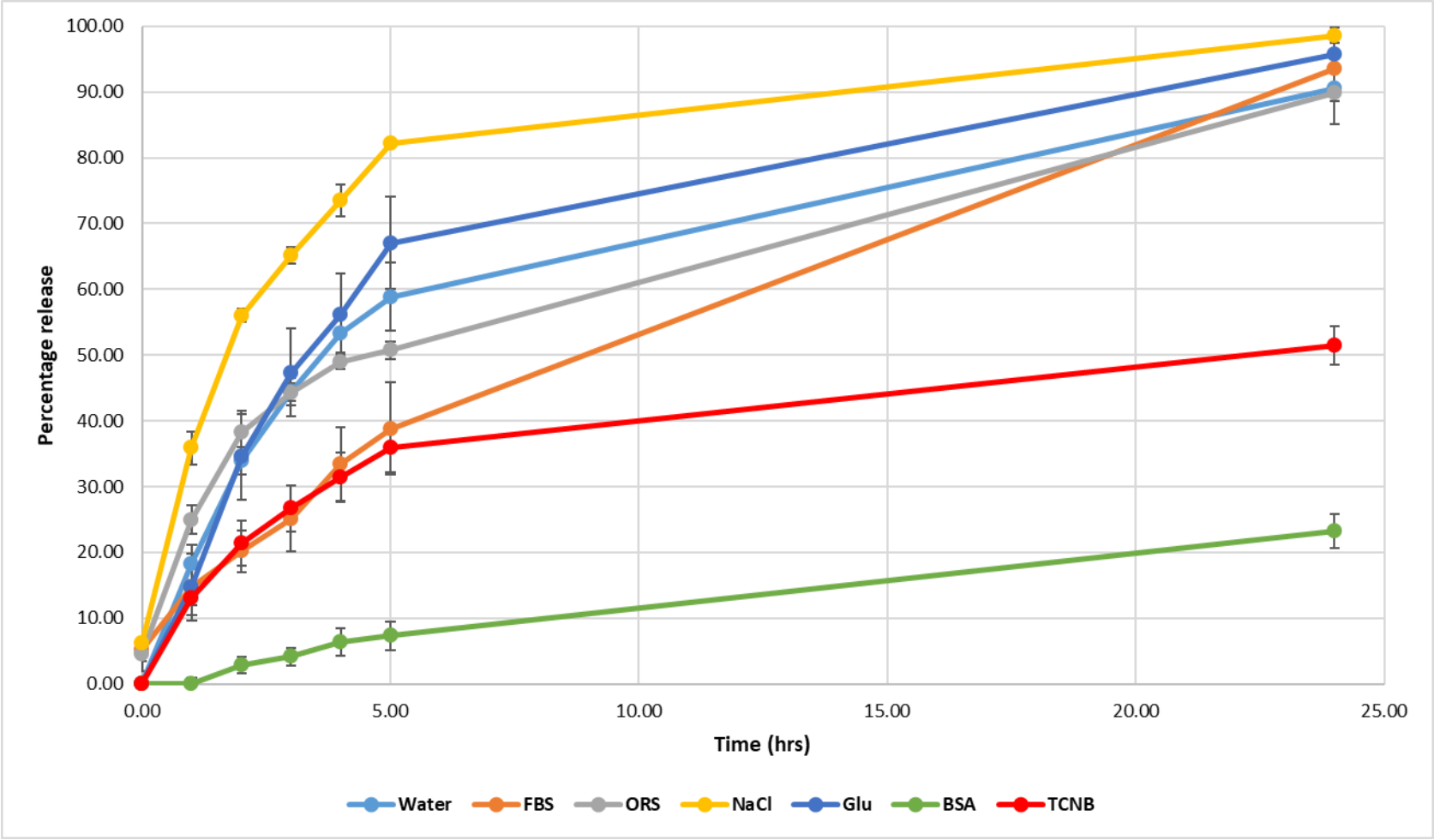

Figure 5. 16. Percentage release profile for FSS in the presence of different solutions, such as: BSA (4 mg/mL), NaCl (0.9%), Glucose (7.8 mmol as normal body level), foetal bovine serum (FBS), distilled water, TCNB buffer (used to activate MMP-9) and Dioralyte an oral rehydrating solution containing glucose 3.56 g/200 mL (18 mol), NaCl (0.47 g, 12 mmol), potassium chloride (0.30 g, 4 mmol), disodium hydrogen citrate (0.53 g, 2 mmol).

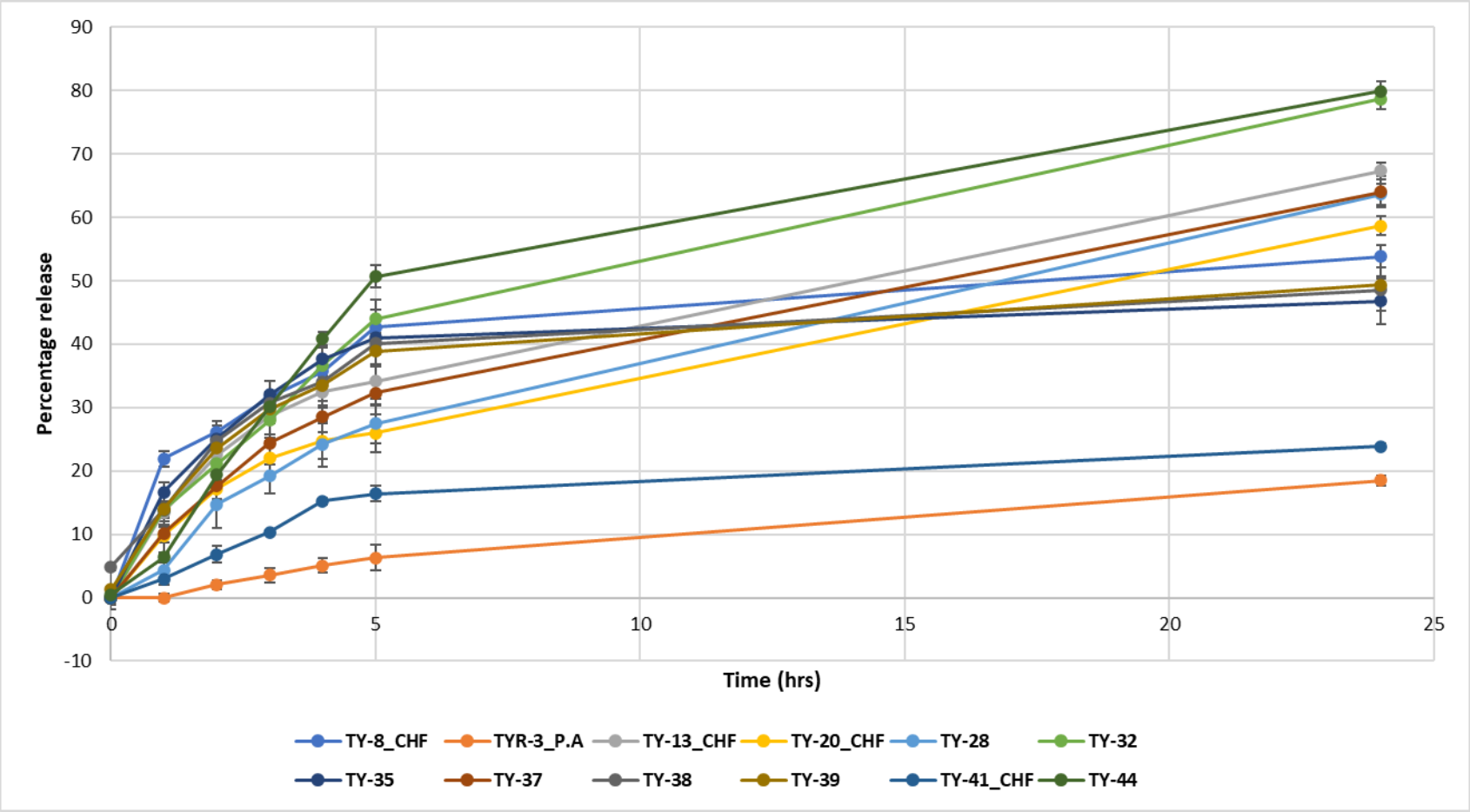

Figure 5. 17. Percentage release profile for FSS from all enzyme-responsive self-assembled NPs in the presence of activated MMP-9 (2 nM).

Release patterns of the encapsulated FSS were investigated in the presence of different external stimuli to mimic the physiological conditions. Release of the FSS changed in the presence of different stimuli. In distilled water, release of FSS in TY-13, TY-32, TY-35, TY-37, TY-39, TY-41_CHF and TY-44 was around 50% or more, whereas 40% of FSS was released in TYR-3_PA, TY-20_CHF and TY-28. This demonstrated that the self-assembled NPs were stable in water for up to 24 h. Interestingly, in the first hour 13% FSS was released in TYR-3_PA compared to 31% TY-13. TY-39 showed unusual release compared with other NPs, almost all encapsulated FSS was released in the presence of water suggesting that it is not stable enough to maintain its structure. Release of FSS in the presence of FBS was very high. It is suggested that the presence of enzymes/peptidases start metabolizing the peptide and hence the release of FSS. Almost 100% of FSS was released after 24 h in the presence of FBS in most of the NP formulations. Surprisingly, the release of FSS from self-assembled NPs in the presence of BSA was low. In most cases, release was around 30-40%. Release of FSS from the dialysis bag in the presence of external stimuli without NPs showed that about 90% released, whereas in the presence of TCNB buffer and BSA it was around 51% and 23% respectively as shown in Figure 5.16. All the NP formulations showed a range of responses to MMP-9. TY-32 and TY-44 were among the most responsive to MMP-9 cleavability whereas TYR-3_PA and TY-41 were least responsive to MMP-9. Although being highly responsive to MMP-9, TY-32 was not investigated further due to precipitation caused in FBS. TY-13_CHF, TY-28 and TY-37 sensitivities were found to be between the highest and lowest. Interestingly, for TY-35, TY-38, TY-39, and TY-41 in the presence of active MMP-9, the release of the FSS was closer to other stimuli like water, NaCl and glucose. However, for rest of the NPs formulations the release of FSS was higher than other stimuli except FBS. To have an insight into the degradation kinetics of NPs in the presence of MMP-9, TYR-

3_CHF was synthesized with *F (C27-GGGRPLGLWCDI*FTNSRGKRA). The construct easily was dissolved in aqueous media against the parent construct with phenylalanine only. These NPs were incubated with MMP-9 and NMR spectra were obtained. Surprisingly, the NMR signal was not strong and were comparable to the background noise, while the NMR spectra of an MMP-9 responsive peptide (PLGLWG*FQ) showed a strong signal, which changed with time in the presence of MMP-9. These observations suggested that MMP-9 cleavable sequences might not have been available to MMP-9 and buried inside the NPs.

In the presence of BSA, release of FSS was significantly lower. One of the possible explanations was the formation of a protein corona that prevents the release of encapsulated drugs (395). This protein corona can affect the targeting ability of NPs (530). In DLS data, it was observed that the particle size before addition of BSA was around 90 nm and after addition of BSA increased to 615 nm.

After these release experiments, it can be deduced that these self-assembled peptide nanoparticles were sensitive to MMP-9 and can be tailored to exhibit desired release pattern. It was observed that the release profile in the presence of water, NaCl and glucose was almost similar, whereas in the presence of MMP-9 and FBS it was much quicker. It should also be noted that the sensitivity of novel enzyme-responsive self-assembled peptide NPs towards MMP-9 was lower than anticipated and measured by NMR experiment in NMR. One of the possible explanations could be due the dilution of MMP-9 inside the dialysis bag. In addition, MMP-9 require specific condition/environment (TCNB) to remain active and cleave peptide in experimental conditions. In the presence of BSA, release of FSS was very slow and only 20-30% released after 24 h. In the previous studies saline water (0.9 %) (531) and PBS (532) buffers are most commonly used.

In vitro toxicity of self-assembled NPs was assessed by LDH (Figures 5.18 – 5.20) and MTT (Figures 5.22 – 5.24) using HeLa and SH-SY5Y cell lines. It was found that the NPs were toxic at higher concentration whereas non-toxic at lower concentrations. At lower concentrations cells released less amount of LDH indicating relatively less toxic/safe. TY-20_CHF was found to be the most toxic formulation as shown in Figure 5.20. One of the possible explanations for that is positive charges in the peptide sequences as reported previously (533). Highly positively charged NPs can bind to negatively charged membrane and permeates easily in contrast to negatively charged and neutral NPs (534). Microscopic images for toxicity at different concentration is shown in Figure 5.21. TY-8 and TY-20 were not further investigated after toxicity studies. The reason behind that is the high toxicity of the NPs by both methods. NPs used in this project used up to 400 µg/mL were found to be significantly less toxic, whereas at higher concentrations of 0.75 mg/mL were found toxic. Similar findings were reported in previous studies (535, 536).

It was observed from all cytotoxicity experiments that self-assembled NP formulations with higher positively charged amino acids exhibited higher toxicity compared with less positively charged sequences (534). For example, TY-20_CHF is the NP formulation with six positively charged amino acids exhibited highest cytotoxicity even at its lowest concentration. However, TY-13_CHF, a NP formulation with only one positively charged amino acid in the sequence was found to be least cytotoxic. The toxicity and immunogenicity of these peptides decorated NPs depends on the surface charge (zeta potential), surface functional group, particle size and chemical composition (537). Lee et al. reported, Ag-CALNNK-NPs (positively charged) have lower toxicity than the Ag-CALNNE-NPs (negatively charged) (537). Kai et al. reported different toxicities of three similarly sized oleic acid-coated Fe_3O_4, carbon-coated Fe, and Fe_3O_4 NPs with different zeta potentials of

4.5, 23.7 and 14.5 mV. Baek et al. reported positively charged ZnO NPs exhibited greater toxicity compared with negatively charged ZnO NPs. Smaller particle sizes (20 nm) showed more toxicity than the larger size NPs (70 nm) (538). This suggests that the higher the surface charge, the greater the electrostatic interaction with the cell membrane. (535, 536). Tudisco et al. tested Fe_3O_4 magnetic NPs for toxicity using human brain microvascular endothelial cells (HBMEC) and A-172 cells. They used different concentration (10 and 20µg/mL) for 24, 48 and 72 hours. It was reported that all the formulations have around 90% cell viability in both cell lines (539). Based on the encapsulation, release and toxicity data NPs were shortlisted for further experiments. TY-13_CHF, TYR-3_PA, TY-28, TY-39, and TY-44 were selected for BBB (endothelial monolayer) *in vitro* experiments and *in vivo* brain delivery using the self-assembled peptide NPs. The selection of these NPs for *in vitro* experiment was based on various factors such as targeting ligand used, optimum particle size, suitable encapsulation capacity, rate of encapsulated drug release and lesser toxicity. TY-13_CHF were around 81 nm in size and the viability of the cells at a concentration of 0.75 mg/mL was around 85% and unique mini-Ap4 targeting was used. TYR-3_P.A exhibited the particle size of about 75 nm with encapsulation capacity of around 80%. Although cell viability at a concentration of 0.75 mg/mL was extremely low but inclusion of P.A and sRVG targeting ligand made it a candidate for further investigation. TY-28 were the smallest NPs with the size of about 42 nm and relatively safer at a concentration of 0.75 mg/mL. No hydrophobic moiety (CHF or P.A) was conjugated to facilitate the self-assembly. This modification and lesser toxicity made it suitable candidate for further investigation. In case of TY-39 and TY-44, although the particle size was larger than 200 nm, however encapsulation capacity was around 75 %. Furthermore, TY-39 was found to be safe at a concentration of 0.75mg/mL, however cell viability for TY-44 was lower. Another reason

that contributed for TY-44 selection was targeting ligand used. Targeting ligand used in TY-44 is reported to bind with TfR. These all characteristics were considered for further investigation of NPs.

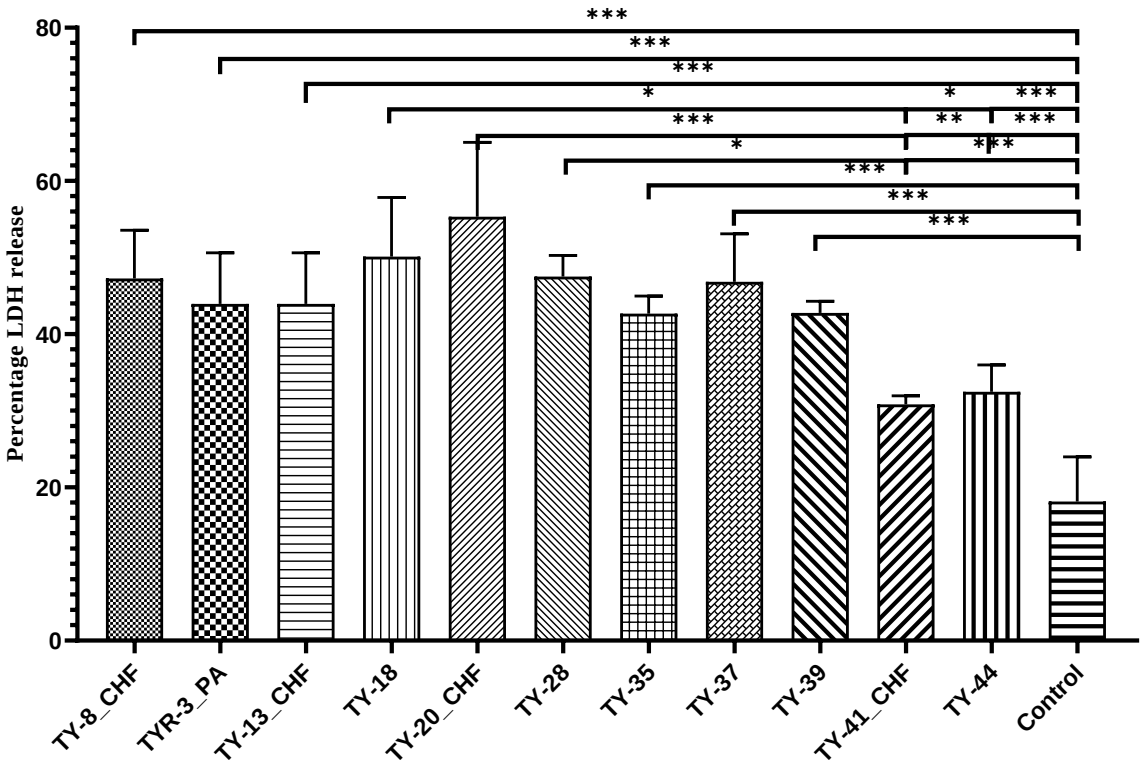

Figure 5. 18. In vitro cellular toxicity of enzyme-responsive self-assembled peptide nanoparticles at 0.0469 mg/mL) in SH-SY5Y cells measured by using LDH assay. Sterile water served as control.

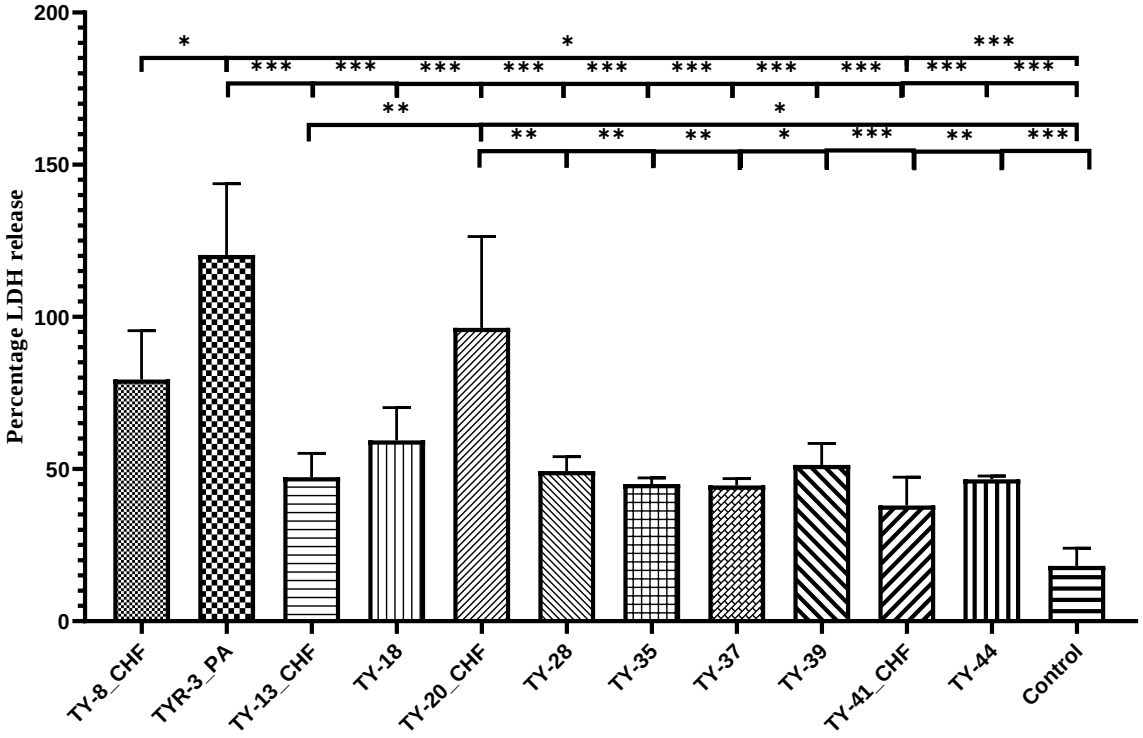

Figure 5. 19. In vitro cellular toxicity of enzyme-responsive self-assembled peptide nanoparticles at 0.1875 mg/mL) in SH-SY5Y cells measured by using LDH assay. Sterile water served as control.

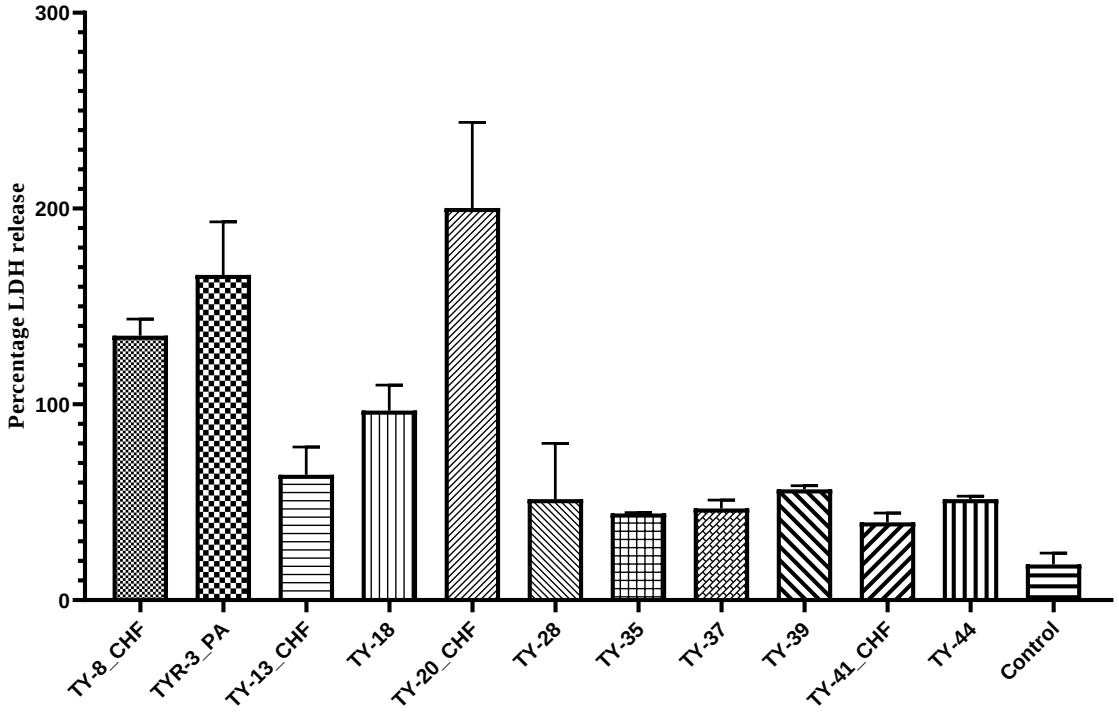

Figure 5. 20. In vitro cellular toxicity of enzyme-responsive self-assembled peptide nanoparticles at 0. 75 mg/mL) in SH-SY5Y cells measured by using LDH assay. Significance bars are not drawn here as it will make the graph more complex. Sterile water served as control.

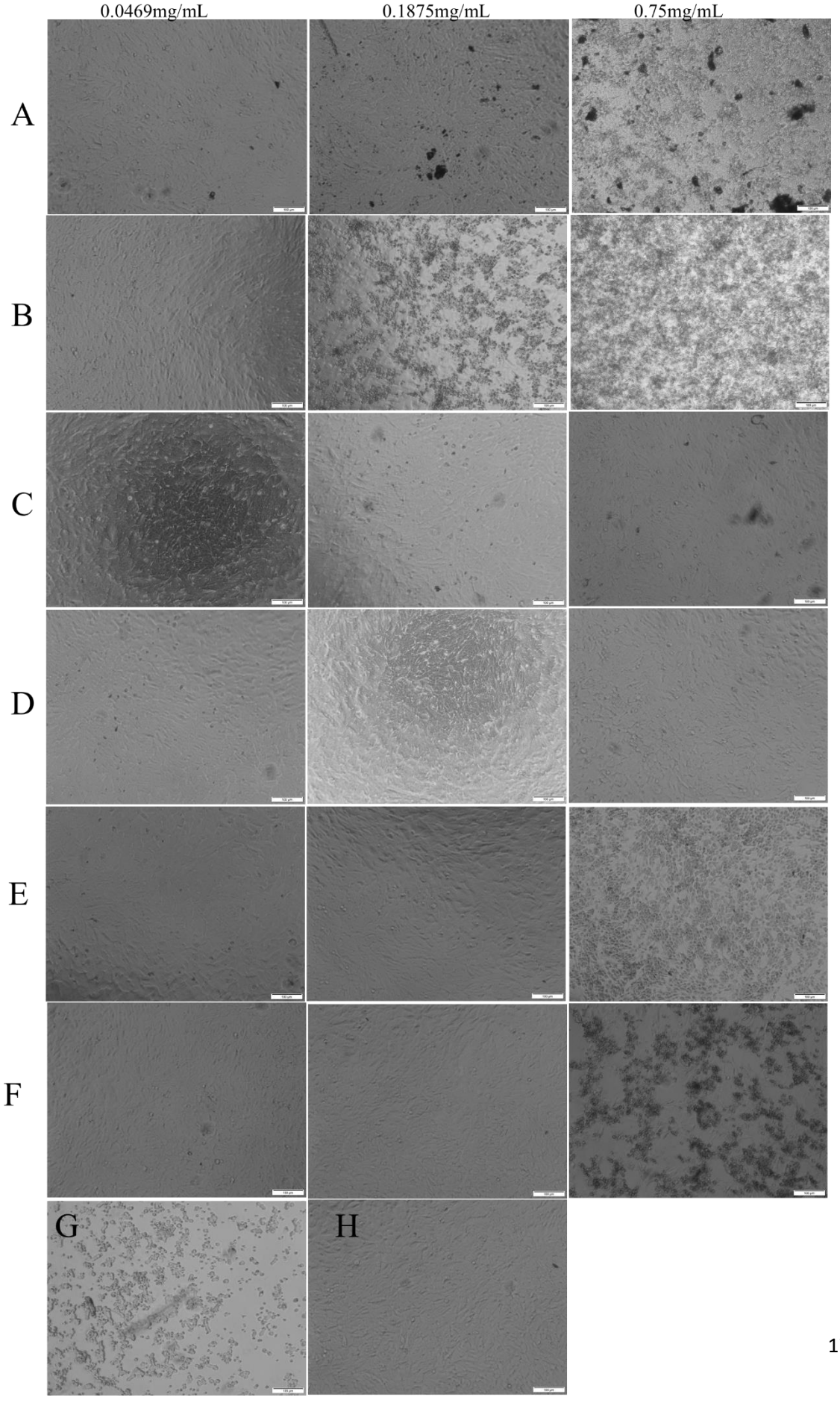
0.0469mg/mL
0.1875mg/mL
0.75mg/mL
A
B
C
D
E
F
G
H

Figure 5. 21. Microscopic images of SH-SY5Y cells treated with self-assembled peptide nanoparticles for 24 hours at different concentration (0.0469, 0.1875 and 0.75 mg/mL). ***A)*** *TY-8_CHF,* ***B)*** *TYR-3_PA,* ***C)*** *TY-13_CHF,* ***D)*** *TY-18,* ***E)*** *TY-20_CHF,* ***F)*** *TY-28,* ***G)*** *DMSO 5% and* ***H)*** *negative control (media only).*

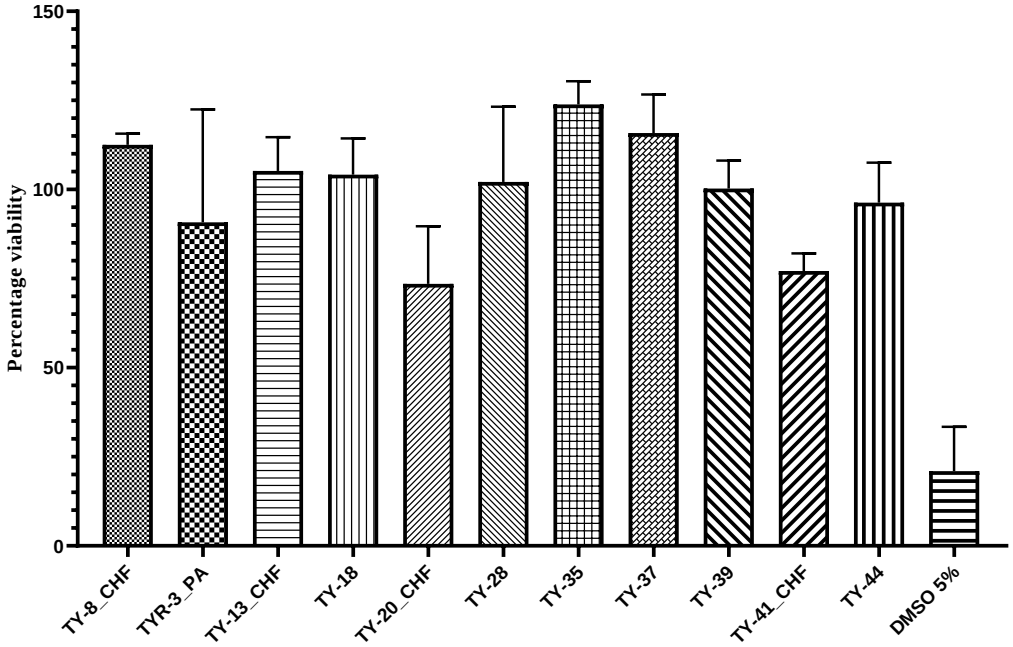

Figure 5. 22. In vitro cellular toxicity of enzyme-responsive self-assembled peptide nanoparticles at 0.0469 mg/mL) in SH-SY5Y cells measured by using MTT assay.

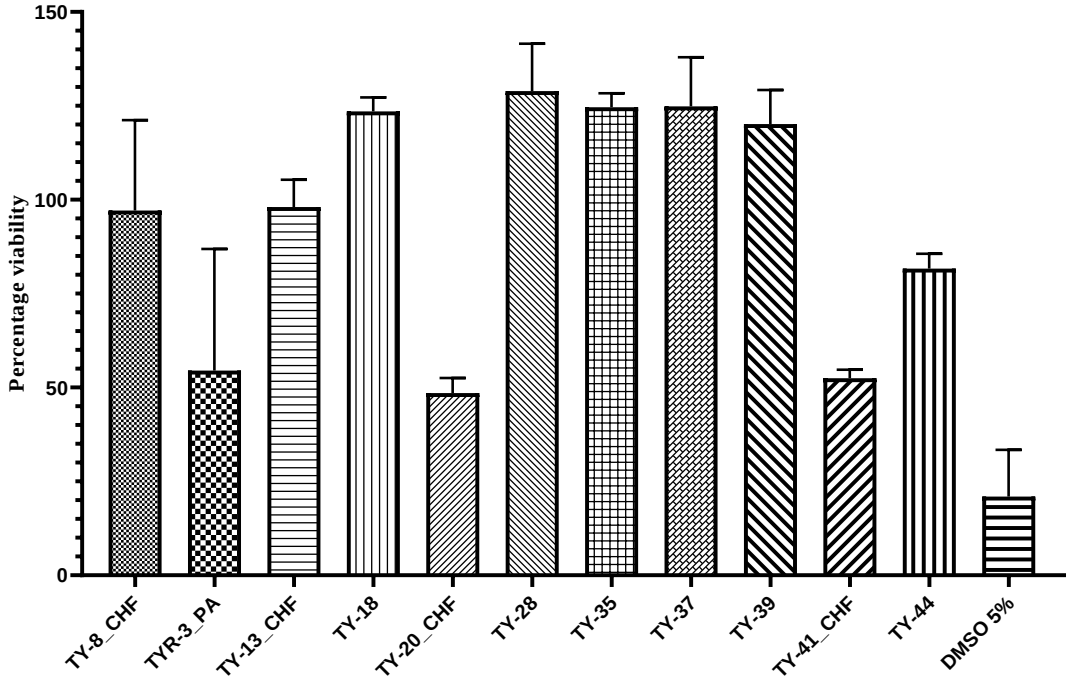

Figure 5. 23. In vitro cellular toxicity of enzyme-responsive self-assembled peptide nanoparticles at 0.1875 mg/mL) in SH-SY5Y cells measured by using MTT assay.

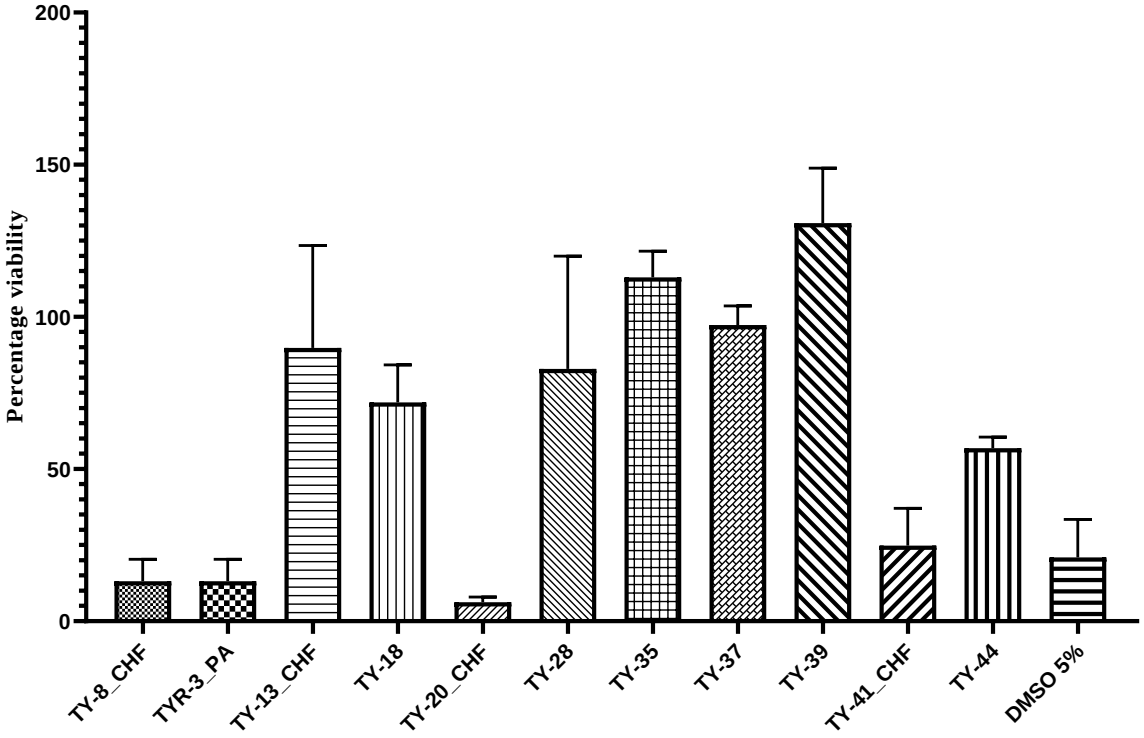

Figure 5. 24. In vitro cellular toxicity of enzyme-responsive self-assembled peptide nanoparticles at 0. 75 mg/mL) in SH-SY5Y cells measured by using MTT assay.

5.4. Conclusion

In this chapter, encapsulation capacities for novel enzyme-responsive self-assembled peptide nanoparticles were calculated by an indirect method. The encapsulation (FSS) capacity ranges from 40-80%. TY-28, TY-39 and TY-44 were among the highest encapsulation capacity nano-formulations. TY-32 and TY-35 had poorest encapsulation capacity. All NP formulations exhibited different release patterns of model drug in the presence of external stimuli. NP formulations were found to be MMP-9 sensitive. The sensitivity towards MMP-9 can be tailored by manipulating the sequence. Novel enzyme-responsive self-assembled peptide nanoparticles were found to be least cytotoxic at lower concentration, however at higher concentration they were found to be cytotoxic, showing a range of cell viabilities.

CHAPTER – 6 *IN VITRO* ENDOTHELIAL MONOLAYER PERMEABILITY

6.1. Introduction

Various techniques have been reported to measure and visualize the *in vitro* uptake of NPs by cells. Flow cytometry is a well-established diagnostic method that revolutionized cell diagnostics *in vitro* (540). Flow cytometry is a robust method to assess fluorescently labelled/fluorescent encapsulated NPs, taken up by cells (541). It rapidly analyses the single cell/particle suspended in buffered salt-based solution as it flow past single or multiple lasers. Each particle is analysed for visible light scatter and for various fluorescence parameters (542). Light scattered is measured in the forward direction (Forward Scatter or FSC) and at 90° (Side Scatter or SSC) these are indicative of relative size of the cell and internal complexity/granularity respectively (543) as shown in Figure 1. Samples for fluorescent measurements are prepared by transfection or expression of proteins (green fluorescent protein) (544, 545), encapsulating fluorescent substance such as dye or fluorescently labelled siRNA (546).

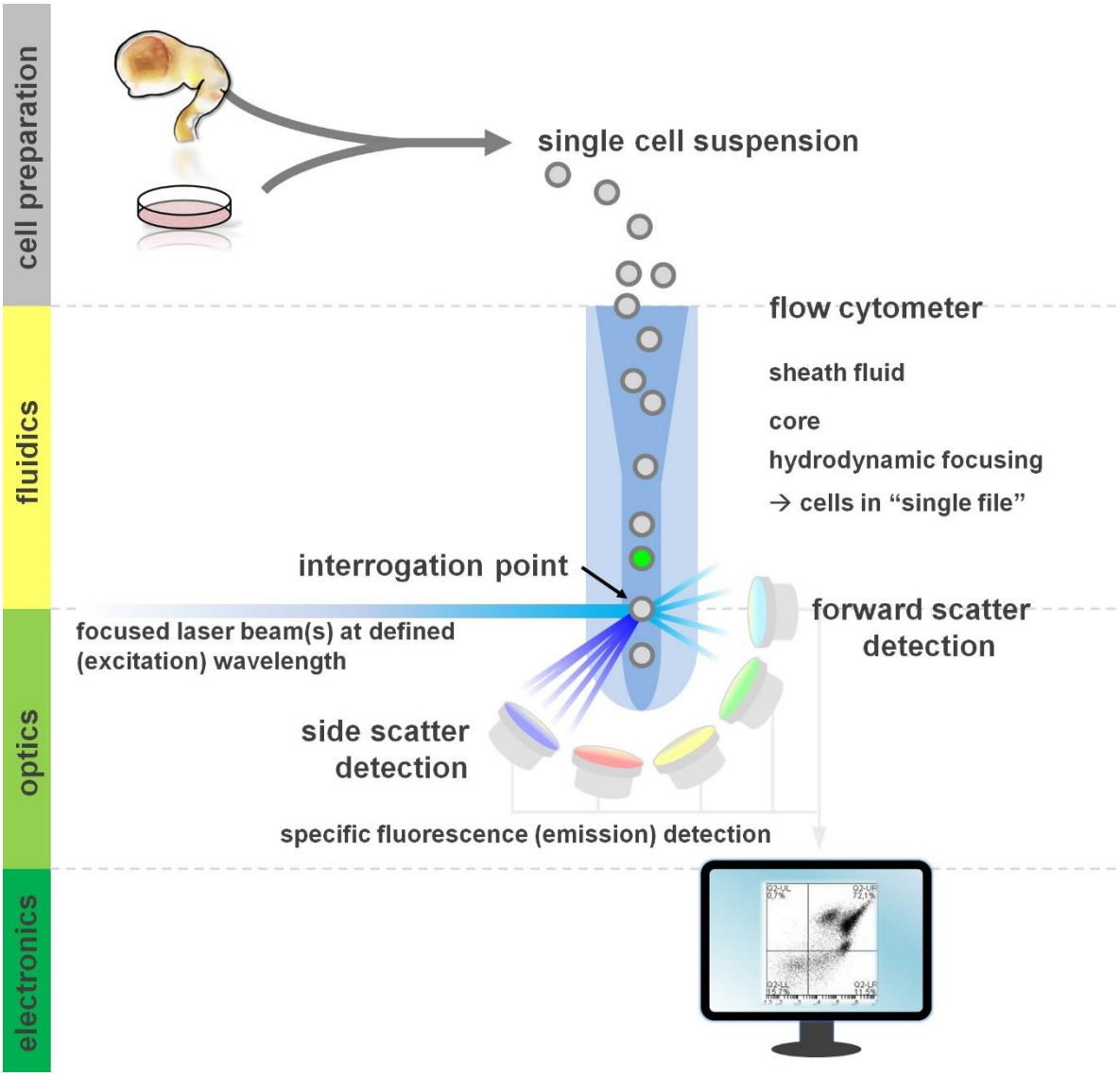

Figure 6. 1. Schematic presentation of FACS flow cytometry (547).

The visualization of nanoparticles/nano-carriers has become increasingly important in biomedical imaging (548). The confocal microscope utilizes pinhole technology that removes out of focus light at the image plane. It allows only focused light to the detector (549). Confocal microscopy offers a valuable tool to assess the delivery and function of siRNA at single cell resolution (550). Various fluorescent dyes and fluorescently labelled siRNA have been employed to track the NPs into cells. Risnayanti et al. have used Cy5.5-

labeled siRNA@PLGA NPs to evaluate the delivery of siRNA in SKOV3-TR and A2780-CP20 cancer cells (551). *In vitro* blood brain barrier models have been employed to assess the permeability of drugs and drug delivery systems. *In vitro* endothelial monolayer models offer the advantage of being inexpensive, robust and the potential for high throughput screening (552). The transwell migration assay has been employed to assess the ability of NPs to cross the membrane in numerous studies (264). These models range from simple monolayer to sophisticated spheroid and chip style models (553, 554). In this assay, cells are grown on the thin mesh surface until a layer of cells is formed. Monolayer formation is assessed by measuring Transepithelial/transendothelial electrical resistance (TEER). TEER is a widely used quantitative technique to assess the integrity of tight junctions in endothelial monolayer models. TEER values are indicative of endothelial monolayer integrity and are performed pre- and post-permeability experiments as shown in Figure 2. As mentioned in chapter 1, that histamine and bradykinin increase the permeability by disrupting the TJ (555). Numerous *in vivo* studies have reported increased BBB permeability by opening the interendothelial cell TJ when administered luminally or abluminally to microvasculature of the brain (556, 557). We investigated the effects of histamine and cimetidine (H_2 receptor antagonist) on the TEER values of hCMECD/3 cell line.

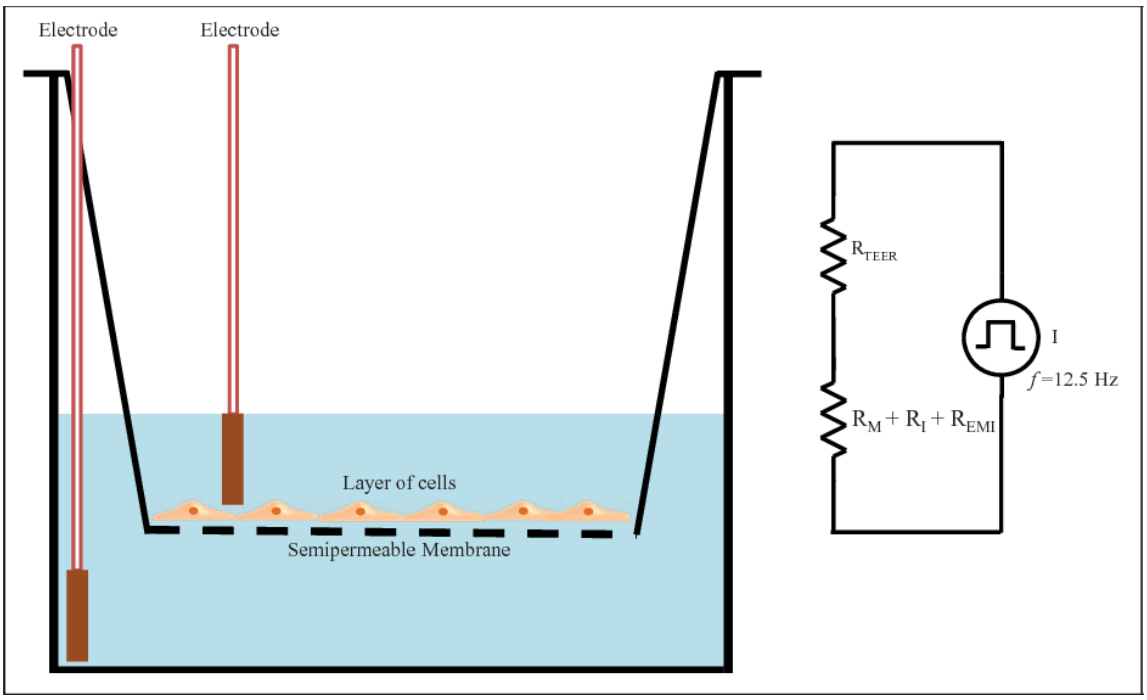

Figure 6. 2. Schematic presentation of TEER measurement and cell migration assay.

In this chapter, *in vitro* uptake and permeability was assessed by using multiple techniques such as flow cytometry, confocal microscopy, and *in vitro* blood brain barrier models. In addition, agarose gel electrophoresis was performed to assess the complex formation and protection of siRNA from serum enzymes. In chapter 5, following encapsulation efficiency, release profiling and cytotoxicity studies, the five best formulations were selected for further investigation based on various factors: higher encapsulation, better release profile, sensitivity to MMP-9, least cytotoxicity and different brain targeting ligands.

6.2. Material and Methods

6.2.1. Materials

Immortalized human brain endothelial (hCMEC/D3 cells) and EndoGRO-MV kit media (supplemented with EndoGRO-LS supplement, rh EGF, L-glutamine, hydrocortisone hemisuccinate, heparin sulfate, ascorbic acid and fetal bovine serum) were purchased from Merck EMD Millipore Corporation, 28820 Temecula, USA. Gibco DMEM growth media

with 10% FBS, 5% L-glutamine, FAM tagged negative siRNA and 5% anti-anti were purchased from Sigma Aldrich. Passage number used was from 1 to 11 with Lot number of 3,130,216. FITC-dextran with a molecular weight of 70 kDa, Histamine and Cimetidine were purchased from Sigma-Aldrich (Dorset, UK). Polyethylene terephthalate 0.4 μm inserts (Sarstedt, Leicester, UK) were obtained from Sarstedt. EVOM2 Trans Epithelial electric resistance (TEER) meter was obtained from world precision instruments, USA. FITC-dextran with a molecular weight of 70 kDa was purchased from Sigma-Aldrich (Dorset, UK). Polyethylene terephthalate 0.4 mm transwell inserts (Sarstedt, Leicester, UK) were obtained from Sarstedt.

6.2.2. Methods

6.2.2.1. In vitro cellular uptake/ Flow Cytometry

SH-SY5Y cells were seeded with a density of 20000 in a 24 well plate. Briefly, formulations containing siRNA-Fam and FSS were added to the wells. The plate was incubated with NPs for 1, 2 and 4 h. The DMEM media was aspirated and cells were washed to remove the excess of the formulation using PBS. The cells were detached from the plate by trypsinising (100 μL of trypsin) the cells. The trypsin was neutralized with addition of 200 μL of media. The cells were analysed using a BD Accuri™ C6 flow cytometer employing 488 nm and 640 nm lasers with fluorescence detection of FAM positive viable cells assessed using the FL-1 detector (λ_{ex} 488 nm; λ_{em} 533/30 nm). For the analysis, BD Flow software was used, and viable cells were positively gated based on forward and side scatter parameters and dead cells and cellular debris excluded from fluorescence measurement.

6.2.2.2. Confocal microscopy

To visualize the cellular uptake, confocal microscopy was performed by using Zeiss LSM 780 confocal microscopy system (Carl Zeiss Meditec AG, Jena, Germany). siRNA solution

(500 nM) was prepared in nuclease free water. Peptide (10 mg) was added to a pre-prepared solution of siRNA+FAM (1 mL). The self-assembly of the NPs facilitate the encapsulation/adsorption of siRNA. hCMEC/D3 cells were seeded into 4 chambered glass slides at a density of 30000 cells/well. Cells were incubated for 2 days and desired confluence was achieved. TYR-3_PA and TY-13 (0.3 mg/mL) were added to wells and incubated for 24 h. Cells were washed three time with PBS. 600 µL of cold methanol was added and the slide was placed in the freezer for 10 minutes. Methanol was decanted and cells were washed with PBS (2-3 times). DAPI (100 nM) solution (500 µL) was added to each well and left for 10 minutes. DAPI was decanted and washed with PBS 2-3 times and let it dry. Three to four drops of mounting media were added, and cover slip was placed. The slide was visualized under confocal microscope. Images were processed by using ImageJ software.

6.2.2.3. Electrophoresis/Agarose gel retardation

Complex formation and serum protection assay for enzyme-responsive self-assembled peptide NPs with siRNA was performed using an agarose gel retardation electrophoresis assay. Briefly, 1% gel was cast in the mould (1.5 g of agarose was dissolved in 100 mL of Tris/Borate/EDTA (TBE) buffer by boiling). Red dye (GelRed) (2 µL) was added to the solution and left to cool.

After cooling to room temperature, the sample was added into each well (8 µL of peptide + siRNA with 3 µL of loading dye (bromophenol blue and xylene cyanol FF)) siRNA and FBS mixture (50:50) was also analysed over a period of 24 h to measure any degradation of siRNA. For complex formation dilutions of peptide solutions were prepared and siRNA was added. Electrophoresis was performed by using BIO-RAD PowerPack High Current Power Supply at 70mV for 20mniutes. The gel was analysed with a BIO-RAD spectrophotometer.

6.2.2.4. Transepithelial electrical resistance (TEER) measurement and preliminary experiment

For the assessment of NPs permeability across the endothelial monolayer, hCMEC/D3 cells were seeded in Sarstedt TC inserts (24 well, PET 0.4 µm) at the densities of 30000, 60000 and 90000 cells/insert. 500 µL of EndoGRO media was added to the apical compartment and 1.6 mL of EndoGRO media was added to basolateral compartment. The culture plate was placed in an incubator at 37ºC with 5% CO_2. Cells were grown for 24, 48, 72 and 140 h and TEER values were measured using Epithelial Volt/Ohm (TEER) Meter via standard STX2 handheld "chopstick" electrodes. Briefly, STX2 electrodes were dipped into 100% ethanol for 10-15 min then dried to ensure the complete evaporation of ethanol. After assurance of complete removal of ethanol, STX electrodes were dipped in a way that one arm embedded in the insert and the other arm was dipping in the media around the insert in the well.

6.2.2.5. In vitro endothelial monolayer permeability

The endothelial monolayer *in vitro* model was constructed using a protocol supplied by Merck Millipore. *In vitro* permeability across the mono layer of neural cells was performed using immortalized hCMEC/D3 cells in a Transwell-type endothelial monolayer model (Figure 6.3). hCMEC/D3 cells were seeded (90000 cells/insert) in Sarstedt transwell inserts (PET 0.4 µm, TP) pre-coated with Collagen I, rat tail as described in protocol. Cells were cultured using EndoGRO media (SCME004) supplemented with hydrocortisone, ascorbic acid, heparin sulfate, rh EGF, L-glutamine, EndoGRO-LS supplement and 5% FBS. TC inserts were placed in a 24 well plate containing 1.6 mL of pre-warmed (37ºC) in each well (basolateral compartment). After 24 h, TEER was measured by using EVOM^2 (World Precision Instruments, Sarasota, Florida, USA). The contents of the (300 µL) was replaced every 24 h with fresh media. At the highest TEER values, NP (0.380 mg/mL except TYR-3_PA 0.200 mg/mL) formulations (encapsulated with FAM+siRNA) were added to the

apical compartment at final concentration. Fluorescence in the basolateral compartment was measured after every h using a SpectraMax i3X multi-mode microplate reader (Molecular Devices, USA) at excitation wavelengths of 460 nm and emission at 495 nm. Fluorescence was measured up to 6 h and each experiment was performed in triplicate. Furthermore, active MMP-9 (2 nM / 140 ng) was added to the basolateral compartment in order to assess whether after crossing the endothelial monolayer, NPs get metabolized by the MMP-9.

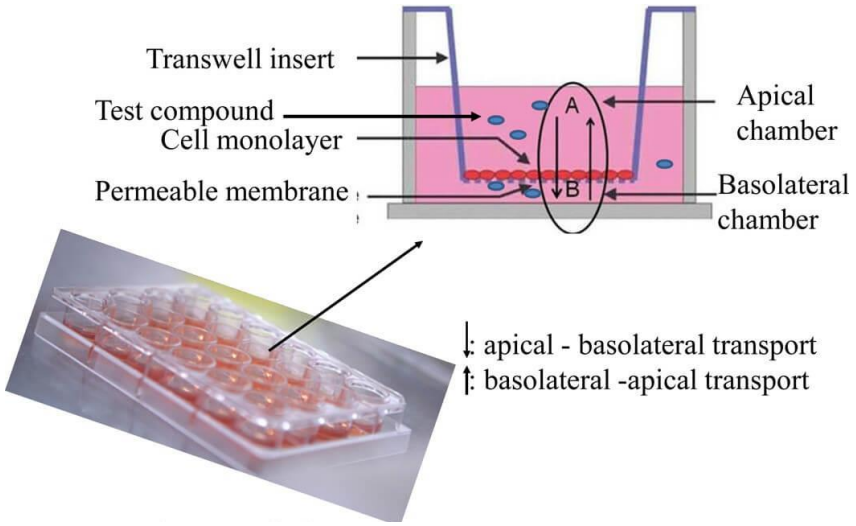

Figure 6. 3. Schematic representation of the transwell setup used for endothelial monolayer permeability experiments.

Prior to the permeability experiment, the sensitivity of the endothelial monolayer was tested by using histamine and cimetidine. Briefly, media were replaced, and histamine was added in to inserts at a final concentration of 50 mM. The plate was incubated for 30 min at 37 ^{o}C. TEER values were measured at 36 h. Cells were washed with sterile PBS buffer and fresh media were added. Cimetidine was added into inserts at a final concertation of 50 mM. The plate was incubated for 1 h and TEER values were measured. Culture media were replaced with fresh media and incubated for 12 h. TEER values were measured again after 48 h. Furthermore, TEER values were determined after transmigration tests. All

measurements were carried out in triplicate, means and standard deviations (SD) were also calculated (558).

6.2.2.6. In vitro endothelial monolayer permeability by mimicking physiological conditions

In addition, two experiments were conducted in the presence of MMP-9. MMP-9 was added to apical and basolateral compartments to mimic the healthy (50 ng/mL) and diseased individuals (100 ng/mL) (559, 560). After 6 h, cells were washed with PBS carefully and pre-heated media was added. TEER values were measured again and media was replaced with pre-heated fresh media. 10 µL of FITC-Dextran solution (1 mg/mL) was added to the inserts and florescence (λ_{exc} 485, λ_{ems} 520) was measured in the basolateral compartment for 6h.

6.2.2.7. Statistical Analysis

GraphPad Prism Software 8.0.1 for Windows (GraphPad Software, Inc., La Jolla, CA, USA) was used to conduct one-way analysis of variance (ANOVA) followed by Tukey's post-hoc test for multiple comparisons in order to identify any statistically significant differences between the treatment groups. For statistical comparisons, $P<0.05$ was considered a statistically significant difference.

6.3. **Results and Discussion**

The uptake of enzyme-responsive self-assembled peptide NPs loaded with siRNA+FAM was investigated by flow cytometry (561). In a previous study, uptake of AgNPs was studied by flow cytometry (562). It was reported that positively charged AgNPs accumulated more readily than other AgNPs (562). Lin et al. reported a 2.5-fold increased uptake of bovine serum albumin NPs decorated with a cell-penetrating peptide (LWMP) compared to non-decorated NPs in U87 cells (262). Enzyme-responsive self-assembled NPs developed in this project exhibited the same characteristics. Clear differences in the fluorescence were

observed after 4 h for both TY-13_CHF and TYR-3_PA as shown in Figure 6.4. Cellular uptake of encapsulated siRNA was significantly higher than the naked siRNA. These novel enzyme-responsive self-assembled NPs were able to penetrate the neural cells because of the brain-targeting ligand. (138, 171) It was noticed that penetration was time dependent. In the first hour, uptake was less but with the passage of time, up to 4 h, it increased substantially. Cellular uptake was confirmed by confocal microscopy.

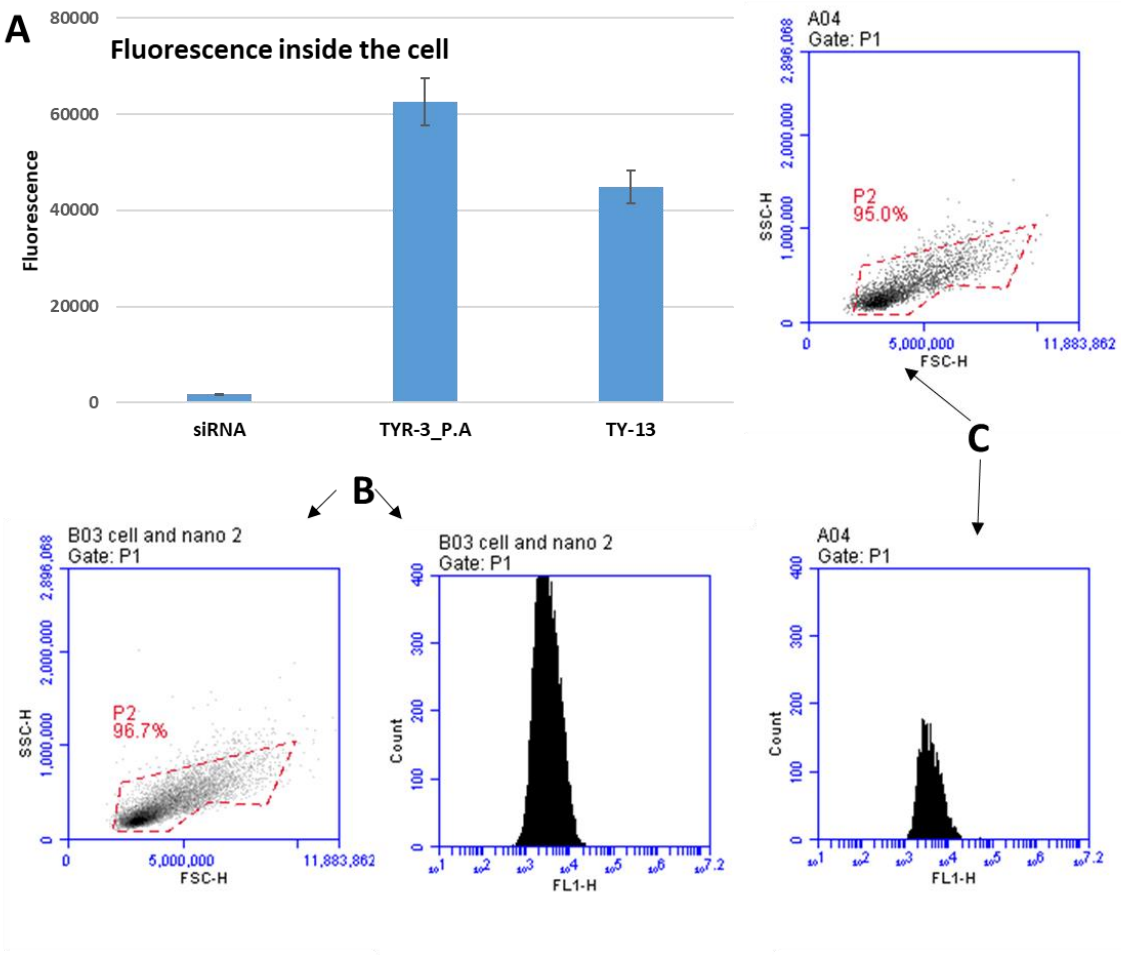

*Figure 6. 4. In vitro cellular uptake of self-assembled peptide NPs. **A**) FACS analysis for cellular uptake (fluorescence) shown in bar chart. **B**) FACS chromatogram for TYR-3_PA after 4 h and **C**) FACS chromatogram for TY-13_CHF after 4 h.*

The uptake of enzyme-responsive self-assembled peptide NPs showed higher uptake compared to naked siRNA, with the exception for TY-20 as shown in Figure 6.5. The uptake of TY-28 and TY-44 was highest compared to other formulations as shown in Figure 6.7. The uptake of NPs was time-dependent and was confirmed in TY-28 as shown in Figure 6.6.

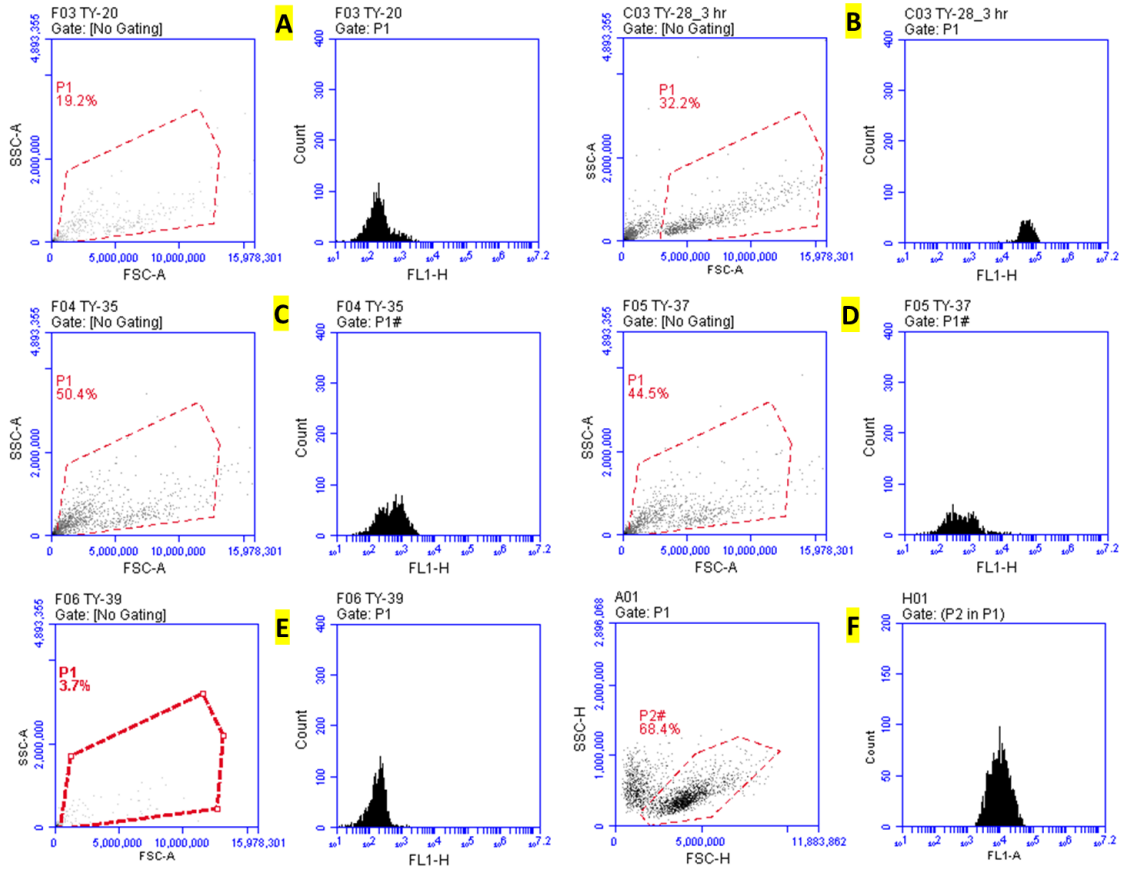

*Figure 6. 5. In vitro cellular uptake of self-assembled peptide NPs. **A**) FACS chromatogram for TY-20 after 1 h. **B**) FACS chromatogram for TY-28 after 3 h and **C**) FACS chromatogram for TY-35 after 1 h. **D**) FACS chromatogram for TY-37 after 1 h **E**) FACS chromatogram for TY-39 after 1 h **F**) FACS chromatogram for TY-44 after 1 h.*

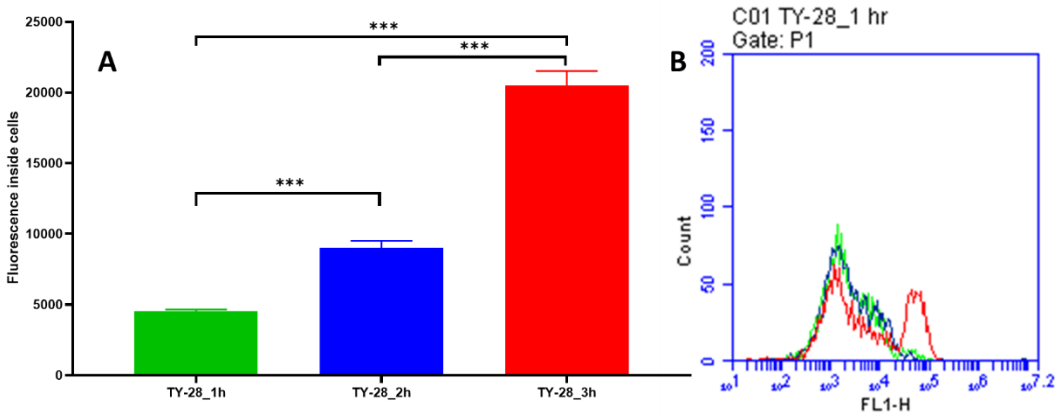

*Figure 6. 6. In vitro cellular uptake of TY-28, an enzyme-responsive self-assembled peptide NP. **A**) Uptake of the NPs by SH-SY5Y cells was time-dependent shown in bar chart. **B**) Uptake of the NPs over a period of 3 h: green denotes the uptake after 1 h incubation, blue represents uptake after 2 h and red line corresponds to uptake after 3 h.*

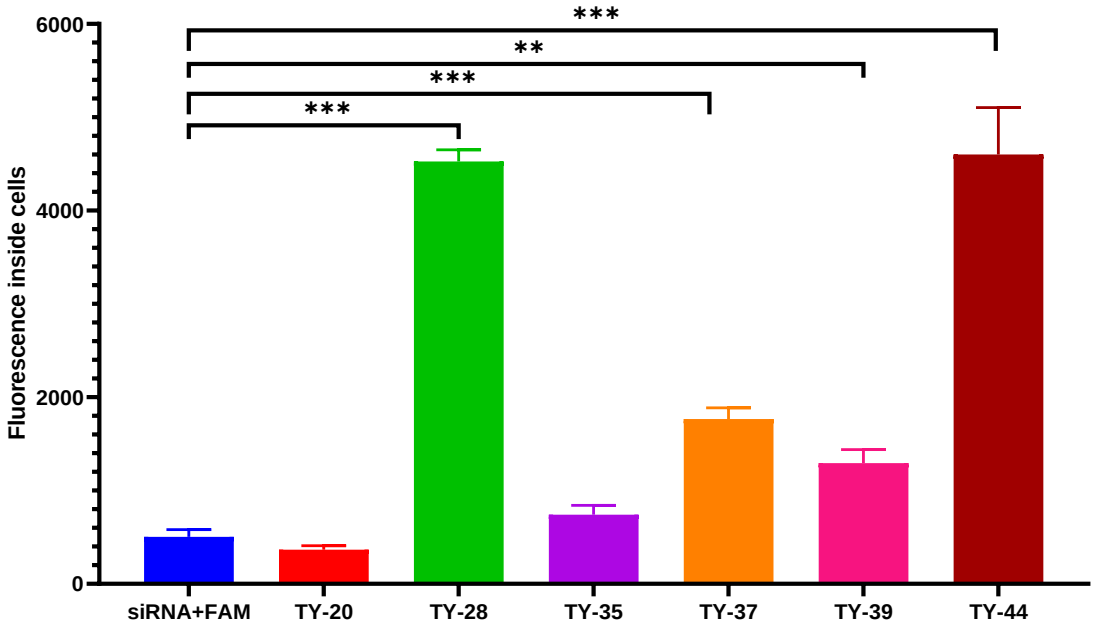

Figure 6. 7. FACS analysis for cellular uptake of siRNA+FAM encapsulated in enzyme-responsive self-assembled NPs in SH-SY5Y cells incubated for 1 h shown in bar chart.

The uptake of enzyme-responsive self-assembled peptide NPs loaded with siRNA+FAM was visualized by confocal microscopy (563). Briefly, hCMEC/D3 cells were cultured in pre-coated chambered slides. After desired confluence, NPs were added and incubated after 24 h. Cells were washed with PBS, fixed with ice cold methanol, mounted on the slide and

observed using confocal microscopy. siRNA+FAM on its own was employed as a control. From the images presented in Figure 6.8 – 6.11, uptake of NPs can be observed and can be seen in the cell cytoplasm around the nucleus. However, no evidence of siRNA+FAM administered as a control was found inside cells.

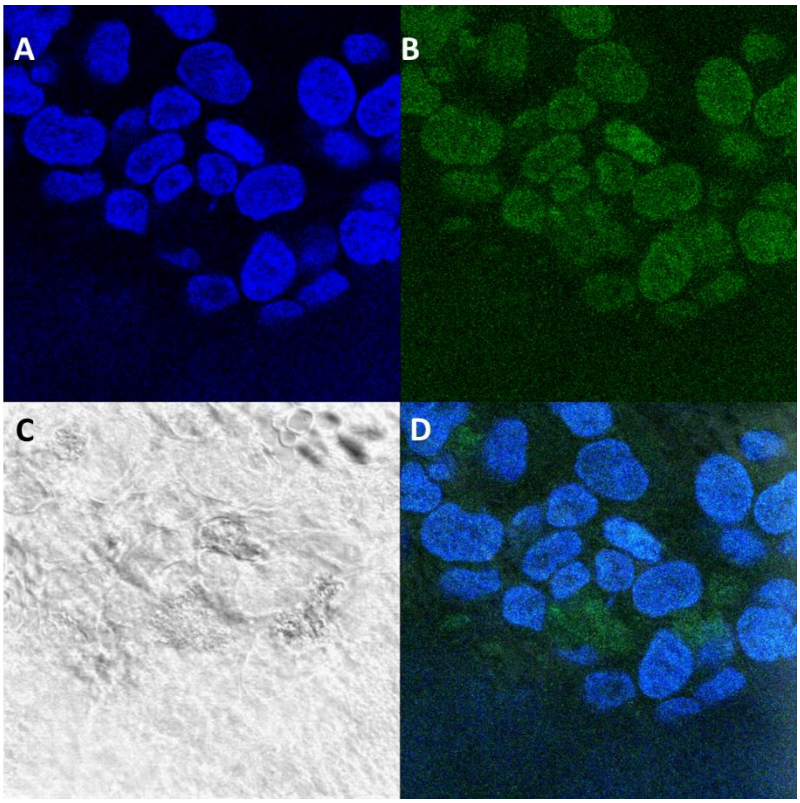

Figure 6. 8. Confocal microscope images of hCMEC/D3 cells following incubation with TY-13_CHF NPs for 24 h. ***A)*** *DAPI channel,* ***B)*** *FAM channel,* ***C)*** *bright field channel and* ***D)*** *merged image, DAPI stained nucleus as blue, green colour (FAM) around the nucleus.*

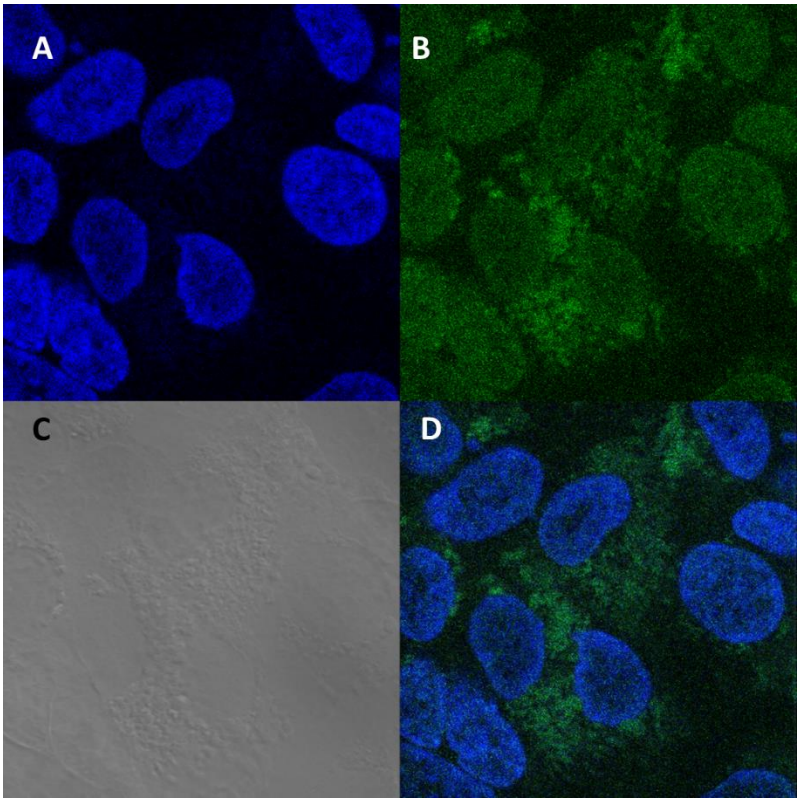

Figure 6. 9. Confocal microscope images of hCMEC/D3 cells following incubation with TYR-3_PA NPs for 24 h. ***A)*** *DAPI channel,* ***B)*** *FAM channel,* ***C)*** *bright field channel and* ***D)*** *merged image, DAPI stained nucleus as blue, green colour (FAM) around the nucleus.*

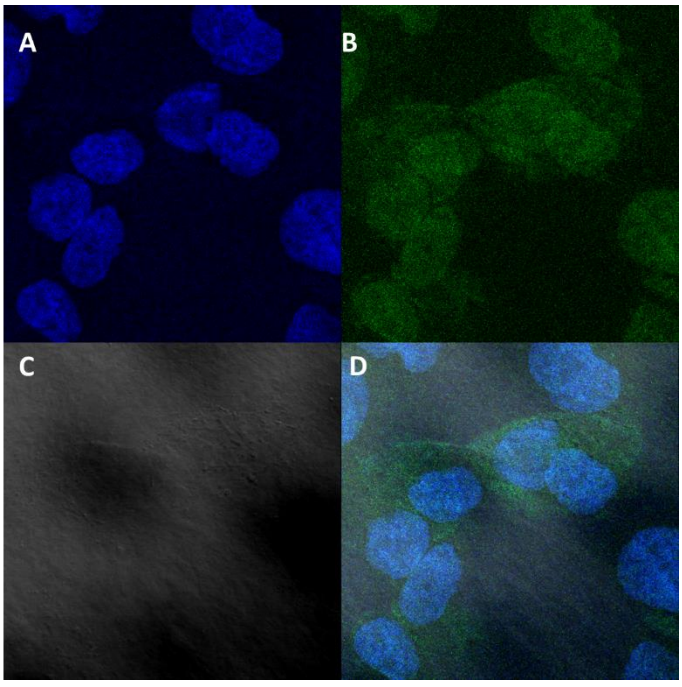

Figure 6. 10. Confocal microscope images of hCMEC/D3 cells following incubation with TY-28 NPs for 24 h. ***A)*** *DAPI channel,* ***B)*** *FAM channel,* ***C)*** *bright field channel and* ***D)*** *merged image, DAPI stained nucleus as blue, green colour (FAM) around the nucleus.*

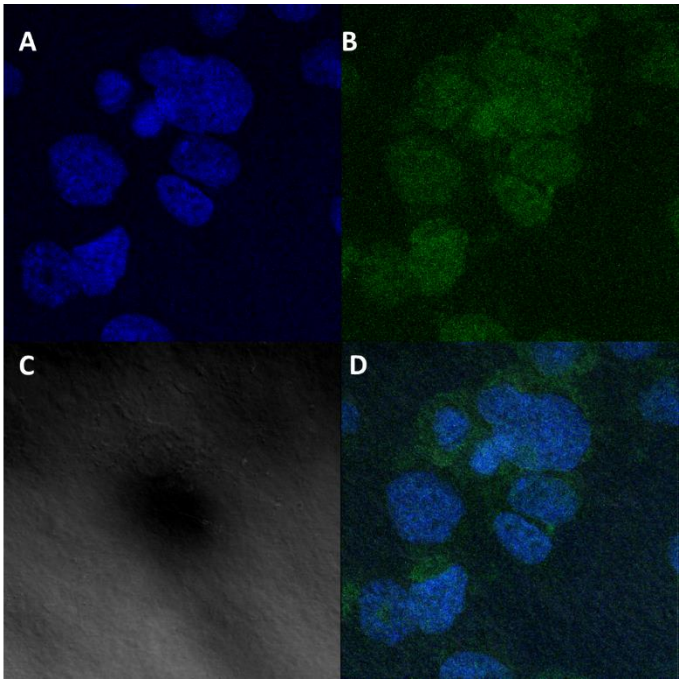

Figure 6. 11. Confocal microscope images of hCMEC/D3 cells following incubation with TY-44 NPs for 24 h. ***A)*** *DAPI channel,* ***B)*** *FAM channel,* ***C)*** *bright field channel and* ***D)*** *merged image, DAPI stained nucleus as blue, green colour (FAM) around the nucleus.*

To assess the complex formation and siRNA loading ability, agarose gel retardation was used. It was found that TYR-3_PA formed a complex with siRNA as shown in Figure 6.12. Complex formation of siRNA with siRNA was achieved at N/P of 20, suggesting that TYR-3_PA NP was able to bind with siRNA to hinder degradation in the process of electrophoresis. However, in blank where siRNA+FAM was subjected to electrophoresis on its own, the gel indicated the presence of siRNA. A similar pattern was observed for TY-28 NPs as shown in Figure 6.12C. Results for the agarose gel retardation assay in this study coincide with the literature reported results by Xia et al. (564). On the other hand, TY-13 did not form a complex with nucleotide across a wide range of concentrations according to agarose gel retardation assay, perhaps due to having only a single positive electrostatic charge in the construct. However, in the following (Figure 6.17) it will be shown that TY-13_CHF NPs were able to transport siRNA across the endothelial monolayer model. It may be speculated that TY-13_CHF encapsulated siRNA in a similar way as liposomes, i.e. TY-

13_CHF NPs were nano-hollow-vesicles. As mentioned in chapter 4, majority of enzyme-responsive self-assembled peptide NPs were positively charged, however siRNA was negatively charged. This opposite charge facilitated the adsorption/encapsulation of siRNA on the NPs. It should also be noted that FSS is relatively small molecule than the siRNA that enables its encapsulation. However, siRNA is larger molecule with negative charge favours the adsorption on the surface of NPs.

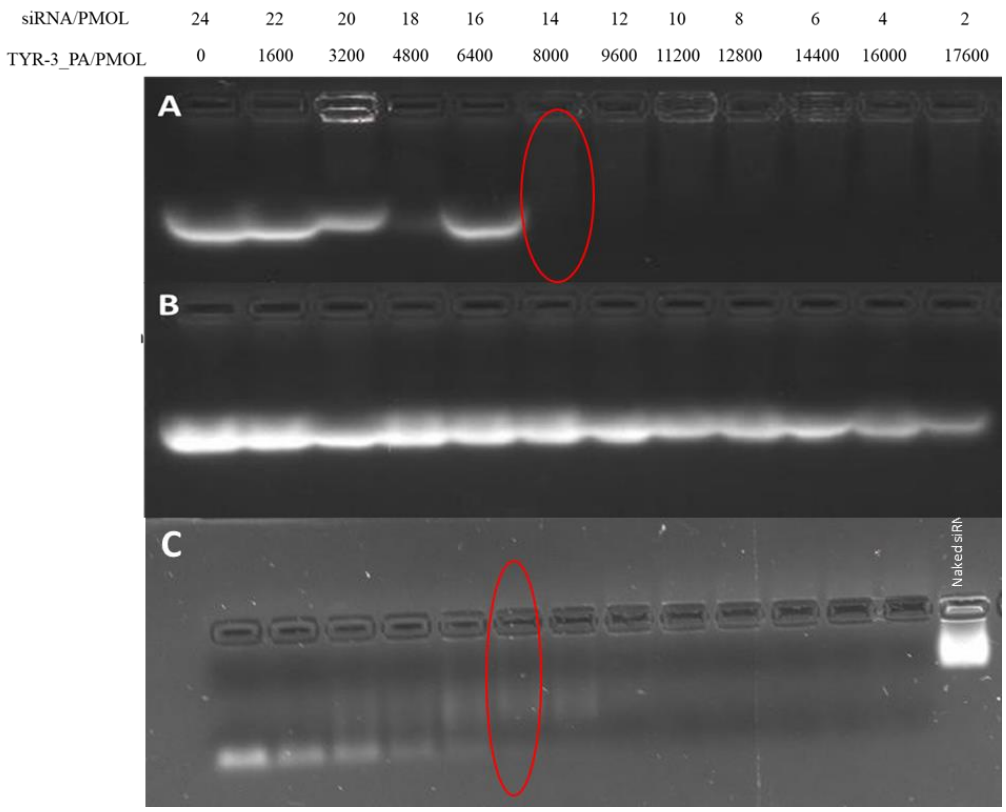

*Figure 6. 12. Agarose gel electrophoresis of siRNA-Fam and in complex with peptide NPs. **A**) It shows the siRNA-Fam and TYR-3_PA NPs in combination. Formation of complex and disappearance of siRNA is encircled red **B**) siRNA+FAM only. At N/P of 20 peptide forms complex and no signal observed in gel. **C**) It shows the siRNA-Fam and TY-28 NPs in combination suggesting the complex formation and disappearance of the siRNA encircled red.*

RNAse present in the serum can completely degrade the siRNA (565). There is a need to ensure the stability of siRNA in the presence of serum to improve the intracellular transfection efficiency (566). For evaluating the ability of enzyme-responsive self-assembled

peptide NPs to protect siRNA from degradation in serum, NPs encapsulating siRNA were incubated in DMEM medium with 50% FBS and the stability was assessed by gel retardation assay. siRNA on its own was almost degraded by RNAse after 1 h incubation. After 2 h incubation, naked siRNA was completely digested by RNAse and no signal was observed in the gel. However, siRNA encapsulated in TY-28 NPs was protected reasonably after 2 h incubation. This suggests that the NPs could protect siRNA from RNAse up to a certain time (2h) (564).

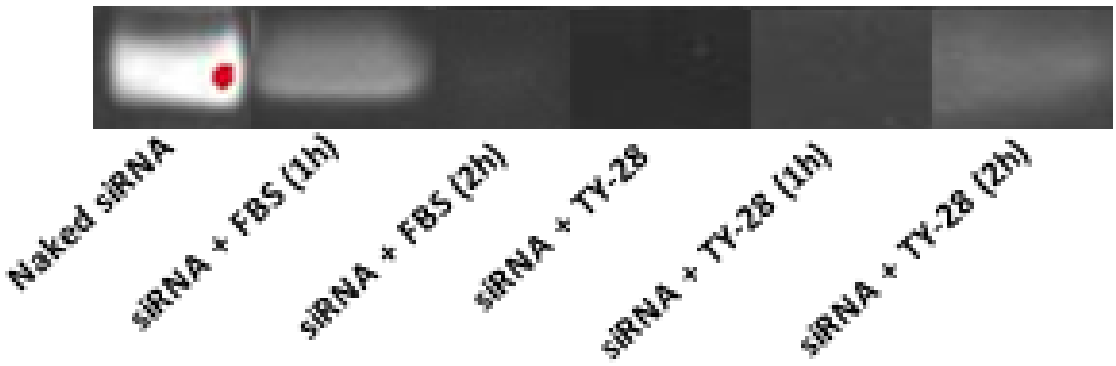

Figure 6. 13. Agarose gel electrophoretogram showing siRNA protection by TY-28 for different incubation compared to naked siRNA in serum. Naked siRNA not exposed to RNAse was used as control.

In order to assess the endothelial monolayer permeability, the same protocol was used as described in our previously published work (558). The human endothelial hCMEC/D3 cell line was chosen as a suitable model for simulation of the endothelial monolayer. hCMEC/D3 cell lines have been employed in numerous studies exploring permeability or transmigration (567-570). Although Biemans et al. questioned the hCMEC/D endothelial monolayer integrity, it remains one the most used cell line for permeability experiments. Numerous studies have reported the use of hCMEC/D3 as a endothelial monolayer model (571, 572).

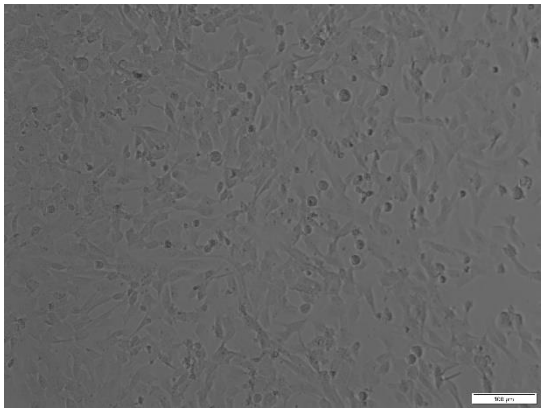

Figure 6. 14. hCMEC/D3 cell grown for 24 h, 10x magnification. Images taken by OLYMPUS IX71 microscope.

For *in vitro* permeability, preliminary experiments were performed to assess the formation and integrity of the endothelial monolayer model. TEER was measured as it has been linked with this integrity (573). hCMEC/D3 cells were seeded at 30000, 60000 and 90000 cells/insert. TEER values were measured. These were found to be 16, 34 and 56 Ω cm^2 respectively. It was observed the TEER values increased with increasing density up to a certain time. But after that, TEER values slumped due to the cell's death in the inserts. TEER values for insert with 90000 cells went to 92 from 147 Ω cm^2 after 140 h as the cells started dying. However, 136 Ω cm^2 was recorded for the insert with 30000 cells after 140 h. It is indicative that the cells are still growing and have enough nutrients. Maherally et al. reported the highest TEER value of 920 Ω cm^2 at a density of 75000 cells/well after 60 h (574). Biemans et al. reported TEER value of 8.7 Ω cm^2 after a 4-day incubation.

Various factors can affect the TEER values in both experiments, firstly, Biemans used passage 28-35 (575), whereas we used passage number from 1-10. Secondly, EBM2 basal media was used, but we used EndoGRO™ basal media. Hydrocortisone in the experiments by Biemans et al. was at 1.4 µM whereas we used 2.76 µM at final concertation. It has been reported that addition of extra hydrocortisone leads to higher TEER values (576). TEER values in the range of 20 to 200 Ωcm^2 have been reported (576). High TEER values (reaching

levels of 1000-1200 Ω cm^2) have been achieved under specific experimental conditions (577). Winger et al. reported the TEER values between 200-250 Ω cm^2 (578). These TEER values coincide with our findings. From this preliminary experiment 90000 cells/ insert was selected for further experiments.

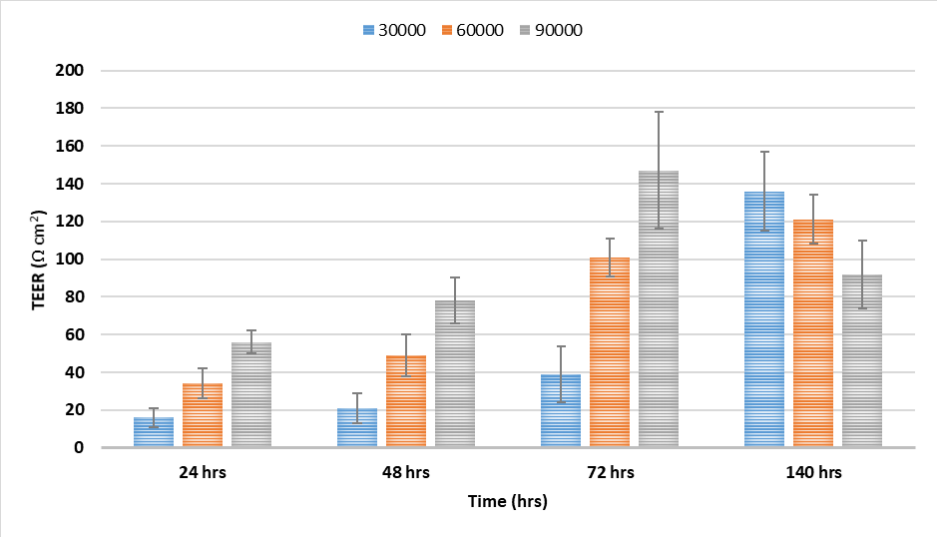

Figure 6. 15. TEER values for hCMEC/D3 cells grown in EndoGRO media for different time intervals at density of 30000, 60000 and 90000 cells/insert.

For further assessment of the NP formulations, cells were seeded in the inserts at 90000 cells/insert. TEER values were measured at 24, 36 and 48 h. These conditions were used to assess the effect and response of hCMEC/D3 cells towards different external stimuli such as Histamine, a H_{1-4} G-protein coupled receptor (50 µM at final concentration), Cimetidine, a H_2 receptor antagonist (50 µM at final concentration) and siRNA. TEER values were measured after 24 h. Histamine was added into one of the inserts. In another insert cimetidine and histamine were added and TEER values were measured.

The TEER values of the endothelial monolayer model reached 239 ± 28 Ω cm^2 after 48 h of incubation; and slightly increased to 250 ± 13 Ω cm^2 after the treatment of the cells with MMP-9 inhibiting NPs. Histamine treatment resulted in the reduction of TEER values from

200 Ω cm^2 to 62 Ω cm^2. Treatment with cimetidine helped the TJ to restore their integrity up to 145 Ω cm^2 as shown in Figure 6.16.

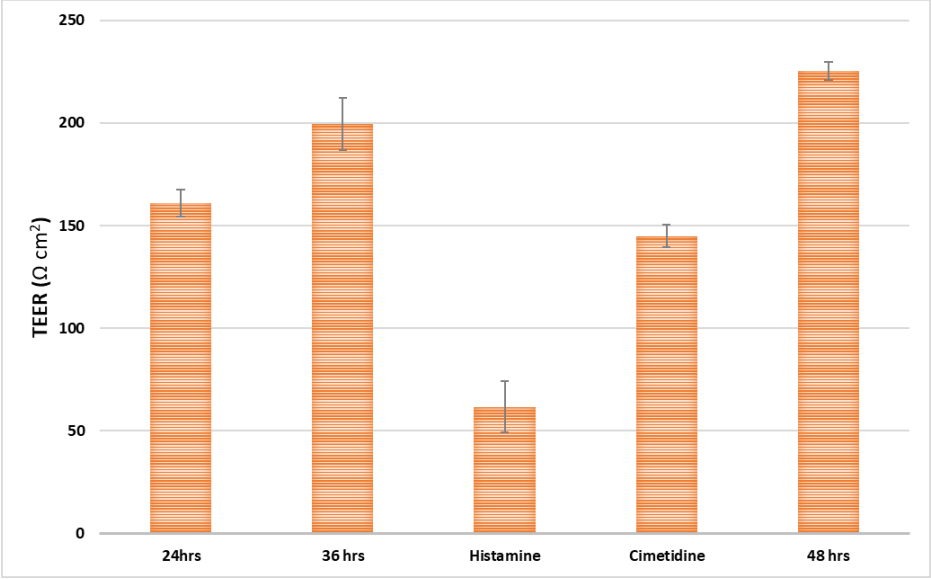

Figure 6. 16. TEER values for in vitro endothelial monolayer prepared by hCMEC/D3 cells seeded at 90,000 cells/insert after 24 h, 36 h, post histamine and post cimetidine treatment, presenting formation of a biological barrier that can be compromised by pharmacological compounds (histamine) and restated by pharmacological agents (cimetidine). Error bar indicate SD (n = 3).

After 48 h when the TEER values were restored to their highest, NP formulations encapsulating/adsorbing siRNA+FAM were added. siRNA+FAM was added to one insert serving as control. In addition to that, histamine and cimetidine were added to the inserts along with siRNA+FAM. Fluorescence was measured in the basolateral compartment every hour up to 6 h at excitation λ of 465 and emission λ of 495 nm and TEER values were measured after the experiment.

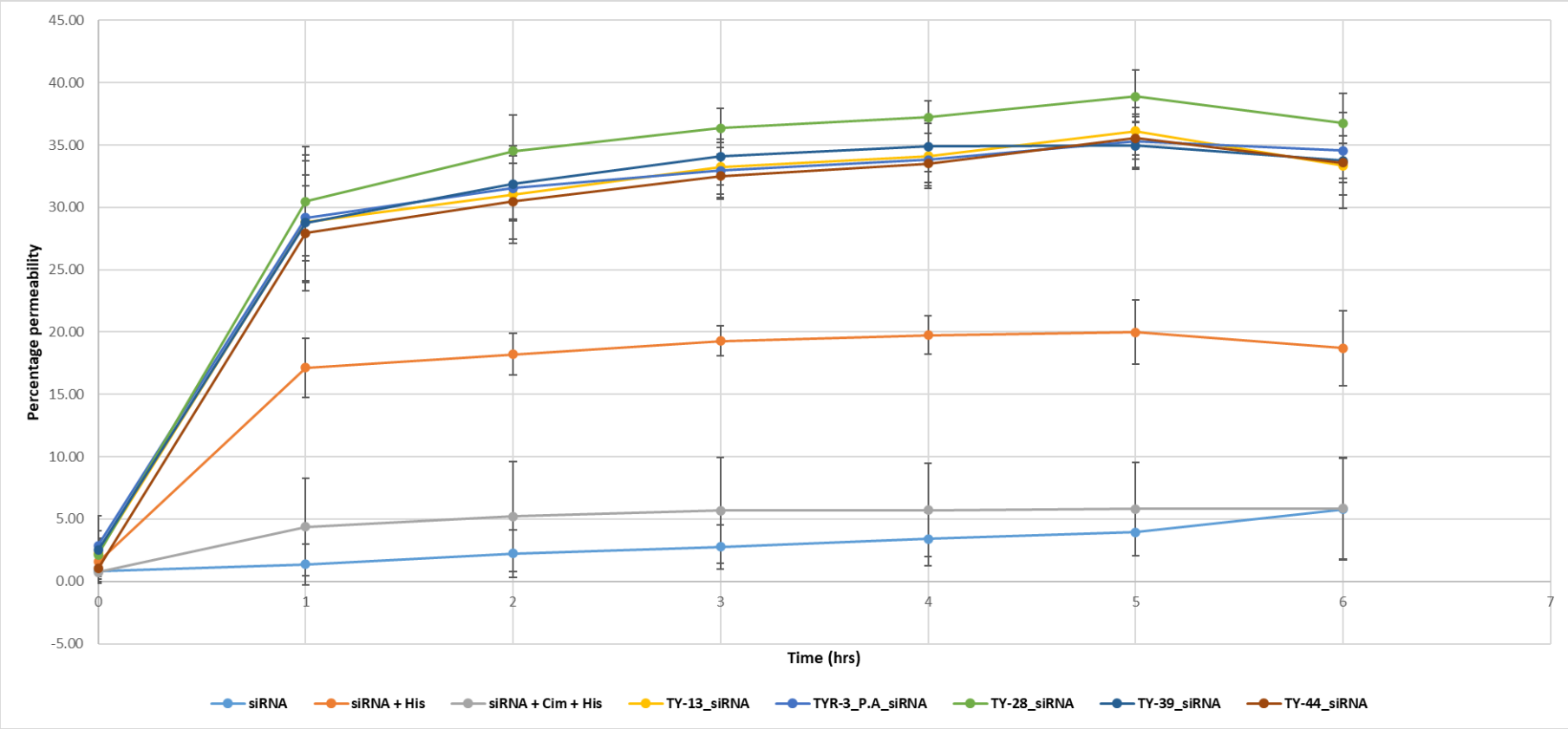

Figure 6. 17. In vitro percentage permeability of enzyme-responsive self-assembled peptide nano-formulations across the endothelial monolayer model (hCMEC/D3 cells) seeded at 90000/insert after 24 h, 36 h, post histamine and post cimetidine treatment.

The permeability of siRNA+FAM on its own was measured at around 5.78 ± 4.09 after 6 h, whilst siRNA+FAM in the presence of histamine was around 18.71 ± 3.01 and in the presence of cimetidine was 5.84 ± 4.07. Chemical compounds influence the endothelial monolayer integrity as has been reported previous in another study (579). Enzyme-responsive self-assembled peptide NPs showed permeability of around 34%. The permeability of TY-28_siRNA was 36.77 ±2 .40 and for TY-39_siRNA it was 33.74 ± 3.85.

To mimic the pathological conditions, active MMP-9 (140 ng/mL) (580) was added to the basolateral compartment. TY-13_siRNA showed the highest permeability of 41.62±3.09% and for TYR-3_PA_siRNA was around 27.66 ± 2.69% after 24 h. TY-28_siRNA and TY-44_siRNA showed permeability of more than 50%. TY-39_siRNA was about 28.56 ± 1.48% as shown in Figure 6.18. Khongkow et al. reported a maximum of 20% permeability of surface-modified gold NPs (581). In another study conducted by Song et al. reported an *in vitro* permeation of 11.6% - 21.3% was found to depend on the size (582). Enzyme-responsive self-assembled peptide NPs used in this study showed permeability in range of 30-40%. Brain targeting ligand used in TY-13_siRNA and TY-39_siRNA has been reported to show 50% permeability compared to apamin (parent compound, apamin; a bee venom) (171). Similarly, brain targeting ligand used in TYR-3_PA_siRNA and TY-28_siRNA have been reported to show an excellent permeability by targeting nAchR (138, 168). Brain targeting ligand used has been reported to increase doxorubicin accumulation by 1.7-fold in the tumor by targeting transferrin receptor (210) and 1.3 × times higher than the naked liposomes (212). *In vitro* data demonstrated the permeation of siRNA across the endothelial monolayer with the caveat of no significant permeability observed in *in vivo* data.

A further two experiments sought to mimic the healthy physiological (50 ng MMP-9 in apical) and diseased conditions (100 ng MMP-9 in apical) (559, 560). Cells were grown in

the same pattern except for the addition of MMP-9 in both compartments. TEER values were measured and are shown in Figure 6.19. TEER values were in the range of 230-260 Ω cm^2.

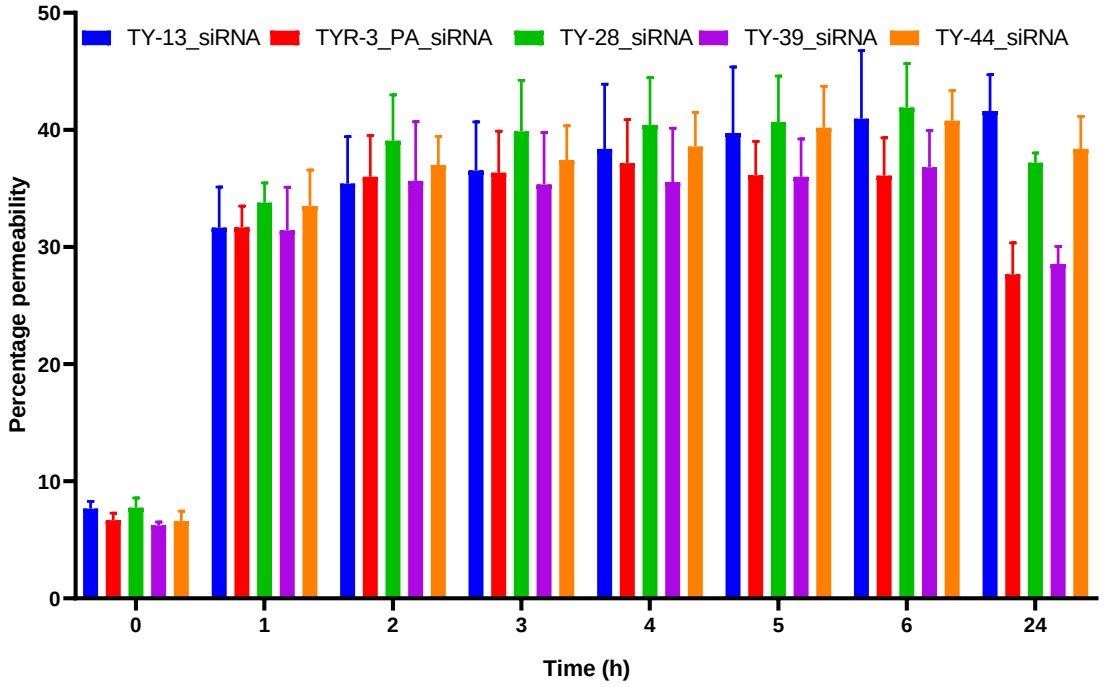

Figure 6. 18. In vitro percentage permeability of enzyme-responsive self-assembled peptide nano-formulations across the endothelial monolayer model (hCMEC/D3 cells) seeded at 90000 cells/insert after 24 h in the presence of 140 ng in basolateral compartment, demonstrating ability of the NPs to cross the endothelial monolayer. Error bars present SD (n = 3).

The permeability of enzyme-responsive self-assembled peptide NPs was higher at the healthy MMP-9 levels. For TY-13_siRNA it was noticed around 70.75 ± 5.77 and TY-39_siRNA and TY-44_siRNA also showed more than 50%. The encouraging results of this *in vitro* study now pave the way for an *in vivo* experiment to explore the potential of our novel NPs in delivering therapeutic agents to the brain (583). Surprisingly, TYR-3_PA_siRNA and TY-28_siRNA showed lower permeation of 29.64 ± 0.91 and 41.12 ± 5.18, respectively, as shown in Figure 6.20. One possible explanation for the lower measured permeability of TYR-3_PA_siRNA was precipitation in the apical compartment. Although TYR-3_PA_siRNA did not show any precipitation in the release profiling experiments with

FBS and MMP-9. The precipitation in permeability experiment could be due to the presence of supplementary ingredients in EndoGRO media which were not present in FBS. Due to precipitation, TYR-3_PA_siRNA was excluded from diseased condition experiment and TY-41_CHF_siRNA was included which had the same brain targeting ligand except MMP-9 cleavable sequence.

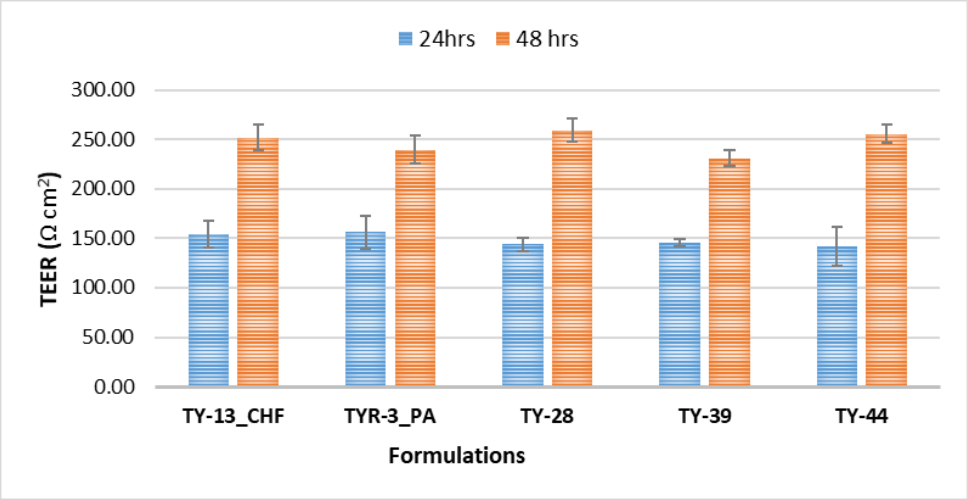

Figure 6. 19. TEER values for in vitro endothelial monolayer prepared by hCMEC/D3 cells seeded at 90,000 cells/insert after 24 h and 48 h, presenting formation of a biological barrier. Error bar indicate SD (n = 3).

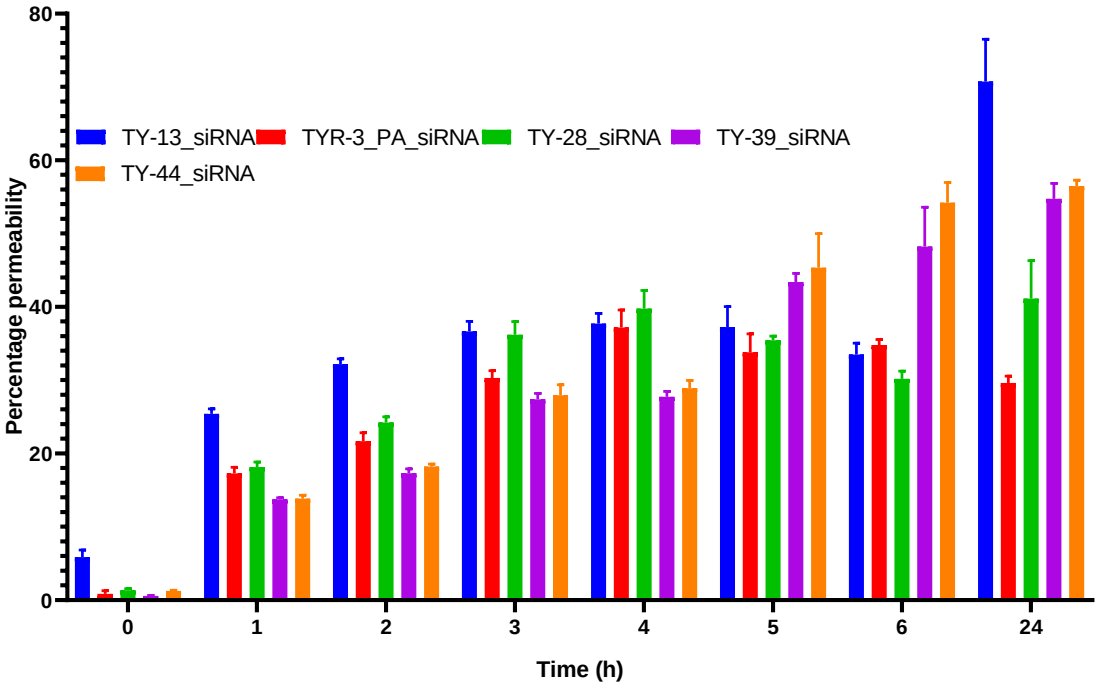

Figure 6. 20. In vitro Percentage permeability of self-assembled enzyme-responsive peptide Nano-formulations across the endothelial monolayer model (hCMEC/D3 cells) seeded at 90000/insert after 48hrs in the presence of MMP-9 (apical 50ng) and (basolateral 140ng).

For verification of the permeability results and assessment of the integrity of the endothelial monolayer model, FITC-dextran 70000 was added to the inserts after stabilizing the cells for 30 minutes. Permeation of FITC-dextran was measured every h up to 6 h by reading the sample in the basolateral compartment at 485 nm and 535 nm excitation and emission, respectively. Very low amounts of FITC-dextran managed to cross the endothelial monolayer after the NPs permeability experiment. 0.32 ± 0.02 – 2.46 ± 0.31% of FITC-dextran escaped through the endothelial monolayer suggesting the integrity of endothelial monolayer before and after experiment. TEER values measured after the experiment did not change significantly, suggesting the integrity of monolayer.

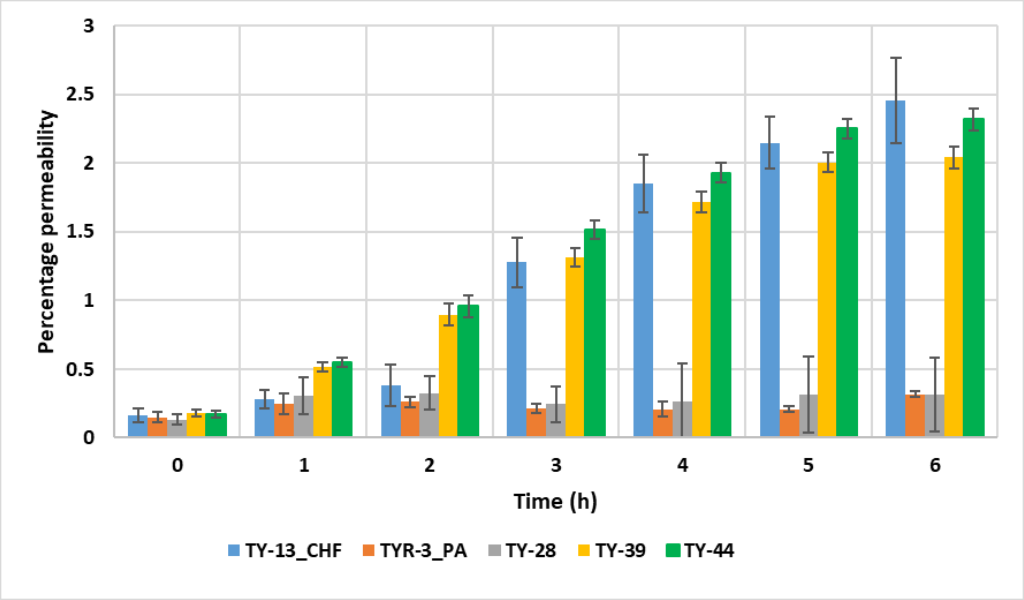

Figure 6. 21. Percentage permeability of FITC-dextran across the endothelial monolayer after the NPs formulations. It showed negligible amount of FITC-dextran managed to get though the endothelial monolayer, suggesting the endothelial monolayer integrity, and confirming that the permeability of siRNA+FAM is due to NPs formulations.

In the diseased state experiment where the MMP-9 level is higher, the permeability for TY-13_siRNA NPs was 51.19 ± 2.05 that is almost 20% less compared to the level of MMP-9 in healthy individuals. This decline in permeability can be attributed to MMP-9 enzymatic action that cleaves the NPs and hence reduced the permeability. A similar pattern was observed for TY-39_siRNA and TY-44_siRNA, however TY-28_siRNA remained almost unchanged as shown in Figure 6.22.

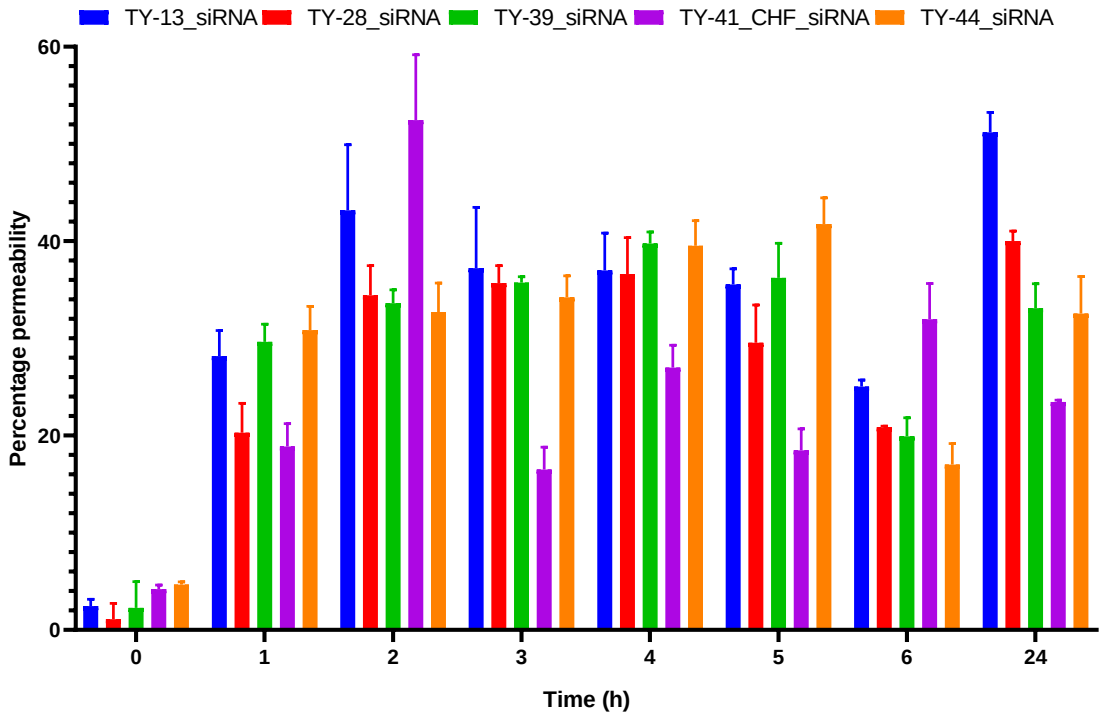

Figure 6. 22. In vitro Percentage permeability of self-assembled enzyme-responsive peptide Nano-formulations across the endothelial monolayer model (hCMEC/D3 cells) seeded at 90000/insert after 48hrs in the presence of MMP-9 (apical 100ng) and (basolateral 140ng).

TEER values were measured again after the experiment to ensure the integrity of endothelial monolayer and it was noticed that TEER values did not change significantly as shown in Figure 6.23 after *in vitro* permeability experiments. We chose three different ligands targeting different receptors on the neuronal cells (584). Enzyme-responsive self-assembled NPs showed higher transport across the endothelial monolayer BBB model when

MMP-9 levels were elevated and the brain-targeting ligand was responsive to MMP-9. The data suggested that these NPs would transport more therapeutic agent across the endothelial monolayer when the active MMP-9 levels are elevated in both the blood stream and brain interstitial fluid.

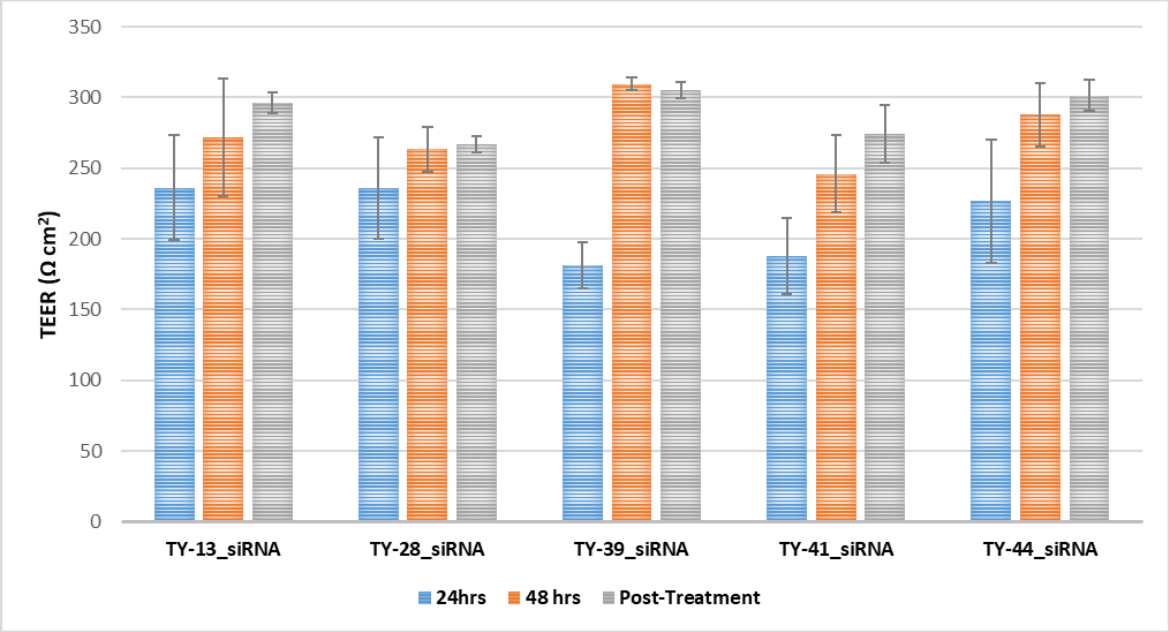

Figure 6. 23. TEER values for in vitro endothelial monolayer prepared by hCMEC/D3 cells seeded at 90,000 cells/insert after 24 h and 48 h, presenting formation of a biological barrier. Error bar indicate SD (n = 3).

It should be noted that here that TY-13_siRNA was around 84 nm in size with a positive charge of 36 mV. The targeting ligand used was reported to follow the receptor mediated transport. However, TYR-3_P.A_siRNA with sRVG as a targeting ligand that targets nAchR receptor with the slightly lower positive charge showed lesser permeability across the endothelial monolayer model. It should also be noted that the CMC for TY-13_siRNA was around 40 mg/L, whereas it was around for 100 mg/L for TYR-3_P.A_siRNA. Similarly, TY-28_siRNA with particle size of 40 nm showed better permeability compared to TY-39_siRNA.

Furthermore, in the presence of active MMP-9 in the basolateral compartment, better permeability was observed. As the NPs were designed in a way that make them highly sensitive to MMP-9. It can be suspected/assumed that NPs after passing through the endothelial monolayer get metabolized in the basolateral compartment by MMP-9 and release the adsorbed/encapsulated siRNA. Improved permeability was observed in the 50ng of MMP-9 (healthy state) compared to 100 ng of MMP-9 (diseased state). This decreased permeability can be attributed to enzymatic degradation of NPs.

6.4. **Conclusion**

In vitro uptake of enzyme-responsive self-assembled peptide NPs was confirmed by confocal microscopy and flow cytometry. NPs used in this study were found around the nucleus using confocal microscopy. Enzyme-responsive self-assembled peptide NPs were significantly more readily taken up by SH-SY5Y cells compared to naked siRNA+FAM in flow cytometry. Enzyme-responsive self-assembled peptide NPs showed up to 40-70% permeability when investigated by *in vitro* hCMEC/D3 endothelial monolayer model in healthy (50ng) and diseased (100 ng) conditions. TEER values were measured before and after permeability experiments to ensure the integrity of the endothelial monolayer model. FITC-dextran permeability was negligible (2.5 %) compared to enzyme-responsive self-assembled peptide NPs. Results of *in vitro* studies have shown the potential of enzyme-responsive self-assembled peptide NPs as permeating carriers/vectors in brain drug delivery applications therefore justifying their further investigation.

CHAPTER – 7 *IN VIVO* BBB PERMEABILITY

7.1. Introduction

NP mediated drug delivery has been extensively investigated by *in vivo* techniques (585). *In vivo* is a Latin word meaning "within the living". Any *in vivo* experiments should be conducted in animals that mimic the human clinical situation as closely as possible. An ideal animal model is one in which the outcome and systems in the specific animals used completely coincide with those relevant to the system of interest (usually the human system) and this can be almost achieved in certain engineered animals. A model that exhibits pathogenesis and disease progression closely analogous to those in humans might be considered an ideal model (586). The most commonly used animals for experiments are rabbits, mice, rats, goats, sheep, pigs, dogs, and cats (587).

For tissue engineering research, rats are used due to their low cost and easy maintenance (586). Mice are also widely used for *in vivo* experiments due their easily modifiable genome and easy handling. Mice have been used to study brain drug delivery via the nasal route (588). Mice can be used as normal healthy animals or can be engineered genetically or via their environment to mimic disease states (589). Multiple sclerosis (MS) is a disease that involves the BBB. Experimental Autoimmune Encephalomyelitis (EAE) is widely investigated model of demyelinating diseases such as MS (590). Angiogenesis (formation of new blood vessels), contributes towards formation of the BBB in newly formed brain microvasculature. It starts at gestational week 8, (591) and peaks at gestational week 35 (592). However, in mice, it starts at embryonic day (E) 9.75 and completes shortly after birth (593). Male Fisher 344 rats have been used for the evaluation of the ability of iron oxide NPs to accumulate in tumors in the presence of magnetic fields (594). Lin et al. used glioma

bearing Balb/c nude mice (3−4 weeks old) to evaluate the therapeutic effects of LMWP-BSA-NPs (262). In another study, conducted by Xin et al. ANG-NP-PTX were successfully used for treatment of glioma by using Balb/C mice (264).

Alzheimer's disease (AD) is an irreversible, progressive neurodegenerative disorder. Amyloid-beta (Aβ), a 42-amino acid peptide isoform is considered to be one of several candidates for a possible causative agent in AD. AD pathogenesis is characterized by age-related Aβ misfolding, aggregation, deposition, neurofibrillary tangles, and neuronal loss (595). β-secretase-1 (BACE-1) has been associated with neurodegeneration and accumulation of amyloid precursor protein (APP) products (405, 406). The inhibition of BACE-1 reduces the levels of Aβ and is a possible therapeutic strategy for AD treatment (407).

siRNA against BACE-1 have been used to halt Aβ production directly, leading to less neurodegenerative and behavioral deficits in APP transgenic mice (406, 596). Numerous studies have reported the use of rabies virus glycoprotein (RVG) as a brain-targeting ligand on the siRNA delivery vectors, such as exosomes (597), poly(mannitol-co-PEI) (598), trimethylated chitosan (271), chitosan coated solid lipid NPs (372, 599) and BACE-1 siRNA delivery to the mouse brain via systemic injection.

In this chapter, enzyme-responsive self-assembled peptide NPs were tested for their ability to deliver FAM tagged siRNA to the brain in Balb/C mice. Preliminary experiments were performed to develop an optimum method for the experiment. For *in vivo* experiments, TY-28 and TY-44 were selected for several reasons including having: a) better release profiles, b) sensitivity to MMP-9, c) lower toxicity, d) a targeting ligand (sRVG) and e) functioning as a better *in vivo* imaging system (IVIS) signal in preliminary experiments.

Subsequently, enzyme-responsive self-assembled peptide NPs were investigated for their ability to silence BACE-1 in SH-SY5Y cells by using BACE-1 mRNA and BACE-1-antisense transcript (BACE-1-AS) (600, 601). The *in vitro* BACE1 silencing efficacy was evaluated by real-time polymerase chain reaction (RT-PCR).

7.2. Material and Methods

7.2.1. Materials

Balb/C female mice (weighing 22.33±0.55gm and 6 months old) were obtained from Liverpool John Moores University animal house (563). FAM tagged negative siRNA was purchased from Sigma Aldrich. Imaging services were used at the University of Liverpool, United Kingdom. The animal handling license used for the experiment was PA693P221. All animal experiments were performed under a license granted under the UK Animals (Scientific Procedures) Act 6 1986 and were approved by the Liverpool John Moores University ethics committee. BACE-1 siRNA (SASI_Hs01_00126124, CUGUUAUCAUGGAGGGCUU [dT][dT]) and BACE-1_AS (SASI_Hs01_00126124_AS, AAGCCCUCCAUGAUAACAG [dT][dT]) with a molecular weight of 13302 were purchased from Merck, KGaA, Darmstadt, Germany. LunaScript RT SuperMix kit was purchased from ThermoFisher, UK. ReliaPrep RNA Cell Miniprep System was purchased from Promega Corporation, Madison, USA. QuantiTect Primer Assay was purchased from Qiagen, UK. SH-SY5Y cells passage 22 was used.

7.2.2. Methods

7.2.2.1. *Preparation of the enzyme-responsive self-assembled peptide NPs for injection*

Peptide solution (1 mg/mL) was prepared in sterile saline solution (1 mL) and was added (360 µL) to siRNA+FAM (30 µg) in an Eppendorf tube. The ratio of the siRNA to peptide was 10:1.

7.2.2.2. *In vivo Injection and imaging*

In order to study the capability of enzyme-responsive self-assembled peptide NPs to access the brain, Balb/C mice were used. NP formulations encapsulating siRNA+FAM and siRNA+FAM control on its own (control) were administered to each animal via tail vein injection (n = 3). Nine healthy Balb/C mice were selected and divided into 3 categories. One serving as control and two triplicates were used for enzyme-responsive self-assembled peptide NPs. Each mouse was weighed and placed into a small laboratory scale heating device. This was to ensure the dilation of veins to facilitate the injection. Each animal received 10 µg of siRNA and 100 µL in terms of volume. After injection, animals were placed in the ventilated cages and their behavior was observed. Animals were culled (CO_2) after 3 h and transferred to Liverpool university for imaging. Fluorescence was measured by using a fluorescence imager (IVIS Spectrum, Perkin Elmer, UK) at λ_{exc} 465 nm and λ_{ems} 520 nm. Imaging data were normalized to the acquisition conditions and expressed as radiance (photons/second/cm^2 /steradian (p/s/cm^2 /sr)), and the colour scale was adjusted according to the strength of signal detected.

7.2.2.3. *Ex vivo imaging*

Animals were removed from the imaging system and placed on the dissection board. Each animal was dissected from the dorsal/supine side. Liver, kidneys, lungs, heart, spleen and brain were harvested from the body and placed on parafilm. Parafilm along with organs was placed in the imaging device and fluorescence was measured.

7.2.2.4. *Cell culture*

SH-SY5Y cells were grown in Dulbecco's Modified Eagle Medium (DMEM) supplemented with 10% FBS and 2 mM L-glutamine. They were then washed with phosphate-buffered saline, trypsinised, re-suspended in the growth medium, counted and seeded into an opaque, micro-clear, flat bottom 12 well tissue culture plate at a density of 1.2

x 10^5 cells/mL (120000 cells/ well at 100 µL/well). The plate was then incubated overnight at 37°C with a 5% CO_2 supply. After 24 h incubation, media was aspirated and serum free DMEM only media was added, and cells were transfected with enzyme-responsive self-assembled peptide NPs encapsulating siRNA. Cells were incubated for 4 h. DMEM was replaced with fresh growth media. Cells were left in the incubator for 48 h.

7.2.2.5. *Cell harvesting*

After 48 h, media was aspirated, and adherent cells were harvested by following the protocol from the supplier and total RNA from transfected cells was extracted using ReliaPrep Minicolumn. Briefly, adherent cells were washed with ice cold PBS. 150 µL of BL+TG buffer was added to the cells and the plate was gently rocked. Cells were rinsed by repeated pipetting of the lysate over the well surface, 8-10 times. Lysate was collected from each well and transferred in to micro-centrifuge tubes. Cells were centrifuged at 300 x g for 5 min. Cell pellet was carefully washed with ice cold sterile PBS. Supernatant was discarded and 50 µL isopropanol was added to the cells. Lysate was transferred to ReliaPrep Minicolumn and centrifuged at 12,000 x g for 30 s at room temperature. Filtrate was discarded and 500 µL of RNA Wash Solution was added to the ReliaPrep Minicolumn. It was centrifuged at 12,000 – 14,000 x g for 30 s. 30 µL of this freshly prepared DNase I incubation mix was added directly to the membrane inside the column by making sure that the solution is in direct contact with and thoroughly covering the membrane. It was incubated for 15 min at room temperature. After incubation, 200 µL of column wash solution was added to ReliaPrep Minicolumn and centrifuged at 12,000 – 14,000 x g for 15 s. Filtrate was discarded, 500 µL of fresh RNA wash solution was added and centrifuge at 12,000–14,000 × g for 30 s. Filtrate was discarded. 300 µL of RNA wash solution was added and centrifuged at high speed for 2 min. ReliaPrep™ Minicolumn was placed into elution tube and 20 µL nuclease-free water was added to column and centrifuged at 12,000 – 14,000 x g for 1 min.

The yield of RNA was measured by using a NanoDrop spectrophotometer. A small droplet was placed on spectrophotometer. RNA yield was measured at 260 nm. The RNA was reverse transcribed into cDNAs (T100 Thermal Cycler, Singapore) using LunaScript RT SuperMix kit according to the protocol of the manufacturer for 200 ng of RNA from each sample. The cDNA amplification (Rotor-Gene Q, Germany) was performed using QuantiTect Primer Assay with SYBR green based RT-PCR.

7.2.2.6. *Statistical Analysis*

GraphPad Prism Software 8.0.1 for Windows (GraphPad Software, Inc., La Jolla, CA, USA) was used to conduct one-way analysis of variance (ANOVA) followed by Tukey's post-hoc test for multiple comparisons in order to identify any statistically-significant differences between the means of treatment groups. For statistical comparisons, $P<0.05$ was considered a statistically significant difference.

7.3. **Results and Discussion**

The ability of enzyme-responsive self-assembled peptide NPs to penetrate to the brain was assessed by injecting the NPs into mice tail veins. Post-injection, all the animals behaved reasonably, and behavior was not indicative of toxicity. Surprisingly, mice were found to be more active, running and playing on the running wheel. This confirms that the enzyme-responsive self-assembled peptide NPs were safe upon injection.

From the ventral side scan, no increasing signal ($P < 0.05$) was observed amongst the animals including control and tests as shown in Figure 7.1. One of the possible reasons could be that the fluorescence is too low to be visualized in full body/animal. The fluorescence from (602). Another reason was the low dose of siRNA (10 µg/mouse) used in this experiment, whereas studies reported in the literature used 50 µg/mouse (155, 602). In another study, 20 µg/mouse of coumarin-6 was injected and visualized in whole mice (263).

The use of higher dose of siRNA might have led to successful visualization of the signals in the mouse. In this study, 10 µg/mouse was used, due to financial constraints and the encapsulating capacity of enzyme-responsive self-assembled peptide NPs. Wang et al. reported that the highest penetration of CGN-PEG-PDMAEMA NPs occurs in the first hour after injection with each mouse receiving 32 µg siRNA (603).

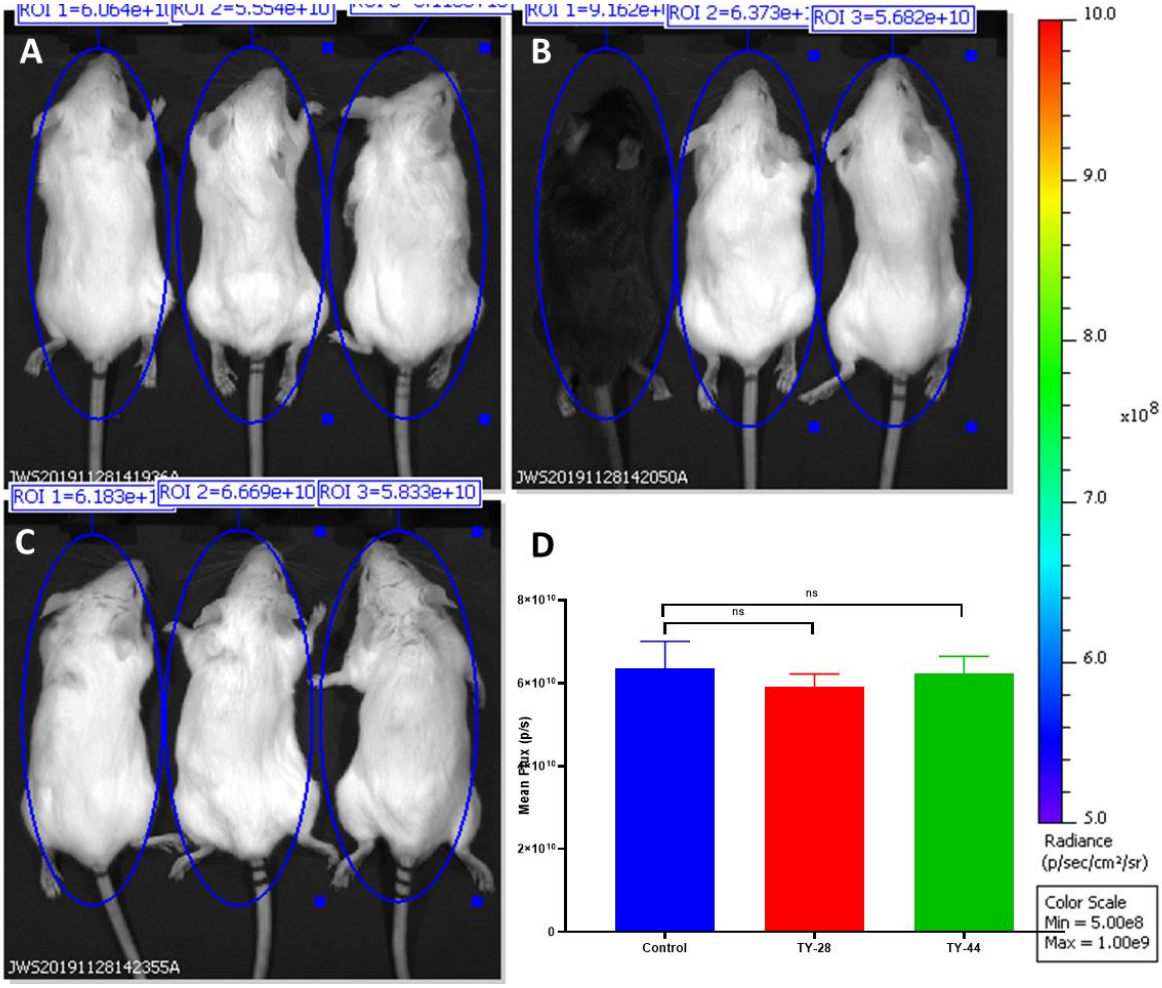

Figure 7. 1. In vivo distribution of enzyme-responsive self-assembled peptide NPs in mice after intravenous administration and culling after 3 h. ***A****) TY-28 NPs* ***B****) Control,* ***C****) TY-44 NPs and* ***D****) Mean flux (p/s) control vs tests (n=3).*

When there was no signal observed in full body mouse, further investigations were conducted after dissecting the mice and different organs were scanned at 465/520 nm. It was observed that *ex vivo* experiments showed fluorescence in brain that was higher than other

organs except liver and kidneys (Figure 7.2). This might be because drug metabolism takes place in the liver (604) and elimination of the drug from the body is carried out by the kidneys (605). We established that the liver or bile (fluid that is made and released by the liver and stored in the gallbladder) must be auto-fluorescent as the controls showed the signal too.

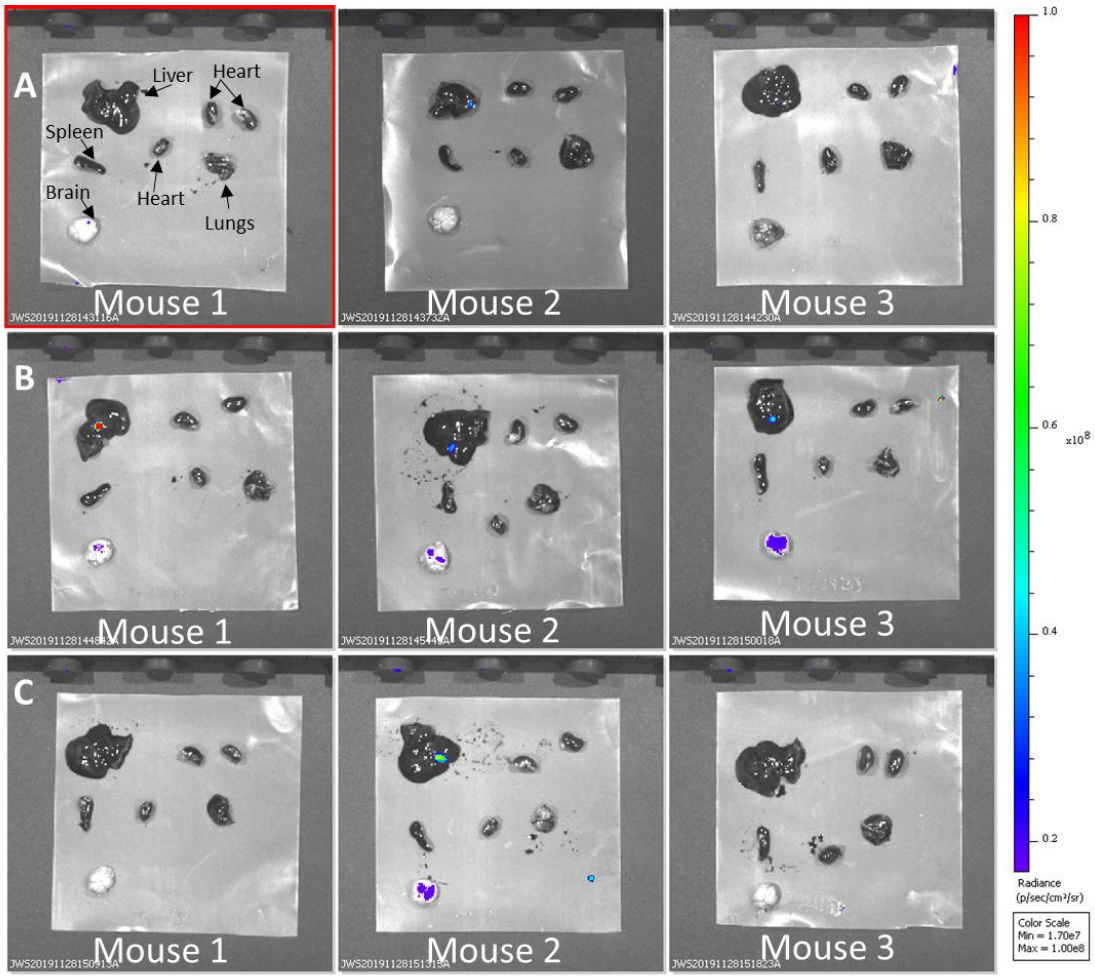

Figure 7. 2. Ex vivo distribution of enzyme-responsive self-assembled peptide NPs in mice organs dissected following intravenous administration and culling after 3 h. A) Control B) TY-28 NPs and C) TY-44 NPs (n=3).

There was increased fluorescence in the brains of the treated mice, the differences are small and not statistically significant as shown in Figure 7.3. Data from this study and literature, suggests that animals should have been culled and the brains should be scanned 1 h post-injection, rather than 3 h. Xia et al. harvested the mice organs at different time intervals

starting from 0.08 – 12 h and reported highest penetration after 30 minutes (263). Huang et al. dissected and scanned mouse organs 1 h post injection and reported the penetration of lactoferrin-modified NPs (155). NPs designed in this project were for diseased brain, when the MMP-9 levels are high, therefore, in healthy mice, there may not be a strong brain accumulation as would be expected.

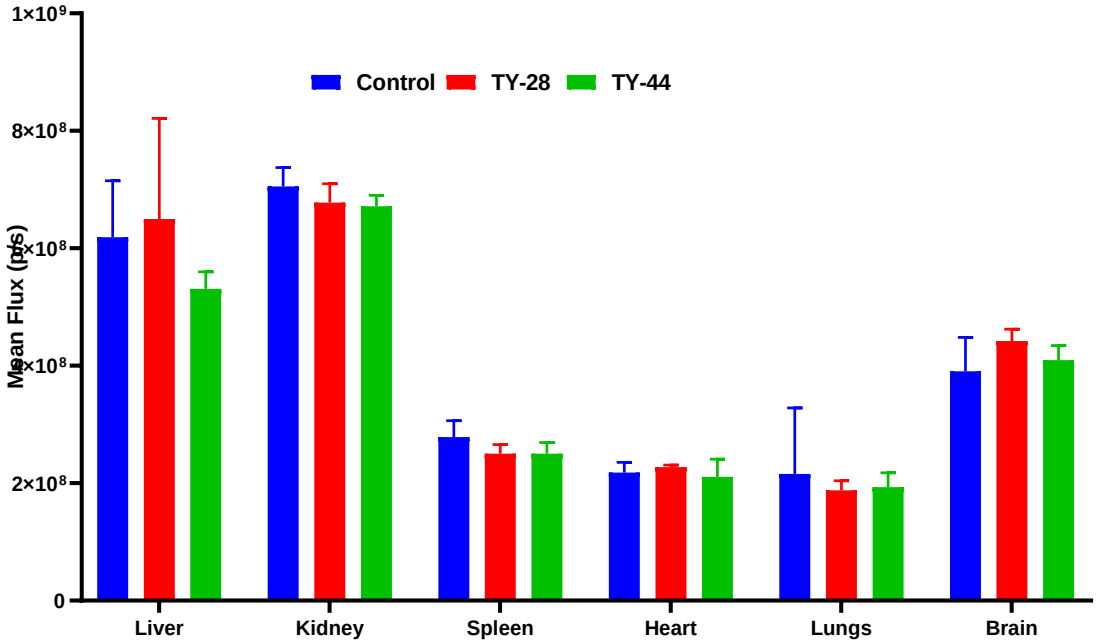

Figure 7. 3. Ex vivo distribution of enzyme-responsive self-assembled peptide NPs into mice organs dissected after intravenous administration and culling after 3 h (n=3).

Time duration (3 h) post injection, was enough for serum enzymes and RNAse to digest/metabolize the enzyme-responsive self-assembled peptide NPs and siRNA respectively as shown in chapter 5 (5.2.2.2) and 6 (section 6.2.2.3). It has been shown that the enzymes present in the serum start digesting NPs and siRNA. This digestion could have been avoided if the animals were scanned 1 h post-injection. *In vivo* experiment showed that enzyme-responsive self-assembled NPs were unable to permeate/penetrate into the mice brain significantly.

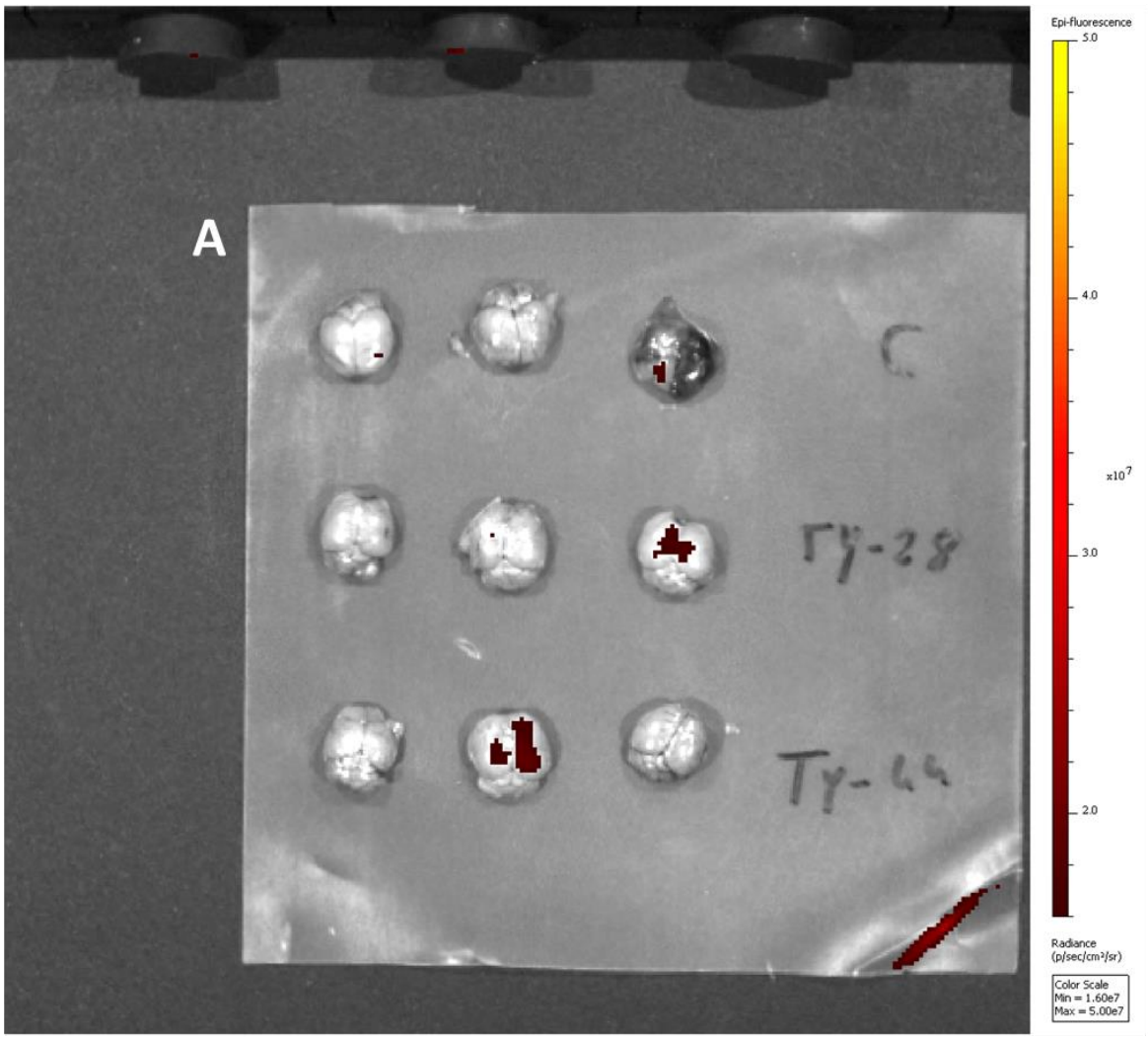
A
C
TY-28
TY-44
Epi-fluorescence
5.0
4.0
x10^7
3.0
2.0
Radiance (p/sec/cm²/sr)
Color Scale
Min = 1.60e7
Max = 5.00e7

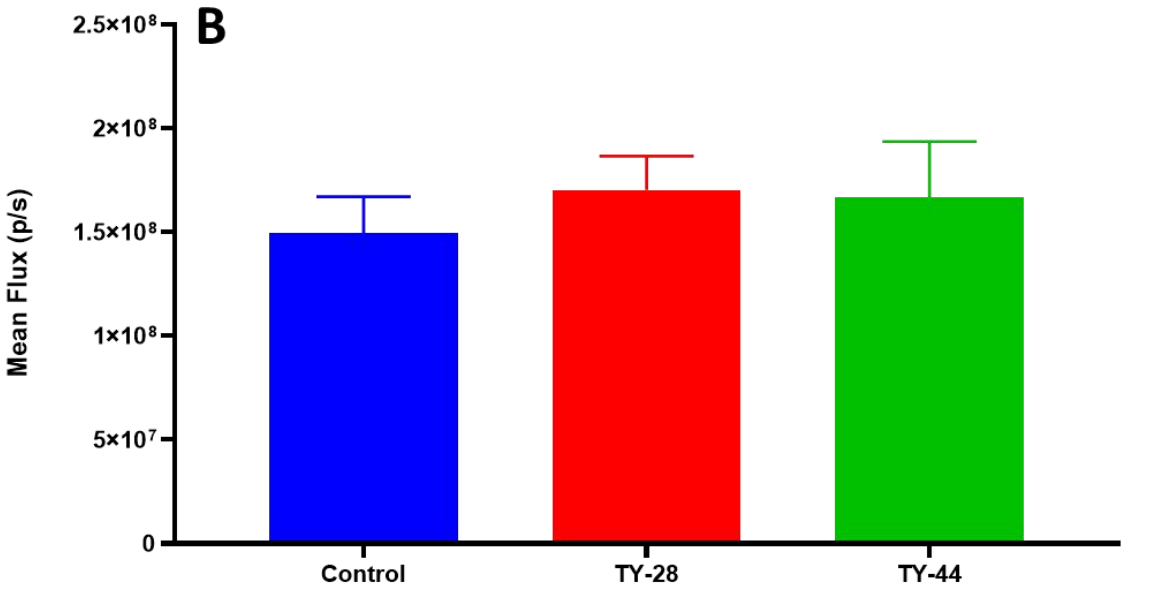
B
2.5×10^8
2×10^8
1.5×10^8
1×10^8
5×10^7
0
Mean Flux (p/s)
Control
TY-28
TY-44

*Figure 7. 4. Ex vivo distribution of enzyme-responsive self-assembled peptide NPs. **A**) mice brain dissected after intravenous administration and culling after 3 h (n=3). **B**) Graphical representation of mean fluorescence in the mice brains.*

The therapeutic potential of enzyme-responsive self-assembled NPs constructed in this project was investigated for their ability to silence BACE-1 expression *in vitro*. Cells transfected with NPs were harvested for RNA. RNA measured in each sample ranged from 93.3 – 527.3 ng/µL. Volumes needed for cDNA synthesis were calculated and 4 µL of LunaScript RT SuperMix was used. The yield and volume of RNA used are summarized in Table 7.1. Slight BACE-1 gene silencing but not significant statistically was observed in the SH-SY5Y cells compared to medium and negative control as shown in Figure 7.5.

Table 7. 1. Practical yield of RNA collected from the transfected cells by treating SH-SY5Y cells with enzyme-responsive self-assembled peptide NPs. In addition, calculation of the volumes used of reagents such as RNA, Water and LunaScript SuperMix cDNA synthesis.

Treatment	RNA (ng/µL)	260/280 (Purity ratio)	LunaScript RT SuperMix (µL)	RNA Volume (µL)	Nuclease-free water (µL)	Total Volume (µL)
Medium only	93.3	2.29	4	2.14	13.86	20
TY-28 only	132.6	2.21	4	1.51	14.49	20
TY-28 + siRNA Test (100 pm)	191.4	2.2	4	1.04	14.96	20
TY-28 + siRNA Control	171.1	2.18	4	1.17	14.83	20
Medium only	164.5	2.2	4	1.22	14.78	20
TY-28 only	131	2.23	4	1.53	14.47	20
TY-28 + siRNA Test (100 pm)	149.5	2.2	4	1.34	14.66	20
TY-28 + siRNA Control	184.2	2.19	4	1.09	14.91	20
Medium only	427	2.12	4	0.47	15.53	20
TY-28 only	352.6	2.12	4	0.57	15.43	20
TY-28 + siRNA Test (100 pm)	527.3	2.11	4	0.38	15.62	20
TY-28 + siRNA Control	474.7	2.12	4	0.42	15.58	20
TY-28 + siRNA Test (50 pm)	448.9	2.12	4	0.45	15.55	20

TY-28 + siRNA Test (25 pm)	428.4	2.12	4	0.47	15.53	20
TY-28 + siRNA Test (50 pm)	473.7	2.13	4	0.42	15.58	20
TY-28 + siRNA Test (25 pm)	426.4	2.13	4	0.47	15.53	20
TY-28 + siRNA Test (50 pm)	519.4	2.13	4	0.39	15.61	20
TY-28 + siRNA Test (25 pm)	448.8	2.12	4	0.45	15.55	20

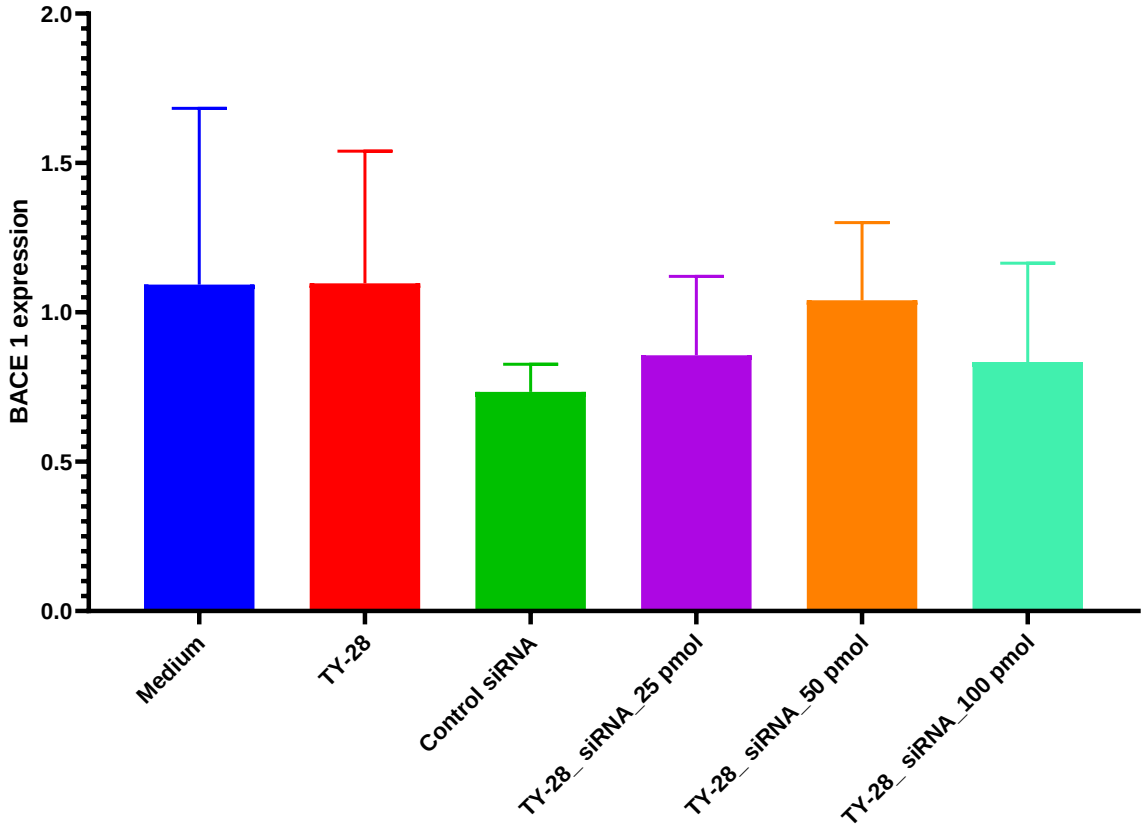

Figure 7. 5. The BACE1 mRNA expression in SH-SY5Y cells treated with enzyme-responsive self-assembled peptide NPs encapsulating BACE-1 siRNA at 37 °C for 4 h. Data were presented as Mean ± SD (n = 3).

Results from the transfection experiment to silence the BACE-1 showed that enzyme-responsive self-assembled peptide NPs were not effective at silencing the BACE-1. One of the possible reasons could be due to compromised complex formation and encapsulation of BACE-1 siRNA (606). Secondly, lipofectamine was not used as a positive control due to financial constraints, a well-known transfecting agent. This cationic lipid binds with negatively charged siRNA and promotes the internalization of payload (606, 607). Lastly, the ability of BACE-1 siRNA used in this study to silent the BACE-1 should be investigated by using lipofectamine, a well-established transfecting agent and in the SH-SY5Y cell line as used in this study.

7.4. **Conclusion**

In vivo studies suggested that the enzyme-responsive self-assembled peptide NPs managed to get into the brain of mice. Although in full body scans, no increasing signal was observed, *ex vivo* examination showed that enzyme-responsive self-assembled NPs managed to permeate into the brain but not significantly. Results from the transfecting experiment showed that enzyme-responsive self-assembled peptide NPs were unable to silence the BACE-1. It could be explained in multiple ways. Complex formation ability of NPs with the BACE-1 siRNA, ability of BACE-1 siRNA to silence the BACE-1 in this particular cell line (SH-SY5Y). Further studies including lipofectamine as a positive control could shed more light on the efficacy of NPs to transfect the cells.

GENRAL DISCUSSION

Neurodegenerative diseases (NDs) have devastating effects on the quality of life and socio-economic status of sufferers and potentially lead to permanent disability. Numerous invasive (intrathecal/intracerebral ventricle route) (68, 489) and non-invasive (such as chemical modification of the drug molecule, physiological transport mechanism, chemical and physical disruption of the BBB and nasal drug delivery) (73) techniques have been employed to treat NDs. Nanotechnology has gained significant attention in past decade for the delivery of drug across the BBB (490-493). Polymeric (494), liposomes (276), exosomes (328), dendrimers (330), metallic NPs (495) and shuttle peptides (496) have been explored for brain drug delivery.

Peptide decorated NPs have been reported to efficiently cross the BBB with minimum toxicity. Diaz-Perlas et al. used linear and branched THRre (pwvpswmpprht) peptide to cross the BBB, that binds transferrin receptor (216). They found branched THRre peptides has 2.6 fold increase permeability (216). Apolipoprotein E (Apo E, residues 141-150), which binds with low-density lipoprotein (LDL) have been extensively explored for brain drug delivery to treat mucopolysaccharidosis (MPS) type I, most common lysosomal storage disorders with CNS deficits (206, 608).

The 29-mer (YTIWMPENPRPGTPCDIFTNSRGKRASNG) of rabies virus glycoprotein (RVG), which binds specifically to the acetylcholine receptor (nAchR), has been used to transport drug molecule and siRNA across the BBB (609). sRVG (CDIFTNSRGKRA) a 12-mer of RVG, is also reported to bind with nAchR and able to cross the BBB (138). MiniAp-4 (H-[Dap]KAPETALD-NH_2), a venom derived peptide able to cross the BBB with minimum toxicity, immunogenicity and protease resistance (171). All of the mentioned work used shuttle peptides to decorate the NPs, which rendered the ability to cross the BBB.

In this project we developed Novel enzyme-responsive self-assembled NPs with aim to deliver the drug (FSS) across the endothelial monolayer. In the first phase, peptide sequences which are substrates for the MMP-9 enzyme were identified by using state of the art statistical and molecular modelling techniques. Those sequences were synthesised, tested and experimentally validated using a novel *F-labelling technique to assess their specificity towards MMP-9. In the second phase, highly sensitive peptides to MMP-9 were synthesized with a little modification (attachment of BBB targeting ligand peptides). In addition, lipophilic moieties were conjugated to maintain the hydrophilic/lipophilic balance to facilitate the self-assembly and finally NPs formation.

For statistical and molecular modelling, a total of 369 peptide sequences were downloaded including some that feature non-natural amino acids from MEROPS. Gly at P4 was most prominent comprising more than 32% of all the sequences followed by Ala and Leu with 8.45% for each. At P3, Pro was the most frequent, occupying about 41% followed by Ala for more than 14%. Interestingly, at P2 several amino acids were frequent: Ala, Gly, Pro, Arg, Ser; comprising 14.6%, 10.3%, 10%, 9.5% and 7.3 % respectively. Gly (almost 33%) and Ala predominantly occupy P1 (around 12.6%).

It was observed that the percentage (rate of incidence of amino acid in any sequence) for all amino acids in any given peptide (MMP-9 cleavable reported in MEROPS) sequence at any position includes at least one amino acid that is much higher than the standard natural occurrence from the human gene bank. It was observed that factor values of amino acids in MMP-9 substrate sequences is significantly different than the standard natural occurrence from human gene bank. Natural and Non-natural Amino Acids Index (NNAAIndex) was applied to describe the amino acids by assigning them factor values. About 100800 sequences were generated from combinations and permutations of the residues with most significant influence were identified from P5-P5'. Computational docking has been used to explore protein-ligand interactions for better understanding. It was observed that that Leu's

sidechain extends into the S1′ pocket of the catalytic cleft. The S1′ pocket consists of Val 398, Leu 397, His 401, Pro 421, Met 422 and Tyr 423, most of which are hydrophobic in nature (apart from His and Tyr which have polar groups but also are significantly hydrophobic). Novel MMP-9 sensitive sequences were identified with range of Y-scores. Predicted novel MMP-9 sensitive peptide sequences with a range of Y-scores have been synthesized; importantly, this includes a peptide predicted to be a poor substrate. Novel MMP-9 sensitive peptides were subjected to enzymatic degradation in the presence of active MMP-9 using *F NMR. Various predicted MMP-9 sensitive peptides with a range of Y-score were synthesized and to enzymatic degradation in NMR. TY-26 was found to be the most sensitive to MMP-9. Ability to cross the BBB depends on the brain targeting ligand, therefore a range of brain targeting ligands were selected from literature. We used three different targeting ligands which have been reported to cross the BBB efficiently in numerous studies (138, 500, 501, 610, 611). Brain targeting peptides with the incorporation of MMP-9 sensitive sequence and conjugation of lipophilic moiety to facilitate the self-assembly.

In the previous study, gold NPs of around 48 ± 1.5 with polydispersity index (PDI) 0.247 and exosomes coated gold NPs of 225 ± 33.4 (612) polysaccharides NPs (531) of below 200 nm showed higher membrane permeability in astrocyte cell and mouse brain endothelial cells (bEnd3) respectively. In another study, chitosan coated human serum albumin NPs of 261± 8 with a zeta potential of 45± 1mV showed excellent permeability in hCEMC/D3 cells as BBB model (572). Novel enzyme responsive self-assembled peptide NPs were of about 200 nm with almost similar PDI and zeta potential of 16-40mV. Most of the NPs were of spherical in shape as reported in earlier studies (531, 572). NPs used in this work were of the same size range and morphology reported in literature. Interestingly, NPs were visualized in TEM without any staining compared negative stained literature reported NPs. Even in the absence of staining agent, NPs were visualized clearly.

The particle size of enzyme-responsive self-assembled range from 41.66 nm - 2796 nm with zeta potential of 2-40 mV. The NPs formulations which exhibited larger particle sizes were not dissolved readily and cloudy appearance was observed. Studies suggest that NCs should have sizes in the range of 10-24 nm to cross the glia limitans and penetrate the brain parenchyma following crossing the BBB or after intrathecal injection. It should be added that larger NPs may manage to cross the glia limitans, if the surface of the NPs is decorated with appropriate targeting ligands. For example, as explained above, albumin NPs decorated with ApoE entered neurons following i.v. injection into mice (504). The NPs showed positive zeta potential values, which is a desirable property since it will further facilitate the binding of the particles to the negatively charged lipid bilayer membrane of the BBB (375).

CMC is an important parameter, above which an amphiphilic macromolecule forms core/shell structured NPs. As the NPs are self-assembled so CMC was measured for each formulation using pyrene (613) as a probe in distilled water. The CMCs for all the formulations were closer to the reported CMC of antimicrobial peptides of 36.1 mg/L (375) except for TYR-3_CHF. TYR-3_CHF exhibited two CMC concentrations for unknown reasons (one possible explanation could be: two tier self-assembly, firstly, few molecules arrange themselves in to smaller structures and secondly, formation of larger assemblies. The physicochemical properties of NPs such as size, charge and encapsulation efficiency can highly influence their in vivo stability and kinetics (614). In a previous study, mPEG-chitosan micelles with 50-200 nm and encapsulation efficiency of more than 80% have been reported (615). In another study chitosan NPs of 292.5nm with entrapment efficiency of over 91% showed excellent diffusion across the membrane (616). Similarly, PLGA NPs with particle size of 140-170 nm and encapsulation efficiency of above 69% showed higher permeation across the BBB (617). Novel enzyme responsive self-assembled peptide NPs used in this work also showed similar encapsulation efficiency of 70-80%.

In vitro release of encapsulated drug was conducted by using a dialysis bag. Seven external stimuli were used to assess the pattern of release from the NPs. It was observed that the release profile in the presence of water, NaCl and glucose was almost similar, whereas in the presence of MMP-9 and FBS it was much quicker. In the presence of BSA, release of FSS was very slow and only 20-30% released after 24 h. In the previous studies saline water (0.9 %) (531) and PBS (532) buffers are most commonly used. It should also be noted that the sensitivity of novel enzyme-responsive self-assembled peptide NPs towards MMP-9 was lower than anticipated and measured by NMR experiment in NMR. One of the possible explanations could be due the dilution of MMP-9 inside the dialysis bag. In addition, MMP-9 require specific condition/environment (TCNB) to remain active and cleave peptide in experimental conditions. In the presence of BSA, release of FSS was very slow and only 20-30% released after 24 h. In the previous studies saline water (0.9 %) (531) and PBS (532) buffers are most commonly used. *In vitro* cellular toxicity was assessed by LDH and MTT using HeLa and SH-SY5Y cell lines. NPs used in this study used, up to 400 µg/mL were found to be significantly less toxic, whereas at higher concentrations of 0.75 mg/mL were found toxic. Similar findings were reported in previous studies (535, 536). It was observed from all cytotoxicity experiments that self-assembled NP formulations with higher positively charged amino acids exhibited higher toxicity compared with less positively charged sequences (534). Lee et al. reported, Ag-CALNNK-NPs (positively charged) have lower toxicity than the Ag-CALNNE-NPs (negatively charged) (537).

In vitro cellular uptake assessed by FACS and confirmed by confocal microscopy. It was reported that positively charged AgNPs accumulated more readily than other AgNPs (562). Lin et al. reported a 2.5-fold increased uptake of bovine serum albumin NPs decorated with a cell-penetrating peptide (LWMP) compared to non-decorated NPs in U87 cells (262). Enzyme-responsive self-assembled NPs developed in this project exhibited the same characteristics.

In vitro permeability was assessed using hCMEC/D3 BBB model. Numerous studies have reported the use of hCMEC/D3 as a BBB model (571, 572). We chose three different targeting ligands targeting different receptors on the neuronal cells (584). The permeability of siRNA+FAM on its own was measured at around 5.78 ± 4.09 after 6 h, whilst siRNA+FAM in the presence of histamine was around 18.71 ± 3.01 and in the presence of cimetidine was 5.84 ± 4.07. TY-13_siRNA_NPs achieved up to 71% of total NPs crossing the BBB model in the presence of active MMP-9, indicating that NPs could achieve a high efficiency in crossing the BBB in the presence of active MMP-9 when the brain-targeting motif is responsive to MMP-9, which mediated cleavage.

Chemical compounds influence the endothelial monolayer integrity as has been reported previous in another study (579). Enzyme-responsive self-assembled peptide NPs showed permeability of around 34%. The permeability of TY-28_siRNA was 36.77 ±2 .40 and for TY-39_siRNA it was 33.74 ± 3.85. Significant signals/permeation/delivery of siRNA was not observed in *in vivo* experiments. Similarly, enzyme-responsive self-assembled peptide NPs were unable to transfect the SH-SY5Y cells. One of the possible reasons in failure of transfection could be due to compromised complex formation.

State of the art statistical and molecular modelling techniques were employed to identify the most suitable substrate for MMP-9. The statistical predictions were tested experimentally by using novel *F NMR technique. We are the pioneer that used this technique to study the kinetics of MMP-9. Enzyme-responsive self-assembled peptide NPs were synthesized successfully and characterized in terms of size, surface charge, CMC, encapsulation efficiency, release profiling and toxicity. Enzyme-responsive self-assembled peptide NPs were evaluated to deliver the FSS in *in vitro* endothelial monolayer BBB model. These NPs were tested *in vivo* to assess the ability to deliver siRNA into mouse brain. Enzyme-responsive self-assembled peptide NPs were able to deliver the FSS across the endothelial monolayer model but were unable to deliver significant amount *in vivo*.

GENRAL CONCLUSION

In this project, novel enzyme-responsive peptide NPs were synthesized for drug delivery to brain for the treatment of neurodegenerative diseases. In this study, the MMP-9 enzyme has been targeted, which is believed to play a crucial role in the pathogenesis of neurodegenerative diseases. In the first phase of project, State of the art statistical and molecular modelling tools were employed to identify the most suitable substrate for MMP-9. Y-scores were calculated for more than 1 million sequences after combinations and permutations of the influential amino acids at all positions from P5 – P5'. NNAAIndex was used to assign factor values and to calculate Y-scores. Novel MMP-9 substrates were identified with a range of Y-score. Peptide sequences with higher Y-scores were predicted to be the better substrates for MMP-9. In this study, we introduced the use of fluorine labels for ^{19}F NMR to study the kinetics of MMP-9 mediated proteolysis of the designed substrates, providing real time monitoring compared to fluorescence-based studies. We supported our findings with auto docking (Chapter 2) of the peptide molecules in 25 reported MMP-9 enzyme structures. We found sequences, especially TY-26, that are better than those in previously reported studies.

Novel enzyme-responsive self-assembled peptide nanoparticles were successfully synthesized with different combinations of MMP-9 sensitive and brain-targeting ligands. Adding hydrophobic moiety such as cholesteryl chloroformate and palmitic acid led to self-assembly. In addition, the MMP-9 cleavable peptide sequence was hydrophobic enough to facilitate the self-assembly. Most of the formulations self-assembled to form nanoparticles without sonication of 41-200 nm diameter with a zeta potential/ surface charge of 2-48 mV. All self-assembled peptide nanoparticle formulations were characterized by LC-MS. All self-assembled peptide nanoparticles were spherical in shape upon microscopy except TY-35. CMCs for all the self-assembled peptide nanoparticles calculated were around 7-110 mg/L.

The encapsulation capacity ranged from 40-80%. TY-28, TY-39 and TY-44 were among the highest encapsulation capacity nano-formulations. TY-32 and TY-35 had poorest encapsulation capacity. All NP formulations exhibited different release patterns of model drug in the presence of external stimuli. NP formulations were found to be MMP-9 sensitive. The sensitivity towards MMP-9 can be tailored by manipulating the sequence. Novel enzyme-responsive self-assembled peptide nanoparticles were found to be least cytotoxic at lower concentration, however at higher concentration they were found to be cytotoxic, showing a range of cell viabilities.

In vitro endothelial monolayer permeability model was used to assess the ability of NPs, to cross the endothelial monolayer. A monolayer of hCMEC/D3 cells was used and TEER values were measured. *In vitro* uptake of enzyme-responsive self-assembled peptide NPs was confirmed by confocal microscopy and flow cytometry. NPs used in this study were found around the nucleus using confocal microscopy. Enzyme-responsive self-assembled peptide NPs were significantly more readily taken up by SH-SY5Y cells compared to naked siRNA+FAM in flow cytometry. Enzyme-responsive self-assembled peptide NPs showed up to 40-70% permeability when investigated by *in vitro* hCMEC/D3 endothelial monolayer model in healthy (50 ng/mL) and diseased (100 ng/mL) conditions. TEER values were measured before and after permeability experiments to ensure the integrity of the endothelial monolayer model. FITC-dextran permeability was negligible (2.5 %) compared to enzyme-responsive self-assembled peptide NPs. Results of *in vitro* studies have shown the potential of enzyme-responsive self-assembled peptide NPs as permeating carriers/vectors in brain drug delivery applications therefore justifying their further investigation.

In vivo experiments were conducted using BALB/c to visualize the targeting ability of the NPs. IVIS was used to scan the mouse for the assessment of targeting. Novel enzyme-responsive self-assembled NPs were subjected to test their transfection efficiency by using BACE-1 siRNA and knock down of BACE-1 gene was assessed by real time PCR. *In vivo*

studies suggested that the enzyme-responsive self-assembled peptide NPs penetrated the brains of mouse models. Although, in full body scans, no significant signal was observed, *ex vivo* experiments confirmed that enzyme-responsive self-assembled NPs managed to permeate into the brain. However, the results could have been different/better if animals were scanned 1 h post injection. Results from the transfecting experiment showed that enzyme-responsive self- assembled peptide NPs were unable to silence the BACE-1 gene. This could be explained in multiple ways. Complex formation ability of NPs with the BACE-1 siRNA should have been investigated and the ability of BACE-1 siRNA to silence the BACE-1 should be assessed by using transfecting agent. Further studies including lipofectamine as a positive control could shed more light on the efficacy of NPs to transfect the cells. Enzyme-responsive self-assembled NPs were developed that can target the brain cells and penetrate the BBB with minimal toxicity and are able to deliver the drug.

FUTURE WORK

Neurodegenerative disorders are challenging to treat pharmacologically due to the shielding provided by the endothelial monolayer. Brain drug delivery has been investigated extensively in the last two decades. Numerous barriers in delivering drugs to the brain lead to the pathway of developing a brain targeting drug delivery systems. A promising drug delivery system should address basic concerns such as biodegradability and elimination of the delivery system from the brain, specific targeting of the brain and minimal toxicity.

In this project, we used multiple MMP-9 responsive substrates with literature reported brain targeting ligands. Numerous MMP-9 sequences can be used other brain targeting ligands to improve encapsulation, toxicity and targeting ability. A combination of two or more different ligands can be used to improve the targeting by dual targeting. For example, ApoE ligand which bind to LDLR and transferrin receptor binding ligands can target the transferrin receptors expressed on the brain cells. Furthermore, multiple MMP-9 responsive

peptides can be used to facilitate the self-assembly and can offer a range of sensitivity towards MMP-9. Prolonged circulation of the self-assembled enzyme responsive nanoparticles can be achieved by using various MMP-9 responsive peptides.

These novel enzyme-responsive self-assembled peptide nanoparticles should be tested in diseased animals when MMP-9 levels are elevated in the brain. Screening other novel enzyme-responsive self-assembled peptide nanoparticles TY-37, TY-38 and TY-39 for siRNA delivery. Delivery of therapeutic peptides like NGF to the brain, by the novel enzyme-responsive self-assembled peptide nanoparticles should be investigated. Blood compatibility and complement activation tests for the novel enzyme-responsive self-assembled peptide nanoparticles, both in blood samples of healthy volunteers and patients with diseased brain such as multiple sclerosis should be investigated. Evaluating the immunogenicity of the novel nanoparticles. Employing Circular dichroism to analyse the formation of alpha helix or beta sheets in the amphiphilic peptides.

Self-assembly of these enzyme-responsive nanoparticles can be used for dual targeting by encapsulating particle inside particle. Smaller nanoparticles encapsulating the siRNA/drug can be encapsulated into larger nanoparticles for dual targeting and protection of siRNA/drug. For example, siRNA encapsulated in 30 – 40 nm nanoparticle can be encapsulated in larger nanoparticles of 70 – 80 nm. This can be investigated. Protein corona influences the targeting ability of nanoparticles. Another step for further investigation could be to study the effect of protein corona on enzyme-responsive self-assembled peptide nanoparticles.

REFERENCES

1. Islam Y, Leach AG, Smith J, Pluchino S, Coxonl CR, Sivakumaran M, et al. Peptide based drug delivery systems to the brain. Nano Express. 2020;1(1):012002.
2. Steward MM, Sridhar A, Meyer JS. Neural Regeneration. In: Heber-Katz E, Stocum DL, editors. New Perspectives in Regeneration. Berlin, Heidelberg: Springer Berlin Heidelberg; 2013. p. 163-91.
3. Mahar M, Cavalli V. Intrinsic mechanisms of neuronal axon regeneration. Nature Reviews Neuroscience. 2018;19(6):323-37.
4. Chekani F, Bali V, Aparasu RR. Quality of life of patients with Parkinson's disease and neurodegenerative dementia: A nationally representative study. Research in Social and Administrative Pharmacy. 2016;12(4):604-13.
5. Josephs KA, Ahlskog JE, Parisi JE, Boeve BF, Crum BA, Giannini C, et al. Rapidly progressive neurodegenerative dementias. Arch Neurol. 2009;66(2):201-7.
6. Gitler AD, Dhillon P, Shorter J. Neurodegenerative disease: models, mechanisms, and a new hope. Disease models & mechanisms. 2017;10(5):499-502.
7. Wichterle H, Przedborski S. What can pluripotent stem cells teach us about neurodegenerative diseases? Nature Neuroscience. 2010;13(7):800-4.
8. Organization WH. Neurological disorders affect millions globally: WHO report 2007 [Available from: http://www.who.int/mediacentre/news/releases/2007/pr04/en/.
9. Wenborn J, Hynes S, Moniz-Cook E, Mountain G, Poland F, King M, et al. Community occupational therapy for people with dementia and family carers (COTiD-UK) versus treatment as usual (Valuing Active Life in Dementia [VALID] programme): study protocol for a randomised controlled trial. Trials. 2016;17(1):65.
10. Gooch CL, Pracht E, Borenstein AR. The burden of neurological disease in the United States: A summary report and call to action. Annals of Neurology. 2017;81(4):479-84.
11. Prince M, Wimo, A., Guerchet, M., Ali, G., Wu, Y., Prina, M. World Alzheimer Report, 2015. The Global Impact of Dementia: An Analysis of Prevalence, Incidence, Cost and Trends. Alzheimer's Disease International (ADI). 2015.
12. Cummings J, Aisen PS, DuBois B, Frölich L, Jack CR, Jones RW, et al. Drug development in Alzheimer's disease: the path to 2025. Alzheimer's Research & Therapy. 2016;8(1):39.
13. Gustavsson A, Svensson M, Jacobi F, Allgulander C, Alonso J, Beghi E, et al. Cost of disorders of the brain in Europe 2010. European neuropsychopharmacology. 2011;21(10):718-79.
14. Georgieff MK. Nutrition and the developing brain: nutrient priorities and measurement. The American journal of clinical nutrition. 2007;85(2):614S-20S.
15. Pardridge WM. The blood-brain barrier: bottleneck in brain drug development. NeuroRx. 2005;2(1):3-14.
16. Gururangan S, Friedman HS. Innovations in design and delivery of chemotherapy for brain tumors. Neuroimaging Clinics of North America. 2002;12(4):583-97.
17. Saraiva C, Praça C, Ferreira R, Santos T, Ferreira L, Bernardino L. Nanoparticle-mediated brain drug delivery: Overcoming blood–brain barrier to treat neurodegenerative diseases. Journal of Controlled Release. 2016;235:34-47.
18. Rip J, Schenk G, De Boer A. Differential receptor-mediated drug targeting to the diseased brain. Expert opinion on drug delivery. 2009;6(3):227-37.
19. Treat LH, McDannold N, Zhang Y, Vykhodtseva N, Hynynen K. Improved anti-tumor effect of liposomal doxorubicin after targeted blood-brain barrier disruption by MRI-guided focused ultrasound in rat glioma. Ultrasound in medicine & biology. 2012;38(10):1716-25.
20. Pardridge WM. BBB-Genomics: creating new openings for brain-drug targeting. Drug Discov Today. 2001;6(8):381-3.
21. Potjewyd G, Moxon S, Wang T, Domingos M, Hooper NM. Tissue Engineering 3D Neurovascular Units: A Biomaterials and Bioprinting Perspective. Trends in Biotechnology. 2018;36(4):457-72.
22. Hawkins BT, Egleton RD. Pathophysiology of the blood–brain barrier: animal models and methods. Current topics in developmental biology. 2007;80:277-309.

23. Winkler EA, Bell RD, Zlokovic BV. Central nervous system pericytes in health and disease. Nature Neuroscience. 2011;14(11):1398-405.
24. Sweeney MD, Ayyadurai S, Zlokovic BV. Pericytes of the neurovascular unit: key functions and signaling pathways. Nature Neuroscience. 2016;19:771.
25. Golden PL, Pollack GM. Blood–brain barrier efflux transport. Journal of pharmaceutical sciences. 2003;92(9):1739-53.
26. Ito S, Yanai M, Yamaguchi S, Couraud P-O, Ohtsuki S. Regulation of Tight-Junction Integrity by Insulin in an In Vitro Model of Human Blood–Brain Barrier. Journal of pharmaceutical sciences. 2017;106(9):2599-605.
27. Lalatsa A, Butt AM. Chapter 3 - Physiology of the Blood–Brain Barrier and Mechanisms of Transport Across the BBB A2 - Kesharwani, Prashant. In: Gupta U, editor. Nanotechnology-Based Targeted Drug Delivery Systems for Brain Tumors: Academic Press; 2018. p. 49-74.
28. Chinta SJ, Pai HV, Upadhya SC, Boyd MR, Ravindranath V. Constitutive expression and localization of the major drug metabolizing enzyme, cytochrome P4502D in human brain. Molecular Brain Research. 2002;103(1):49-61.
29. Stewart PA. Endothelial vesicles in the blood–brain barrier: are they related to permeability? Cellular and molecular neurobiology. 2000;20(2):149-63.
30. Abbott NJ. Dynamics of CNS barriers: evolution, differentiation, and modulation. Cellular and molecular neurobiology. 2005;25(1):5-23.
31. Abbott NJ, Rönnbäck L, Hansson E. Astrocyte–endothelial interactions at the blood–brain barrier. Nature Reviews Neuroscience. 2006;7(1):41-53.
32. Hawkins BT, Davis TP. The blood-brain barrier/neurovascular unit in health and disease. Pharmacological reviews. 2005;57(2):173-85.
33. Abbott NJ, Patabendige AA, Dolman DE, Yusof SR, Begley DJ. Structure and function of the blood–brain barrier. Neurobiology of disease. 2010;37(1):13-25.
34. Weiss N, Miller F, Cazaubon S, Couraud P-O. The blood-brain barrier in brain homeostasis and neurological diseases. Biochimica et Biophysica Acta (BBA)-Biomembranes. 2009;1788(4):842-57.
35. Alyautdin R, Khalin I, Nafeeza MI, Haron MH, Kuznetsov D. Nanoscale drug delivery systems and the blood-brain barrier. International journal of nanomedicine. 2014;9:795-811.
36. Wang Y-Z, Xu Q, Wu W, Liu Y, Jiang Y, Cai Q-Q, et al. Brain Transport Profiles of Ginsenoside Rb1 by Glucose Transporter 1: In Vitro and in Vivo. Frontiers in Pharmacology. 2018;9(398).
37. Chikamoto A, Inoue R, Komohara Y, Sakamaki K, Hashimoto D, Shiraishi S, et al. Preoperative High Maximum Standardized Uptake Value in Association with Glucose Transporter 1 Predicts Poor Prognosis in Pancreatic Cancer. Annals of Surgical Oncology. 2017;24(7):2040-6.
38. Kärkkäinen J, Gynther M, Kokkola T, Petsalo A, Auriola S, Lahtela-Kakkonen M, et al. Structural properties for selective and efficient l-type amino acid transporter 1 (LAT1) mediated cellular uptake. Int J Pharm. 2018;544(1):91-9.
39. Zhao Y, Wang L, Pan J. The role of L-type amino acid transporter 1 in human tumors. Intractable & Rare Diseases Research. 2015;4(4):165-9.
40. Pardridge WM, Boado RJ, Giugliani R, Schmidt M. Plasma Pharmacokinetics of Valanafusp Alpha, a Human Insulin Receptor Antibody-Iduronidase Fusion Protein, in Patients with Mucopolysaccharidosis Type I. BioDrugs. 2018;32(2):169-76.
41. Thom G, Burrell M, Haqqani AS, Yogi A, Lessard E, Brunette E, et al. Enhanced Delivery of Galanin Conjugates to the Brain through Bioengineering of the Anti-Transferrin Receptor Antibody OX26. Molecular Pharmaceutics. 2018;15(4):1420-31.
42. Main BS, Villapol S, Sloley SS, Barton DJ, Parsadanian M, Agbaegbu C, et al. Apolipoprotein E4 impairs spontaneous blood brain barrier repair following traumatic brain injury. Molecular Neurodegeneration. 2018;13(1):17.
43. Dal Magro R, Albertini B, Beretta S, Rigolio R, Donzelli E, Chiorazzi A, et al. Artificial apolipoprotein corona enables nanoparticle brain targeting. Nanomedicine: Nanotechnology, Biology and Medicine. 2018;14(2):429-38.

44. Sapkota S, Bäckman L, Dixon RA. Executive function performance and change in aging is predicted by apolipoprotein E, intensified by catechol-O-methyltransferase and brain-derived neurotrophic factor, and moderated by age and lifestyle. Neurobiology of Aging. 2017;52:81-9.
45. Aryal M, Fischer K, Gentile C, Gitto S, Zhang Y-Z, McDannold N. Effects on P-Glycoprotein Expression after Blood-Brain Barrier Disruption Using Focused Ultrasound and Microbubbles. PLoS One. 2017;12(1):e0166061.
46. Cornaire G, Woodley J, Hermann P, Cloarec A, Arellano C, Houin G. Impact of excipients on the absorption of P-glycoprotein substrates in vitro and in vivo. Int J Pharm. 2004;278(1):119-31.
47. Urayama A, Dohgu S, Robinson SM, Sly WS, Grubb JH, Banks WA. Alpha Adrenergic Induction of Transport of Lysosomal Enzyme across the Blood-Brain Barrier. PLoS One. 2015;10(11):e0142347.
48. Beis D, von Känel R, Heimgartner N, Zuccarella-Hackl C, Bürkle A, Ehlert U, et al. The role of norepinephrine and alpha-adrenergic receptors in acute stress-induced changes in granulocytes and monocytes. Psychosom Med. 2018.
49. Liu G, Zhang W, Guo J, Kong F, Zhou S, Chen S, et al. Adenosine binds predominantly to adenosine receptor A1 subtype in astrocytes and mediates an immunosuppressive effect. Brain Research. 2018;1700:47-55.
50. Mills JH, Alabanza L, Weksler BB, Couraud P-O, Romero IA, Bynoe MS. Human brain endothelial cells are responsive to adenosine receptor activation. Purinergic Signalling. 2011;7(2):265-73.
51. Fischer WJ, Altheimer S, Cattori V, Meier PJ, Dietrich DR, Hagenbuch B. Organic anion transporting polypeptides expressed in liver and brain mediate uptake of microcystin. Toxicology and Applied Pharmacology. 2005;203(3):257-63.
52. Takano J, Maeda K, Kusuhara H, Sugiyama Y. Organic anion transporting polypeptide 1a4 is responsible for the hepatic uptake of cardiac glycosides in mice. Drug Metabolism and Disposition. 2018.
53. Bennani-Baiti B, Toegel S, Viernstein H, Urban E, Noe CR, Bennani-Baiti IM. Inflammation Modulates RLIP76/RALBP1 Electrophile-Glutathione Conjugate Transporter and Housekeeping Genes in Human Blood-Brain Barrier Endothelial Cells. PLoS One. 2015;10(9):e0139101.
54. Gajbhiye KR, Gajbhiye V, Siddiqui IA, Pilla S, Soni V. Ascorbic acid tethered polymeric nanoparticles enable efficient brain delivery of galantamine: An in vitro-in vivo study. Scientific Reports. 2017;7(1):11086.
55. Sardi I, Fantappiè O, la Marca G, Giovannini MG, Iorio AL, da Ros M, et al. Delivery of doxorubicin across the blood–brain barrier by ondansetron pretreatment: a study in vitro and in vivo. Cancer Letters. 2014;353(2):242-7.
56. Alli S, Figueiredo CA, Golbourn B, Sabha N, Wu MY, Bondoc A, et al. Brainstem blood brain barrier disruption using focused ultrasound: A demonstration of feasibility and enhanced doxorubicin delivery. Journal of Controlled Release. 2018;281:29-41.
57. Abbott NJ, Romero IA. Transporting therapeutics across the blood-brain barrier. Molecular medicine today. 1996;2(3):106-13.
58. Lipinski CA. Drug-like properties and the causes of poor solubility and poor permeability. Journal of Pharmacological and Toxicological Methods. 2000;44(1):235-49.
59. Pajouhesh H, Lenz GR. Medicinal chemical properties of successful central nervous system drugs. NeuroRx : the journal of the American Society for Experimental NeuroTherapeutics. 2005;2(4):541-53.
60. Lipinski CA, Lombardo F, Dominy BW, Feeney PJ. Experimental and computational approaches to estimate solubility and permeability in drug discovery and development settings1PII of original article: S0169-409X(96)00423-1. The article was originally published in Advanced Drug Delivery Reviews 23 (1997) 3–25.1. Advanced Drug Delivery Reviews. 2001;46(1):3-26.
61. Pardridge WM. Drug transport across the blood–brain barrier. Journal of Cerebral Blood Flow & Metabolism. 2012;32(11):1959-72.

62. Alam MI, Beg S, Samad A, Baboota S, Kohli K, Ali J, et al. Strategy for effective brain drug delivery. Eur J Pharm Sci. 2010;40(5):385-403.
63. Mathon B, Nassar M, Simonnet J, Le Duigou C, Clemenceau S, Miles R, et al. Increasing the effectiveness of intracerebral injections in adult and neonatal mice: a neurosurgical point of view. Neuroscience Bulletin. 2015;31(6):685-96.
64. Xue M, Del Bigio MR. Intracerebral injection of autologous whole blood in rats: time course of inflammation and cell death. Neuroscience letters. 2000;283(3):230-2.
65. Vezzani A, Moneta D, Conti M, Richichi C, Ravizza T, De Luigi A, et al. Powerful anticonvulsant action of IL-1 receptor antagonist on intracerebral injection and astrocytic overexpression in mice. Proceedings of the National Academy of Sciences. 2000;97(21):11534-9.
66. Qi X-M, Wang C, Chu X-K, Li G, Ma J-F. Intraventricular infusion of clusterin ameliorated cognition and pathology in Tg6799 model of Alzheimer's disease. BMC Neuroscience. 2018;19(1):2.
67. Pan S, Huang X, Wang Y, Li L, Zhao C, Yao Z, et al. Efficacy of intravenous plus intrathecal/intracerebral ventricle injection of polymyxin B for post-neurosurgical intracranial infections due to MDR/XDR Acinectobacter baumannii: a retrospective cohort study. Antimicrobial Resistance & Infection Control. 2018;7(1):8.
68. Kim J-Y, Grunke SD, Levites Y, Golde TE, Jankowsky JL. Intracerebroventricular Viral Injection of the Neonatal Mouse Brain for Persistent and Widespread Neuronal Transduction. Journal of Visualized Experiments : JoVE. 2014(91):51863.
69. Mygind N, Dahl R. Anatomy, physiology and function of the nasal cavities in health and disease. Adv Drug Deliv Rev. 1998;29(1):3-12.
70. Khan A, Aqil M, Imam SS, Ahad A, Sultana Y, Ali A, et al. Temozolomide loaded nano lipid based chitosan hydrogel for nose to brain delivery: Characterization, nasal absorption, histopathology and cell line study. International Journal of Biological Macromolecules. 2018;116:1260-7.
71. Liu S, Yang S, Ho PC. Intranasal administration of carbamazepine-loaded carboxymethyl chitosan nanoparticles for drug delivery to the brain. Asian Journal of Pharmaceutical Sciences. 2018;13(1):72-81.
72. Kaur S, Manhas P, Swami A, Bhandari R, Sharma KK, Jain R, et al. Bioengineered PLGA-chitosan nanoparticles for brain targeted intranasal delivery of antiepileptic TRH analogues. Chemical Engineering Journal. 2018;346:630-9.
73. Rodriguez M, Lapierre J, Ojha CR, Kaushik A, Batrakova E, Kashanchi F, et al. Intranasal drug delivery of small interfering RNA targeting Beclin1 encapsulated with polyethylenimine (PEI) in mouse brain to achieve HIV attenuation. Scientific Reports. 2017;7(1):1862.
74. Illum L. Nasal drug delivery—possibilities, problems and solutions. Journal of Controlled Release. 2003;87(1):187-98.
75. Illum L. Nasal drug delivery: new developments and strategies. Drug Discovery Today. 2002;7(23):1184-9.
76. Pardridge WM. Brain drug targeting: the future of brain drug development. J Clin Pathol. 2002;55:158.
77. Pardridge WM. Recent advances in blood-brain barrier transport. Annual review of pharmacology and toxicology. 1988;28(1):25-39.
78. Halbsguth U, Rentsch KM, Eich-Höchli D, Diterich I, Fattinger K. Oral diacetylmorphine (heroin) yields greater morphine bioavailability than oral morphine: bioavailability related to dosage and prior opioid exposure. British Journal of Clinical Pharmacology. 2008;66(6):781-91.
79. Sawynok J. The therapeutic use of heroin: a review of the pharmacological literature. Canadian journal of physiology and pharmacology. 1986;64(1):1-6.
80. Greig NH, Daly EM, Sweeney DJ, Rapoport SI. Pharmacokinetics of chlorambucil-tertiary butyl ester, a lipophilic chlorambucil derivative that achieves and maintains high concentrations in brain. Cancer chemotherapy and pharmacology. 1990;25(5):320-5.
81. Temsamani J, Scherrmann J-M, Rees AR, Kaczorek M. Brain drug delivery technologies: novel approaches for transporting therapeutics. Pharmaceutical science & technology today. 2000;3(5):155-62.

82. Pardridge WM. Drug targeting to the brain. Pharmaceutical research. 2007;24(9):1733-44.
83. Banks WA. Characteristics of compounds that cross the blood-brain barrier. BMC Neurology. 2009;9(Suppl 1):S3-S.
84. Rautio J, Laine K, Gynther M, Savolainen J. Prodrug approaches for CNS delivery. The AAPS journal. 2008;10(1):92-102.
85. Pavan B, Dalpiaz A, Ciliberti N, Biondi C, Manfredini S, Vertuani S. Progress in drug delivery to the central nervous system by the prodrug approach. Molecules. 2008;13(5):1035-65.
86. Hsieh P-W, Hung C-F, Fang J-Y. Current prodrug design for drug discovery. Current pharmaceutical design. 2009;15(19):2236-50.
87. Zawilska JB, Wojcieszak J, Olejniczak AB. Prodrugs: a challenge for the drug development. Pharmacological reports. 2013;65(1):1-14.
88. Tomicic MT, Thust R, Kaina B. Ganciclovir-induced apoptosis in HSV-1 thymidine kinase expressing cells: critical role of DNA breaks, Bcl-2 decline and caspase-9 activation. Oncogene. 2002;21:2141.
89. Hu L. Prodrugs: effective solutions for solubility, permeability and targeting challenges. IDrugs:The Investigational Drugs Journal. 2004;7(8):736-42.
90. Gynther M, Jalkanen A, Lehtonen M, Forsberg M, Laine K, Ropponen J, et al. Brain uptake of ketoprofen–lysine prodrug in rats. Int J Pharm. 2010;399(1):121-8.
91. Linhui W, Li Z, Yi Z, Qiuyi F, Wenjiao X, Runxin L, et al. Design, synthesis, and neuroprotective effects of dual‐brain targeting naproxen prodrug. Archiv der Pharmazie. 2018;351(5):1700382.
92. Cockle SM, Aitken A, Beg F, Smyth DG. A novel peptide, pyroglutamylglutamylproline amide, in the rabbit prostate complex, structurally related to thyrotrophin-releasing hormone. Journal of Biological Chemistry. 1989;264(14):7788-91.
93. Nguyen V, Zharikova AD, Prokai-Tatrai K, Prokai L. [Glu(2)]TRH dose-dependently attenuates TRH-evoked analeptic effect in the mouse brain. Brain research bulletin. 2010;82(1-2):83-6.
94. Prokai-Tatrai K, Prokai L. Prodrug Design for Brain Delivery of Small- and Medium-Sized Neuropeptides. In: Merighi A, editor. Neuropeptides: Methods and Protocols. Totowa, NJ: Humana Press; 2011. p. 313-36.
95. Prokai-Tatrai K, Nguyen V, Zharikova AD, Braddy AC, Stevens SM, Prokai L. Prodrugs to enhance central nervous system effects of the TRH-like peptide pGlu-Glu-Pro-NH2. Bioorganic & Medicinal Chemistry Letters. 2003;13(6):1011-4.
96. Saito Y, Nishio K, Akazawa YO, Yamanaka K, Miyama A, Yoshida Y, et al. Cytoprotective effects of vitamin E homologues against glutamate-induced cell death in immature primary cortical neuron cultures: Tocopherols and tocotrienols exert similar effects by antioxidant function. Free Radical Biology and Medicine. 2010;49(10):1542-9.
97. Selvaraju TR, Khaza'ai H, Vidyadaran S, Abd Mutalib MS, Vasudevan R. The neuroprotective effects of tocotrienol rich fraction and alpha tocopherol against glutamate injury in astrocytes. Bosnian Journal of Basic Medical Sciences. 2014;14(4):195-204.
98. Comitato R, Ambra R, Virgili F. Tocotrienols: A Family of Molecules with Specific Biological Activities. Antioxidants. 2017;6(4):93.
99. Zhou J, Tao P, Fisher JF, Shi Q, Mobashery S, Schlegel HB. QM/MM Studies of the Matrix Metalloproteinase 2 (MMP2) Inhibition Mechanism of (S)-SB-3CT and its Oxirane Analogue. Journal of chemical theory and computation. 2010;6(11):3580-7.
100. Lee M, Chen Z, Tomlinson BN, Gooyit M, Hesek D, Juárez MR, et al. Water-Soluble MMP-9 Inhibitor Reduces Lesion Volume after Severe Traumatic Brain Injury. ACS chemical neuroscience. 2015;6(10):1658-64.
101. Ruan H, Chai Z, Shen Q, Chen X, Su B, Xie C, et al. A novel peptide ligand RAP12 of LRP1 for glioma targeted drug delivery. Journal of Controlled Release. 2018;279:306-15.
102. Bodor N. Drug targeting and retrometabolic drug design approaches introduction. Adv Drug Deliv Rev. 1994;14(2-3):157-66.

103. Somogyi G, Buchwald P, Nomi D, Prokai L, Bodor N. Targeted drug delivery to the brain via phosphonate derivatives II. Anionic chemical delivery system for zidovudine (AZT). International journal of pharmaceutics. 1998;166(1):27-35.
104. Yi Z, Li Z, Yao P, Qiming Y, Li H, Li G, et al. GLUT1‐mediated venlafaxine‐thiamine disulfide system‐glucose conjugates with "lock‐in" function for central nervous system delivery. Chemical Biology & Drug Design. 2018;91(3):707-16.
105. Bodor N, Buchwald P. Drug targeting via retrometabolic approaches. Pharmacology & therapeutics. 1997;76(1-3):1-27.
106. Jones EM, Polt R. CNS active O-linked glycopeptides. Frontiers in Chemistry. 2015;3:40.
107. Chen Y, Liu L. Modern methods for delivery of drugs across the blood–brain barrier. Adv Drug Deliv Rev. 2012;64(7):640-65.
108. Kratz F. Albumin as a drug carrier: design of prodrugs, drug conjugates and nanoparticles. Journal of controlled release. 2008;132(3):171-83.
109. Kang Y-S, Pardridge WM. Brain delivery of biotin bound to a conjugate of neutral avidin and cationized human albumin. Pharmaceutical research. 1994;11(9):1257-64.
110. Neves V, Aires-da-Silva F, Morais M, Gano L, Ribeiro E, Pinto A, et al. Novel Peptides Derived from Dengue Virus Capsid Protein Translocate Reversibly the Blood–Brain Barrier through a Receptor-Free Mechanism. ACS Chemical Biology. 2017;12(5):1257-68.
111. Tsuji A, Tamai I. Carrier-mediated or specialized transport of drugs across the blood–brain barrier. Adv Drug Deliv Rev. 1999;36(2):277-90.
112. Leviel V. Dopamine release mediated by the dopamine transporter, facts and consequences. Journal of neurochemistry. 2011;118(4):475-89.
113. Haqqani AS, Delaney CE, Brunette E, Baumann E, Farrington GK, Sisk W, et al. Endosomal trafficking regulates receptor-mediated transcytosis of antibodies across the blood brain barrier. Journal of Cerebral Blood Flow & Metabolism. 2018;38(4):727-40.
114. Kuai Z, Xu Y, Zhao Q, Liu J, Guan S, Qiao Y, et al. Effects of insulin on transcriptional response and permeability in an in vitro model of human blood‐brain barrier. Journal of cellular biochemistry. 2018;119(7):5657-64.
115. Giugliani R, Giugliani L, Corte AD, Poswar F, Donis K, Schmidt M, et al. Safety and clinical efficacy of AGT-181, a brain penetrating human insulin receptor antibody-iduronidase fusion protein, in a 26-week study with pediatric patients with mucopolysaccharidosis type I. Molecular Genetics and Metabolism. 2018;123(2):S54.
116. Bien-Ly N, Yu YJ, Bumbaca D, Elstrott J, Boswell CA, Zhang Y, et al. Transferrin receptor (TfR) trafficking determines brain uptake of TfR antibody affinity variants. Journal of Experimental Medicine. 2014:jem. 20131660.
117. Liu K, Lei R, Li Q, Wang X-X, Wu Q, An P, et al. Transferrin Receptor Controls AMPA Receptor Trafficking Efficiency and Synaptic Plasticity. Scientific reports. 2016;6.
118. Lundin A, Rondahl H, Walum E, Wilcke M. Expression and intracellular localization of leptin receptor long isoform-GFP chimera. Biochimica et Biophysica Acta (BBA)-Molecular Cell Research. 2000;1499(1):130-8.
119. Tamaru M, Akita H, Fujiwara T, Kajimoto K, Harashima H. Leptin-derived peptide, a targeting ligand for mouse brain-derived endothelial cells via macropinocytosis. Biochemical and biophysical research communications. 2010;394(3):587-92.
120. Steckelbroeck S, Nassen A, Ugele B, Ludwig M, Watzka M, Reissinger A, et al. Steroid sulfatase (STS) expression in the human temporal lobe: enzyme activity, mRNA expression and immunohistochemistry study. Journal of neurochemistry. 2004;89(2):403-17.
121. Aller SG, Yu J, Ward A, Weng Y, Chittaboina S, Zhuo R, et al. Structure of P-glycoprotein reveals a molecular basis for poly-specific drug binding. Science. 2009;323(5922):1718-22.
122. Loo TW, Bartlett MC, Clarke DM. Identification of residues in the drug translocation pathway of the human multidrug resistance P-glycoprotein by arginine mutagenesis. Journal of Biological Chemistry. 2009;284(36):24074-87.
123. van Herwaarden AE, Schinkel AH. The function of breast cancer resistance protein in epithelial barriers, stem cells and milk secretion of drugs and xenotoxins. Trends in pharmacological sciences. 2006;27(1):10-6.

124. Vlaming ML, Lagas JS, Schinkel AH. Physiological and pharmacological roles of ABCG2 (BCRP): recent findings in Abcg2 knockout mice. Advanced drug delivery reviews. 2009;61(1):14-25.
125. Ulbrich K, Knobloch T, Kreuter J. Targeting the insulin receptor: nanoparticles for drug delivery across the blood–brain barrier (BBB). Journal of drug targeting. 2011;19(2):125-32.
126. Boado RJ, Hui EKW, Lu JZ, Pardridge WM. Insulin receptor antibody‐iduronate 2‐sulfatase fusion protein: Pharmacokinetics, anti‐drug antibody, and safety pharmacology in Rhesus monkeys. Biotechnology and Bioengineering. 2014;111(11):2317-25.
127. Kuo Y-C, Ko H-F. Targeting delivery of saquinavir to the brain using 83-14 monoclonal antibody-grafted solid lipid nanoparticles. Biomaterials. 2013;34(20):4818-30.
128. Boado RJ, Lu JZ, Hui EK-W, Pardridge WM. Insulin Receptor Antibody–Sulfamidase Fusion Protein Penetrates the Primate Blood–Brain Barrier and Reduces Glycosoaminoglycans in Sanfilippo Type A Cells. Molecular Pharmaceutics. 2014;11(8):2928-34.
129. Sonoda H, Morimoto H, Yoden E, Koshimura Y, Kinoshita M, Golovina G, et al. A blood-brain-barrier-penetrating anti-human transferrin receptor antibody fusion protein for neuronopathic mucopolysaccharidosis II. Molecular Therapy. 2018;26(5):1366-74.
130. Johnsen KB, Burkhart A, Melander F, Kempen PJ, Vejlebo JB, Siupka P, et al. Targeting transferrin receptors at the blood-brain barrier improves the uptake of immunoliposomes and subsequent cargo transport into the brain parenchyma. Scientific Reports. 2017;7(1):10396.
131. Sonali, Agrawal P, Singh RP, Rajesh CV, Singh S, Vijayakumar MR, et al. Transferrin receptor-targeted vitamin E TPGS micelles for brain cancer therapy: preparation, characterization and brain distribution in rats. Drug Delivery. 2016;23(5):1788-98.
132. Cabezón I, Manich G, Martín-Venegas R, Camins A, Pelegrí C, Vilaplana J. Trafficking of Gold Nanoparticles Coated with the 8D3 Anti-Transferrin Receptor Antibody at the Mouse Blood–Brain Barrier. Molecular Pharmaceutics. 2015;12(11):4137-45.
133. Webster CI, Hatcher J, Burrell M, Thom G, Thornton P, Gurrell I, et al. Enhanced delivery of IL-1 receptor antagonist to the central nervous system as a novel anti–transferrin receptor-IL-1RA fusion reverses neuropathic mechanical hypersensitivity. Pain. 2017;158(4):660-8.
134. Oganesyan V, Gao C, Shirinian L, Wu H, Dall'Acqua WF. Structural characterization of a human Fc fragment engineered for lack of effector functions. Acta Crystallographica Section D: Biological Crystallography. 2008;64(Pt 6):700-4.
135. Kreuter J, Shamenkov D, Petrov V, Ramge P, Cychutek K, Koch-Brandt C, et al. Apolipoprotein-mediated Transport of Nanoparticle-bound Drugs Across the Blood-Brain Barrier. Journal of drug targeting. 2002;10(4):317-25.
136. Huang S, Li J, Han L, Liu S, Ma H, Huang R, et al. Dual targeting effect of Angiopep-2-modified, DNA-loaded nanoparticles for glioma. Biomaterials. 2011;32(28):6832-8.
137. Kuo Y-C, Chen Y-C. Targeting delivery of etoposide to inhibit the growth of human glioblastoma multiforme using lactoferrin- and folic acid-grafted poly(lactide-co-glycolide) nanoparticles. Int J Pharm. 2015;479(1):138-49.
138. Javed H, Menon SA, Al-Mansoori KM, Al-Wandi A, Majbour NK, Ardah MT, et al. Development of Nonviral Vectors Targeting the Brain as a Therapeutic Approach For Parkinson's Disease and Other Brain Disorders. Molecular therapy : the journal of the American Society of Gene Therapy. 2016;24(4):746-58.
139. Gong C, Li X, Xu L, Zhang Y-H. Target delivery of a gene into the brain using the RVG29-oligoarginine peptide. Biomaterials. 2012;33(12):3456-63.
140. Banks WA, Jaspan JB, Huang W, Kastin AJ. Transport of Insulin Across the Blood-Brain Barrier: Saturability at Euglycemic Doses of Insulin. Peptides. 1997;18(9):1423-9.
141. Plum L, Schubert M, Brüning JC. The role of insulin receptor signaling in the brain. Trends in Endocrinology & Metabolism. 2005;16(2):59-65.
142. Bickel U, Yoshikawa T, Pardridge WM. Delivery of peptides and proteins through the blood–brain barrier. Adv Drug Deliv Rev. 2001;46(1):247-79.
143. Duffy KR, Pardridge WM, Rosenfeld RG. Human blood-brain barrier insulin-like growth factor receptor. Metabolism. 1988;37(2):136-40.

144. Venepalli NK, Emmadi R, Danciu OC, Chowdhery R, Cabay RJ, Gaitonde S, et al. Phase I study of IGF-methotrexate conjugate in the treatment of advanced tumors expressing IGF-1R. American journal of clinical oncology. 2019;42(11):862-9.
145. Boado RJ, Pardridge WM. Brain and Organ Uptake in the Rhesus Monkey in Vivo of Recombinant Iduronidase Compared to an Insulin Receptor Antibody–Iduronidase Fusion Protein. Molecular Pharmaceutics. 2017;14(4):1271-7.
146. Pardridge WM, Boado RJ, inventors; Google Patents, assignee. Compositions and methods for blood-brain barrier delivery of igg-decoy receptor fusion proteins patent US15357894A1. 2012.
147. Jefferies WA, Brandon MR, Hunt SV, Williams AF, Gatter KC, Mason DY. Transferrin receptor on endothelium of brain capillaries. Nature. 1984;312:162.
148. Friden PM, Walus LR, Musso GF, Taylor MA, Malfroy B, Starzyk RM. Anti-transferrin receptor antibody and antibody-drug conjugates cross the blood-brain barrier. Proceedings of the National Academy of Sciences of the United States of America. 1991;88(11):4771-5.
149. Ponka P, Lok CN. The transferrin receptor: role in health and disease. The International Journal of Biochemistry & Cell Biology. 1999;31(10):1111-37.
150. Sharma G, Modgil A, Layek B, Arora K, Sun C, Law B, et al. Cell penetrating peptide tethered bi-ligand liposomes for delivery to brain in vivo: Biodistribution and transfection. Journal of Controlled Release. 2013;167(1):1-10.
151. Urbiola K, Blanco-Fernández L, Ogris M, Rödl W, Wagner E, Tros de Ilarduya C. Novel PAMAM-PEG-Peptide Conjugates for siRNA Delivery Targeted to the Transferrin and Epidermal Growth Factor Receptors. Journal of Personalized Medicine. 2018;8(1):4.
152. Hultqvist G, Syvänen S, Fang XT, Lannfelt L, Sehlin D. Bivalent Brain Shuttle Increases Antibody Uptake by Monovalent Binding to the Transferrin Receptor. Theranostics. 2017;7(2):308-18.
153. Macdonald J, Henri J, Goodman L, Xiang D, Duan W, Shigdar S. Development of a Bifunctional Aptamer Targeting the Transferrin Receptor and Epithelial Cell Adhesion Molecule (EpCAM) for the Treatment of Brain Cancer Metastases. ACS Chemical Neuroscience. 2017;8(4):777-84.
154. McConnell EM, Ventura K, Dwyer Z, Hunt V, Koudrina A, Holahan MR, et al. In Vivo Use of a Multi-DNA Aptamer-Based Payload/Targeting System To Study Dopamine Dysregulation in the Central Nervous System. ACS Chem Neurosci. 2019;10(1):371-83.
155. Huang R, Ke W, Han L, Liu Y, Shao K, Jiang C, et al. Lactoferrin-modified nanoparticles could mediate efficient gene delivery to the brain in vivo. Brain Research Bulletin. 2010;81(6):600-4.
156. Yang T, Williams BO. Low-Density Lipoprotein Receptor-Related Proteins in Skeletal Development and Disease. Physiological Reviews. 2017;97(3):1211-28.
157. Dehouck B, Fenart L, Dehouck M-P, Pierce A, Torpier G, Cecchelli R. A New Function for the LDL Receptor: Transcytosis of LDL across the Blood–Brain Barrier. The Journal of cell biology. 1997;138(4):877-89.
158. Benchenane K, Berezowski V, Ali C, Fernández-Monreal M, López-Atalaya JP, Brillault J, et al. Tissue-Type Plasminogen Activator Crosses the Intact Blood-Brain Barrier by Low-Density Lipoprotein Receptor–Related Protein-Mediated Transcytosis. Circulation. 2005;111(17):2241-9.
159. Candela P, Gosselet F, Miller F, Buee-Scherrer V, Torpier G, Cecchelli R, et al. Physiological Pathway for Low-Density Lipoproteins across the Blood-Brain Barrier: Transcytosis through Brain Capillary Endothelial Cells In Vitro. Endothelium. 2008;15(5-6):254-64.
160. Kurzrock R, Gabrail N, Chandhasin C, Moulder S, Smith C, Brenner A, et al. Safety, pharmacokinetics, and activity of GRN1005, a novel conjugate of angiopep-2, a peptide facilitating brain penetration, and paclitaxel, in patients with advanced solid tumors. Molecular cancer therapeutics. 2012;11(2):308-16.
161. Drappatz J, Brenner A, Wong ET, Eichler A, Schiff D, Groves MD, et al. Phase I study of GRN1005 in recurrent malignant glioma. Clinical Cancer Research. 2013;19(6):1567-76.
162. Tang S, Bates S, Kesari S, Brenner A, Anders C, Garcia A, et al., editors. A phase II, open-label, multi-center study of ANG1005, a novel brain penetrant taxane derivative, in breast cancer

patients with recurrent CNS metastases. CANCER RESEARCH; 2016: AMER ASSOC CANCER RESEARCH 615 CHESTNUT ST, 17TH FLOOR, PHILADELPHIA, PA ….
163. Datta G, Chaddha M, Garber DW, Chung BH, Tytler EM, Dashti N, et al. The Receptor Binding Domain of Apolipoprotein E, Linked to a Model Class A Amphipathic Helix, Enhances Internalization and Degradation of LDL by Fibroblasts. Biochemistry. 2000;39(1):213-20.
164. Yamada K, Hashimoto T, Yabuki C, Nagae Y, Tachikawa M, Strickland DK, et al. The Low Density Lipoprotein Receptor-related Protein 1 Mediates Uptake of Amyloid β Peptides in an in Vitro Model of the Blood-Brain Barrier Cells. The Journal of Biological Chemistry. 2008;283(50):34554-62.
165. Wang D, El-Amouri SS, Dai M, Kuan C-Y, Hui DY, Brady RO, et al. Engineering a lysosomal enzyme with a derivative of receptor-binding domain of apoE enables delivery across the blood–brain barrier. Proceedings of the National Academy of Sciences of the United States of America. 2013;110(8):2999-3004.
166. Papademetriou J, Garnacho C, Serrano D, Bhowmick T, Schuchman EH, Muro S. Comparative binding, endocytosis, and biodistribution of antibodies and antibody-coated carriers for targeted delivery of lysosomal enzymes to ICAM-1 versus transferrin receptor. Journal of Inherited Metabolic Disease. 2013;36(3):467-77.
167. Pardridge WM. Receptor-mediated peptide transport through the blood-brain barrier. Endocrine reviews. 1986;7(3):314-30.
168. Kumar P, Wu H, McBride JL, Jung K-E, Hee Kim M, Davidson BL, et al. Transvascular delivery of small interfering RNA to the central nervous system. Nature. 2007;448:39.
169. Alvarez-Erviti L, Seow Y, Yin H, Betts C, Lakhal S, Wood MJA. Delivery of siRNA to the mouse brain by systemic injection of targeted exosomes. Nature Biotechnology. 2011;29:341.
170. Conceição M, Mendonça L, Nóbrega C, Gomes C, Costa P, Hirai H, et al. Intravenous administration of brain-targeted stable nucleic acid lipid particles alleviates Machado-Joseph disease neurological phenotype. Biomaterials. 2016;82:124-37.
171. Oller‐Salvia B, Sánchez‐Navarro M, Ciudad S, Guiu M, Arranz‐Gibert P, Garcia C, et al. MiniAp‐4: A Venom‐Inspired Peptidomimetic for Brain Delivery. Angewandte Chemie. 2016;128(2):582-5.
172. Lee J-H, Zhang A, You SS, Lieber CM. Spontaneous internalization of cell penetrating peptide-modified nanowires into primary neurons. Nano letters. 2016;16(2):1509-13.
173. Prades R, Oller-Salvia B, Schwarzmaier SM, Selva J, Moros M, Balbi M, et al. Applying the Retro-Enantio Approach To Obtain a Peptide Capable of Overcoming the Blood–Brain Barrier. Angewandte Chemie International Edition. 2015;54(13):3967-72.
174. Zandl-Lang M, Fanaee-Danesh E, Sun Y, Albrecher NM, Gali CC, Čančar I, et al. Regulatory effects of simvastatin and apoJ on APP processing and amyloid-β clearance in blood-brain barrier endothelial cells. Biochimica et Biophysica Acta (BBA) - Molecular and Cell Biology of Lipids. 2018;1863(1):40-60.
175. Li X, Peng J, Pang J, Wu Y, Huang X, Li Y, et al. Apolipoprotein E-Mimetic Peptide COG1410 Promotes Autophagy by Phosphorylating GSK-3β in Early Brain Injury Following Experimental Subarachnoid Hemorrhage. Frontiers in Neuroscience. 2018;12(127).
176. Spencer BJ, Verma IM. Targeted delivery of proteins across the blood–brain barrier. Proceedings of the National Academy of Sciences of the United States of America. 2007;104(18):7594-9.
177. Gao H, Qian J, Cao S, Yang Z, Pang Z, Pan S, et al. Precise glioma targeting of and penetration by aptamer and peptide dual-functioned nanoparticles. Biomaterials. 2012;33(20):5115-23.
178. Srivastava A, Lusby E, Berns KI. Nucleotide sequence and organization of the adeno-associated virus 2 genome. Journal of virology. 1983;45(2):555-64.
179. Merkel SF, Andrews AM, Lutton EM, Mu D, Hudry E, Hyman BT, et al. Trafficking of adeno-associated virus vectors across a model of the blood-brain barrier; a comparative study of transcytosis and transduction using primary human brain endothelial cells. Journal of neurochemistry. 2017;140(2):216-30.

180. Aubourg P, Sevin C, Zerah M, Roujeau T, Cartier N. Intracerebral gene therapy for children with early onset forms of metachromatic leukodystrophy (TG-MLD). Clinical Trials gov (NCT01801709). 2015.
181. Rafii MS, Tuszynski MH, Thomas RG, Barba D, Brewer JB, Rissman RA, et al. Adeno-Associated Viral Vector (Serotype 2)-Nerve Growth Factor for Patients With Alzheimer Disease: A Randomized Clinical Trial. JAMA neurology. 2018;75(7):834-41.
182. Mandel RJ. CERE-110, an adeno-associated virus-based gene delivery vector expressing human nerve growth factor for the treatment of Alzheimer's disease. Current opinion in molecular therapeutics. 2010;12(2):240-7.
183. Marc T, Michel Z, Béatrice H, Stéphanie dB, Kumaran D, Catherine A, et al. Intracerebral Administration of Adeno-Associated Viral Vector Serotype rh.10 Carrying Human SGSH and SUMF1 cDNAs in Children with Mucopolysaccharidosis Type IIIA Disease: Results of a Phase I/II Trial. Human Gene Therapy. 2014;25(6):506-16.
184. Zhang X, He T, Chai Z, Samulski RJ, Li C. Blood-brain barrier shuttle peptides enhance AAV transduction in the brain after systemic administration. Biomaterials. 2018;176:71-83.
185. Körbelin J, Dogbevia G, Michelfelder S, Ridder DA, Hunger A, Wenzel J, et al. A brain microvasculature endothelial cell‐specific viral vector with the potential to treat neurovascular and neurological diseases. EMBO Molecular Medicine. 2016;8(6):609-25.
186. Samaranch L, Blits B, San Sebastian W, Hadaczek P, Bringas J, Sudhakar V, et al. MR-guided parenchymal delivery of adeno-associated viral vector serotype 5 in non-human primate brain. Gene Therapy. 2017;24:253.
187. Watakabe A, Ohtsuka M, Kinoshita M, Takaji M, Isa K, Mizukami H, et al. Comparative analyses of adeno-associated viral vector serotypes 1, 2, 5, 8 and 9 in marmoset, mouse and macaque cerebral cortex. Neuroscience Research. 2015;93:144-57.
188. Tordo J, O'Leary C, Antunes A, Palomar N, Aldrin-Kirk P, Basche M, et al. A novel adeno-associated virus capsid with enhanced neurotropism corrects a lysosomal transmembrane enzyme deficiency. Brain A Journal of Neurology. 2018;141(7):2014-31.
189. Costantino L, Gandolfi F, Tosi G, Rivasi F, Vandelli MA, Forni F. Peptide-derivatized biodegradable nanoparticles able to cross the blood–brain barrier. Journal of Controlled Release. 2005;108(1):84-96.
190. Elmagbari NO, Egleton RD, Palian MM, Lowery JJ, Schmid WR, Davis P, et al. Antinociceptive Structure-Activity Studies with Enkephalin-Based Opioid Glycopeptides. Journal of Pharmacology and Experimental Therapeutics. 2004;311(1):290-7.
191. Vilella A, Tosi G, Grabrucker AM, Ruozi B, Belletti D, Vandelli MA, et al. Insight on the fate of CNS-targeted nanoparticles. Part I: Rab5-dependent cell-specific uptake and distribution. Journal of Controlled Release. 2014;174(Supplement C):195-201.
192. Tosi G, Bondioli L, Ruozi B, Badiali L, Severini GM, Biffi S, et al. NIR-labeled nanoparticles engineered for brain targeting: in vivo optical imaging application and fluorescent microscopy evidences. Journal of Neural Transmission. 2011;118(1):145-53.
193. Borros GS, RIVERO MFX, CASCANTE CA, inventors; Google Patents, assignee. Polypeptides for blood brain barrier transport patent WO2014076655A1. 2014.
194. Demeule M, Régina A, Ché C, Poirier J, Nguyen T, Gabathuler R, et al. Identification and Design of Peptides as a New Drug Delivery System for the Brain. Journal of Pharmacology and Experimental Therapeutics. 2008;324(3):1064-72.
195. Bertrand Y, Currie J-C, Demeule M, Régina A, Ché C, Abulrob A, et al. Transport characteristics of a novel peptide platform for CNS therapeutics. Journal of Cellular and Molecular Medicine. 2010;14(12):2827-39.
196. Schwarze SR, Ho A, Vocero-Akbani A, Dowdy SF. In Vivo Protein Transduction: Delivery of a Biologically Active Protein into the Mouse. Science. 1999;285(5433):1569-72.
197. Arranz-Gibert P, Guixer B, Malakoutikhah M, Muttenthaler M, Guzmán F, Teixidó M, et al. Lipid Bilayer Crossing—The Gate of Symmetry. Water-Soluble Phenylproline-Based Blood-Brain Barrier Shuttles. Journal of the American Chemical Society. 2015;137(23):7357-64.

198. Gregori M, Taylor M, Salvati E, Re F, Mancini S, Balducci C, et al. Retro-inverso peptide inhibitor nanoparticles as potent inhibitors of aggregation of the Alzheimer's Aβ peptide. Nanomedicine. 2017;13(2):723-32.
199. Drin G, Cottin S, Blanc E, Rees AR, Temsamani J. Studies on the Internalization Mechanism of Cationic Cell-penetrating Peptides. Journal of Biological Chemistry. 2003;278(33):31192-201.
200. Malcor J-D, Payrot N, David M, Faucon A, Abouzid K, Jacquot G, et al. Chemical Optimization of New Ligands of the Low-Density Lipoprotein Receptor as Potential Vectors for Central Nervous System Targeting. Journal of Medicinal Chemistry. 2012;55(5):2227-41.
201. Liu Y, Li J, Shao K, Huang R, Ye L, Lou J, et al. A leptin derived 30-amino-acid peptide modified pegylated poly-l-lysine dendrigraft for brain targeted gene delivery. Biomaterials. 2010;31(19):5246-57.
202. Zhang C, Wan X, Zheng X, Shao X, Liu Q, Zhang Q, et al. Dual-functional nanoparticles targeting amyloid plaques in the brains of Alzheimer's disease mice. Biomaterials. 2014;35(1):456-65.
203. Li J, Feng L, Fan L, Zha Y, Guo L, Zhang Q, et al. Targeting the brain with PEG-PLGA nanoparticles modified with phage-displayed peptides. Biomaterials. 2011;32(21):4943-50.
204. Zheng X, Pang X, Yang P, Wan X, Wei Y, Guo Q, et al. A hybrid siRNA delivery complex for enhanced brain penetration and precise amyloid plaque targeting in Alzheimer's disease mice. Acta Biomaterialia. 2017;49(Supplement C):388-401.
205. Yao H, Wang K, Wang Y, Wang S, Li J, Lou J, et al. Enhanced blood–brain barrier penetration and glioma therapy mediated by a new peptide modified gene delivery system. Biomaterials. 2015;37(Supplement C):345-52.
206. Böckenhoff A, Cramer S, Wölte P, Knieling S, Wohlenberg C, Gieselmann V, et al. Comparison of Five Peptide Vectors for Improved Brain Delivery of the Lysosomal Enzyme Arylsulfatase A. The Journal of Neuroscience. 2014;34(9):3122.
207. Georgieva JV, Brinkhuis RP, Stojanov K, Weijers CAGM, Zuilhof H, Rutjes FPJT, et al. Peptide‐Mediated Blood–Brain Barrier Transport of Polymersomes. Angewandte Chemie International Edition. 2012;51(33):8339-42.
208. Zhang Y, Zhang W, Johnston AH, Newman TA, Pyykkö I, Zou J. Targeted delivery of Tet1 peptide functionalized polymersomes to the rat cochlear nerve. International Journal of Nanomedicine. 2012;7:1015-22.
209. Lee JH, Engler JA, Collawn JF, Moore BA. Receptor mediated uptake of peptides that bind the human transferrin receptor. European Journal of Biochemistry. 2001;268(7):2004-12.
210. Han L, Huang R, Liu S, Huang S, Jiang C. Peptide-Conjugated PAMAM for Targeted Doxorubicin Delivery to Transferrin Receptor Overexpressed Tumors. Molecular Pharmaceutics. 2010;7(6):2156-65.
211. Xie Y, Killinger B, Moszczynska A, Merkel O. Targeted Delivery of siRNA to Transferrin Receptor Overexpressing Tumor Cells via Peptide Modified Polyethylenimine. Molecules. 2016;21(10):1334.
212. Wang Z, Zhao Y, Jiang Y, Lv W, Wu L, Wang B, et al. Enhanced anti-ischemic stroke of ZL006 by T7-conjugated PEGylated liposomes drug delivery system. Scientific Reports. 2015;5:12651.
213. Lledó EG, Turà MT, Cosano RP, inventors; Google Patents, assignee. Protease-resistant compounds useful as shuttles through the blood-brain barrier and shuttle-cargo constructs patent US20150044140A1. 2016.
214. Arranz-Gibert P, Ciudad S, Seco J, García J, Giralt E, Teixidó M. Immunosilencing peptides by stereochemical inversion and sequence reversal: retro-D-peptides. Scientific Reports. 2018;8(1):6446.
215. Prades R, Guerrero S, Araya E, Molina C, Salas E, Zurita E, et al. Delivery of gold nanoparticles to the brain by conjugation with a peptide that recognizes the transferrin receptor. Biomaterials. 2012;33(29):7194-205.
216. Díaz-Perlas C, Oller-Salvia B, Sánchez-Navarro M, Teixidó M, Giralt E. Branched BBB-shuttle peptides: chemoselective modification of proteins to enhance blood–brain barrier transport. Chemical science. 2018;9(44):8409-15.

217. Teixidó M, Zurita E, Mendieta L, Oller‐Salvia B, Prades R, Tarragó T, et al. Dual system for the central nervous system targeting and blood‐brain barrier transport of a selective prolyl oligopeptidase inhibitor. Peptide Science. 2013;100(6):662-74.
218. Lindqvist A, Rip J, Gaillard PJ, Björkman S, Hammarlund-Udenaes M. Enhanced Brain Delivery of the Opioid Peptide DAMGO in Glutathione PEGylated Liposomes: A Microdialysis Study. Molecular Pharmaceutics. 2013;10(5):1533-41.
219. Rotman M, Welling MM, Bunschoten A, de Backer ME, Rip J, Nabuurs RJA, et al. Enhanced glutathione PEGylated liposomal brain delivery of an anti-amyloid single domain antibody fragment in a mouse model for Alzheimer's disease. Journal of Controlled Release. 2015;203(Supplement C):40-50.
220. Gaillard PJ, Appeldoorn CCM, Rip J, Dorland R, van der Pol SMA, Kooij G, et al. Enhanced brain delivery of liposomal methylprednisolone improved therapeutic efficacy in a model of neuroinflammation. Journal of Controlled Release. 2012;164(3):364-9.
221. Wei X, Zhan C, Shen Q, Fu W, Xie C, Gao J, et al. A D‐Peptide Ligand of Nicotine Acetylcholine Receptors for Brain‐Targeted Drug Delivery. Angewandte Chemie International Edition. 2015;54(10):3023-7.
222. Zhan C, Li B, Hu L, Wei X, Feng L, Fu W, et al. Micelle‐Based Brain‐Targeted Drug Delivery Enabled by a Nicotine Acetylcholine Receptor Ligand. Angewandte Chemie International Edition. 2011;50(24):5482-5.
223. Staquicini FI, Ozawa MG, Moya CA, Driessen WHP, Barbu EM, Nishimori H, et al. Systemic combinatorial peptide selection yields a non-canonical iron-mimicry mechanism for targeting tumors in a mouse model of human glioblastoma. The Journal of Clinical Investigation. 2011;121(1):161-73.
224. Urich E, Schmucki R, Ruderisch N, Kitas E, Certa U, Jacobsen H, et al. Cargo Delivery into the Brain by in vivo identified Transport Peptides. Scientific Reports. 2015;5:14104.
225. Obermeier B, Daneman R, Ransohoff RM. Development, maintenance and disruption of the blood-brain barrier. Nature Medicine. 2013;19(12):1584-96.
226. Doolittle ND, Petrillo A, Bell S, Cummings P, Eriksen S. Blood-brain barrier disruption for the treatment of malignant brain tumors: The National Program. Journal of Neuroscience Nursing. 1998;30(2):81-90.
227. Joshi S, Ergin A, Wang M, Reif R, Zhang J, Bruce JN, et al. Inconsistent blood brain barrier disruption by intraarterial mannitol in rabbits: implications for chemotherapy. Journal of neuro-oncology. 2011;104(1):11-9.
228. Salahuddin T, Johansson B, Kalimo H, Olsson Y. Structural changes in the rat brain after carotid infusions of hyperosmolar solutions: a light microscopic and immunohistochemical study. Neuropathology and applied neurobiology. 1988;14(6):467-82.
229. Bellavance M-A, Blanchette M, Fortin D. Recent Advances in Blood–Brain Barrier Disruption as a CNS Delivery Strategy. The AAPS Journal. 2008;10(1):166-77.
230. Bartus R, Elliott P, Hayward N, Dean R, McEwen E, Fisher S. Permeability of the blood brain barrier by the bradykinin agonist, RMP-7: evidence for a sensitive, auto-regulated, receptor-mediated system. Immunopharmacology. 1996;33(1-3):270-8.
231. Ma T, Xue Y-x. MiRNA-200b Regulates RMP7-Induced Increases in Blood-Tumor Barrier Permeability by Targeting RhoA and ROCKII. Frontiers in molecular neuroscience. 2016;9:9.
232. Zhang X, Xie Y, Jin Y, Hou X, Ye L, Lou J. The effect of RMP-7 and its derivative on transporting evens blue liposomes into the brain. Drug delivery. 2004;11(5):301-9.
233. Hui A, Zhu S, Yin H, Yang L, Zhang Z, Zhou A, et al. Novel ginkgolide B derivative attenuated the function and expression of P-glycoprotein at the blood–brain barrier, presenting brain-targeting ability. Royal Society of Chemistry Advances. 2016;6(37):31101-6.
234. Doi H, Sato K, Shindou H, Sumi K, Koyama H, Hosoya T, et al. Blood–brain barrier permeability of ginkgolide: Comparison of the behavior of PET probes 7α-[18 F] fluoro-and 10-O-p-[11 C] methylbenzyl ginkgolide B in monkey and rat brains. Bioorganic & Medicinal Chemistry. 2016;24(21):5148-57.

235. Saija A, Princi P, Trombetta D, Lanza M, Pasquale AD. Changes in the permeability of the blood-brain barrier following sodium dodecyl sulphate administration in the rat. Experimental brain research. 1997;115(3):546-51.
236. Kobiler D, Lustig S, Gozes Y, Ben-Nathan D, Akov Y. Sodium dodecylsulphate induces a breach in the blood-brain barrier and enables a West Nile virus variant to penetrate into mouse brain. Brain research. 1989;496(1):314-6.
237. Singh AK, Jiang Y, Gupta S, Benlhabib E. Effects of chronic ethanol drinking on the blood–brain barrier and ensuing neuronal toxicity in alcohol-preferring rats subjected to intraperitoneal LPS injection. Alcohol and alcoholism. 2007;42(5):385-99.
238. Hanig JP, Morrison JM, Krop S. Ethanol enhancement of blood-brain barrier permeability to catecholamines in chicks. European journal of pharmacology. 1972;18(1):79-82.
239. Gautier J-C, Bellamy R, inventors; Google Patents, assignee. Pharmaceutical amiodarone composition for parenteral delivery patent EP0835105A1. 2000.
240. Azmin MN, Stuart JF, Florence AT. The distribution and elimination of methotrexate in mouse blood and brain after concurrent administration of polysorbate 80. Cancer chemotherapy and pharmacology. 1985;14(3):238-42.
241. Kreuter J, Ramge P, Petrov V, Hamm S, Gelperina SE, Engelhardt B, et al. Direct evidence that polysorbate-80-coated poly (butylcyanoacrylate) nanoparticles deliver drugs to the CNS via specific mechanisms requiring prior binding of drug to the nanoparticles. Pharmaceutical research. 2003;20(3):409-16.
242. Alyautdin RN, Petrov VE, Langer K, Berthold A, Kharkevich DA, Kreuter J. Delivery of loperamide across the blood-brain barrier with polysorbate 80-coated polybutylcyanoacrylate nanoparticles. Pharmaceutical research. 1997;14(3):325-8.
243. Gulyaev AE, Gelperina SE, Skidan IN, Antropov AS, Kivman GY, Kreuter J. Significant transport of doxorubicin into the brain with polysorbate 80-coated nanoparticles. Pharmaceutical research. 1999;16(10):1564-9.
244. Takeuchi I, Nobata S, Oiri N, Tomoda K, Makino K. Biodistribution and excretion of colloidal gold nanoparticles after intravenous injection: Effects of particle size. Bio-Medical Materials and Engineering. 2017;28(3):315-23.
245. Kreuter J, Shamenkov D, Petrov V, Ramge P, Cychutek K, Koch-Brandt C, et al. Apolipoprotein-mediated transport of nanoparticle-bound drugs across the blood-brain barrier. Journal of drug targeting. 2002;10(4):317-25.
246. Begley DJ. Delivery of therapeutic agents to the central nervous system: the problems and the possibilities. Pharmacol Ther. 2004;104(1):29-45.
247. Kim C, Qin R, Xu JS, Wang LV, Xu R. Multifunctional microbubbles and nanobubbles for photoacoustic and ultrasound imaging. Journal of Biomedical Optics. 2010;15(1):010510.
248. Konofagou EE, Tung Y-S, Choi J, Deffieux T, Baseri B, Vlachos F. Ultrasound-Induced Blood-Brain Barrier Opening. Current pharmaceutical biotechnology. 2012;13(7):1332-45.
249. Chen H, Hwang JH. Ultrasound-targeted microbubble destruction for chemotherapeutic drug delivery to solid tumors. Journal of Therapeutic Ultrasound. 2013;1:10-.
250. Chen CC, Sheeran PS, Wu S-Y, Olumolade OO, Dayton PA, Konofagou EE. Targeted Drug Delivery with Focused Ultrasound-Induced Blood-Brain Barrier Opening Using Acoustically-Activated Nanodroplets. J Control Release. 2013;172(3):795-804.
251. Mesiwala AH, Farrell L, Wenzel HJ, Silbergeld DL, Crum LA, Winn HR, et al. High-intensity focused ultrasound selectively disrupts the blood-brain barrier in vivo. Ultrasound in medicine & biology. 2002;28(3):389-400.
252. Hynynen K, McDannold N, Vykhodtseva N, Jolesz FA. Noninvasive MR Imaging–guided Focal Opening of the Blood-Brain Barrier in Rabbits. Radiology. 2001;220(3):640-6.
253. Sheikov N, McDannold N, Vykhodtseva N, Jolesz F, Hynynen K. Cellular mechanisms of the blood-brain barrier opening induced by ultrasound in presence of microbubbles. Ultrasound in medicine & biology. 2004;30(7):979-89.
254. Cho C-W, Liu Y, Cobb WN, Henthorn TK, Lillehei K, Christians U, et al. Ultrasound-Induced Mild Hyperthermia as a Novel Approach to Increase Drug Uptake in Brain Microvessel Endothelial Cells. Pharmaceutical Research. 2002;19(8):1123-9.

255. Prokop A, Davidson JM. Nanovehicular Intracellular Delivery Systems. Journal of pharmaceutical sciences. 2008;97(9):3518-90.
256. Nunzio D, Adriana T, Valentino L, Angela L, Giuseppe T. Recent Advances in Medicinal Chemistry and Pharmaceutical Technology- Strategies for Drug Delivery to the Brain. Current Topics in Medicinal Chemistry. 2009;9(2):182-96.
257. Arnold AE, Czupiel P, Shoichet M. Engineered polymeric nanoparticles to guide the cellular internalization and trafficking of small interfering ribonucleic acids. Journal of Controlled Release. 2017;259:3-15.
258. Dong X. Current Strategies for Brain Drug Delivery. Theranostics. 2018;8(6):1481-93.
259. Verrecchia T, Spenlehauer G, Bazile DV, Murry-Brelier A, Archimbaud Y, Veillard M. Non-stealth (poly(lactic acid/albumin)) and stealth (poly(lactic acid-polyethylene glycol)) nanoparticles as injectable drug carriers. Journal of Controlled Release. 1995;36(1):49-61.
260. Salvalaio M, Rigon L, Belletti D, D'Avanzo F, Pederzoli F, Ruozi B, et al. Targeted Polymeric Nanoparticles for Brain Delivery of High Molecular Weight Molecules in Lysosomal Storage Disorders. PLoS One. 2016;11(5):e0156452.
261. Ana Rute N, Joana Fontes Q, Babette W, Ignacio AR, Pierre-Olivier C, Salette R. Solid lipid nanoparticles as a vehicle for brain-targeted drug delivery: two new strategies of functionalization with apolipoprotein E. Nanotechnology. 2015;26(49):495103.
262. Lin T, Zhao P, Jiang Y, Tang Y, Jin H, Pan Z, et al. Blood–Brain-Barrier-Penetrating Albumin Nanoparticles for Biomimetic Drug Delivery via Albumin-Binding Protein Pathways for Antiglioma Therapy. ACS Nano. 2016;10(11):9999-10012.
263. Xia H, Gao X, Gu G, Liu Z, Hu Q, Tu Y, et al. Penetratin-functionalized PEG–PLA nanoparticles for brain drug delivery. International Journal of Pharmaceutics. 2012;436(1):840-50.
264. Xin H, Jiang X, Gu J, Sha X, Chen L, Law K, et al. Angiopep-conjugated poly(ethylene glycol)-co-poly(ε-caprolactone) nanoparticles as dual-targeting drug delivery system for brain glioma. Biomaterials. 2011;32(18):4293-305.
265. Liu L, Guo K, Lu J, Venkatraman SS, Luo D, Ng KC, et al. Biologically active core/shell nanoparticles self-assembled from cholesterol-terminated PEG–TAT for drug delivery across the blood–brain barrier. Biomaterials. 2008;29(10):1509-17.
266. Hua H, Zhang X, Mu H, Meng Q, Jiang Y, Wang Y, et al. RVG29-modified docetaxel-loaded nanoparticles for brain-targeted glioma therapy. International Journal of Pharmaceutics. 2018;543(1):179-89.
267. Kanazawa T, Kaneko M, Niide T, Akiyama F, Kakizaki S, Ibaraki H, et al. Enhancement of nose-to-brain delivery of hydrophilic macromolecules with stearate- or polyethylene glycol-modified arginine-rich peptide. International Journal of Pharmaceutics. 2017;530(1):195-200.
268. Tosi G, Costantino L, Rivasi F, Ruozi B, Leo E, Vergoni AV, et al. Targeting the central nervous system: In vivo experiments with peptide-derivatized nanoparticles loaded with Loperamide and Rhodamine-123. Journal of Controlled Release. 2007;122(1):1-9.
269. Tosi G, Fano RA, Bondioli L, Badiali L, Benassi R, Rivasi F, et al. Investigation on mechanisms of glycopeptide nanoparticles for drug delivery across the blood–brain barrier. Nanomedicine. 2011;6(3):423-36.
270. You L, Wang J, Liu T, Zhang Y, Han X, Wang T, et al. Targeted Brain Delivery of Rabies Virus Glycoprotein 29-Modified Deferoxamine-Loaded Nanoparticles Reverses Functional Deficits in Parkinsonian Mice. ACS Nano. 2018;12(5):4123-39.
271. Gao Y, Wang Z-Y, Zhang J, Zhang Y, Huo H, Wang T, et al. RVG-Peptide-Linked Trimethylated Chitosan for Delivery of siRNA to the Brain. Biomacromolecules. 2014;15(3):1010-8.
272. Zhang E, Fu A. A new strategy for specific imaging of neural cells based on peptide-conjugated gold nanoclusters. International journal of nanomedicine. 2015;10:2115.
273. Ammar HO, Ghorab MM, Mahmoud AA, Higazy IM. Lamotrigine loaded poly-ε-(d,l-lactide-co-caprolactone) nanoparticles as brain delivery system. Eur J Pharm Sci. 2018;115:77-87.
274. Sánchez-López E, Ettcheto M, Egea MA, Espina M, Cano A, Calpena AC, et al. Memantine loaded PLGA PEGylated nanoparticles for Alzheimer's disease: in vitro and in vivo characterization. Journal of Nanobiotechnology. 2018;16(1):32.

275. Singh RP, Gangadharappa HV, Mruthunjaya K. Phospholipids: Unique carriers for drug delivery systems. Journal of Drug Delivery Science and Technology. 2017;39:166-79.
276. Miao Y-F, Peng T, Moody MR, Klegerman ME, Aronowski J, Grotta J, et al. Delivery of xenon-containing echogenic liposomes inhibits early brain injury following subarachnoid hemorrhage. Scientific Reports. 2018;8(1):450.
277. Mancini S, Nardo L, Gregori M, Ribeiro I, Mantegazza F, Delerue-Matos C, et al. Functionalized liposomes and phytosomes loading Annona muricata L. aqueous extract: Potential nanoshuttles for brain-delivery of phenolic compounds. Phytomedicine. 2018;42:233-44.
278. Pulford B, Reim N, Bell A, Veatch J, Forster G, Bender H, et al. Liposome-siRNA-Peptide Complexes Cross the Blood-Brain Barrier and Significantly Decrease PrP(C) on Neuronal Cells and PrP(RES) in Infected Cell Cultures. PLoS One. 2010;5(6):e11085.
279. Bender HR, Kane S, Zabel MD. Delivery of therapeutic siRNA to the CNS using cationic and anionic liposomes. JoVE. 2016;113(113):54106.
280. Rotman M, Welling MM, Bunschoten A, de Backer ME, Rip J, Nabuurs RJA, et al. Enhanced glutathione PEGylated liposomal brain delivery of an anti-amyloid single domain antibody fragment in a mouse model for Alzheimer's disease. J Control Release. 2015;203:40-50.
281. Szilvia V, Maria M, Lorand K, Zoltan K, Tibor P, Zsofia H, et al. Biotin and Glutathione Targeting of Solid Nanoparticles to Cross Human Brain Endothelial Cells. Current Pharmaceutical Design. 2017;23(28):4198-205.
282. Lin K-H, Hong S-T, Wang H-T, Lo Y-L, Lin A, Yang J. Enhancing Anticancer Effect of Gefitinib across the Blood–Brain Barrier Model Using Liposomes Modified with One α-Helical Cell-Penetrating Peptide or Glutathione and Tween 80. International Journal of Molecular Sciences. 2016;17(12):1998.
283. Mohamed M, Abu Lila AS, Shimizu T, Alaaeldin E, Hussein A, Sarhan HA, et al. PEGylated liposomes: immunological responses. Sci Technol Adv Mater. 2019;20(1):710-24.
284. Schwendener RA. Liposomes as vaccine delivery systems: a review of the recent advances. Therapeutic advances in vaccines. 2014;2(6):159-82.
285. Badiee A, Khamesipour A, Samiei A, Soroush D, Shargh VH, Kheiri MT, et al. The role of liposome size on the type of immune response induced in BALB/c mice against leishmaniasis: rgp63 as a model antigen. Experimental Parasitology. 2012;132(4):403-9.
286. Pisal DS, Kosloski MP, Balu‐Iyer SV. Delivery of therapeutic proteins. Journal of pharmaceutical sciences. 2010;99(6):2557-75.
287. Puri A, Loomis K, Smith B, Lee J-H, Yavlovich A, Heldman E, et al. Lipid-based nanoparticles as pharmaceutical drug carriers: from concepts to clinic. Critical Reviews™ in Therapeutic Drug Carrier Systems. 2009;26(6).
288. Diab R, Jaafar-Maalej C, Fessi H, Maincent P. Engineered nanoparticulate drug delivery systems: the next frontier for oral administration? The AAPS journal. 2012;14(4):688-702.
289. Manjunath K, Venkateswarlu V. Pharmacokinetics, tissue distribution and bioavailability of clozapine solid lipid nanoparticles after intravenous and intraduodenal administration. Journal of Controlled Release. 2005;107(2):215-28.
290. Grinberg S, Linder C, Kolot V, Waner T, Wiesman Z, Shaubi E, et al. Novel Cationic Amphiphilic Derivatives from Vernonia Oil: Synthesis and Self-Aggregation into Bilayer Vesicles, Nanoparticles, and DNA Complexants. Langmuir. 2005;21(17):7638-45.
291. Popov M, Grinberg S, Linder C, Waner T, Levi-Hevroni B, Deckelbaum RJ, et al. Site-directed decapsulation of bolaamphiphilic vesicles with enzymatic cleavable surface groups. Journal of Controlled Release. 2012;160(2):306-14.
292. Haney MJ, Klyachko NL, Zhao Y, Gupta R, Plotnikova EG, He Z, et al. Exosomes as drug delivery vehicles for Parkinson's disease therapy. Journal of Controlled Release. 2015;207:18-30.
293. Robbins PD, Morelli AE. Regulation of immune responses by extracellular vesicles. Nature Reviews Immunology. 2014;14:195.
294. Valadi H, Ekström K, Bossios A, Sjöstrand M, Lee JJ, Lötvall JO. Exosome-mediated transfer of mRNAs and microRNAs is a novel mechanism of genetic exchange between cells. Nature Cell Biology. 2007;9:654.

295. Skog J, Würdinger T, van Rijn S, Meijer DH, Gainche L, Curry Jr WT, et al. Glioblastoma microvesicles transport RNA and proteins that promote tumour growth and provide diagnostic biomarkers. Nature Cell Biology. 2008;10:1470.
296. Das CK, Jena BC, Banerjee I, das S, Parekh A, Bhutia SK, et al. Exosome as a Novel Shuttle for Delivery of Therapeutics across Biological Barriers. Mol Pharm. 2018.
297. Yamashita T, Takahashi Y, Takakura Y. Possibility of Exosome-Based Therapeutics and Challenges in Production of Exosomes Eligible for Therapeutic Application. Biological & pharmaceutical bulletin. 2018;41(6):835-42.
298. Barile L, Vassalli G. Exosomes: Therapy delivery tools and biomarkers of diseases. Pharmacology & therapeutics. 2017;174:63-78.
299. Ha D, Yang N, Nadithe V. Exosomes as therapeutic drug carriers and delivery vehicles across biological membranes: current perspectives and future challenges. Acta Pharm Sin B. 2016;6(4):287-96.
300. Rufino-Ramos D, Albuquerque PR, Carmona V, Perfeito R, Nobre RJ, Pereira de Almeida L. Extracellular vesicles: Novel promising delivery systems for therapy of brain diseases. Journal of controlled release : official journal of the Controlled Release Society. 2017;262:247-58.
301. Druzhkova TA, Yakovlev AA. Exosome Drug Delivery through the Blood–Brain Barrier: Experimental Approaches and Potential Applications. Neurochemical Journal. 2018;12(3):195-204.
302. Kooijmans SA, Vader P, van Dommelen SM, van Solinge WW, Schiffelers RM. Exosome mimetics: a novel class of drug delivery systems. Int J Nanomedicine. 2012;7:1525-41.
303. Lu M, Xing H, Xun Z, Yang T, Zhao X, Cai C, et al. Functionalized extracellular vesicles as advanced therapeutic nanodelivery systems. European journal of pharmaceutical sciences : official journal of the European Federation for Pharmaceutical Sciences. 2018;121:34-46.
304. Luan X, Sansanaphongpricha K, Myers I, Chen H, Yuan H, Sun D. Engineering exosomes as refined biological nanoplatforms for drug delivery. Acta pharmacologica Sinica. 2017;38(6):754-63.
305. Haqqani AS, Delaney CE, Tremblay T-L, Sodja C, Sandhu JK, Stanimirovic DB. Method for isolation and molecular characterization of extracellular microvesicles released from brain endothelial cells. Fluids and barriers of the CNS. 2013;10:4-.
306. Yuan D, Zhao Y, Banks WA, Bullock KM, Haney M, Batrakova E, et al. Macrophage exosomes as natural nanocarriers for protein delivery to inflamed brain. Biomaterials. 2017;142:1-12.
307. Quiñonez-Silvero C, Hübner K, Herzog W. Development of the brain vasculature and the blood-brain barrier in zebrafish. Developmental Biology. 2020;457(2):181-90.
308. Yang T, Martin P, Fogarty B, Brown A, Schurman K, Phipps R, et al. Exosome delivered anticancer drugs across the blood-brain barrier for brain cancer therapy in Danio rerio. Pharmaceutical research. 2015;32(6):2003-14.
309. Yang T, Fogarty B, LaForge B, Aziz S, Pham T, Lai L, et al. Delivery of Small Interfering RNA to Inhibit Vascular Endothelial Growth Factor in Zebrafish Using Natural Brain Endothelia Cell-Secreted Exosome Nanovesicles for the Treatment of Brain Cancer. The AAPS Journal. 2017;19(2):475-86.
310. Tian T, Zhang H-X, He C-P, Fan S, Zhu Y-L, Qi C, et al. Surface functionalized exosomes as targeted drug delivery vehicles for cerebral ischemia therapy. Biomaterials. 2018;150:137-49.
311. Long Q, Upadhya D, Hattiangady B, Kim D-K, An SY, Shuai B, et al. Intranasal MSC-derived A1-exosomes ease inflammation, and prevent abnormal neurogenesis and memory dysfunction after status epilepticus. Proceedings of the National Academy of Sciences. 2017;114(17):E3536.
312. Zhuang X, Xiang X, Grizzle W, Sun D, Zhang S, Axtell RC, et al. Treatment of Brain Inflammatory Diseases by Delivering Exosome Encapsulated Anti-inflammatory Drugs From the Nasal Region to the Brain. Molecular Therapy. 2011;19(10):1769-79.
313. Pusic AD, Pusic KM, Clayton BL, Kraig RP. IFNgamma-stimulated dendritic cell exosomes as a potential therapeutic for remyelination. Journal of neuroimmunology. 2014;266(1-2):12-23.
314. Jia G, Han Y, An Y, Ding Y, He C, Wang X, et al. NRP-1 targeted and cargo-loaded exosomes facilitate simultaneous imaging and therapy of glioma in vitro and in vivo. Biomaterials. 2018;178:302-16.

315. Iraci N, Gaude E, Leonardi T, Costa ASH, Cossetti C, Peruzzotti-Jametti L, et al. Extracellular vesicles are independent metabolic units with asparaginase activity. Nature chemical biology. 2017;13(9):951-5.
316. Cooper JM, Wiklander PBO, Nordin JZ, Al-Shawi R, Wood MJ, Vithlani M, et al. Systemic exosomal siRNA delivery reduced alpha-synuclein aggregates in brains of transgenic mice. Movement Disorders. 2014;29(12):1476-85.
317. Qu M, Lin Q, Huang L, Fu Y, Wang L, He S, et al. Dopamine-loaded blood exosomes targeted to brain for better treatment of Parkinson's disease. Journal of Controlled Release. 2018;287:156-66.
318. Gui Y, Liu H, Zhang L, Lv W, Hu X. Altered microRNA profiles in cerebrospinal fluid exosome in Parkinson disease and Alzheimer disease. Oncotarget. 2015;6(35):37043-53.
319. Liu Y, Li D, Liu Z, Zhou Y, Chu D, Li X, et al. Targeted exosome-mediated delivery of opioid receptor Mu siRNA for the treatment of morphine relapse. Scientific Reports. 2015;5:17543.
320. Xin H, Li Y, Cui Y, Yang JJ, Zhang ZG, Chopp M. Systemic Administration of Exosomes Released from Mesenchymal Stromal Cells Promote Functional Recovery and Neurovascular Plasticity After Stroke in Rats. Journal of Cerebral Blood Flow & Metabolism. 2013;33(11):1711-5.
321. Wu T, Yu M, Zhang L, Chen X, Pei Z. I02 Systemic injection of exosomal sirna significantly reduced huntingtin expression in transgenic mice of huntington’s disease. Journal of Neurology, Neurosurgery & Psychiatry. 2018;89(Suppl 1):A88-A9.
322. Didiot M-C, Hall LM, Coles AH, Haraszti RA, Godinho BMDC, Chase K, et al. Exosome-mediated Delivery of Hydrophobically Modified siRNA for Huntingtin mRNA Silencing. Molecular Therapy. 2016;24(10):1836-47.
323. Doeppner TR, Herz J, Gorgens A, Schlechter J, Ludwig AK, Radtke S, et al. Extracellular Vesicles Improve Post-Stroke Neuroregeneration and Prevent Postischemic Immunosuppression. Stem cells translational medicine. 2015;4(10):1131-43.
324. Lee JY, Kim E, Choi SM, Kim DW, Kim KP, Lee I, et al. Microvesicles from brain-extract-treated mesenchymal stem cells improve neurological functions in a rat model of ischemic stroke. Sci Rep. 2016;6:33038.
325. Betzer O, Perets N, Barnoy E, Offen D, Popovtzer R, editors. Labeling and tracking exosomes within the brain using gold nanoparticles. SPIE BiOS; 2018: SPIE.
326. Kim D-k, Nishida H, An SY, Shetty AK, Bartosh TJ, Prockop DJ. Chromatographically isolated CD63⁺CD81⁺ extracellular vesicles from mesenchymal stromal cells rescue cognitive impairments after TBI. Proceedings of the National Academy of Sciences. 2016;113(1):170-5.
327. Shen H, Yao X, Li H, Li X, Zhang T, Sun Q, et al. Role of Exosomes Derived from miR-133b Modified MSCs in an Experimental Rat Model of Intracerebral Hemorrhage. Journal of Molecular Neuroscience. 2018;64(3):421-30.
328. Kojima R, Bojar D, Rizzi G, Hamri GC-E, El-Baba MD, Saxena P, et al. Designer exosomes produced by implanted cells intracerebrally deliver therapeutic cargo for Parkinson’s disease treatment. Nature Communications. 2018;9(1):1305.
329. Bunggulawa EJ, Wang W, Yin T, Wang N, Durkan C, Wang Y, et al. Recent advancements in the use of exosomes as drug delivery systems. J Nanobiotechnology. 2018;16(1):81.
330. Moscariello P, Ng DYW, Jansen M, Weil T, Luhmann HJ, Hedrich J. Brain Delivery of Multifunctional Dendrimer Protein Bioconjugates. Advanced Science.0(0):1700897.
331. Mishra V, Kesharwani P. Dendrimer technologies for brain tumor. Drug Discovery Today. 2016;21(5):766-78.
332. Zhang C, Gu Z, Shen L, Liu X, Lin H. A Dual Targeting Drug Delivery System for Penetrating Blood-Brain Barrier and Selectively Delivering siRNA to Neurons for Alzheimer's Disease Treatment. Curr Pharm Biotechnol. 2017;18(14):1124-31.
333. Ke W, Shao K, Huang R, Han L, Liu Y, Li J, et al. Gene delivery targeted to the brain using an Angiopep-conjugated polyethyleneglycol-modified polyamidoamine dendrimer. Biomaterials. 2009;30(36):6976-85.

334. Al-Azzawi S, Masheta D, Guildford A, Phillips G, Santin M. Designing and Characterization of a Novel Delivery System for Improved Cellular Uptake by Brain Using Dendronised Apo-E-Derived Peptide. Frontiers in Bioengineering and Biotechnology. 2019;7:49.
335. Kang H, DeLong R, Fisher MH, Juliano RL. Tat-conjugated PAMAM dendrimers as delivery agents for antisense and siRNA oligonucleotides. Pharm Res. 2005;22(12):2099-106.
336. Chen HT, Neerman MF, Parrish AR, Simanek EE. Cytotoxicity, hemolysis, and acute in vivo toxicity of dendrimers based on melamine, candidate vehicles for drug delivery. J Am Chem Soc. 2004;126(32):10044-8.
337. Perez AP, Romero EL, Morilla MJ. Ethylendiamine core PAMAM dendrimers/siRNA complexes as in vitro silencing agents. Int J Pharm. 2009;380(1-2):189-200.
338. Ghorbani M, Bigdeli B, Jalili-baleh L, Baharifar H, Akrami M, Dehghani S, et al. Curcumin-lipoic acid conjugate as a promising anticancer agent on the surface of gold-iron oxide nanocomposites: A pH-sensitive targeted drug delivery system for brain cancer theranostics. Eur J Pharm Sci. 2018;114:175-88.
339. Coluccia D, Figueiredo CA, Wu MY, Riemenschneider AN, Diaz R, Luck A, et al. Enhancing glioblastoma treatment using cisplatin-gold-nanoparticle conjugates and targeted delivery with magnetic resonance-guided focused ultrasound. Nanomedicine. 2018;14(4):1137-48.
340. Ivask A, Pilkington EH, Blin T, Käkinen A, Vija H, Visnapuu M, et al. Uptake and transcytosis of functionalized superparamagnetic iron oxide nanoparticles in an in vitro blood brain barrier model. Biomaterials Science. 2018;6(2):314-23.
341. Vinzant N, Scholl JL, Wu C-M, Kindle T, Koodali R, Forster GL. Iron Oxide Nanoparticle Delivery of Peptides to the Brain: Reversal of Anxiety during Drug Withdrawal. Frontiers in neuroscience. 2017;11:608-.
342. Ghadiri M, Vasheghani‐Farahani E, Atyabi F, Kobarfard F, Mohamadyar‐Toupkanlou F, Hosseinkhani H. Transferrin‐conjugated magnetic dextran‐spermine nanoparticles for targeted drug transport across blood‐brain barrier. Journal of Biomedical Materials Research Part A. 2017;105(10):2851-64.
343. Sun Z, Worden M, Thliveris JA, Hombach-Klonisch S, Klonisch T, van Lierop J, et al. Biodistribution of negatively charged iron oxide nanoparticles (IONPs) in mice and enhanced brain delivery using lysophosphatidic acid (LPA). Nanomedicine. 2016;12(7):1775-84.
344. Enteshari Najafabadi R, Kazemipour N, Esmaeili A, Beheshti S, Nazifi S. Using superparamagnetic iron oxide nanoparticles to enhance bioavailability of quercetin in the intact rat brain. BMC Pharmacology and Toxicology. 2018;19(1):59.
345. Kirschbaum K, Sonner JK, Zeller MW, Deumelandt K, Bode J, Sharma R, et al. In vivo nanoparticle imaging of innate immune cells can serve as a marker of disease severity in a model of multiple sclerosis. Proceedings of the National Academy of Sciences of the United States of America. 2016;113(46):13227-32.
346. Kang J, Joo J, Kwon EJ, Skalak M, Hussain S, She Z-G, et al. Self-Sealing Porous Silicon-Calcium Silicate Core–Shell Nanoparticles for Targeted siRNA Delivery to the Injured Brain. Advanced Materials. 2016;28(36):7962-9.
347. Lee C, Hwang HS, Lee S, Kim B, Kim JO, Oh KT, et al. Rabies Virus-Inspired Silica-Coated Gold Nanorods as a Photothermal Therapeutic Platform for Treating Brain Tumors. Advanced Materials. 2017;29(13):1605563.
348. Etame AB, Smith CA, Chan WCW, Rutka JT. Design and potential application of PEGylated gold nanoparticles with size-dependent permeation through brain microvasculature. Nanomedicine. 2011;7(6):992-1000.
349. Hanada S, Fujioka K, Inoue Y, Kanaya F, Manome Y, Yamamoto K. Cell-Based in Vitro Blood–Brain Barrier Model Can Rapidly Evaluate Nanoparticles' Brain Permeability in Association with Particle Size and Surface Modification. International Journal of Molecular Sciences. 2014;15(2):1812.
350. Sonavane G, Tomoda K, Makino K. Biodistribution of colloidal gold nanoparticles after intravenous administration: Effect of particle size. Colloids and Surfaces B: Biointerfaces. 2008;66(2):274-80.

351. Ruff J, Hüwel S, Kogan MJ, Simon U, Galla H-J. The effects of gold nanoparticles functionalized with ß-amyloid specific peptides on an in vitro model of blood–brain barrier. Nanomedicine. 2017;13(5):1645-52.
352. Shilo M, Sharon A, Baranes K, Motiei M, Lellouche J-PM, Popovtzer R. The effect of nanoparticle size on the probability to cross the blood - brain barrier: an in-vitro endothelial cell model. J Nanobiotechnology. 2015;13:19.
353. Kang MH, Lee SJ, Park JY, Park JK. Carbon-coated copper nanoparticles: Characterization and fabrication via ultrasonic irradiation. Journal of Alloys and Compounds. 2018;735:2162-6.
354. Zhang P, Hu L, Yin Q, Zhang Z, Feng L, Li Y. Transferrin-conjugated polyphosphoester hybrid micelle loading paclitaxel for brain-targeting delivery: Synthesis, preparation and in vivo evaluation. Journal of Controlled Release. 2012;159(3):429-34.
355. Niu J, Wang A, Ke Z, Zheng Z. Glucose transporter and folic acid receptor-mediated Pluronic P105 polymeric micelles loaded with doxorubicin for brain tumor treating. Journal of Drug Targeting. 2014;22(8):712-23.
356. Lopalco A, Ali H, Denora N, Rytting E. Oxcarbazepine-loaded polymeric nanoparticles: development and permeability studies across in vitro models of the blood–brain barrier and human placental trophoblast. International Journal of Nanomedicine. 2015;10:1985-96.
357. Kubota Y, Sohn J, Hatada S, Schurr M, Straehle J, Gour A, et al. A carbon nanotube tape for serial-section electron microscopy of brain ultrastructure. Nature Communications. 2018;9(1):437.
358. Herlem G, Picaud F, Girardet C, Micheau O. Chapter 16 - Carbon Nanotubes: Synthesis, Characterization, and Applications in Drug-Delivery Systems. In: Mohapatra SS, Ranjan S, Dasgupta N, Mishra RK, Thomas S, editors. Nanocarriers for Drug Delivery: Elsevier; 2019. p. 469-529.
359. Costa PM, Wang JT-W, Morfin J-F, Khanum T, To W, Sosabowski J, et al. Functionalised Carbon Nanotubes Enhance Brain Delivery of Amyloid-Targeting Pittsburgh Compound B (PiB)-Derived Ligands. Nanotheranostics. 2018;2(2):168-83.
360. Journet C, Maser WK, Bernier P, Loiseau A, de la Chapelle ML, Lefrant S, et al. Large-scale production of single-walled carbon nanotubes by the electric-arc technique. Nature. 1997;388(6644):756-8.
361. Huang ZP, Xu JW, Ren ZF, Wang JH, Siegal MP, Provencio PN. Growth of highly oriented carbon nanotubes by plasma-enhanced hot filament chemical vapor deposition. Applied Physics Letters. 1998;73(26):3845-7.
362. Zhang W, Zhang Z, Zhang Y. The application of carbon nanotubes in target drug delivery systems for cancer therapies. Nanoscale research letters. 2011;6(1):555.
363. Ren J, Shen S, Wang D, Xi Z, Guo L, Pang Z, et al. The targeted delivery of anticancer drugs to brain glioma by PEGylated oxidized multi-walled carbon nanotubes modified with angiopep-2. Biomaterials. 2012;33(11):3324-33.
364. Kafa H, Wang JT-W, Rubio N, Klippstein R, Costa PM, Hassan HAFM, et al. Translocation of LRP1 targeted carbon nanotubes of different diameters across the blood–brain barrier in vitro and in vivo. Journal of Controlled Release. 2016;225:217-29.
365. Kafa H, Wang JT-W, Rubio N, Venner K, Anderson G, Pach E, et al. The interaction of carbon nanotubes with an in vitro blood-brain barrier model and mouse brain in vivo. Biomaterials. 2015;53:437-52.
366. You Y, Wang N, He L, Shi C, Zhang D, Liu Y, et al. Designing dual-functionalized carbon nanotubes with high blood–brain-barrier permeability for precise orthotopic glioma therapy. Dalton Transactions. 2019;48(5):1569-73.
367. Muldoon LL, Pagel MA, Kroll RA, Roman-Goldstein S, Jones RS, Neuwelt EA. A physiological barrier distal to the anatomic blood-brain barrier in a model of transvascular delivery. AJNR American journal of neuroradiology. 1999;20(2):217-22.
368. Decuzzi P, Godin B, Tanaka T, Lee SY, Chiappini C, Liu X, et al. Size and shape effects in the biodistribution of intravascularly injected particles. Journal of Controlled Release. 2010;141(3):320-7.

369. Jucker BM, Alsaid H, Rambo M, Lenhard SC, Hoang B, Xie F, et al. Multimodal imaging approach to examine biodistribution kinetics of Cabotegravir (GSK1265744) long acting parenteral formulation in rat. Journal of Controlled Release. 2017;268(Supplement C):102-12.
370. Lockman PR, Koziara JM, Mumper RJ, Allen DD. Nanoparticle Surface Charges Alter Blood–Brain Barrier Integrity and Permeability. Journal of Drug Targeting. 2004;12(9-10):635-41.
371. Torchilin VP. Multifunctional nanocarriers. Advanced Drug Delivery Reviews. 2006;58(14):1532-55.
372. Rassu G, Soddu E, Posadino AM, Pintus G, Sarmento B, Giunchedi P, et al. Nose-to-brain delivery of BACE1 siRNA loaded in solid lipid nanoparticles for Alzheimer's therapy. Colloids and Surfaces B: Biointerfaces. 2017;152:296-301.
373. Bramini M, Ye D, Hallerbach A, Nic Raghnaill M, Salvati A, Aberg C, et al. Imaging approach to mechanistic study of nanoparticle interactions with the blood-brain barrier. ACS Nano. 2014;8(5):4304-12.
374. Wiley DT, Webster P, Gale A, Davis ME. Transcytosis and brain uptake of transferrin-containing nanoparticles by tuning avidity to transferrin receptor. Proceedings of the National Academy of Sciences of the United States of America. 2013;110(21):8662-7.
375. Liu L, Xu K, Wang H, Jeremy Tan PK, Fan W, Venkatraman SS, et al. Self-assembled cationic peptide nanoparticles as an efficient antimicrobial agent. Nature Nanotechnology. 2009;4:457.
376. Shaki H, Ganji F, Kempen PJ, Dolatshahi-Pirouz A, Vasheghani-Farahani E. Self-assembled amphiphilic-dextran nanomicelles for delivery of rapamycin. J Drug Deliv Sci Technol. 2018;44:333-41.
377. Oh JY, Kim HS, Palanikumar L, Go EM, Jana B, Park SA, et al. Cloaking nanoparticles with protein corona shield for targeted drug delivery. Nature Communications. 2018;9(1):4548.
378. Gorshkov V, Bubis JA, Solovyeva EM, Gorshkov MV, Kjeldsen F. Protein corona formed on silver nanoparticles in blood plasma is highly selective and resistant to physicochemical changes of the solution. Environmental Science: Nano. 2019;6(4):1089-98.
379. García-Álvarez R, Hadjidemetriou M, Sánchez-Iglesias A, Liz-Marzán LM, Kostarelos K. In vivo formation of protein corona on gold nanoparticles. The effect of their size and shape. Nanoscale. 2018;10(3):1256-64.
380. Nierenberg D, Khaled AR, Flores O. Formation of a protein corona influences the biological identity of nanomaterials. Reports of Practical Oncology & Radiotherapy. 2018;23(4):300-8.
381. Phogat N, Kohl M, Uddin I, Jahan A. Chapter 11 - Interaction of Nanoparticles With Biomolecules, Protein, Enzymes, and Its Applications. In: Deigner H-P, Kohl M, editors. Precision Medicine: Academic Press; 2018. p. 253-76.
382. Mosquera J, García I, Henriksen-Lacey M, González-Rubio G, Liz-Marzán LM. Reducing Protein Corona Formation and Enhancing Colloidal Stability of Gold Nanoparticles by Capping with Silica Monolayers. Chemistry of Materials. 2018;31(1):57-61.
383. Walczyk D, Bombelli FB, Monopoli MP, Lynch I, Dawson KA. What the cell "sees" in bionanoscience. Journal of the American Chemical Society. 2010;132(16):5761-8.
384. Gräfe C, Weidner A, Lühe Mvd, Bergemann C, Schacher FH, Clement JH, et al. Intentional formation of a protein corona on nanoparticles: Serum concentration affects protein corona mass, surface charge, and nanoparticle–cell interaction. The International Journal of Biochemistry & Cell Biology. 2016;75:196-202.
385. Rodriguez PL, Harada T, Christian DA, Pantano DA, Tsai RK, Discher DE. Minimal" Self" peptides that inhibit phagocytic clearance and enhance delivery of nanoparticles. Science. 2013;339(6122):971-5.
386. Fleischer CC, Payne CK. Nanoparticle-cell interactions: molecular structure of the protein corona and cellular outcomes. Acc Chem Res. 2014;47(8):2651-9.
387. Lynch I, Dawson KA. Protein-nanoparticle interactions. Nano today. 2008;3(1-2):40-7.
388. Asuri P, Bale SS, Pangule RC, Shah DA, Kane RS, Dordick JS. Structure, function, and stability of enzymes covalently attached to single-walled carbon nanotubes. Langmuir. 2007;23(24):12318-21.

389. Hühn D, Kantner K, Geidel C, Brandholt S, De Cock I, Soenen SJH, et al. Polymer-Coated Nanoparticles Interacting with Proteins and Cells: Focusing on the Sign of the Net Charge. ACS Nano. 2013;7(4):3253-63.
390. Lesniak A, Fenaroli F, Monopoli MP, Åberg C, Dawson KA, Salvati A. Effects of the Presence or Absence of a Protein Corona on Silica Nanoparticle Uptake and Impact on Cells. ACS Nano. 2012;6(7):5845-57.
391. Maiorano G, Sabella S, Sorce B, Brunetti V, Malvindi MA, Cingolani R, et al. Effects of Cell Culture Media on the Dynamic Formation of Protein−Nanoparticle Complexes and Influence on the Cellular Response. ACS Nano. 2010;4(12):7481-91.
392. Monopoli MP, Walczyk D, Campbell A, Elia G, Lynch I, Baldelli Bombelli F, et al. Physical−Chemical Aspects of Protein Corona: Relevance to in Vitro and in Vivo Biological Impacts of Nanoparticles. Journal of the American Chemical Society. 2011;133(8):2525-34.
393. Tenzer S, Docter D, Kuharev J, Musyanovych A, Fetz V, Hecht R, et al. Rapid formation of plasma protein corona critically affects nanoparticle pathophysiology. Nature Nanotechnology. 2013;8(10):772.
394. Bhogale A, Patel N, Mariam J, Dongre PM, Miotello A, Kothari DC. Comprehensive studies on the interaction of copper nanoparticles with bovine serum albumin using various spectroscopies. Colloids and Surfaces B: Biointerfaces. 2014;113:276-84.
395. Su G, Jiang H, Xu B, Yu Y, Chen X. Effects of Protein Corona on Active and Passive Targeting of Cyclic RGD Peptide-Functionalized PEGylation Nanoparticles. Molecular Pharmaceutics. 2018;15(11):5019-30.
396. Salvati A, Pitek AS, Monopoli MP, Prapainop K, Bombelli FB, Hristov DR, et al. Transferrin-functionalized nanoparticles lose their targeting capabilities when a biomolecule corona adsorbs on the surface. Nature Nanotechnology. 2013;8(2):137.
397. Ding D, Zhang Y, Sykes EA, Chen L, Chen Z, Tan W. The influence of physiological environment on the targeting effect of aptamer-guided gold nanoparticles. Nano Research. 2019;12(1):129-35.
398. El-Marakby EM, Hathout RM, Taha I, Mansour S, Mortada ND. A novel serum-stable liver targeted cytotoxic system using valerate-conjugated chitosan nanoparticles surface decorated with glycyrrhizin. International Journal of Pharmaceutics. 2017;525(1):123-38.
399. Oliveira CL, Veiga F, Varela C, Roleira F, Tavares E, Silveira I, et al. Characterization of polymeric nanoparticles for intravenous delivery: Focus on stability. Colloids and Surfaces B: Biointerfaces. 2017;150:326-33.
400. Almalik A, Alradwan I, Kalam MA, Alshamsan A. Effect of cryoprotection on particle size stability and preservation of chitosan nanoparticles with and without hyaluronate or alginate coating. Saudi Pharmaceutical Journal. 2017;25(6):861-7.
401. Abdelwahed W, Degobert G, Stainmesse S, Fessi H. Freeze-drying of nanoparticles: Formulation, process and storage considerations. Advanced Drug Delivery Reviews. 2006;58(15):1688-713.
402. Gokce Y, Cengiz B, Yildiz N, Calimli A, Aktas Z. Ultrasonication of chitosan nanoparticle suspension: Influence on particle size. Colloids and Surfaces A: Physicochemical and Engineering Aspects. 2014;462:75-81.
403. Rampino A, Borgogna M, Blasi P, Bellich B, Cesàro A. Chitosan nanoparticles: Preparation, size evolution and stability. International Journal of Pharmaceutics. 2013;455(1):219-28.
404. Cesur H, Rubinstein I, Pai A, Önyüksel H. Self-associated indisulam in phospholipid-based nanomicelles: a potential nanomedicine for cancer. Nanomedicine: Nanotechnology, Biology and Medicine. 2009;5(2):178-83.
405. Faghihi MA, Modarresi F, Khalil AM, Wood DE, Sahagan BG, Morgan TE, et al. Expression of a noncoding RNA is elevated in Alzheimer's disease and drives rapid feed-forward regulation of β-secretase. Nature Medicine. 2008;14(7):723-30.
406. Singer O, Marr RA, Rockenstein E, Crews L, Coufal NG, Gage FH, et al. Targeting BACE1 with siRNAs ameliorates Alzheimer disease neuropathology in a transgenic model. Nature Neuroscience. 2005;8(10):1343-9.

407. Yan R, Vassar R. Targeting the β secretase BACE1 for Alzheimer's disease therapy. The Lancet Neurology. 2014;13(3):319-29.
408. Fersht A. Structure and mechanism in protein science: a guide to enzyme catalysis and protein folding: Macmillan; 1999.
409. Mulholland AJ. Computational enzymology: modelling the mechanisms of biological catalysts. Portland Press Limited; 2008.
410. Petsalaki E, Russell RB. Peptide-mediated interactions in biological systems: new discoveries and applications. Current opinion in biotechnology. 2008;19(4):344-50.
411. Warshel A, Levitt M. Theoretical studies of enzymic reactions: dielectric, electrostatic and steric stabilization of the carbonium ion in the reaction of lysozyme. Journal of molecular biology. 1976;103(2):227-49.
412. Sorsa T, Tjäderhane L, Salo T. Matrix metalloproteinases (MMPs) in oral diseases. Oral diseases. 2004;10(6):311-8.
413. Nagase H. Substrate specificity of MMPs. Matrix metalloproteinase inhibitors in cancer therapy: Springer; 2001. p. 39-66.
414. Tallant C, Marrero A, Gomis-Rüth FX. Matrix metalloproteinases: fold and function of their catalytic domains. Biochimica et Biophysica Acta (BBA)-Molecular Cell Research. 2010;1803(1):20-8.
415. Rowsell S, Hawtin P, Minshull CA, Jepson H, Brockbank SM, Barratt DG, et al. Crystal structure of human MMP9 in complex with a reverse hydroxamate inhibitor. Journal of molecular biology. 2002;319(1):173-81.
416. Nagase H, Woessner JF. Matrix metalloproteinases. Journal of Biological chemistry. 1999;274(31):21491-4.
417. Becker JW, Marcy AI, Rokosz LL, Axel MG, Burbaum JJ, Fitzgerald P, et al. Stromelysin‐1: Three‐dimensional structure of the inhibited catalytic domain and of the C‐truncated proenzyme. Protein Science. 1995;4(10):1966-76.
418. Gururajan R, Grenet J, Lahti JM, Kidd VJ. Isolation and Characterization of Two Novel Metalloproteinase Genes Linked to theCdc2LLocus on Human Chromosome 1p36. 3. Genomics. 1998;52(1):101-6.
419. Pei D, Weiss SJ. Furin-dependent intracellular activation of the human stromelysin-3 zymogen. Nature. 1995;375(6528):244.
420. Pei D, Weiss SJ. Transmembrane-deletion mutants of the membrane-type matrix metalloproteinase-1 process progelatinase A and express intrinsic matrix-degrading activity. Journal of Biological Chemistry. 1996;271(15):9135-40.
421. Tochowicz A, Maskos K, Huber R, Oltenfreiter R, Dive V, Yiotakis A, et al. Crystal structures of MMP-9 complexes with five inhibitors: contribution of the flexible Arg424 side-chain to selectivity. Journal of molecular biology. 2007;371(4):989-1006.
422. Opdenakker G, Van den Steen PE, Dubois B, Nelissen I, Van Coillie E, Masure S, et al. Gelatinase B functions as regulator and effector in leukocyte biology. Journal of leukocyte biology. 2001;69(6):851-9.
423. Fry SA, Van den Steen PE, Royle L, Wormald MR, Leathem AJ, Opdenakker G, et al. Cancer-associated glycoforms of gelatinase B exhibit a decreased level of binding to galectin-3. Biochemistry. 2006;45(51):15249-58.
424. Dubois B, Starckx S, Pagenstecher A, Oord Jvd, Arnold B, Opdenakker G. Gelatinase B deficiency protects against endotoxin shock. European Journal of Immunology. 2002;32(8):2163-71.
425. Vu TH, Shipley JM, Bergers G, Berger JE, Helms JA, Hanahan D, et al. MMP-9/Gelatinase B Is a Key Regulator of Growth Plate Angiogenesis and Apoptosis of Hypertrophic Chondrocytes. Cell. 1998;93(3):411-22.
426. Buisson AC, Zahm JM, Polette M, Pierrot D, Bellon G, Puchelle E, et al. Gelatinase B is involved in the in vitro wound repair of human respiratory epithelium. Journal of Cellular Physiology. 1996;166(2):413-26.

427. Kobayashi T, Kim H, Liu X, Sugiura H, Kohyama T, Fang Q, et al. Matrix metalloproteinase-9 activates TGF-β and stimulates fibroblast contraction of collagen gels. American Journal of Physiology-Lung Cellular and Molecular Physiology. 2014;306(11):L1006-L15.
428. Kowluru RA. Role of Matrix Metalloproteinase-9 in the Development of Diabetic Retinopathy and Its Regulation by H-Ras. Investigative Ophthalmology & Visual Science. 2010;51(8):4320-6.
429. Egeblad M, Werb Z. New functions for the matrix metalloproteinases in cancer progression. Nature Reviews Cancer. 2002;2(3):161-74.
430. Bergers G, Brekken R, McMahon G, Vu TH, Itoh T, Tamaki K, et al. Matrix metalloproteinase-9 triggers the angiogenic switch during carcinogenesis. Nature cell biology. 2000;2(10):737-44.
431. Iurlaro M, Loverro G, Vacca A, Cormio G, Ribatti D, Minischetti M, et al. Angiogenesis extent and expression of matrix metalloproteinase-2 and-9 correlate with upgrading and myometrial invasion in endometrial carcinoma. European journal of clinical investigation. 1999;29:793-801.
432. Brown DL, Hibbs MS, Kearney M, Loushin C, Isner JM. Identification of 92-kD gelatinase in human coronary atherosclerotic lesions. Circulation. 1995;91(8):2125-31.
433. Vandooren J, Van den Steen PE, Opdenakker G. Biochemistry and molecular biology of gelatinase B or matrix metalloproteinase-9 (MMP-9): The next decade. Critical Reviews in Biochemistry and Molecular Biology. 2013;48(3):222-72.
434. Bruno MA, Mufson EJ, Wuu J, Cuello AC. Increased Matrix Metalloproteinase-9 Activity in Mild Cognitive Impairment. Journal of neuropathology and experimental neurology. 2009;68(12):1309-18.
435. Wang X-X, Tan M-S, Yu J-T, Tan L. Matrix Metalloproteinases and Their Multiple Roles in Alzheimer’s Disease. BioMed Research International. 2014;2014:8.
436. Cossins JA, Clements JM, Ford J, Miller KM, Pigott R, Vos W, et al. Enhanced expression of MMP-7 and MMP-9 in demyelinating multiple sclerosis lesions. Acta Neuropathologica. 1997;94(6):590-8.
437. Kouwenhoven M, Özenci V, Gomes A, Yarilin D, Giedraitis V, Press R, et al. Multiple sclerosis: elevated expression of matrix metalloproteinases in blood monocytes. Journal of Autoimmunity. 2001;16(4):463-70.
438. Trentini A, Castellazzi M, Cervellati C, Manfrinato MC, Tamborino C, Hanau S, et al. Interplay between Matrix Metalloproteinase-9, Matrix Metalloproteinase-2, and Interleukins in Multiple Sclerosis Patients. Disease Markers. 2016;2016:3672353.
439. He X, Zhang L, Yao X, Hu J, Yu L, Jia H, et al. Association Studies of MMP-9 in Parkinson's Disease and Amyotrophic Lateral Sclerosis. PLOS ONE. 2013;8(9):e73777.
440. Yılmaz Ü, Gücüyener K, Gürkaş E, Demir E, Serdaroğlu A, Atak A, et al. Matrix Metalloproteinase-7, Matrix Metalloproteinase-9, and Disease Activity in Pediatric Multiple Sclerosis. Pediatric Neurology.48(3):255-6.
441. Hannocks MJ, Zhang X, Gerwien H, Chashchina A, Burmeister M, Korpos E, et al. The gelatinases, MMP-2 and MMP-9, as fine tuners of neuroinflammatory processes. Matrix Biology. 2017.
442. Toth M, Chvyrkova I, Bernardo MM, Hernandez-Barrantes S, Fridman R. Pro-MMP-9 activation by the MT1-MMP/MMP-2 axis and MMP-3: role of TIMP-2 and plasma membranes. Biochemical and Biophysical Research Communications. 2003;308(2):386-95.
443. Ramos-DeSimone N, Hahn-Dantona E, Sipley J, Nagase H, French DL, Quigley JP. Activation of Matrix Metalloproteinase-9 (MMP-9) via a Converging Plasmin/Stromelysin-1 Cascade Enhances Tumor Cell Invasion. Journal of Biological Chemistry. 1999;274(19):13066-76.
444. Yu Q, Stamenkovic I. Localization of matrix metalloproteinase 9 to the cell surface provides a mechanism for CD44-mediated tumor invasion. Genes & Development. 1999;13(1):35-48.
445. Coussens LM, Tinkle CL, Hanahan D, Werb Z. MMP-9 Supplied by Bone Marrow–Derived Cells Contributes to Skin Carcinogenesis. Cell. 2000;103(3):481-90.

446. Rowsell S, Hawtin P, Minshull CA, Jepson H, Brockbank SMV, Barratt DG, et al. Crystal Structure of Human MMP9 in Complex with a Reverse Hydroxamate Inhibitor. Journal of Molecular Biology. 2002;319(1):173-81.
447. Cha H, Kopetzki E, Huber R, Lanzendörfer M, Brandstetter H. Structural Basis of the Adaptive Molecular Recognition by MMP9. Journal of Molecular Biology. 2002;320(5):1065-79.
448. Olson MW, Bernardo MM, Pietila M, Gervasi DC, Toth M, Kotra LP, et al. Characterization of the monomeric and dimeric forms of latent and active matrix metalloproteinase-9 differential rates for activation by stromelysin 1. Journal of Biological Chemistry. 2000;275(4):2661-8.
449. Elkins PA, Ho YS, Smith WW, Janson CA, D'Alessio KJ, McQueney MS, et al. Structure of the C-terminally truncated human ProMMP9, a gelatin-binding matrix metalloproteinase. Acta Crystallographica Section D: Biological Crystallography. 2002;58(7):1182-92.
450. Henley SS, Golden RM, Kashner TM. Statistical modeling methods: challenges and strategies. Biostatistics & Epidemiology. 2020;4(1):105-39.
451. Yang H. The case for being automatic: introducing the automatic linear modeling (LINEAR) procedure in SPSS statistics. Multiple Linear Regression Viewpoints. 2013;39(2):27-37.
452. Rawlings ND, Barrett AJ, Finn R. Twenty years of the MEROPS database of proteolytic enzymes, their substrates and inhibitors. Nucleic acids research. 2015:gkv1118.
453. Kridel SJ, Chen E, Kotra LP, Howard EW, Mobashery S, Smith JW. Substrate Hydrolysis by Matrix Metalloproteinase-9*. Journal of Biological Chemistry. 2001;276(23):20572-8.
454. Chen EI, Kridel SJ, Howard EW, Li W, Godzik A, Smith JW. A Unique Substrate Recognition Profile for Matrix Metalloproteinase-2. Journal of Biological Chemistry. 2002;277(6):4485-91.
455. Chen EI, Li W, Godzik A, Howard EW, Smith JW. A Residue in the S2 Subsite Controls Substrate Selectivity of Matrix Metalloproteinase-2 and Matrix Metalloproteinase-9. Journal of Biological Chemistry. 2003;278(19):17158-63.
456. Schilling O, Overall CM. Proteome-derived, database-searchable peptide libraries for identifying protease cleavage sites. Nature biotechnology. 2008;26:685.
457. Schilling O, Huesgen PF, Barré O, auf dem Keller U, Overall CM. Characterization of the prime and non-prime active site specificities of proteases by proteome-derived peptide libraries and tandem mass spectrometry. Nature Protocols. 2011;6:111.
458. Turk BE, Huang LL, Piro ET, Cantley LC. Determination of protease cleavage site motifs using mixture-based oriented peptide libraries. Nature biotechnology. 2001;19(7):661-7.
459. Turk BE, Huang LL, Piro ET, Cantley LC. Determination of protease cleavage site motifs using mixture-based oriented peptide libraries. Nature Biotechnology. 2001;19:661.
460. Tauro JR, Lee B-S, Lateef SS, Gemeinhart RA. Matrix metalloprotease selective peptide substrates cleavage within hydrogel matrices for cancer chemotherapy activation. Peptides. 2008;29(11):1965-73.
461. Ratnikov BI, Cieplak P, Gramatikoff K, Pierce J, Eroshkin A, Igarashi Y, et al. Basis for substrate recognition and distinction by matrix metalloproteinases. Proceedings of the National Academy of Sciences of the United States of America. 2014;111(40):E4148-E55.
462. Lamort A-S, Gravier R, Laffitte A, Juliano L, Zani M-L, Moreau T. New insights into the substrate specificity of macrophage elastase MMP-12. Biological chemistry. 2016;397(5):469-84.
463. Ghisaidoobe ABT, Chung SJ. Intrinsic Tryptophan Fluorescence in the Detection and Analysis of Proteins: A Focus on Förster Resonance Energy Transfer Techniques. International Journal of Molecular Sciences. 2014;15(12):22518-38.
464. Yang H, Xiao X, Zhao X, Wu Y, editors. Intrinsic fluorescence spectra of tryptophan, tyrosine and phenyloalanine. Selected Papers of the Chinese Society for Optical Engineering Conferences held October and November 2016; 2017: SPIE.
465. Liang G, Liu Y, Shi B, Zhao J, Zheng J. An Index for Characterization of Natural and Non-Natural Amino Acids for Peptidomimetics. PLoS ONE. 2013;8(7):e67844.
466. Schmidt RL, Simonović M. Synthesis and decoding of selenocysteine and human health. Croat Med J. 2012;53(6):535-50.
467. Gaston MA, Zhang L, Green-Church KB, Krzycki JA. The complete biosynthesis of the genetically encoded amino acid pyrrolysine from lysine. Nature. 2011;471(7340):647-50.

468. Trott O, Olson AJ. AutoDock Vina: improving the speed and accuracy of docking with a new scoring function, efficient optimization and multithreading. Journal of computational chemistry. 2010;31(2):455-61.
469. Forli S, Huey R, Pique ME, Sanner M, Goodsell DS, Olson AJ. Computational protein-ligand docking and virtual drug screening with the AutoDock suite. Nature protocols. 2016;11(5):905-19.
470. Trott O, Olson AJ. AutoDock Vina: improving the speed and accuracy of docking with a new scoring function, efficient optimization, and multithreading. J Comput Chem. 2010;31(2):455-61.
471. Chegeni S, Khaki Z, Shirani D, Vajhi A, Taheri M, Tamrchi Y, et al. Investigation of MMP-2 and MMP-9 activities in canine sera with dilated cardiomyopathy. Iranian Journal of Veterinary Research. 2015;16(2):182-7.
472. Kridel SJ, Chen E, Kotra LP, Howard EW, Mobashery S, Smith JW. Substrate hydrolysis by matrix metalloproteinase-9. Journal of Biological Chemistry. 2001;276(23):20572-8.
473. Turk BE, Huang LL, Piro ET, Cantley LC. Determination of protease cleavage site motifs using mixture-based oriented peptide libraries. Nature biotechnology. 2001;19(7):661-7.
474. Ratnikov BI, Cieplak P, Gramatikoff K, Pierce J, Eroshkin A, Igarashi Y, et al. Basis for substrate recognition and distinction by matrix metalloproteinases. Proceedings of the National Academy of Sciences. 2014;111(40):E4148-E55.
475. Grünwald B, Vandooren J, Locatelli E, Fiten P, Opdenakker G, Proost P, et al. Matrix metalloproteinase-9 (MMP-9) as an activator of nanosystems for targeted drug delivery in pancreatic cancer. Journal of Controlled Release. 2016;239:39-48.
476. Kukreja M, Shiryaev SA, Cieplak P, Muranaka N, Routenberg DA, Chernov AV, et al. High-throughput multiplexed peptide-centric profiling illustrates both substrate cleavage redundancy and specificity in the MMP family. Chemistry & biology. 2015;22(8):1122-33.
477. Rao MB, Tanksale AM, Ghatge MS, Deshpande VV. Molecular and Biotechnological Aspects of Microbial Proteases. Microbiology and Molecular Biology Reviews. 1998;62(3):597-635.
478. Shen S, Kai B, Ruan J, Huzil JT, Carpenter E, Tuszynski JA. Probabilistic analysis of the frequencies of amino acid pairs within characterized protein sequences. Physica A: Statistical Mechanics and its Applications. 2006;370(2):651-62.
479. Dhanaraj V, Ye Q-Z, Johnson L, Hupe D, Ortwine D, Dunbar Jr J, et al. X-ray structure of a hydroxamate inhibitor complex of stromelysin catalytic domain and its comparison with members of the zinc metalloproteinase superfamily. Structure. 1996;4(4):375-86.
480. Bode W, Reinemer P, Huber R, Kleine T, Schnierer S, Tschesche H. The X-ray crystal structure of the catalytic domain of human neutrophil collagenase inhibited by a substrate analogue reveals the essentials for catalysis and specificity. The EMBO Journal. 1994;13(6):1263.
481. Wimley WC, White SH. Experimentally determined hydrophobicity scale for proteins at membrane interfaces. Nat Struct Mol Biol. 1996;3(10):842-8.
482. Kyte J, Doolittle RF. A simple method for displaying the hydropathic character of a protein. Journal of Molecular Biology. 1982;157(1):105-32.
483. Wu R, McMahon TB. Protonation sites and conformations of peptides of glycine (Gly1−5H+) by IRMPD spectroscopy. The Journal of Physical Chemistry B. 2009;113(25):8767-75.
484. Kridel SJ, Sawai H, Ratnikov BI, Chen EI, Li W, Godzik A, et al. A unique substrate binding mode discriminates membrane type-1 matrix metalloproteinase from other matrix metalloproteinases. Journal of Biological Chemistry. 2002;277(26):23788-93.
485. Her C, Alonzo AP, Vang JY, Torres E, Krishnan VV. Real-Time Enzyme Kinetics by Quantitative NMR Spectroscopy and Determination of the Michaelis–Menten Constant Using the Lambert-W Function. Journal of Chemical Education. 2015;92(11):1943-8.
486. Papeo G, Giordano P, Brasca MG, Buzzo F, Caronni D, Ciprandi F, et al. Polyfluorinated Amino Acids for Sensitive 19F NMR-Based Screening and Kinetic Measurements. Journal of the American Chemical Society. 2007;129(17):5665-72.
487. Kuzmic P. Integrated Michaelis-Menten equation in DynaFit. 2. Application to 5α-ketosteroid reductase. BioKin Ltd Technical Note TN-2016-02, http://www. biokin. com/TN/2016/02 …; 2016.

488. Zhang D, Kovach IM, Sheehy JP. Locating the rate-determining step (s) for three-step hydrolase-catalyzed reactions with DYNAFIT. Biochimica et Biophysica Acta (BBA)-Proteins and Proteomics. 2008;1784(5):827-33.
489. Pan S, Huang X, Wang Y, Li L, Zhao C, Yao Z, et al. Efficacy of intravenous plus intrathecal/intracerebral ventricle injection of polymyxin B for post-neurosurgical intracranial infections due to MDR/XDR Acinectobacter baumannii: a retrospective cohort study. Antimicrobial Resistance & Infection Control. 2018;7(1):8.
490. Gonzalez-Carter DA, Ong ZY, McGilvery CM, Dunlop IE, Dexter DT, Porter AE. L-DOPA functionalized, multi-branched gold nanoparticles as brain-targeted nano-vehicles. Nanomedicine: Nanotechnology, Biology and Medicine. 2019;15(1):1-11.
491. Lakkadwala S, Singh J. Co-delivery of doxorubicin and erlotinib through liposomal nanoparticles for glioblastoma tumor regression using an in vitro brain tumor model. Colloids and Surfaces B: Biointerfaces. 2019;173:27-35.
492. Rassu G, Porcu E, Fancello S, Obinu A, Senes N, Galleri G, et al. Intranasal Delivery of Genistein-Loaded Nanoparticles as a Potential Preventive System against Neurodegenerative Disorders. Pharmaceutics. 2018;11(1):8.
493. Yuan B, ZHAO Y, DONG S, SUN Y, HAO F, XIE J, et al. Cell-penetrating Peptide-coated Liposomes for Drug Delivery Across the Blood–Brain Barrier. Anticancer Research. 2019;39(1):237-43.
494. Ammar HO, Ghorab MM, Mahmoud AA, Higazy IM. Lamotrigine loaded poly-ε-(d,l-lactide-co-caprolactone) nanoparticles as brain delivery system. European Journal of Pharmaceutical Sciences. 2018;115:77-87.
495. . !!! INVALID CITATION !!! .
496. Oller-Salvia B, Sánchez-Navarro M, Giralt E, Teixidó M. Blood–brain barrier shuttle peptides: an emerging paradigm for brain delivery. Chemical Society Reviews. 2016;45(17):4690-707.
497. Horii A, Wang X, Gelain F, Zhang S. Biological Designer Self-Assembling Peptide Nanofiber Scaffolds Significantly Enhance Osteoblast Proliferation, Differentiation and 3-D Migration. PLoS ONE. 2007;2(2):e190.
498. Koutsopoulos S. Self-assembling peptide nanofiber hydrogels in tissue engineering and regenerative medicine: Progress, design guidelines, and applications. Journal of Biomedical Materials Research Part A. 2016;104(4):1002-16.
499. Wu L-P, Ahmadvand D, Su J, Hall A, Tan X, Farhangrazi ZS, et al. Crossing the blood-brain-barrier with nanoligand drug carriers self-assembled from a phage display peptide. Nature Communications. 2019;10(1):4635.
500. Datta G, Chaddha M, Garber DW, Chung BH, Tytler EM, Dashti N, et al. The receptor binding domain of apolipoprotein E, linked to a model class A amphipathic helix, enhances internalization and degradation of LDL by fibroblasts. Biochemistry. 2000;39(1):213-20.
501. Oller-Salvia B, Sanchez-Navarro M, Ciudad S, Guiu M, Arranz-Gibert P, Garcia C, et al. MiniAp-4: A Venom-Inspired Peptidomimetic for Brain Delivery. Angew Chem Int Ed Engl. 2016;55(2):572-5.
502. He C, Hu Y, Yin L, Tang C, Yin C. Effects of particle size and surface charge on cellular uptake and biodistribution of polymeric nanoparticles. Biomaterials. 2010;31(13):3657-66.
503. Fan X, Zhao F, Wang X, Wu G. Doxorubicin-triggered self-assembly of native amphiphilic peptides into spherical nanoparticles. Oncotarget. 2016;7(36):58445.
504. Zensi A, Begley D, Pontikis C, Legros C, Mihoreanu L, Wagner S, et al. Albumin nanoparticles targeted with Apo E enter the CNS by transcytosis and are delivered to neurones. Journal of controlled release : official journal of the Controlled Release Society. 2009;137(1):78-86.
505. Fatouros DG, Lamprou DA, Urquhart AJ, Yannopoulos SN, Vizirianakis IS, Zhang S, et al. Lipid-like self-assembling peptide nanovesicles for drug delivery. ACS applied materials & interfaces. 2014;6(11):8184-9.

506. Kanazawa T, Kaneko M, Niide T, Akiyama F, Kakizaki S, Ibaraki H, et al. Enhancement of nose-to-brain delivery of hydrophilic macromolecules with stearate-or polyethylene glycol-modified arginine-rich peptide. International Journal of Pharmaceutics. 2017;530(1-2):195-200.
507. Lim J, Yeap SP, Che HX, Low SC. Characterization of magnetic nanoparticle by dynamic light scattering. Nanoscale Research Letters. 2013;8(1):381.
508. Domingos RF, Baalousha MA, Ju-Nam Y, Reid MM, Tufenkji N, Lead JR, et al. Characterizing Manufactured Nanoparticles in the Environment: Multimethod Determination of Particle Sizes. Environmental Science & Technology. 2009;43(19):7277-84.
509. Fissan H, Ristig S, Kaminski H, Asbach C, Epple M. Comparison of different characterization methods for nanoparticle dispersions before and after aerosolization. Analytical Methods. 2014;6(18):7324-34.
510. Souza TGF, Ciminelli VST, Mohallem NDS. A comparison of TEM and DLS methods to characterize size distribution of ceramic nanoparticles. Journal of Physics: Conference Series. 2016;733:012039.
511. Greenwood R, Kendall K. Selection of suitable dispersants for aqueous suspensions of zirconia and titania powders using acoustophoresis. Journal of the European Ceramic Society. 1999;19(4):479-88.
512. Nasiru T, Avila L, Levine M. Determination of critical micelle concentrations using UV-visible spectroscopy. Journal of high school research. 2011;2:1-5.
513. Mohr A, Talbiersky P, Korth HG, Sustmann R, Boese R, Blaser D, et al. A new pyrene-based fluorescent probe for the determination of critical micelle concentrations. The journal of physical chemistry B. 2007;111(45):12985-92.
514. De Jong WH, Borm PJA. Drug delivery and nanoparticles:applications and hazards. International journal of nanomedicine. 2008;3(2):133-49.
515. Zhang Z, Feng S-S. The drug encapsulation efficiency, in vitro drug release, cellular uptake and cytotoxicity of paclitaxel-loaded poly(lactide)–tocopheryl polyethylene glycol succinate nanoparticles. Biomaterials. 2006;27(21):4025-33.
516. Weng J, Tong HHY, Chow SF. In Vitro Release Study of the Polymeric Drug Nanoparticles: Development and Validation of a Novel Method. Pharmaceutics. 2020;12(8):732.
517. Lu X-Y, Wu D-C, Li Z-J, Chen G-Q. Chpater 7 - Polymer Nanoparticles. In: Villaverde A, editor. Progress in Molecular Biology and Translational Science. 104: Academic Press; 2011. p. 299-323.
518. Hua S. Comparison of in vitro dialysis release methods of loperamide-encapsulated liposomal gel for topical drug delivery. International journal of nanomedicine. 2014;9:735.
519. Timothy M. Potter BWN, Jamie C. Rodriguez, Anna N. Ilinskaya,, Dobrovolskaia aMA. Analysis of Pro-inflammatory Cytokine and Type II

Interferon Induction by Nanoparticles. In: McNeil SE, editor. Characterization of Nanoparticles Intended for Drug Delivery. 2nd ed: Humana Press; 2018.
520. Riss TL, Moravec RA, Niles AL, Duellman S, Benink HA, Worzella TJ, et al. Cell viability assays. 2016.
521. Präbst K, Engelhardt H, Ringgeler S, Hübner H. Basic colorimetric proliferation assays: MTT, WST, and resazurin. Cell Viability Assays: Methods and Protocols. 2017:1-17.
522. Posimo JM, Unnithan AS, Gleixner AM, Choi HJ, Jiang Y, Pulugulla SH, et al. Viability assays for cells in culture. Journal of visualized experiments : JoVE. 2014(83):e50645-e.
523. Bender HR, Kane S, Zabel MD. Delivery of therapeutic siRNA to the CNS using cationic and anionic liposomes. Journal of visualized experiments: JoVE. 2016(113).
524. Fatokun AA, Liu JO, Dawson VL, Dawson TM. Identification through high-throughput screening of 4'-methoxyflavone and 3',4'-dimethoxyflavone as novel neuroprotective inhibitors of parthanatos. British journal of pharmacology. 2013;169(6):1263-78.
525. Sekerdag E, Lüle S, Bozdağ Pehlivan S, Öztürk N, Kara A, Kaffashi A, et al. A potential non-invasive glioblastoma treatment: Nose-to-brain delivery of farnesylthiosalicylic acid incorporated hybrid nanoparticles. Journal of Controlled Release. 2017;261:187-98.

526. Amini Y, Amel Jamehdar S, Sadri K, Zare S, Musavi D, Tafaghodi M. Different methods to determine the encapsulation efficiency of protein in PLGA nanoparticles. Bio-Medical Materials and Engineering. 2017;28:613-20.
527. Luo Z, Jin K, Pang Q, Shen S, Yan Z, Jiang T, et al. On-Demand Drug Release from Dual-Targeting Small Nanoparticles Triggered by High-Intensity Focused Ultrasound Enhanced Glioblastoma-Targeting Therapy. ACS Applied Materials & Interfaces. 2017;9(37):31612-25.
528. Villaverde A. Nanoparticles in translational science and medicine: Academic Press; 2011.
529. D'Souza S, Faraj JA, Giovagnoli S, DeLuca PP. IVIVC from long acting olanzapine microspheres. International journal of biomaterials. 2014;2014.
530. Salvati A, Pitek AS, Monopoli MP, Prapainop K, Bombelli FB, Hristov DR, et al. Transferrin-functionalized nanoparticles lose their targeting capabilities when a biomolecule corona adsorbs on the surface. Nature Nanotechnology. 2013;8(2):137-43.
531. Bostanudin MF, Lalatsa A, Górecki DC, Barbu E. Engineering butylglyceryl-modified polysaccharides towards nanomedicines for brain drug delivery. Carbohydrate Polymers. 2020;236:116060.
532. Deepika D, Dewangan HK, Maurya L, Singh S. Intranasal Drug Delivery of Frovatriptan Succinate–Loaded Polymeric Nanoparticles for Brain Targeting. Journal of pharmaceutical sciences. 2019;108(2):851-9.
533. Saar K, Lindgren M, Hansen M, Eiríksdóttir E, Jiang Y, Rosenthal-Aizman K, et al. Cell-penetrating peptides: A comparative membrane toxicity study. Analytical Biochemistry. 2005;345(1):55-65.
534. Hühn D, Kantner K, Geidel C, Brandholt S, De Cock I, Soenen S, et al. Polymer-coated nanoparticles interacting with proteins and cells: focusing on the sign of the net charge, ACS Nano 7 (2013) 3253–3263.
535. Yu S, Xu X, Feng J, Liu M, Hu K. Chitosan and chitosan coating nanoparticles for the treatment of brain disease. International Journal of Pharmaceutics. 2019;560:282-93.
536. He H, Yao J, Zhang Y, Chen Y, Wang K, Lee RJ, et al. Solid lipid nanoparticles as a drug delivery system to across the blood-brain barrier. Biochemical and Biophysical Research Communications. 2019;519(2):385-90.
537. Lee KJ, Browning LM, Nallathamby PD, Xu X-HN. Study of charge-dependent transport and toxicity of peptide-functionalized silver nanoparticles using zebrafish embryos and single nanoparticle plasmonic spectroscopy. Chemical research in toxicology. 2013;26(6):904-17.
538. Kai W, Xiaojun X, Ximing P, Zhenqing H, Qiqing Z. Cytotoxic effects and the mechanism of three types of magnetic nanoparticles on human hepatoma BEL-7402 cells. Nanoscale research letters. 2011;6(1):480-.
539. Tudisco C, Cambria MT, Giuffrida AE, Sinatra F, Anfuso CD, Lupo G, et al. Comparison Between Folic Acid and gH625 Peptide-Based Functionalization of Fe3O4 Magnetic Nanoparticles for Enhanced Cell Internalization. Nanoscale Research Letters. 2018;13(1):45.
540. Givan AL. Flow cytometry: first principles: John Wiley & Sons; 2013.
541. Salvati A, Nelissen I, Haase A, Åberg C, Moya S, Jacobs A, et al. Quantitative measurement of nanoparticle uptake by flow cytometry illustrated by an interlaboratory comparison of the uptake of labelled polystyrene nanoparticles. NanoImpact. 2018;9:42-50.
542. Díaz M, Herrero M, García LA, Quirós C. Application of flow cytometry to industrial microbial bioprocesses. Biochemical Engineering Journal. 2010;48(3):385-407.
543. Adan A, Alizada G, Kiraz Y, Baran Y, Nalbant A. Flow cytometry: basic principles and applications. Critical Reviews in Biotechnology. 2017;37(2):163-76.
544. Benfer M, Kissel T. Cellular uptake mechanism and knockdown activity of siRNA-loaded biodegradable DEAPA-PVA-g-PLGA nanoparticles. European Journal of Pharmaceutics and Biopharmaceutics. 2012;80(2):247-56.
545. Xia T, Kovochich M, Liong M, Meng H, Kabehie S, George S, et al. Polyethyleneimine Coating Enhances the Cellular Uptake of Mesoporous Silica Nanoparticles and Allows Safe Delivery of siRNA and DNA Constructs. ACS Nano. 2009;3(10):3273-86.
546. Zhao E, Zhao Z, Wang J, Yang C, Chen C, Gao L, et al. Surface engineering of gold nanoparticles for in vitro siRNA delivery. Nanoscale. 2012;4(16):5102-9.

547. Au - Menon V, Au - Thomas R, Au - Ghale AR, Au - Reinhard C, Au - Pruszak J. Flow Cytometry Protocols for Surface and Intracellular Antigen Analyses of Neural Cell Types. JoVE. 2014(94):e52241.
548. Klein S, Petersen S, Taylor U, Rath D, Barcikowski S. Quantitative visualization of colloidal and intracellular gold nanoparticles by confocal microscopy. Journal of Biomedical Optics. 2010;15(3):036015.
549. Croix CMS, Shand SH, Watkins SC. Confocal microscopy: comparisons, applications, and problems. BioTechniques. 2005;39(6S):S2-S5.
550. Portis AM, Carballo G, Baker GL, Chan C, Walton SP. Confocal microscopy for the analysis of siRNA delivery by polymeric nanoparticles. Microsc Res Tech. 2010;73(9):878-85.
551. Risnayanti C, Jang Y-S, Lee J, Ahn HJ. PLGA nanoparticles co-delivering MDR1 and BCL2 siRNA for overcoming resistance of paclitaxel and cisplatin in recurrent or advanced ovarian cancer. Scientific Reports. 2018;8(1):7498.
552. Bagchi S, Chhibber T, Lahooti B, Verma A, Borse V, Jayant RD. In-vitro blood-brain barrier models for drug screening and permeation studies: an overview. Drug design, development and therapy. 2019;13:3591.
553. Stone NL, England TJ, O'Sullivan SE. A novel transwell blood brain barrier model using primary human cells. Frontiers in cellular neuroscience. 2019;13:230.
554. Bagchi S, Chhibber T, Lahooti B, Verma A, Borse V, Jayant RD. In-vitro blood-brain barrier models for drug screening and permeation studies: an overview. Drug design, development and therapy. 2019;13:3591-605.
555. Uva L, Librizzi L, Marchi N, Noe F, Bongiovanni R, Vezzani A, et al. Acute induction of epileptiform discharges by pilocarpine in the in vitro isolated guinea-pig brain requires enhancement of blood–brain barrier permeability. Neuroscience. 2008;151(1):303-12.
556. Butt AM, Jones HC. Effect of histamine and antagonists on electrical resistance across the blood-brain barrier in rat brain-surface microvessels. Brain research. 1992;569(1):100-5.
557. Sakurai E, Watanabe T, Yanai K. Uptake of L-histidine and histamine biosynthesis at the blood-brain barrier. Inflammation Research. 2009;58:34.
558. Islam Y, Aneesa K, Pluchino S, Sivakumaran M, Teixidò M, Leach A, et al. Development of Brain Targeting Peptide Based MMP-9 Inhibiting Nanoparticles for the Treatment of Brain Diseases with Elevated MMP-9 Activity. Journal of pharmaceutical sciences. 2020.
559. Riedel F, Götte K, Schwalb J, Hörmann K. Serum levels of matrix metalloproteinase-2 and -9 in patients with head and neck squamous cell carcinoma. Anticancer research. 2000;20(5a):3045-9.
560. Jonsson A, Hjalmarsson C, Falk P, Ivarsson M-L. Levels of matrix metalloproteinases differ in plasma and serum – aspects regarding analysis of biological markers in cancer. British Journal of Cancer. 2016;115(6):703-6.
561. Lo Giudice MC, Herda LM, Polo E, Dawson KA. In situ characterization of nanoparticle biomolecular interactions in complex biological media by flow cytometry. Nature Communications. 2016;7(1):13475.
562. Zucker RM, Ortenzio J, Degn LL, Lerner JM, Boyes WK. Biophysical comparison of four silver nanoparticles coatings using microscopy, hyperspectral imaging and flow cytometry. PLoS One. 2019;14(7):e0219078.
563. Lei C, Davoodi P, Zhan W, Chow PK-H, Wang C-H. Development of Nanoparticles for Drug Delivery to Brain Tumor: The Effect of Surface Materials on Penetration Into Brain Tissue. Journal of pharmaceutical sciences. 2019;108(5):1736-45.
564. Xia Y, Wang C, Xu T, Li Y, Guo M, Lin Z, et al. Targeted delivery of HES5-siRNA with novel polypeptide-modified nanoparticles for hepatocellular carcinoma therapy. RSC Advances. 2018;8(4):1917-26.
565. Muralidharan R, Babu A, Amreddy N, Srivastava A, Chen A, Zhao YD, et al. Tumor-targeted Nanoparticle Delivery of HuR siRNA Inhibits Lung Tumor Growth In Vitro and In Vivo By Disrupting the Oncogenic Activity of the RNA-binding Protein HuR. Mol Cancer Ther. 2017;16(8):1470-86.

566. Zhu H, Zhang S, Ling Y, Meng G, Yang Y, Zhang W. pH-responsive hybrid quantum dots for targeting hypoxic tumor siRNA delivery. Journal of controlled release : official journal of the Controlled Release Society. 2015;220(Pt A):529-44.
567. Shimomura K, Okura T, Kato S, Couraud P-O, Schermann J-M, Terasaki T, et al. Functional expression of a proton-coupled organic cation (H+/OC) antiporter in human brain capillary endothelial cell line hCMEC/D3, a human blood–brain barrier model. Fluids and Barriers of the CNS. 2013;10(1):1-10.
568. Gericke B, Römermann K, Noack A, Noack S, Kronenberg J, Blasig IE, et al. A face-to-face comparison of claudin-5 transduced human brain endothelial (hCMEC/D3) cells with porcine brain endothelial cells as blood–brain barrier models for drug transport studies. Fluids and Barriers of the CNS. 2020;17(1):53.
569. Lopalco A, Cutrignelli A, Denora N, Lopedota A, Franco M, Laquintana V. Transferrin functionalized liposomes loading dopamine HCl: development and permeability studies across an in vitro model of human blood–brain barrier. Nanomaterials. 2018;8(3):178.
570. Wu L-P, Ahmadvand D, Su J, Hall A, Tan X, Farhangrazi ZS, et al. Crossing the blood-brain-barrier with nanoligand drug carriers self-assembled from a phage display peptide. Nature communications. 2019;10(1):1-16.
571. Mi Y, Mao Y, Cheng H, Ke G, Liu M, Fang C, et al. Studies of blood–brain barrier permeability of gastrodigenin in vitro and in vivo. Fitoterapia. 2020;140:104447.
572. Piazzini V, Landucci E, D'Ambrosio M, Tiozzo Fasiolo L, Cinci L, Colombo G, et al. Chitosan coated human serum albumin nanoparticles: A promising strategy for nose-to-brain drug delivery. International Journal of Biological Macromolecules. 2019;129:267-80.
573. Srinivasan B, Kolli AR, Esch MB, Abaci HE, Shuler ML, Hickman JJ. TEER measurement techniques for in vitro barrier model systems. J Lab Autom. 2015;20(2):107-26.
574. Maherally Z, Fillmore HL, Tan SL, Tan SF, Jassam SA, Quack FI, et al. Real-time acquisition of transendothelial electrical resistance in an all-human, in vitro, 3-dimensional, blood–brain barrier model exemplifies tight-junction integrity. The FASEB Journal. 2018;32(1):168-82.
575. Biemans EALM, Jäkel L, de Waal RMW, Kuiperij HB, Verbeek MM. Limitations of the hCMEC/D3 cell line as a model for Aβ clearance by the human blood-brain barrier. J Neurosci Res. 2017;95(7):1513-22.
576. Förster C, Burek M, Romero IA, Weksler B, Couraud PO, Drenckhahn D. Differential effects of hydrocortisone and TNFα on tight junction proteins in an in vitro model of the human blood–brain barrier. The Journal of physiology. 2008;586(7):1937-49.
577. Cucullo L, Couraud P-O, Weksler B, Romero I-A, Hossain M, Rapp E, et al. Immortalized human brain endothelial cells and flow-based vascular modeling: a marriage of convenience for rational neurovascular studies. Journal of cerebral blood flow & metabolism. 2008;28(2):312-28.
578. Winger RC, Koblinski JE, Kanda T, Ransohoff RM, Muller WA. Rapid remodeling of tight junctions during paracellular diapedesis in a human model of the blood-brain barrier. J Immunol. 2014;193(5):2427-37.
579. Wang Z, Cai X-J, Qin J, Xie F-J, Han N, Lu H-Y. The role of histamine in opening blood-tumor barrier. Oncotarget. 2016;7(21):31299-310.
580. Wu C-Y, Wu M-S, Chiang E-P, Chen Y-J, Chen C-J, Chi N-H, et al. Plasma Matrix Metalloproteinase-9 Level Is Better than Serum Matrix Metalloproteinase-9 Level to Predict Gastric Cancer Evolution. Clinical Cancer Research. 2007;13(7):2054.
581. Khongkow M, Yata T, Boonrungsiman S, Ruktanonchai UR, Graham D, Namdee K. Surface modification of gold nanoparticles with neuron-targeted exosome for enhanced blood–brain barrier penetration. Scientific Reports. 2019;9(1):8278.
582. Song Y, Du D, Li L, Xu J, Dutta P, Lin Y. In Vitro Study of Receptor-Mediated Silica Nanoparticles Delivery across Blood–Brain Barrier. ACS Applied Materials & Interfaces. 2017;9(24):20410-6.
583. Somani S, Robb G, Pickard BS, Dufès C. Enhanced gene expression in the brain following intravenous administration of lactoferrin-bearing polypropylenimine dendriplex. Journal of Controlled Release. 2015;217:235-42.

584. Böckenhoff A, Cramer S, Wölte P, Knieling S, Wohlenberg C, Gieselmann V, et al. Comparison of five peptide vectors for improved brain delivery of the lysosomal enzyme arylsulfatase A. Journal of Neuroscience. 2014;34(9):3122-9.
585. Sun X, Shi J, Fu X, Yang Y, Zhang H. Long-term in vivo biodistribution and toxicity study of functionalized near-infrared persistent luminescence nanoparticles. Scientific Reports. 2018;8(1):10595.
586. An YH, Freidman RJ. Animal models in orthopaedic research: CRC press; 1998.
587. Bronzino JD, Peterson DR. Tissue engineering and artificial organs: CRC press; 2016.
588. Miwa T, Tachii K, Wei F-Y, Kaitsuka T, Tomizawa K. Intranasal Drug Delivery into Mouse Nasal Mucosa and Brain Utilizing Arginine-Rich Cell-Penetrating Peptide-Mediated Protein Transduction. International Journal of Peptide Research and Therapeutics. 2020;26(3):1643-50.
589. Sohet F, Daneman R. Genetic mouse models to study blood–brain barrier development and function. Fluids and Barriers of the CNS. 2013;10(1):3.
590. Constantinescu CS, Farooqi N, O'Brien K, Gran B. Experimental autoimmune encephalomyelitis (EAE) as a model for multiple sclerosis (MS). Br J Pharmacol. 2011;164(4):1079-106.
591. Marín-Padilla M. The human brain intracerebral microvascular system: development and structure. Frontiers in neuroanatomy. 2012;6:38.
592. Mito T, Konomi H, Houdou S, Takashima S. Immunohistochemical study of the vasculature in the developing brain. Pediatric neurology. 1991;7(1):18-22.
593. Fantin A, Vieira JM, Plein A, Maden CH, Ruhrberg C. The embryonic mouse hindbrain as a qualitative and quantitative model for studying the molecular and cellular mechanisms of angiogenesis. Nature protocols. 2013;8(2):418-29.
594. Chertok B, Moffat BA, David AE, Yu F, Bergemann C, Ross BD, et al. Iron oxide nanoparticles as a drug delivery vehicle for MRI monitored magnetic targeting of brain tumors. Biomaterials. 2008;29(4):487-96.
595. Vance SZ. Modulation of Amyloid-β Aggregation via Small Molecules and Glycine Zipper Alterations: University of South Carolina; 2018.
596. Nilsson P, Iwata N, Muramatsu Si, Tjernberg LO, Winblad B, Saido TC. Gene therapy in Alzheimer's disease–potential for disease modification. Journal of cellular and molecular medicine. 2010;14(4):741-57.
597. Alvarez-Erviti L, Seow Y, Yin H, Betts C, Lakhal S, Wood MJ. Delivery of siRNA to the mouse brain by systemic injection of targeted exosomes. Nature biotechnology. 2011;29(4):341-5.
598. Park TE, Singh B, Li H, Lee JY, Kang SK, Choi YJ, et al. Enhanced BBB permeability of osmotically active poly(mannitol-co-PEI) modified with rabies virus glycoprotein via selective stimulation of caveolar endocytosis for RNAi therapeutics in Alzheimer's disease. Biomaterials. 2015;38:61-71.
599. Tagalakis AD, Castellaro S, Zhou H, Bienemann A, Munye MM, McCarthy D, et al. A method for concentrating lipid peptide DNA and siRNA nanocomplexes that retains their structure and transfection efficiency. International journal of nanomedicine. 2015;10:2673-83.
600. van den Boorn JG, Schlee M, Coch C, Hartmann G. SiRNA delivery with exosome nanoparticles. Nature Biotechnology. 2011;29(4):325-6.
601. Khvorova A, Reynolds A, Leake D, Marshall W, Read S, Scaringe S. siRNA targeting beta secretase (BACE). Google Patents; 2011.
602. Liu Y, An S, Li J, Kuang Y, He X, Guo Y, et al. Brain-targeted co-delivery of therapeutic gene and peptide by multifunctional nanoparticles in Alzheimer's disease mice. Biomaterials. 2016;80:33-45.
603. Wang P, Zheng X, Guo Q, Yang P, Pang X, Qian K, et al. Systemic delivery of BACE1 siRNA through neuron-targeted nanocomplexes for treatment of Alzheimer's disease. Journal of Controlled Release. 2018;279:220-33.
604. Wilkinson GR. Drug metabolism and variability among patients in drug response. New England Journal of Medicine. 2005;352(21):2211-21.
605. Garza AZ, Park SB, Kocz R. Drug Elimination. StatPearls [Internet]: StatPearls Publishing; 2019.

606. Cardarelli F, Digiacomo L, Marchini C, Amici A, Salomone F, Fiume G, et al. The intracellular trafficking mechanism of Lipofectamine-based transfection reagents and its implication for gene delivery. Scientific Reports. 2016;6(1):25879.
607. Mo RH, Zaro JL, Ou J-HJ, Shen W-C. Effects of Lipofectamine 2000/siRNA complexes on autophagy in hepatoma cells. Mol Biotechnol. 2012;51(1):1-8.
608. Wang D, El-Amouri SS, Dai M, Kuan C-Y, Hui DY, Brady RO, et al. Engineering a lysosomal enzyme with a derivative of receptor-binding domain of apoE enables delivery across the blood-brain barrier. Proceedings of the National Academy of Sciences of the United States of America. 2013;110(8):2999-3004.
609. Kumar P, Wu H, McBride JL, Jung K-E, Kim MH, Davidson BL, et al. Transvascular delivery of small interfering RNA to the central nervous system. Nature. 2007;448(7149):39-43.
610. Alvarez-Erviti L, Seow Y, Yin H, Betts C, Lakhal S, Wood MJA. Delivery of siRNA to the mouse brain by systemic injection of targeted exosomes. Nature Biotechnology. 2011;29(4):341-5.
611. Chung EP, Cotter JD, Prakapenka AV, Cook RL, DiPerna DM, Sirianni RW. Targeting small molecule delivery to the brain and spinal cord via intranasal administration of rabies virus glycoprotein (RVG29)-Modified PLGA nanoparticles. Pharmaceutics. 2020;12(2):93.
612. Khongkow M, Yata T, Boonrungsiman S, Ruktanonchai UR, Graham D, Namdee K. Surface modification of gold nanoparticles with neuron-targeted exosome for enhanced blood-brain barrier penetration. Scientific reports. 2019;9(1):8278-.
613. Mohr A, Talbiersky P, Korth H-G, Sustmann R, Boese R, Bläser D, et al. A New Pyrene-Based Fluorescent Probe for the Determination of Critical Micelle Concentrations. The Journal of Physical Chemistry B. 2007;111(45):12985-92.
614. Ong SGM, Ming LC, Lee KS, Yuen KH. Influence of the Encapsulation Efficiency and Size of Liposome on the Oral Bioavailability of Griseofulvin-Loaded Liposomes. Pharmaceutics. 2016;8(3):25.
615. Jeong YI, Kim SH, Jung TY, Kim IY, Kang SS, Jin YH, et al. Polyion complex micelles composed of all-trans retinoic acid and poly (ethylene glycol)-grafted-chitosan. Journal of pharmaceutical sciences. 2006;95(11):2348-60.
616. Raj R, Wairkar S, Sridhar V, Gaud R. Pramipexole dihydrochloride loaded chitosan nanoparticles for nose to brain delivery: Development, characterization and in vivo anti-Parkinson activity. International journal of biological macromolecules. 2018;109:27-35.
617. Lopalco A, Ali H, Denora N, Rytting E. Oxcarbazepine-loaded polymeric nanoparticles: development and permeability studies across in vitro models of the blood-brain barrier and human placental trophoblast. International journal of nanomedicine. 2015;10:1985-96.

Appendices

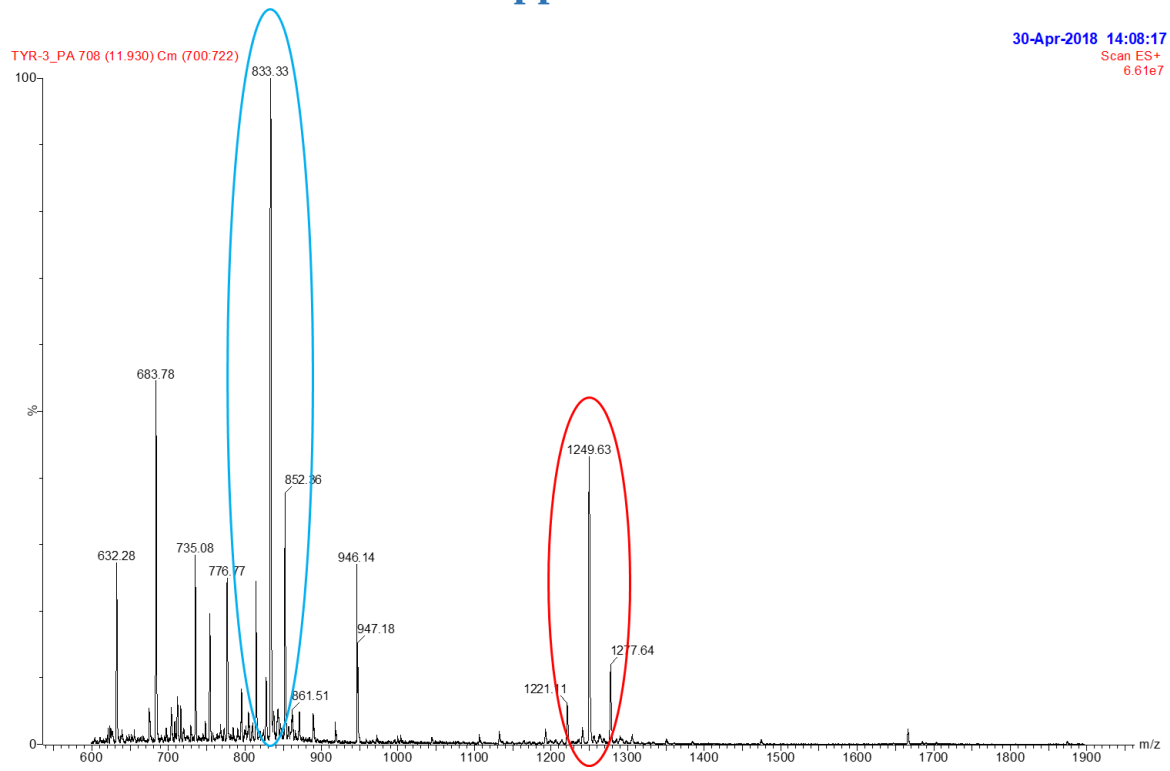

Appendix -1. LCMS chromatogram of TYR-3_PA (C_{16}-GGGRPLGLWCDIFTNSRGKRA) showing the masses of 833.33 (encircled blue, $[M+2H]^{3+}$)and 1249.63(encircled red, $[M+2H]^{2+}$)with retention time of 11.93 minutes.

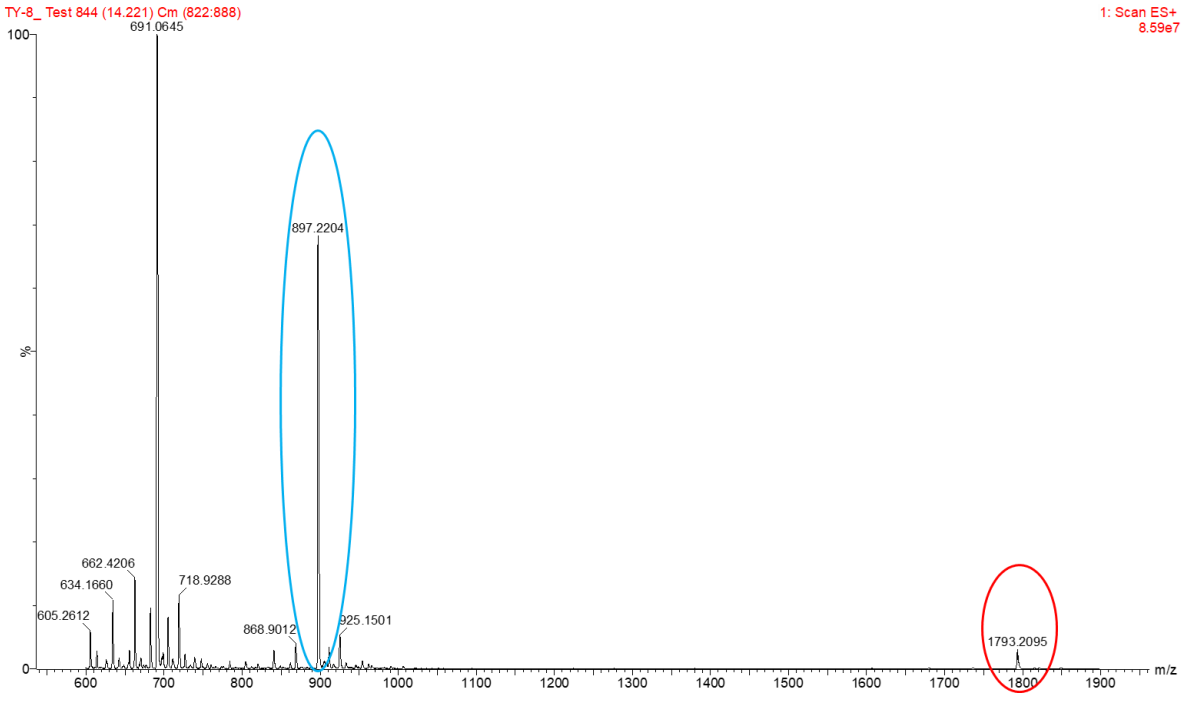

Appendix -2. LCMS chromatogram of TY-8_CHF (C_{27}-GGGWGPIALRKLR) showing the masses of 897.2204 (encircled blue, $[M+2H]^{2+}$)and 1793.2095(encircled red, $[M+2H]^{+}$)with retention time of 14.22 minutes.

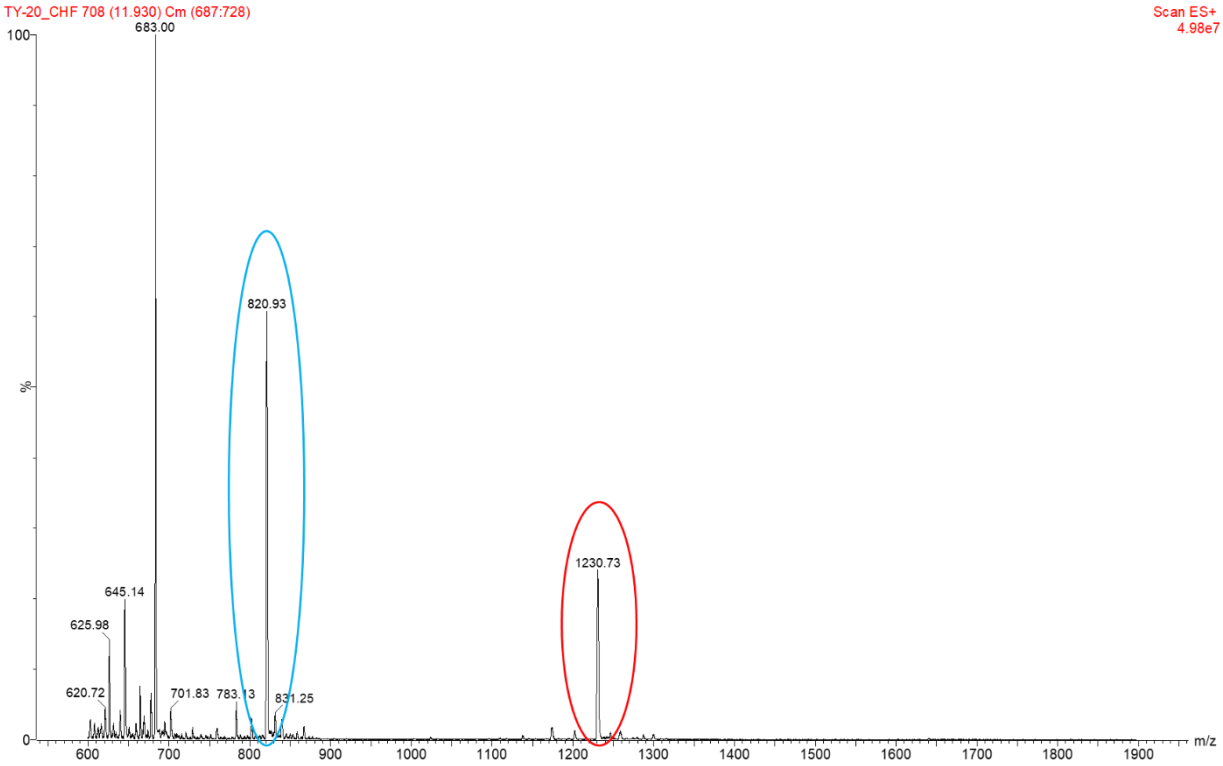

Appendix -3. LCMS chromatogram of TY-20_CHF (C_{27}-GGGWGPIALRKLRKRLLR) showing the masses of 820.93 (encircled blue, $[M+2H]^{2+}$)and 1230.3(encircled red, $[M+2H]^{+}$)with retention time of 11.93 minutes.

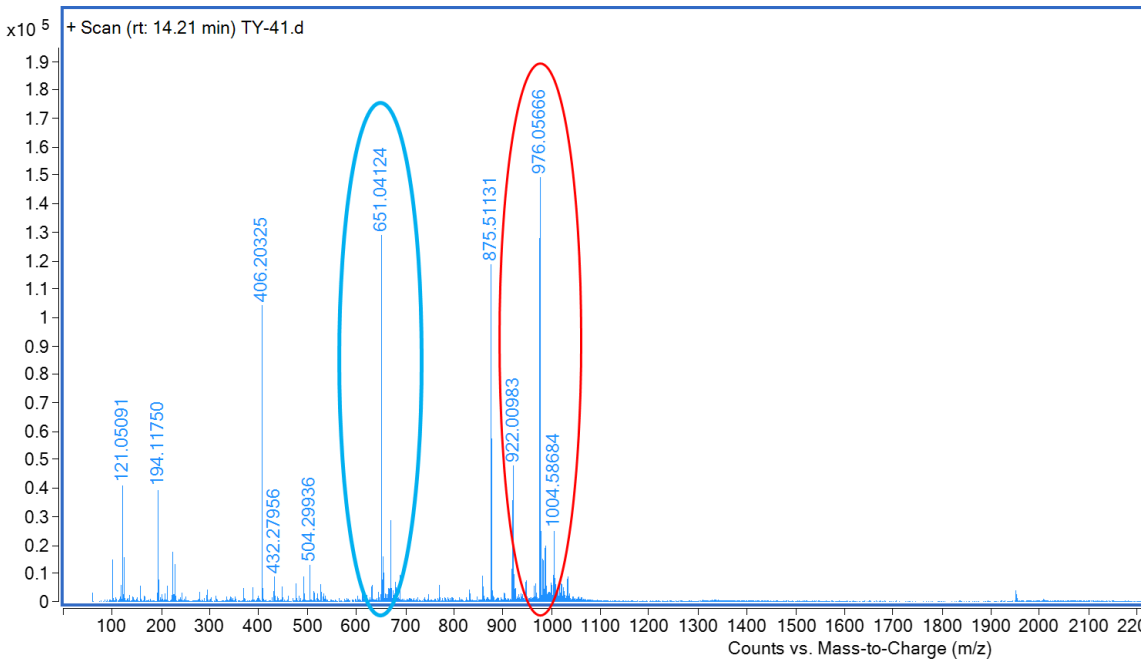

Appendix -4. LCMS chromatogram of TY-41_CHF (C_{27}- GGGCDIFTNSRGKRA) showing the masses of 651.04124 (encircled blue, $[M+2H]^{2+}$)and 976.05666 (encircled red, $[M+2H]^{+}$)with retention time of 14.21 minutes.

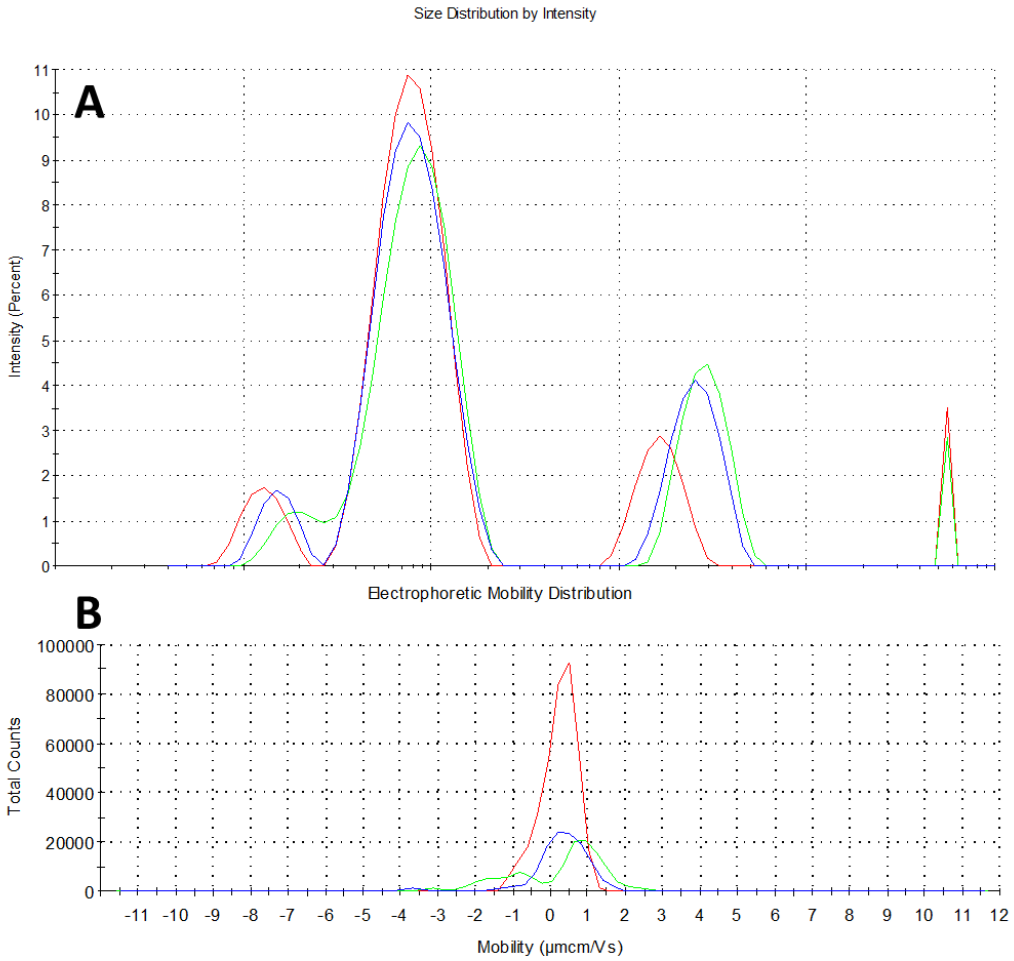

Appendix -5. DLS chromatograms for TY-7_CHF (C_{27}-WGPIALRKLR) at 2.5 mg/mL in distilled water. ***A****) Particle size graph for TY-7_CHF showing NPs size of 111.66 ± 12.39 nm with Pdi of 0.223,* ***B****) Zeta potential graph for TY-7_CHF showing the surface charge of 2.96 ± 6.18.*

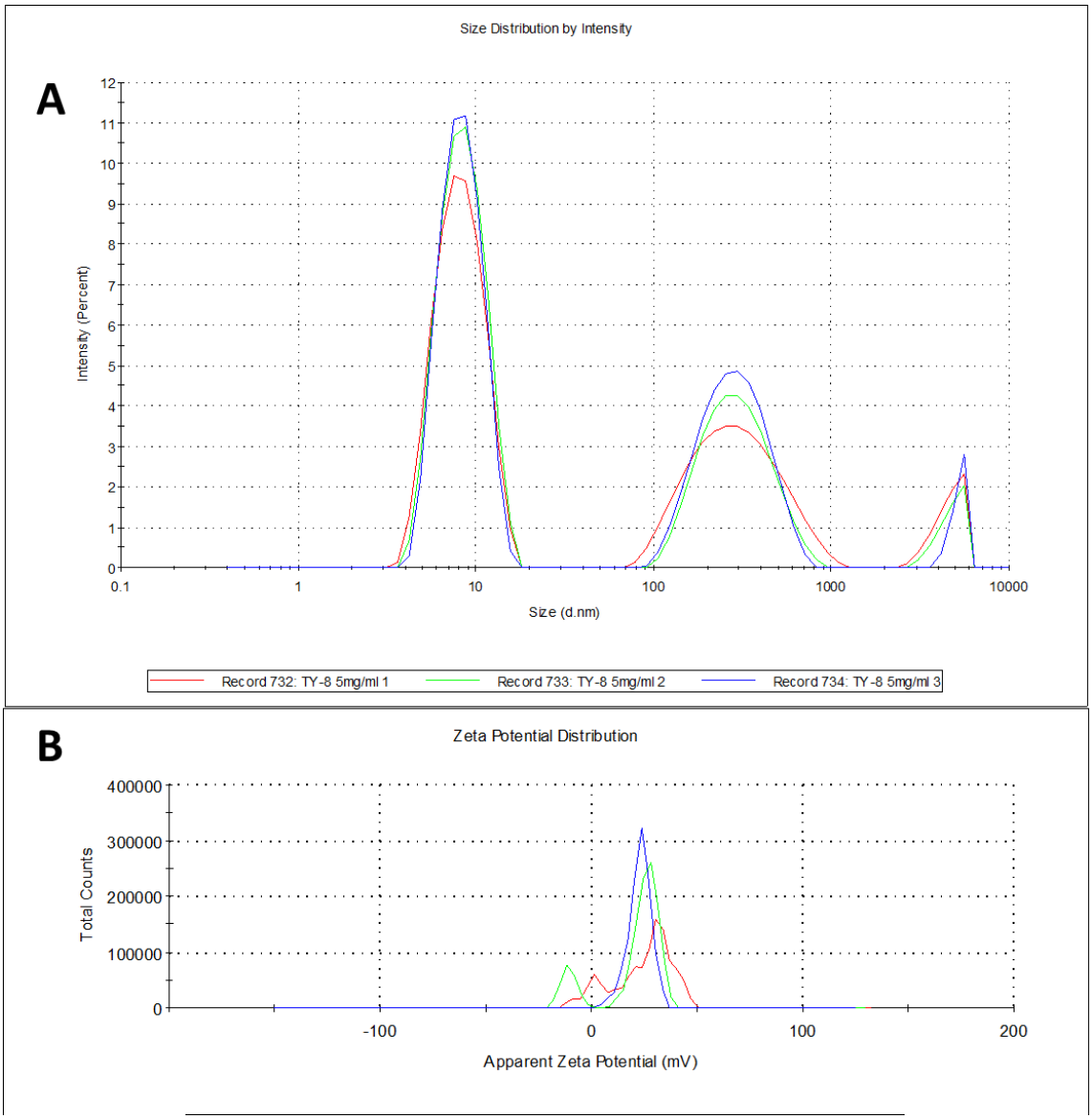

Appendix -6. DLS chromatograms for TY-8_CHF (C_{27}-GGGWGPIALRKLR) at 2.5 mg/mL in distilled water. ***A****) Particle size graph for TY-8_CHF showing NPs size of 32.89 ± 17.17 nm with Pdi of 0.565,* ***B****) Zeta potential graph for TY-8_CHF showing the surface charge of 22.9 ± 5.39.*

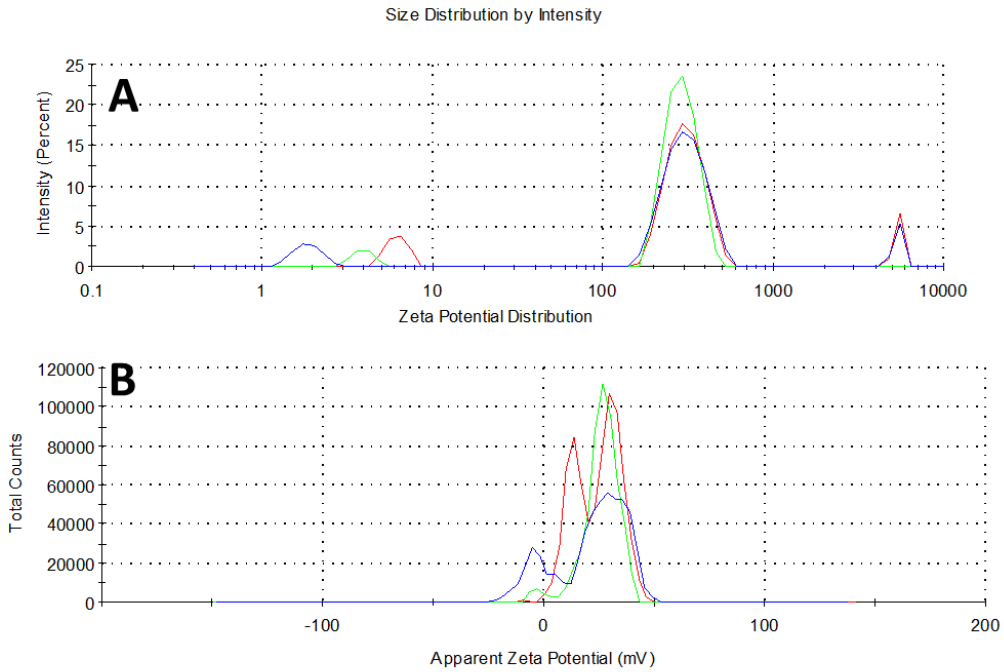

Appendix -7. DLS chromatograms for TY-13_CHF (C_{27}-GGGCKAPETALC) at 2.5 mg/mL in distilled water. ***A****) Particle size graph for TY-13_CHF showing NPs size of 81.4 ± 7.65 nm with Pdi of 0.429,* ***B****) Zeta potential graph for TY-13_CHF showing the surface charge of 36.53 ± 1.37.*

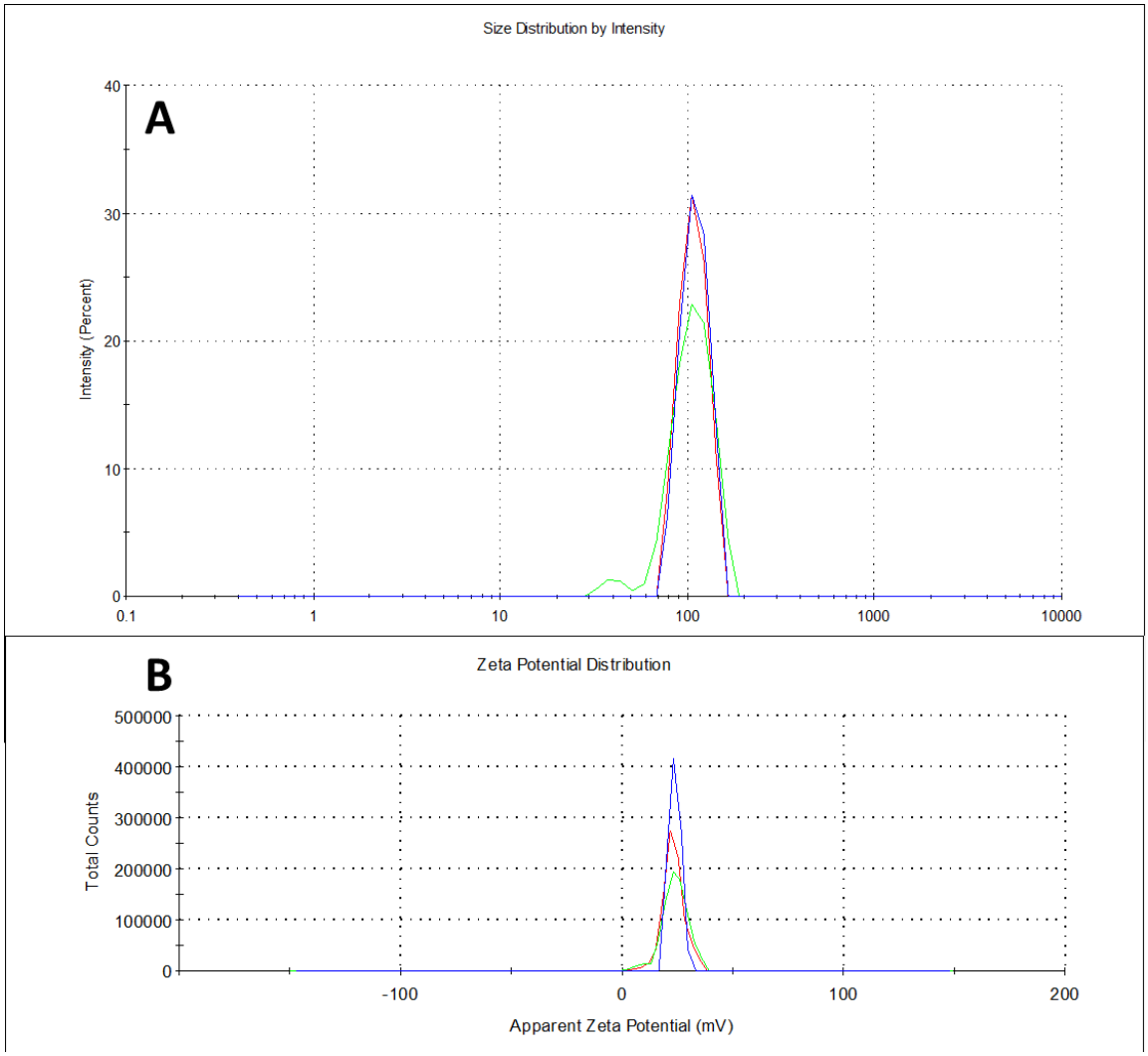

*Appendix -8. DLS chromatograms for TY-37 (PIPLAIFCKAPETALC) at 2.5 mg/mL in distilled water. **A**) Particle size graph for TY-37 showing NPs size of 108.51 ± 17.84 nm with Pdi of 0.577, **B**) Zeta potential graph for TY-37 showing the surface charge of 23.8 ± 2.63.*

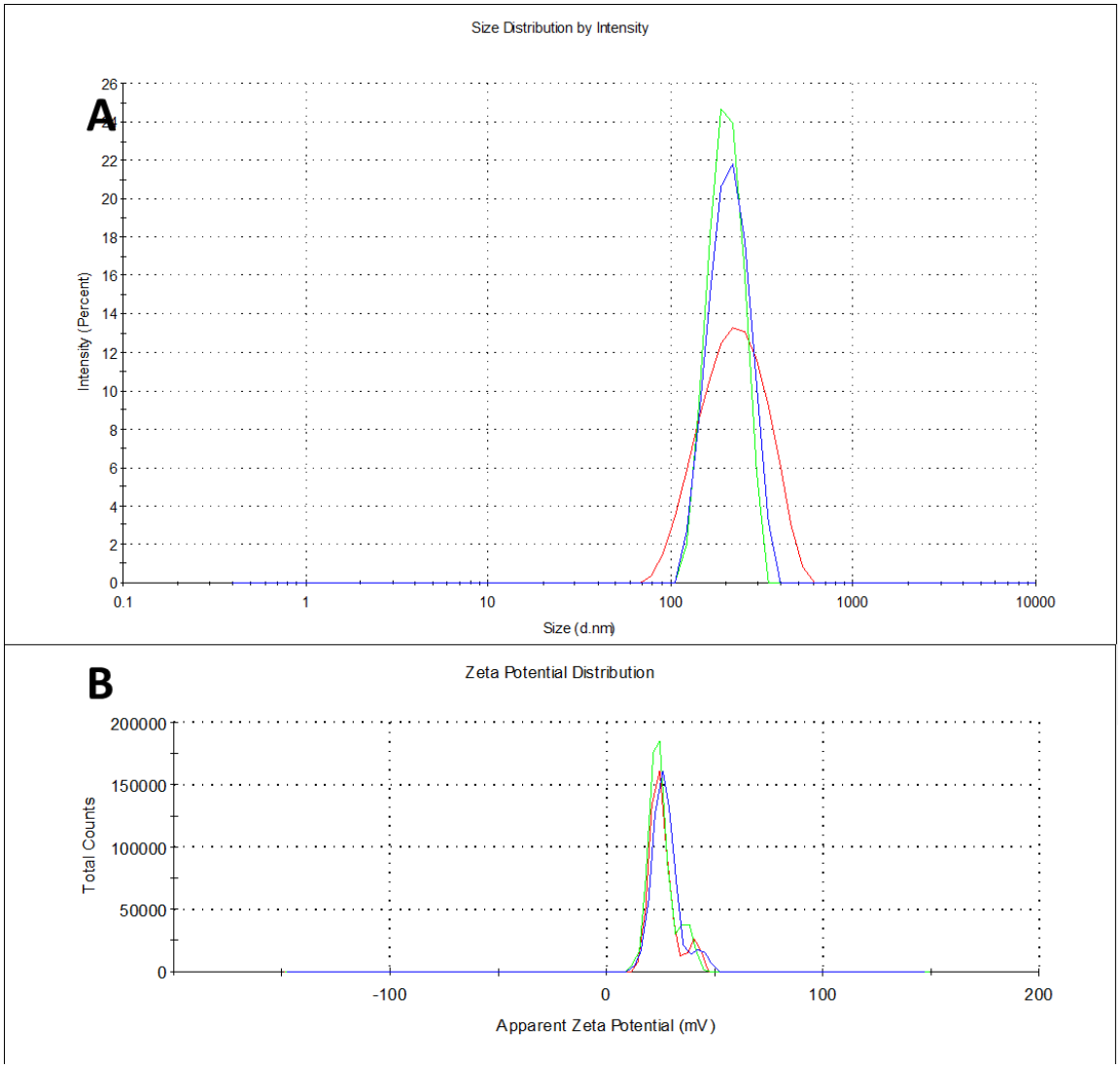

*Appendix -9. DLS chromatograms for TY-44 (PIPLAIFCKAPETALC) at 2.5 mg/mL in distilled water. **A**) Particle size graph for TY-44 showing NPs size of 266.9 ± 22.43 nm with Pdi of 0.408, **B**) Zeta potential graph for TY-44 showing the surface charge of 27.40 ± 4.97.*

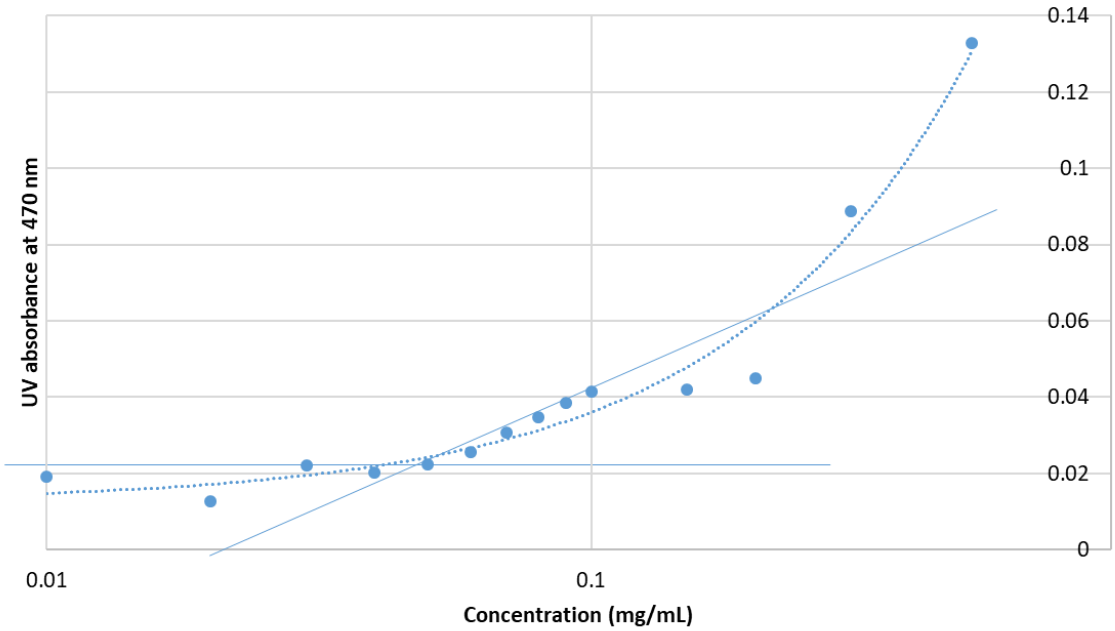

Appendix -10. CMC plot for TYR-3_PA (C16-GGGRPLGLWCDIFTNSRGKRA) in saline solution.

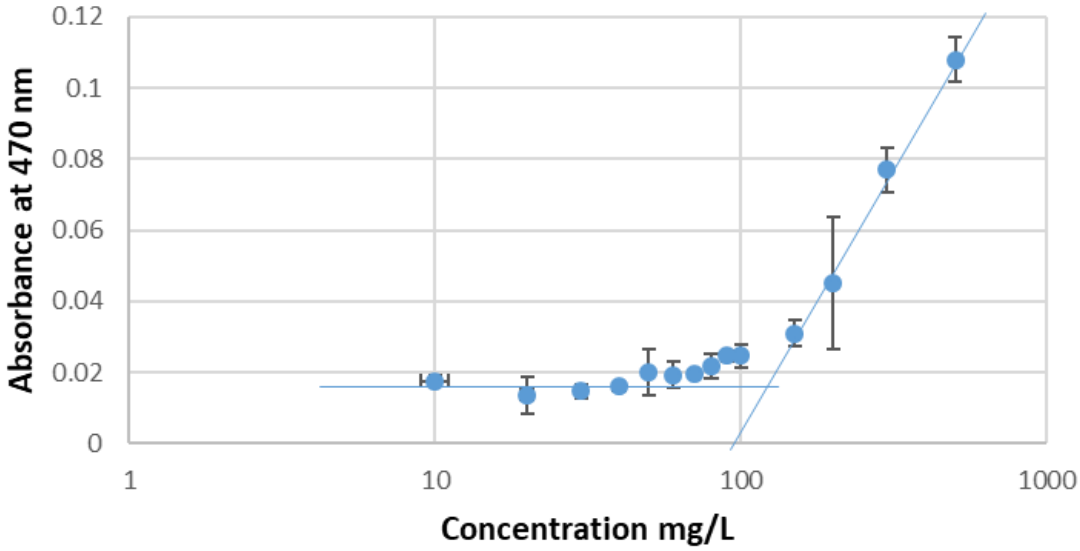

Appendix -11. CMC plot for TY-7_CHF (C_{27}-WGPIALRKLR) in saline solution.

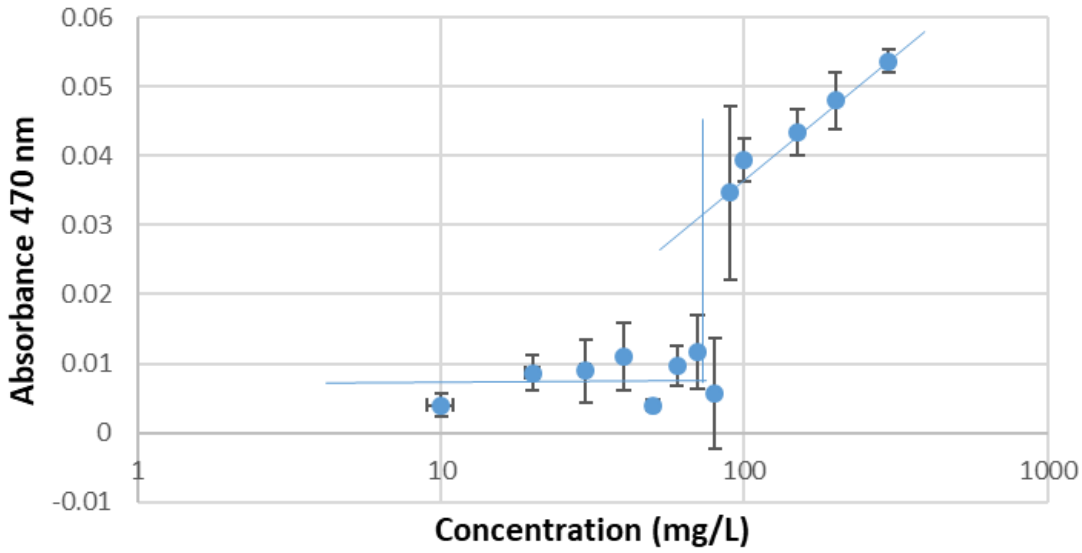

Appendix -12. CMC plot for TY-8_CHF (C_{27}-GGGWGPIALRKLR) in saline solution.

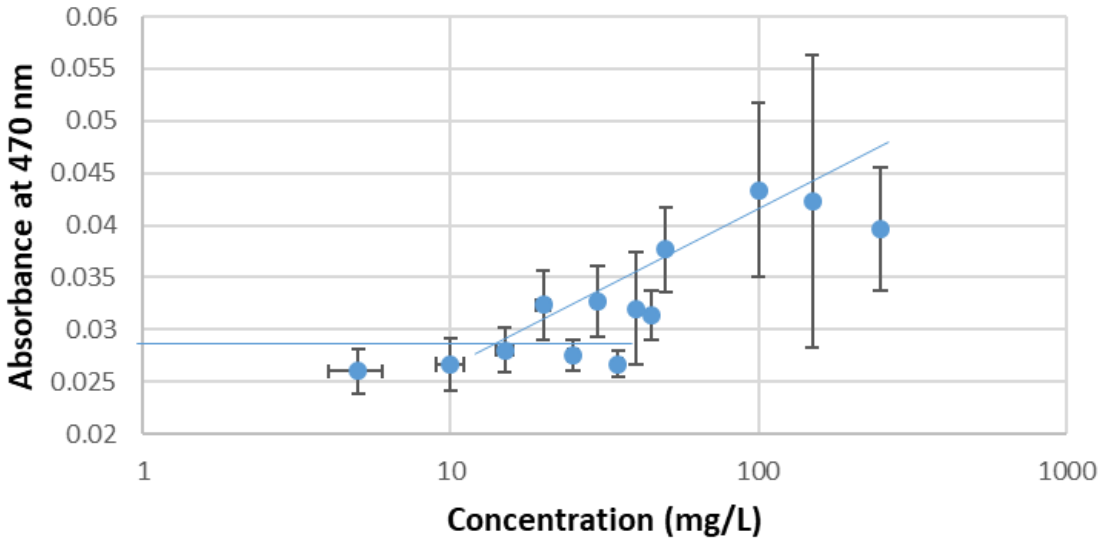

Appendix -13. CMC plot for TY-13_ CHF (C_{27}-GGGCKAPETALC) in saline solution.

List of publications

- Islam Y, Leach AG, Smith J, Pluchino S, Coxonl CR, Sivakumaran M, Downing J, Fatokun AA, Teixidò M, Ehtezazi T. Peptide based drug delivery systems to the brain. Nano Express. 2020 May 21;1(1):012002.
- Islam Y, Khalid A, Pluchino S, Sivakumaran M, Teixidò M, Leach A, Fatokun AA, Downing J, Coxon C, Ehtezazi T. Development of Brain Targeting Peptide Based MMP-9 Inhibiting Nanoparticles for the Treatment of Brain Diseases with Elevated MMP-9 Activity. Journal of Pharmaceutical Sciences. 2020 Oct 1;109(10):3134-44.
- Islam Y, Ehtezazi P, Cashmore A, Marinsalda E, Leach AG, Coxon CR, Fatokun AA, Sexton DW, Khan I, Zouganelis G, Downing J. The Inclusion of a Matrix Metalloproteinase-9 Responsive Sequence in Self-assembled Peptide-based Brain-Targeting Nanoparticles Improves the Efficiency of Nanoparticles Crossing the Blood-Brain Barrier at Elevated MMP-9 Levels. Journal of Pharmaceutical Sciences. 2020 Dec 15.